UNIVERSITÉ DE MONTRÉAL

SYNTHESIS AND APPLICATIONS OF ELECTROMAGNETIC METASURFACES

KARIM ACHOURI
DÉPARTEMENT DE GÉNIE ÉLECTRIQUE
ÉCOLE POLYTECHNIQUE DE MONTRÉAL

THÈSE PRÉSENTÉE EN VUE DE L'OBTENTION
DU DIPLÔME DE PHILOSOPHIÆ DOCTOR
(GÉNIE ÉLECTRIQUE)
AOÛT 2017

UNIVERSITÉ DE MONTRÉAL

ÉCOLE POLYTECHNIQUE DE MONTRÉAL

Cette thèse intitulée :

SYNTHESIS AND APPLICATIONS OF ELECTROMAGNETIC METASURFACES

présentée par: ACHOURI Karim
en vue de l'obtention du diplôme de: Philosophiæ Doctor
a été dûment acceptée par le jury d'examen constitué de :

M. LAURIN Jean-Jacques, Ph. D., président
M. CALOZ Christophe, Ph. D., membre et directeur de recherche
M. MACI Stefano, Ph. D., membre
M. TRETYAKOV Sergei, Ph. D., membre externe

DEDICATION

To my family and friends.

ACKNOWLEDGEMENTS

First and foremost, I would like to thank my supervisor Prof. Christophe Caloz for accepting me as his student and for his continued support, advice and motivation. His guidance has been tremendously helpful for the successful realization of this work.

I would like to acknowledge Prof. Jean-Jacques Laurin from École Polytechnique de Montréal, Prof. Stefano Maci from Siena University and Prof. Sergei Tretyakov from Aalto University, for having accepted to examine this thesis and for their valuable comments.

Specials thanks to Shulabh Gupta and Mohamed Salem with whom I had countless hours of interesting discussions, scientific advice and support. I also would like to thank all the other group members notably Ali, Zoé, Guillaume, Nima, Luzhou, Yousef, Sajjad and all the others who helped me to finish this work and with whom I spent good time.

For their precious help, I would like to thank the technical staffs of Poly-Grames: Mr. Jules Gauthier, Mr. Traian Antonescu, Mr. Steve Dubé, Mr. Maxime Thibault and Mr. Jean-Sebastien Décarie.

Finally, I would like to thank you. Yes, you the reader who takes the time to read this work, which I hope will be useful to you.

RÉSUMÉ

Les métasurfaces électromagnétiques sont des structures bidimensionnelles d'épaisseur fine par rapport à la longueur d'onde d'opération. Elles sont utilisées pour contrôler la diffusion d'ondes électromagnétiques. De telles structures sont conventionnellement composées d'un arrangement périodique de particules diffusantes, de taille plus petite que la longueur d'onde. Ces particules sont conçues de façon à contrôler l'amplitude, la phase, la polarisation et la direction de propagation des ondes réfléchies et transmises par les métasurfaces, lorsque celles-ci sont illuminées par une onde incidente spécifique.

L'idée de contrôler la lumière avec des structures d'épaisseur fine n'est pas nouvelle et existe depuis bien longtemps. Cependant, la compréhension mathématique et physique, ainsi que les capacités technologiques requises pour fabriquer ce genre de structures complexes, particulièrement celles qui réalisent un contrôle avancé du champ électromagnétique, n'ont été essentiellement disponibles que depuis les dix dernières années. En outre, malgré les progrès récents, il y a un manque crucial d'une méthode de synthèse, qui soit à la fois rigoureuse et universelle, et qui permette de traiter n'importe quel type de transformation électromagnétique. Il s'ensuit que l'objectif principal de ce travail est de développer un cadre général de synthèse pour l'implémentation mathématique et pratique de métasurfaces, indépendamment de la transformation électromagnétique prescrite.

Cette thèse présente une discussion détaillée de la synthèse mathématique de métasurfaces, qui est basée sur des conditions aux limites rigoureuses s'appliquant à des interfaces d'épaisseur nulle. La procédure de synthèse est un problème inverse qui fournit les susceptibilités des métasurfaces en fonction des transformations électromagnétiques spécifiées. Dans ce travail, nous considérons le cas général de métasurfaces bianisotropes possédant des termes de susceptibilités à la fois tangentiels et normaux. La procédure de synthèse est alors séparée en plusieurs cas particuliers, avec un ordre croissant de complexité, qui sont chacun traités de manière individuelle. En plus de cela, la méthode de synthèse a également été étendue afin de prendre en compte le cas de susceptibilités monoisotrope non-linéaire de second ordre.

La synthèse mathématique de métasurfaces est illustrée de manière théorique et numérique avec plusieurs exemples qui incluent notamment le design de rotateurs de polarisation réciproques et non-réciproques, ainsi que des transformateurs d'ondes multiples. Une discussion détaillée sur la théorie fondamentale des métasurfaces réfractives est également proposée. Elle décrit différentes configurations de susceptibilités qui permettent de réaliser une transformation réfractive. Pour chacune d'entre elles, l'efficacité de conversion de puissance entre

l'onde incidente et l'onde réfractée est analysée d'un point de vue mathématique et physique.

En se basant sur les développements mathématiques de la méthode de synthèse, la réalisation pratique des métasurfaces est alors abordée. La thèse présente deux différentes approches pour l'implémentation des particules diffusantes composant les métasurfaces. L'une est basée sur des particules faites d'une cascade de couches métallisées, l'autre sur des résonateurs diélectriques. Ces deux types de structures présentent leurs propres avantages et inconvénients en termes de pertes, de complexité de fabrication, de degrés de liberté et de tailles.

Finalement, la thèse présente plusieurs concepts et applications de métasurfaces, qui ont été investigués et développés durant ce programme doctoral, et qui illustrent la mise en œuvre de la procédure de synthèse mathématique et pratique. Parmi ces concepts et applications, nous pouvons notamment citer: des métasurfaces diélectriques pour le contrôle de la dispersion temporelle, la réalisation de lames demi-onde et quart d'onde, de séparateur de polarisations, de générateur d'ondes possédant un moment angulaire orbital, des processeurs à lumière cohérente, le routage d'ondes d'espace par l'utilisation d'ondes de surface, l'implémentation d'un isolateur non-réciproque et non-gyrotrope, l'augmentation de l'efficacité lumineuse des LEDs et le contrôle de la pression de radiation.

ABSTRACT

An electromagnetic metasurface is a two-dimensional structure that is thin with respect to the considered wavelength of operation and that may be used to control the scattering of electromagnetic waves. Such a structure is conventionally composed of a periodic arrangement of engineered subwavelength scattering particles that enables one to control the amplitude, phase, polarization and direction of propagation of the fields reflected and transmitted by the metasurface, when the latter is illuminated by a specific incident field.

While the idea of controlling light with thin surfaces has been around for a very long time, the mathematical and physical understanding as well as the technical capabilities required to realize such complex structures, especially the ones that perform advanced control of the fields, have only been available since the last decade. However, there has been a crucial lack of a rigorous and universal synthesis technique that would apply to any field specification. It follows that the main objective of this work is to provide a general synthesis framework for the mathematical and practical implementation of metasurfaces, irrespectively of the prescribed electromagnetic transformations.

The thesis presents an in-depth discussion on the mathematical synthesis of metasurfaces that is based on rigorous zero-thickness sheet transition conditions. The synthesis procedure is an inverse problem that yields the metasurfaces susceptibilities in terms of the fields corresponding to the specified electromagnetic transformations. We are considering the very general case of fully bianisotropic metasurfaces with both tangential and normal susceptibility components. The synthesis procedure is then split into different particular cases, with increasing order of complexity, that are individually addressed. Additionally, the synthesis technique is also extended so as to include the case of monoisotropic second-order nonlinear susceptibilities.

The mathematical synthesis of metasurfaces is theoretically and numerically illustrated with several examples, which notably include the design of reciprocal and nonreciprocal polarization rotators and multiple wave transformers. A detailed discussion on the fundamental theory of refractive metasurfaces is proposed and which describes various susceptibility configurations that allow one to achieve wave refraction. For each of these configurations, the power conversion efficiency between the incident and refracted wave is also analyzed from a mathematical and physical perspective.

Following the mathematical developments of the synthesis, the practical realization of metasurfaces is then addressed. The thesis discusses two different approaches for the implemen-

tation of the metasurface scattering particles. One that is based on cascaded metallic layers and one based on dielectric resonators. These two structures exhibit their own advantages and disadvantages in terms of loss, fabrication complexity, degrees of freedom and sizes.

Finally, the thesis presents several metasurface concepts and applications, which have been investigated and developed during this PhD program and that illustrate the implementation of the mathematical and practical synthesis procedure. These concepts and applications notably include metasurfaces for temporal dispersion engineering, half- and quarter-wave plate operations, polarization beam splitting, orbital angular momentum generation, coherent light processing, space-wave routing via surface waves, nonreciprocal nongyrotropic isolation, LEDs emission enhancement and radiation pressure control.

TABLE OF CONTENTS

LIST OF TABLES

LIST OF FIGURES

LIST OF SYMBOLS AND ABBREVIATIONS

Symbols

c_0	speed of light in vacuum
ϵ_0	permittivity of free space
η_0	impedance of free space
k_0	wavenumber in free space
$\overline{\overline{\chi}}_{\mathrm{ee}}$	electric susceptibility tensor
$\overline{\overline{\chi}}_{\mathrm{mm}}$	magnetic susceptibility tensor
$\overline{\overline{\chi}}_{\mathrm{em}}$	electromagnetic susceptibility tensor
$\overline{\overline{\chi}}_{\mathrm{me}}$	magnetoelectric susceptibility tensor
$\chi_{\mathrm{ee}}^{(1)}$	first-order (linear) monoisotropic electric susceptibility
$\chi_{\mathrm{ee}}^{(2)}$	second-order (nonlinear) monoisotropic electric susceptibility
$\chi_{\mathrm{mm}}^{(1)}$	first-order (linear) monoisotropic magnetic susceptibility
$\chi_{\mathrm{mm}}^{(2)}$	second-order (nonlinear) monoisotropic magnetic susceptibility

Abbreviations

GSTCs	Generalized Sheet Transition Conditions
FDFD	Finite-Difference Frequency-Domain
FDTD	Finite-Difference Time-Domain
SF	Scattered-Field Region
TF	Total-Field Region
PEC	Perfect Electric Conductor
TIR	Total Internal Reflection
LED	Light Emitting Diode
PBS	Polarization Beam Splitter
HyG	Hypergeometric Gaussian
OAM	Orbital Angular Momentum
IBC	Impedance Boundary Condition
VNA	Vector Network Analyzer
FSS	Frequency-Selective Surface
FZPR	Fresnel Zone Plate Reflector
LHCP	Left-Handed Circular Polarization
RHCP	Right-Handed Circular Polarization

LIST OF APPENDICES

CHAPTER 1 Introduction

This thesis presents and discusses the mathematical synthesis, the practical realization and some applications and concepts of electromagnetic metasurfaces, which are the two-dimensional counterparts of metamaterials. In this introductory chapter, we will start with a brief overview of metamaterials. It will be followed by a review of the steps that led to the developments of metasurfaces. Based on these considerations, we will finally introduce the initial motivation and the objectives of this work.

This work is based on a collection of papers whose complete list is provided in Appendix E.

1.1 What is a Metamaterial?

The term *metamaterial* was originally coined by Rodger M. Walser in 1999 in the context of a DARPA[1] Workshop [4]. It was proposed to describe a class of artificial materials that exhibit electromagnetic properties that are *beyond* those conventionally available in nature [5–8]. According to this definition, it is clear that such kind of artificial structures have been realized and used since long before the invention of the term metamaterial itself. Indeed, one of the earliest known example of metamaterials is that of dichroic glass, which is notably used in stained glass. The Lycurgus cup, which dates back to the 4th-century AD, is probably the most well-known and ancient example of dichroic glass. In these ancient times, controlling the reflection, transmission and absorption properties of glass was achieved by the addition of various metallic powders during the glass manufacturing process [9]. Due to the lack of light-matter interaction theory, these structures were essentially made by trial-and-error experiments.

Coming back to a more recent epoch, soon after Maxwell established the theory of electromagnetism in 1865 [10], people tried to uncover ways of controlling the propagation of electromagnetic waves. Maybe one of the earliest example is that of Bose artificial polarization rotator, in the late 1890s, made of a twisted-jute structure which mimics the chiral behavior of certain sugar solutions [11]. Other artificial chiral media include the spiral resonating structures of Lindman in the 1910s and 1920s [12]. Later in the 1940s, Kock pioneered the realization of artificial dielectrics by inserting resonating metallic elements in dielectric layered media and implemented the first microwave delay lens [13]. In the meantime, Schelkunoff and Friss proposed to use split-ring resonators to artificially increase the permeability

[1] Defense Advanced Research Projects Agency

of materials [14].

While up to that point, most artificial materials were made to control the permittivity and permeability, extreme material parameters such as a refractive index less than unity were not shown before the work of Brown in the 1950s [15] and then, in the 1960s, that of Rotman who associated the electromagnetic behavior of a wire medium to that of an equivalent plasma [16]. Continuing on that path, Veselago theoretically predicted, in 1968, a completely new class of materials where both the permittivity and the permeability are negative values leading to a negative index of refraction [17]. The developments of artificial materials continued through the 1980s and 1990s, notably with the realization of microwave absorbers and bianisotropic media [8]. But it is not before 2001 that the concept of metamaterial really started to attract major attention from the scientific community. Indeed, this rise in interest followed the groundbreaking works of Smith [18][2], who, for the first time, experimentally achieved a negative index of refraction, and that of Pendry [19], who revived the concept of negative refraction (proposed by Veselago) to suggest the realization of a perfect lens. The interest towards metamaterials grew even more when, in 2006, Pendry and Smith proposed and realized the concept of electromagnetic cloaking based on transformation optics [20, 21].

Although a general description of what a metamaterial is was already provided above, we will now rigorously define the meaning of this term. A metamaterial is an artificial structure made of an arrangement of engineered particles, sometimes refereed to as "meta-atoms" or scattering particles [8]. The distance between these meta-atoms as well as their overall dimension must be much smaller than the wavelength such that a wave propagating through the medium does not experience diffraction or Bragg scattering due to the granularity of the structure. In that case, the metamaterial structure can be homogenized to obtain its corresponding effective material parameters. Photonic crystals [22] and electromagnetic band gaps structures [23] (with unit cell size comparable to the wavelength) thus do not qualify as metamaterials since the electromagnetic field inside these structures cannot be averaged to obtain homogenized effective constitutive parameters. From a general perspective, the exceptional effective material parameters that are achievable with metamaterials are not only related to the chemical composition of the scattering particles but also to their shape and orientation. As such the scattering particles may be composed of dielectric or metallic materials, they may be resonant or non-resonant elements, they may exhibit loss, gain and nonlinear effects and may even contain electronic circuitry. Note that composite materials made by mixing different materials together, and whose material parameters may be obtained from mixing formulas such as the Maxwell Garnett equation, are not conventionally considered as meta-

[2]It is also in this work that the term "metamaterial" appeared for the first time in the literature.

materials due to the fact that their electromagnetic properties only depend on the chemical composition of the elements and not on their shape and orientation [24].

1.2 The Concept of Metasurfaces

The interest in metamaterials reached a peak in the first decade of the 21st century. Then, due to their fabrication complexity, their bulkiness and weight, and their limitations in terms of losses, frequency range and scalability, metamaterials became eventually less attractive. It is at this moment that metasurfaces, the two-dimensional counterparts of metamaterials, began to attract notable attention [25–28].

The idea of controlling electromagnetic waves with electromagnetically thin structures is obviously not a new concept. The first example is probably that of Lamb, who studied the reflection and transmission from an array of metallic strips, already back in 1897 [29]. Later in the 1910s, Marconi used straight wires to realize polarization reflectors [30]. These first kind of two-dimensional electromagnetic structures were later followed by a rich diversity of various systems that emerged mainly with the developments of the radar technology during World War II. Many of these systems date back to the 1960s and notably include: the Fresnel zone plate reflectors (FZPR), illustrated in Fig. 1.1a, developed for radio transmitters [31] and which are based on the concept of the Fresnel lens already demonstrated almost 200 hundred years ago. The frequency selective surfaces (FSS) developed as filters [32, 33] and illustrated in Fig. 1.1d. The reflectarray antennas [34], designed as the flat counterparts of parabolic reflectors, and which were initially fabricated using short-ended waveguides [35]. They were later progressively improved and the short-ended waveguides were replaced with mircrostrip printable scattering elements in the late 1970s [36, 37], as shown in Fig. 1.1b. The transmission counterparts of the reflectarrays are the transmitarrays which were used as array lens systems and at least date back to the 1960s [38–40]. They were first implemented by forming two interconnected planar arrays of dipole antennas, one for receiving and one for transmitting, where each antenna on the receiver side was connected via a delay line to an antenna on the transmit side, as depicted in Fig. 1.1c. The transmitarrays evolved through the 1990s from interconnected antenna arrays to layered metallic structures that were essentially the functional extensions of FSS [41–43] and the precursors of the current metasurfaces. At that time, their efficiency was limited due to the inability to control the transmission over a 2π-phase range while maintaining a high enough amplitude. Finally, compact quasi-transparent transmitarrays or phase-shifting surfaces, able to cover a 2π-phase range, were demonstrated in 2010 [44].

FSS, reflectarrays, transmitarrays and phase-shifting surfaces are the precursors of what we

would call today: *metasurfaces*. Note that all structures discussed so far are used in the context of space-wave transformations, however, metasurfaces may also be used for surface-wave transformations. Indeed, patterned surfaces like, for instance, near-field plates [45–47] or even impedance surfaces converting surface waves into space waves [48, 49] also qualify as metasurfaces providing that their unit cell size is much smaller than the wavelength such that Bragg scattering does not occur.

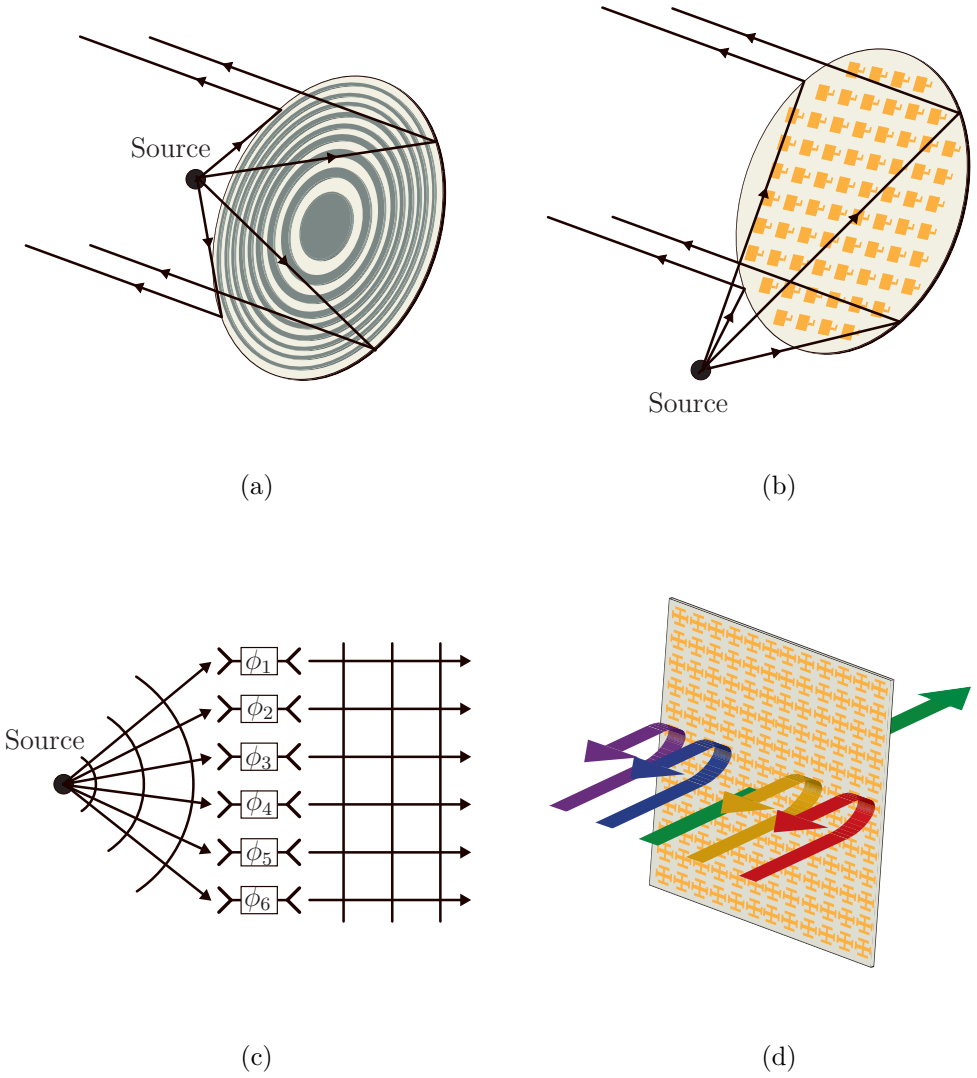

Figure 1.1 Examples of two-dimensional wave manipulating structures: (a) Fresnel zone plate reflector, (b) reflectarray, (c) interconnected array lens and (d) frequency-selective surface. Due to the structural configuration of (a) and (c), they do not qualify as metasurfaces. On the other hand, the structures in (b) and (d) can be homogenized into effective material parameters and thus correspond to metasurfaces.

To this day, a myriad of metasurfaces have been reported in the literature and many more metasurface structures and applications are expected to emerge in coming years. We provide here a non-exhaustive list of some applications of metasurfaces. From a general perspective, metasurfaces can be used to manipulate the polarization, the phase and the amplitude of electromagnetic fields. However, early metasurfaces were only able to affect specific properties of the fields such as, for instance, the polarization. Many metasurfaces have been realized to control the polarization of normally incident waves [50–57], in these examples, linearly polarized waves can be transformed into circularly polarized waves or have their polarization rotated using chiral scattering particles [58]. Another type of specific application is the realization of absorbing surfaces [59–65], where, this time, the amplitude of the field must be affected so that no reflection or transmission can occur. In addition to the reflect/transmitarrays discussed above, there are more recent works that include metasurfaces able to introduce phase variations and that can thus manipulate the directions of wave propagation [66–68]. Wavefront manipulation metasurfaces [69–79] can be used for various applications such as, for instance, generalized refraction, focusing or diverging devices, phase compensation of electromagnetic sources, etc. Many of these phase manipulating metasurfaces are essentially the planar counterparts of Fresnel type structures such as Fresnel lenses [80] and blazed gratings [81, 82] and which are usually implemented in the optical regime. More complex metasurfaces able to transform both phase and polarization have also been realized recently. Notably, vortex beams possessing angular orbital momentum [83] have been successfully generated [84–89]. Metasurfaces that produce holograms have also been reported [90, 91] and even stable tractor beams [92]. Other kinds of exotic operations can be realized, among others, nonreciprocal transformations [93–97], nonlinear interactions [98–100], analog computing [101, 102] and spatial filtering [103–105].

One main drawback of metasurfaces, and metamaterials in general, is their limited bandwidth as most of these structures are constituted of resonant scattering particles. Today, increasing the bandwidth of metasurfaces is an active research topic and several examples have already been reported [106–112]. One other recurrent problem with metal based metasurfaces is the high optical losses in metal at optical frequencies [113,114], which consequently reduces their attractiveness for optical applications. Recent works [115–118] have demonstrated that all-dielectric metasurfaces (at optical or microwave frequencies), that are inspired from artificial dielectric initially developed in the microwave regime [119], are a valid alternative to metal based structures. This is because dielectric resonators do not suffer from high optical losses as metallic structures do.

An important question that arises when considering metasurfaces (or metamaterials in general) is how can such structures be synthesized? Initially, many methods were developed not to

synthesize metamaterials but rather to find an equivalent representation of these structures in terms of effective parameters. These methods, called homogenization techniques [120–127], consist in converting the complex subwavelength structure of a metamaterial into an homogeneous slab of, for instance, effective permittivity and permeability that exhibits the same reflection and transmission coefficients and propagation constant as the original metamaterial structure. In general, homogenization techniques provide direct relations between the reflection and transmission coefficients of the metamaterial, obtained by experimental measurements or electromagnetic simulations, and the effective parameters of the homogeneous slab. Metasurface synthesis techniques are conceptually doing the opposite of the homogenization techniques. They can be decomposed into two main steps. At first, the effective parameters of the metasurface are obtained by specifying the incident, reflected and transmitted fields. Secondly, the scattering particles of the metasurface are designed to correspond to these effective parameters [128–139].

1.3 Motivation and Objectives

As seen above, the concept of metasurface has been around for at least the past 50 years, mostly implemented in the form of FSS and reflect/transmitarrays. More recently, during the past decade, there has been important research developments in the area of metamaterials, and metasurfaces have emerged as better candidates than their 3D counterparts for controlling electromagnetic fields. This is because they are easier to fabricate, lighter, less lossy and have a lower profile [25, 26, 67, 127, 132, 140, 141]. As a consequence, there is today a growing interest towards the development of metasurfaces with always more complex electromagnetic transformation possibilities that surpass those of previous two-dimensional structures. A complete control of the polarization, phase and amplitude of the reflected and transmitted waves, which was not achievable before, is necessary for many applications. However, there has been a lack of reliable and rigorous methods to synthesize these complicated structures. Indeed, in most cases, structures like reflectarrays were designed based on very simple principles such as far-field phase compensation [34], while optical thin films were often designed based on complex amplitude transmittance or holographic methods [142]. These synthesis methods are based on far-field and paraxial approximations, which is obviously not rigorous in an electromagnetic sense as they ignore near-field contributions and the vectorial nature of the fields. These methods are thus not universal and only apply in particular cases. Moreover, they do not provide information about the material properties of the metamaterials but rather on the effects, in terms of scattering behavior, that the structures apply on the fields.

From these considerations, it follows that the initial motivation for this project is to overcome the limitations in terms of metasurface synthesis techniques. We point out that, since the beginning of this work, a few metasurface synthesis techniques have been reported in the literature. In this thesis, we will discuss the synthesis procedure developed in [128] which yields the metasurface susceptibility tensors for specified electromagnetic transformations. Alternatively, the methods proposed by Grbic [131–134] and Eleftheriades [135–137] describe the metasurface in terms of impedance tensors and it can be shown that they represent only a particular case of the general method proposed here. The method proposed by Tretyakov [138, 139] relates the waves reflected and transmitted from the metasurface to the polarizabilities of a single scattering element in a rigorous fashion only in the case of normally propagating waves[3]. In contrast, the method proposed here deals with waves of arbitrary incident angles and arbitrary types. Finally, the method proposed by Salem [129, 130], is a technique called the momentum transformation method, which is a spectral ($\boldsymbol{k}$) method, that is particularly suitable for paraxial wave problems. It can also handle full vectorial problems but this involves extra complexity compared to the scalar case.

The main objectives of this work directly follow from the initial motivation discussed above. In this thesis, we aim to: develop a complete framework that may be used to rigorously synthesize metasurfaces, and use it to implement new kinds of electromagnetic field transformation metasurfaces for various applications. The synthesis framework can be divided into two main steps. Firstly, a mathematical description of the metasurface must be obtained by solving an inverse problem where all the fields around the metasurface (incident, reflected and transmitted fields) are known and the electromagnetic properties, at each point of the metasurface, must be found. The mathematical synthesis technique must be as universal as possible meaning that the specified fields can have arbitrary amplitude, phase, polarization and direction of propagation. Secondly, the metasurface material parameters and electromagnetic transfer functions (obtained from the first step of the synthesis) are discretized into lattice sites, where each one of them corresponds to a unit cell to be implemented. Each of these unit cells must then be physically implemented in order to build the final metasurface. Therefore, this second part of the synthesis technique consists in finding appropriate and convenient design rules to implement the scattering particles. This second step is usually the most tedious as no universal and systematic techniques exist so far to relate the shape of scattering particles to their effective parameters (or transmission and reflection coefficients) and such analysis is usually performed via parametric simulations of well chosen structures [78, 143–150].

[3]In the next chapter, we will provide more details and also compare these synthesis techniques to the one proposed in this work.

1.4 Thesis Contributions and Organization

The main contribution of this work is the metasurface synthesis framework that will be developed and discussed in Chapters 2 to 4. Due to the rigorous nature of its foundation, which is directly derived from Maxwell equations, this metasurface synthesis technique provides the most complete and detailed description of metasurfaces available to date in the literature. It yields the metasurface material parameters, given in terms of susceptibility components, as functions of specified electromagnetic transformations. The utilization of susceptibilities provides an unprecedented physical perspective on the electromagnetic properties of the metasurfaces, which was inaccessible with previous synthesis techniques. Moreover, It also extends previously available synthesis techniques by taking into account normal and nonlinear susceptibility components, which opens up completely new research directions. The combined information available from these three chapters provides the reader with all the necessary tools required to design a metasurface, from the initial specifications in terms of field transformations to the final physical structure as well as the measurement procedure.

In addition to this metasurface synthesis framework, Chapter 5 presents several other contributions that consist in various metasurface concepts and applications. Among the most original are: the realization of a birefringent metasurface generating vortex waves with different topological charge depending on the polarization of the illumination. The implementation of spatial coherent processors that are able to control the metasurface transmitted wave amplitude, phase and direction of propagation based on a coherent superposition of an incident input wave and an incident control wave. The design of a partially-reflecting metasurface cavity enhancing the light extraction efficiency of light-emitting diodes (LEDs), which may find practical and industrial applications in the lighting industry. And the prospective study of the capabilities of metasurfaces to control electromagnetic radiation pressure, notably with the objective of realizing metasurface "solar" sails.

The global organization of this thesis is as follows:

Chapter 2 mathematically introduces the concept of metasurfaces. A synthesis procedure is derived based on rigorous zero-thickness sheet transition conditions, which yields the metasurface susceptibilities in terms of the specified fields. The synthesis technique is general and applies to full bianisotropic susceptibility tensors that include tangential and normal susceptibility components as well as second-order nonlinear terms. This chapter also presents several examples that illustrate the capabilities of the synthesis technique.

Chapter 3 presents a detailed discussion on the synthesis of refractive metasurfaces. This specific type of electromagnetic transformation is an excellent candidate to apply several

of the concepts developed in Chapter 2. We will see and compare four different methods available to synthesize refractive metasurfaces.

Chapter 4 discusses the practical implementation of metasurfaces as well as the measurement procedure used to investigate the scattering properties of the realized structures. We present two possible unit cell structures that are most commonly used to realize metasurfaces. One is based on cascaded metallic layers and the other one is based on dielectric resonators.

Chapter 5 illustrates the application of the synthesis procedure. We present several metasurface concepts and applications, which include: electromagnetic wave plates, polarization beam splitting, orbital angular momentum generation, spatial coherent processing, space-wave routing via surface waves, nonreciprocal nongyrotropic isolation, LEDs emission enhancement and radiation pressure manipulation.

Chapter 6 highlights some of the limitations that are inherent to metasurfaces and to the proposed synthesis technique. We will notably discuss and compare the discrepancies between the scattering behavior of metasurfaces with non-negligible thicknesses and the expected scattering behavior predicted by the zero-thickness model.

Chapter 7 concludes the thesis and proposes directions for future works.

CHAPTER 2 Mathematical Synthesis Based on Susceptibility Tensors

In this chapter[1], we present an extensive discussion on the mathematical synthesis of metasurfaces. We consider that a metasurface is a two-dimensional electromagnetic discontinuity of subwavelength thickness, $t \ll \lambda$. The metasurface synthesis problem is illustrated in Fig. 2.1, where the metasurface lies in the xy-plane at $z = 0$ and is of finite size with dimensions $L_x \times L_y$. Figure 2.1, shows a typical metasurface made of a nonuniform arrangement of scattering particles (here made of planar metallic crosses) that transforms an incident wave into specified reflected and transmitted waves.

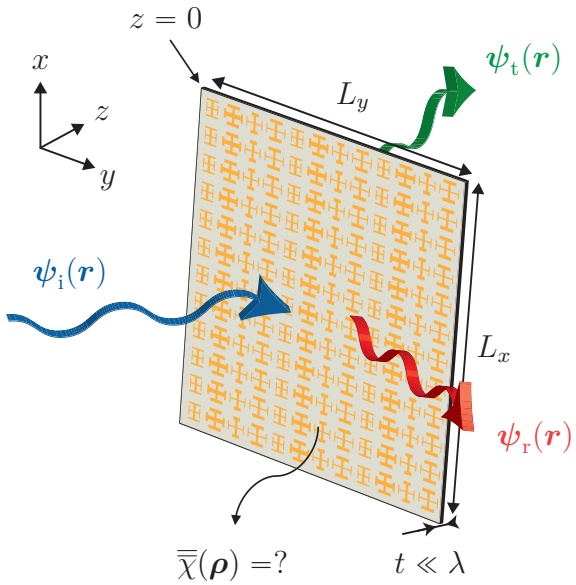

Figure 2.1 The metasurface of subwavelength thickness to be synthesized lies in the xy-plane at $z = 0$. The synthesis procedure consists in finding the susceptibility tensors, $\overline{\overline{\chi}}(\boldsymbol{\rho})$, in terms of specified arbitrary incident, $\boldsymbol{\psi}_\mathrm{i}(\boldsymbol{r})$, reflected, $\boldsymbol{\psi}_\mathrm{r}(\boldsymbol{r})$, and transmitted, $\boldsymbol{\psi}_\mathrm{t}(\boldsymbol{r})$, waves.

The objective of the synthesis procedure is to obtain the metasurface material parameters so that the metasurface performs a specified monochromatic transformation prescribed in terms of an arbitrary incident wave, $\boldsymbol{\psi}_\mathrm{i}(\boldsymbol{r})$, an arbitrary reflected wave, $\boldsymbol{\psi}_\mathrm{r}(\boldsymbol{r})$, and an arbitrary transmitted wave, $\boldsymbol{\psi}_\mathrm{t}(\boldsymbol{r})$. The synthesis procedure provides a solution that is expressed in terms of the bianisotropic surface susceptibility tensors, $\overline{\overline{\chi}}_\mathrm{ee}(\boldsymbol{\rho})$, $\overline{\overline{\chi}}_\mathrm{mm}(\boldsymbol{\rho})$, $\overline{\overline{\chi}}_\mathrm{em}(\boldsymbol{\rho})$ and $\overline{\overline{\chi}}_\mathrm{me}(\boldsymbol{\rho})$, which respectively correspond to the electric, magnetic, electromagnetic and magnetoelectric susceptibility tensors, and where $\boldsymbol{\rho} = x\hat{\boldsymbol{x}} + y\hat{\boldsymbol{y}}$.

[1]This chapter is based on a modified version of [128, 151–153].

We will see that, although the synthesis procedure always yields a mathematical solution, the resulting susceptibilities may not necessarily correspond to physically realizable scattering particles. The difficulty in realizing the metasurface may stem from: rapid spatial variations of the susceptibilities compared to the size of the scattering particles, the presence of electric/magnetic gain/loss or even nonreciprocal features that are beyond the reach of the current state-of-the-art technology. Nevertheless, in many cases it is possible to sacrifice some of the specified design constraints so as to relax the requirements on the susceptibilities and thus synthesize a structure that is physically implementable.

In this chapter, we will present and discuss the mathematical synthesis of metasurfaces, which is only the first step in the broader framework of metasurface synthesis. Upon this mathematical basis, we will address, in the forthcoming chapters, the second main step of the synthesis, which consists in finding the appropriate geometries of the scattering particles.

Note that throughout this document, the time harmonic dependence $e^{j\omega t}$ is assumed and omitted for conciseness.

2.1 Metasurface Boundary Conditions

Let us consider the metasurface depicted in Fig. 2.1 and ask the question: how can one obtain its susceptibilities in terms of the specified fields? The operation described in this question corresponds to solving an inverse problem, which consists in finding the material parameters as functions of space so as to produce specific scattered fields under a specified illumination. As such, this inverse problem has an infinite number of solutions, at least if far-field radiation is concerned. However, even if near-field contributions are taken into account, we will see that several different susceptibilities may produce the exact same scattered fields, as will be demonstrated shortly. Additionally, the metasurface in Fig. 2.1 has a certain thickness and, even if it is deeply subwavelength, it still consists of a thin slab of material with two distinct interfaces. This makes the problem even more complicated since continuity at *both* interfaces must be ensured. In order to simplify this complicated problem, we make the assumption that the metasurface is an electromagnetic discontinuity of exactly zero-thickness and thus consists only of a single interface. This assumption of zero-thickness is supported by the fact that the metasurface is electromagnetically thin, but comes at the cost of a discrepancy between the scattering response of the zero-thickness model and that of the thin metasurface slab, to which we will come back later. Consequently, the synthesis problem reduces to finding the susceptibilities of a polarizable zero-thickness sheet.

Now that we have decided to model the metasurface as a zero-thickness electromagnetic dis-

continuity, we can again ask the question: how can one obtain the susceptibilities, in terms of the specified fields, of an interface inducing both electric and magnetic field discontinuities? It turns out that the conventional boundary conditions found in most electromagnetic textbooks, that may allow relating the fields to the presence of the metasurface, do not rigourously apply to this kind of polarizable interface, as pointed out by Schelkunoff [154]. To illustrate this point, let us look, without loss of generality, at the specific example of the discontinuity of the displacement vector $\boldsymbol{D}$ at an interface between two media. Gauss law stipulates that

$$\nabla \cdot \boldsymbol{D} = \rho, \tag{2.1}$$

where ρ is the charge density per unit volume. Applying Gauss theorem to (2.1), by considering a volume V enclosed by a surface S around the interface, leads to

$$\iiint_V \nabla \cdot \boldsymbol{D} \; dV = \oiint_S \boldsymbol{D} \cdot \hat{\boldsymbol{n}} \; dS = \iiint_V \rho \; dV = \rho_s, \tag{2.2}$$

where $\hat{\boldsymbol{n}}$ is the unit vector normal to S and ρ_s is the surface charge density. After simplifying the surface contour integral of $\boldsymbol{D}$, Eq. (2.2) reduces to

$$\hat{\boldsymbol{z}} \cdot \boldsymbol{D}\big|_{z=0^-}^{0^+} = \rho_s, \tag{2.3}$$

which is the conventional textbook boundary condition for the discontinuity of the displacement vector $\boldsymbol{D}$ in the presence of an impressed surface charge density. There are two reasons why Eq. (2.3) is not rigorous: the first one lies in the fact that the application of Gauss theorem in (2.2) is valid *only* if $\boldsymbol{D}$ is continuous inside the volume V, which is obviously not the case when $\rho_s \neq 0$. Note that (2.3) is correct away from the interface, i.e. up to $z = 0^{\pm}$, but fails to describe the behavior of the field at $z = 0$. The second reason is the incompleteness of (2.3), which implies that $\boldsymbol{D}$ is perfectly continuous in the absence of impressed surface charges but completely fails to consider the contribution of excitable dipole or higher-order multipole moments. Therefore, the conventional boundary conditions are not capable to correctly account for the effects of the metasurface.

Fortunately, rigorous boundary conditions, that apply to zero-thickness sheets, were first developed by Idemen [155] and then applied to metasurfaces by Kuester *et al.* [127]. These boundary conditions are conventionally referred to as the Generalized Sheet Transition Conditions (GSTCs) and are derived in Appendix A for the sake of clarity and completeness of

this work[2]. In the absence of impressed sources, the GSTCs read

$$\hat{\boldsymbol{z}} \times \Delta \boldsymbol{H} = j\omega \boldsymbol{P}_{\parallel} - \hat{\boldsymbol{z}} \times \nabla_{\parallel} M_z, \tag{2.4a}$$

$$\Delta \boldsymbol{E} \times \hat{\boldsymbol{z}} = j\omega \mu_0 \boldsymbol{M}_{\parallel} - \nabla_{\parallel} \left(\frac{P_z}{\epsilon_0} \right) \times \hat{\boldsymbol{z}}, \tag{2.4b}$$

$$\hat{\boldsymbol{z}} \cdot \Delta \boldsymbol{D} = -\nabla \cdot \boldsymbol{P}_{\parallel}, \tag{2.4c}$$

$$\hat{\boldsymbol{z}} \cdot \Delta \boldsymbol{B} = -\mu_0 \nabla \cdot \boldsymbol{M}_{\parallel}, \tag{2.4d}$$

where the terms on the left-hand sides of the equations correspond to the differences of the fields on both sides of the metasurface, which may be expressed as

$$\Delta \Psi_u = \hat{\boldsymbol{u}} \cdot \Delta \boldsymbol{\Psi} \Big|_{z=0^-}^{0^+} = \Psi_{u,\mathrm{t}} - (\Psi_{u,\mathrm{i}} + \Psi_{u,\mathrm{r}}), \; u = x, y, z, \tag{2.5}$$

where $\boldsymbol{\Psi}$ represents any of the fields $\boldsymbol{H}$, $\boldsymbol{E}$, $\boldsymbol{D}$ or $\boldsymbol{B}$, and where the subscripts i, r, and t denote incident, reflected and transmitted fields, and $\boldsymbol{P}$ and $\boldsymbol{M}$ are the electric and magnetic surface polarization densities, respectively. In the general case of a bianisotropic metasurface, these polarization densities are related to the acting (or local) fields, $\boldsymbol{E}_{\mathrm{act}}$ and $\boldsymbol{H}_{\mathrm{act}}$, by [157, 158]

$$\boldsymbol{P} = \epsilon_0 N \overline{\overline{\alpha}}_{\mathrm{ee}} \cdot \boldsymbol{E}_{\mathrm{act}} + \frac{1}{c_0} N \overline{\overline{\alpha}}_{\mathrm{em}} \cdot \boldsymbol{H}_{\mathrm{act}}, \tag{2.6a}$$

$$\boldsymbol{M} = N \overline{\overline{\alpha}}_{\mathrm{mm}} \cdot \boldsymbol{H}_{\mathrm{act}} + \frac{1}{\eta_0} N \overline{\overline{\alpha}}_{\mathrm{mm}} \cdot \boldsymbol{E}_{\mathrm{act}}, \tag{2.6b}$$

where the $\overline{\overline{\alpha}}_{\mathrm{ab}}$ terms represent the polarizabilities of a given scatterer, N is the number of scatterers per unit area, c_0 is the speed of light in vacuum and η_0 is the vacuum impedance. This is a microscopic description of the metasurface response which requires an appropriate definition of the averaging operation as well as the coupling between adjacent scattering particles. In this work, we use the concept of susceptibilities rather than the polarizabilities to provide a macroscopic description of the metasurface, which allows a direct connection with material parameters such as $\overline{\overline{\epsilon}}_r$ and $\overline{\overline{\mu}}_r$. To bring about the susceptibilities, relations (2.6) can be transformed by noting that the acting fields, at the position of a scattering particle, can be defined as the average fields from which the scattered field of the considered scattering particle has been removed [127], i.e. $\boldsymbol{E}_{\mathrm{act}} = \boldsymbol{E}_{\mathrm{av}} - \boldsymbol{E}_{\mathrm{scat}}$. The contributions of the scattering particle may be expressed by considering the particle as a combination of electric and magnetic dipoles contained within a small disk. Then, the scattered fields from this disk can be related to $\boldsymbol{P}$ and $\boldsymbol{M}$ by taking into account the coupling with adjacent scattering particles. Therefore,

[2]It is interesting to note that the GSTCs can also be obtained following the more traditional technique of box integration, as demonstrated in [156].

the acting fields are functions of the average fields and the polarization densities. Upon substitution of this definition of the acting fields in (2.6), the resulting expressions of the polarization densities become

$$\boldsymbol{P} = \epsilon_0 \overline{\overline{\chi}}_{\mathrm{ee}} \cdot \boldsymbol{E}_{\mathrm{av}} + \frac{1}{c_0} \overline{\overline{\chi}}_{\mathrm{em}} \cdot \boldsymbol{H}_{\mathrm{av}}, \tag{2.7a}$$

$$\boldsymbol{M} = \overline{\overline{\chi}}_{\mathrm{mm}} \cdot \boldsymbol{H}_{\mathrm{av}} + \frac{1}{\eta_0} \overline{\overline{\chi}}_{\mathrm{me}} \cdot \boldsymbol{E}_{\mathrm{av}}, \tag{2.7b}$$

where the average fields are defined as

$$\Psi_{u,\mathrm{av}} = \hat{\boldsymbol{u}} \cdot \boldsymbol{\Psi}_{\mathrm{av}} = \frac{\Psi_{u,\mathrm{t}} + (\Psi_{u,\mathrm{i}} + \Psi_{u,\mathrm{r}})}{2}, \; u = x, y, z, \tag{2.8}$$

where $\boldsymbol{\Psi}$ corresponds to $\boldsymbol{E}$ or $\boldsymbol{H}$. The constitutive relations with the convention used in (2.7) are consequently given by

$$\boldsymbol{D} = \epsilon_0 \boldsymbol{E} + \boldsymbol{P} = \epsilon_0 (\overline{\overline{I}} + \overline{\overline{\chi}}_{\mathrm{ee}}) \cdot \boldsymbol{E}_{\mathrm{av}} + \frac{1}{c_0} \overline{\overline{\chi}}_{\mathrm{em}} \cdot \boldsymbol{H}_{\mathrm{av}}, \tag{2.9a}$$

$$\boldsymbol{B} = \mu_0 (\boldsymbol{H} + \boldsymbol{M}) = \mu_0 (\overline{\overline{I}} + \overline{\overline{\chi}}_{\mathrm{mm}}) \cdot \boldsymbol{H}_{\mathrm{av}} + \frac{1}{c_0} \overline{\overline{\chi}}_{\mathrm{me}} \cdot \boldsymbol{E}_{\mathrm{av}}, \tag{2.9b}$$

where $\overline{\overline{I}}$ is the identity matrix. In the general case of a volumetric medium, the susceptibilities in (2.9) are dimensionless quantities. However, the surface susceptibilities that apply to zero-thickness metasurfaces have a dimension of meter, as discussed in Appendix A.

2.2 Conditions of Reciprocity, Passivity and Loss

Before exploring the metasurface synthesis procedure, we shall first discuss the properties of reciprocity, passivity and loss applying to time-invariant linear metasurfaces and which will be precious for the forthcoming discussions. From a general perspective, the reciprocity of a given system can be evaluated by considering the scattering interactions between an arbitrary emitter and receiver and that system. If the position of the emitter and the receiver can be interchanged without affecting the transmission between the two, then the system is reciprocal. The Lorentz reciprocity theorem is the most conventional method to derive the reciprocity conditions of an electromagnetic system. If the system consists of a bianisotropic medium, the reciprocity conditions, that result from the Lorentz theorem, read [157, 158]

$$\overline{\overline{\chi}}_{\mathrm{ee}}^{\mathrm{T}} = \overline{\overline{\chi}}_{\mathrm{ee}}, \quad \overline{\overline{\chi}}_{\mathrm{mm}}^{\mathrm{T}} = \overline{\overline{\chi}}_{\mathrm{mm}}, \quad \overline{\overline{\chi}}_{\mathrm{me}}^{\mathrm{T}} = -\overline{\overline{\chi}}_{\mathrm{em}}, \tag{2.10}$$

where the superscripts T denotes the matrix transpose operation.

We will now investigate how the metasurface susceptibility values can be related to gain or to dissipation. As we will see later, the synthesized metasurface susceptibilities are generally complex values, whose real and imaginary parts may represent gain or loss. In order to precisely determine whether the metasurface is active or lossy, or even a combination of both, we need to explicitly compute the bianisotropic Poynting theorem. Assuming the convention $e^{j\omega t}$, the time-average bianisotropic Poynting theorem is given by [157]

$$\nabla \cdot \big\langle \boldsymbol{S} \big\rangle = -\big\langle \boldsymbol{I}_{\mathrm{Je}} \big\rangle - \big\langle \boldsymbol{I}_{\mathrm{Jm}} \big\rangle - \big\langle \boldsymbol{I}_{\mathrm{P}} \big\rangle - \big\langle \boldsymbol{I}_{\mathrm{M}} \big\rangle, \tag{2.11}$$

where $\big\langle \cdot \big\rangle$ denote the time-average operation, $\boldsymbol{S}$ is the Poynting vector and $\boldsymbol{I}_{\mathrm{Je}}$, $\boldsymbol{I}_{\mathrm{Jm}}$, $\boldsymbol{I}_{\mathrm{P}}$ and $\boldsymbol{I}_{\mathrm{M}}$ are loss (or gain) contributions emerging from the electric currents, magnetic currents, electric polarization and magnetic polarization, respectively. If the metasurface is surrounded by vacuum on both sides, then the terms in (2.11) read

$$\big\langle \boldsymbol{S} \big\rangle = \frac{1}{2} \operatorname{Re}(\boldsymbol{E} \times \boldsymbol{H}^*), \tag{2.12a}$$

$$\big\langle \boldsymbol{I}_{\mathrm{Je}} \big\rangle = \frac{1}{4} \operatorname{Re}(j\omega\epsilon_0 \boldsymbol{E}^* \cdot (\overline{\overline{\chi}}_{\mathrm{ee}} - \overline{\overline{\chi}}_{\mathrm{ee}}^*) \cdot \boldsymbol{E}), \tag{2.12b}$$

$$\big\langle \boldsymbol{I}_{\mathrm{Jm}} \big\rangle = \frac{1}{4} \operatorname{Re}(j\omega\mu_0 \boldsymbol{H}^* \cdot (\overline{\overline{\chi}}_{\mathrm{mm}} - \overline{\overline{\chi}}_{\mathrm{mm}}^*) \cdot \boldsymbol{H}), \tag{2.12c}$$

$$\big\langle \boldsymbol{I}_{\mathrm{P}} \big\rangle = \frac{1}{4} \operatorname{Re}\Big[j\omega\epsilon_0 (\boldsymbol{E}^* \cdot (\overline{\overline{\chi}}_{\mathrm{ee}} - \overline{\overline{\chi}}_{\mathrm{ee}}^{\dagger}) \cdot \boldsymbol{E} + 2\eta_0 \boldsymbol{E}^* \cdot \overline{\overline{\chi}}_{\mathrm{em}} \cdot \boldsymbol{H}) \Big], \tag{2.12d}$$

$$\big\langle \boldsymbol{I}_{\mathrm{M}} \big\rangle = \frac{1}{4} \operatorname{Re}\Big[j\omega\mu_0 (\boldsymbol{H}^* \cdot (\overline{\overline{\chi}}_{\mathrm{mm}} - \overline{\overline{\chi}}_{\mathrm{mm}}^{\dagger}) \cdot \boldsymbol{H} - 2\boldsymbol{E}^* \cdot \overline{\overline{\chi}}_{\mathrm{me}}^{\dagger} \cdot \boldsymbol{H}/\eta_0) \Big], \tag{2.12e}$$

where $\dagger$ is the conjugate transpose operator. Relations (2.11) and (2.12) are derived in Appendix B for completeness. The fields $\boldsymbol{E}$ and $\boldsymbol{H}$ in (2.12) are the fields acting on the metasurface and can be replaced by the corresponding average fields. The term on the left-hand side of (2.11) corresponds to the divergence of the power flow through an arbitrary volume, which, in our case, surrounds the metasurface. If this term is zero, then the amplitude of a wave going through the metasurface remains the same, which may a priori indicate that the metasurface is passive and lossless. However, this is not necessarily the case since the terms on the right-hand side of (2.11) may compensate each other such that gain and loss perfectly cancel out, as will be shown thereafter. Therefore, it is in general necessary to compute all the terms from (2.12b) to (2.12e) to determine whether the metasurface is active, which is the case if these terms are negative, or lossy, in the case where they are positive. If all these terms are zero, then the metasurface is passive and lossless.

By combining relations (2.12b) to (2.12e) and conditions (2.10), one obtains the conditions that make a metasurface simultaneously passive, lossless and reciprocal. These conditions

read

$$\overline{\overline{\chi}}_{\mathrm{ee}}^{\mathrm{T}} = \overline{\overline{\chi}}_{\mathrm{ee}}^{*}, \quad \overline{\overline{\chi}}_{\mathrm{mm}}^{\mathrm{T}} = \overline{\overline{\chi}}_{\mathrm{mm}}^{*}, \quad \overline{\overline{\chi}}_{\mathrm{me}}^{\mathrm{T}} = \overline{\overline{\chi}}_{\mathrm{em}}^{*}. \tag{2.13}$$

We see that the conditions in (2.10) and (2.13) establish relations between different susceptibility components, thus decreasing the number of degrees of freedom available to a metasurface to control electromagnetic fields. We will see in the next section that this has the effect of reducing the diversity of metasurface wave transformations.

2.3 General Solutions for Tangential Susceptibilities

The metasurface synthesis procedure consists in solving the GSTCs relations in (2.4) to obtain the susceptibilities in (2.7), that are the unknown of this inverse problem, so that the metasurface performs a desired electromagnetic transformation specified in terms of incident, reflected and transmitted fields. According to the uniqueness theorem, Eqs. (2.4c) and (2.4d) are redundant relations in the absence of impressed sources since the transverse components of the fields are sufficient to completely describe the electromagnetic problem. Therefore, we usually only consider relations (2.4a) and (2.4b) for the synthesis of metasurfaces.

As they are, the GSTCs form a set of coupled non-homogenous partial differential equations, as evidenced by the presence of the spatial derivatives of the normal components of the polarization densities in relations (2.4a) and (2.4b). As a consequence, solving the inverse problem, in the most general case where all susceptibility components are considered, is nontrivial and may require involved numerical analyses. It is therefore convenient to assume that the metasurface does not possess normal susceptibility components such that $P_z = M_z = 0$ irrespectively of the illumination. In this section, we will only consider cases where $P_z = M_z = 0$, which leads to closed-form solutions of the synthesized susceptibilities; while the more general case of nonzero normal susceptibilities is discussed in Sec. 2.5. Enforcing that $P_z = M_z = 0$ may a priori seem to be an important restriction but, as we will see, it does not have a major impact on the synthesis procedure besides the fact that it reduces the number of available degrees of freedom of the metasurface. This restriction mostly affects the realization of the scattering particles that may be polarizable in the normal direction, which may ultimately alter the scattering response of the structure. However, it should be noted that in the particular case where all the specified waves are propagating normally with respect to the metasurface, then the excitation of normal polarization densities does not induce any discontinuity of the fields. This is because, when all the specified waves propagate normally, their corresponding electric and magnetic fields as well as the synthesized susceptibilities are not functions of the coordinates x and y since no change in the direction of propagation is

specified. In that case, the spatial derivatives of P_z and M_z in Eqs. (2.4a) and (2.4b) are equal to zero, thus inducing no discontinuities of the fields on both sides of the metasurface. This means that the susceptibilities producing normal polarizations can be completely ignored when the metasurface is synthesized for normally propagating waves. In this scenario, only the tangential components of the susceptibilities should be considered.

Let us now simplify the GSTCs so as to obtain the final form of the synthesis relations. Substituting (2.7) into (2.4a) and (2.4b), and dropping the spatial derivatives, leads to

$$\hat{\boldsymbol{z}} \times \Delta \boldsymbol{H} = j\omega\epsilon_0 \overline{\overline{\chi}}_{\mathrm{ee}} \cdot \boldsymbol{E}_{\mathrm{av}} + jk_0 \overline{\overline{\chi}}_{\mathrm{em}} \cdot \boldsymbol{H}_{\mathrm{av}}, \tag{2.14a}$$

$$\Delta \boldsymbol{E} \times \hat{\boldsymbol{z}} = j\omega\mu_0 \overline{\overline{\chi}}_{\mathrm{mm}} \cdot \boldsymbol{H}_{\mathrm{av}} + jk_0 \overline{\overline{\chi}}_{\mathrm{me}} \cdot \boldsymbol{E}_{\mathrm{av}}, \tag{2.14b}$$

where k_0 is the free-space wavenumber and where the susceptibility tensors only contain the tangential susceptibility components. This system can also be written in matrix form to simplify the synthesis procedure. The matrix equivalent of (2.14) is given by

$$\begin{pmatrix} \Delta H_y \\ \Delta H_x \\ \Delta E_y \\ \Delta E_x \end{pmatrix} = \begin{pmatrix} \widetilde{\chi}_{\mathrm{ee}}^{xx} & \widetilde{\chi}_{\mathrm{ee}}^{xy} & \widetilde{\chi}_{\mathrm{em}}^{xx} & \widetilde{\chi}_{\mathrm{em}}^{xy} \\ \widetilde{\chi}_{\mathrm{ee}}^{yx} & \widetilde{\chi}_{\mathrm{ee}}^{yy} & \widetilde{\chi}_{\mathrm{em}}^{yx} & \widetilde{\chi}_{\mathrm{em}}^{yy} \\ \widetilde{\chi}_{\mathrm{me}}^{xx} & \widetilde{\chi}_{\mathrm{me}}^{xy} & \widetilde{\chi}_{\mathrm{mm}}^{xx} & \widetilde{\chi}_{\mathrm{mm}}^{xy} \\ \widetilde{\chi}_{\mathrm{me}}^{yx} & \widetilde{\chi}_{\mathrm{me}}^{yy} & \widetilde{\chi}_{\mathrm{mm}}^{yx} & \widetilde{\chi}_{\mathrm{mm}}^{yy} \end{pmatrix} \cdot \begin{pmatrix} E_{x,\mathrm{av}} \\ E_{y,\mathrm{av}} \\ H_{x,\mathrm{av}} \\ H_{y,\mathrm{av}} \end{pmatrix}, \tag{2.15}$$

where the tilde symbol indicates that the susceptibilities in (2.14) have been normalized. The relationship between the susceptibilities in (2.14) and those in (2.15) is

$$\begin{pmatrix} \chi_{\mathrm{ee}}^{xx} & \chi_{\mathrm{ee}}^{xy} & \chi_{\mathrm{em}}^{xx} & \chi_{\mathrm{em}}^{xy} \\ \chi_{\mathrm{ee}}^{yx} & \chi_{\mathrm{ee}}^{yy} & \chi_{\mathrm{em}}^{yx} & \chi_{\mathrm{em}}^{yy} \\ \chi_{\mathrm{me}}^{xx} & \chi_{\mathrm{me}}^{xy} & \chi_{\mathrm{mm}}^{xx} & \chi_{\mathrm{mm}}^{xy} \\ \chi_{\mathrm{me}}^{yx} & \chi_{\mathrm{me}}^{yy} & \chi_{\mathrm{mm}}^{yx} & \chi_{\mathrm{mm}}^{yy} \end{pmatrix} = \begin{pmatrix} \frac{j}{\omega\epsilon_0}\widetilde{\chi}_{\mathrm{ee}}^{xx} & \frac{j}{\omega\epsilon_0}\widetilde{\chi}_{\mathrm{ee}}^{xy} & \frac{j}{k_0}\widetilde{\chi}_{\mathrm{em}}^{xx} & \frac{j}{k_0}\widetilde{\chi}_{\mathrm{em}}^{xy} \\ -\frac{j}{\omega\epsilon_0}\widetilde{\chi}_{\mathrm{ee}}^{yx} & -\frac{j}{\omega\epsilon_0}\widetilde{\chi}_{\mathrm{ee}}^{yy} & -\frac{j}{k_0}\widetilde{\chi}_{\mathrm{em}}^{yx} & -\frac{j}{k_0}\widetilde{\chi}_{\mathrm{em}}^{yy} \\ -\frac{j}{k_0}\widetilde{\chi}_{\mathrm{me}}^{xx} & -\frac{j}{k_0}\widetilde{\chi}_{\mathrm{me}}^{xy} & -\frac{j}{\omega\mu_0}\widetilde{\chi}_{\mathrm{mm}}^{xx} & -\frac{j}{\omega\mu_0}\widetilde{\chi}_{\mathrm{mm}}^{xy} \\ \frac{j}{k_0}\widetilde{\chi}_{\mathrm{me}}^{yx} & \frac{j}{k_0}\widetilde{\chi}_{\mathrm{me}}^{yy} & \frac{j}{\omega\mu_0}\widetilde{\chi}_{\mathrm{mm}}^{yx} & \frac{j}{\omega\mu_0}\widetilde{\chi}_{\mathrm{mm}}^{yy} \end{pmatrix}. \tag{2.16}$$

As it is, the system (2.15) contains 16 unknown susceptibilities for only 4 equations, which means that it is heavily under-determined and thus cannot be solved directly. This is the basis of two fundamental considerations. The first one is the fact that, to solve the system (2.15), the number of independent unknowns should match the number of equations. Accordingly, the number of independent unknowns must be reduced to 4 so as to have a full-rank system. Since many different sets of 4 susceptibility components may be considered as valid candidates to solve the system, we can assert that different combinations of susceptibilities produce the exact same scattered fields. The second consideration is the fact that one can increase the number of transformations instead of reducing the number of unknowns to 4. This

means that the metasurface has the capability to simultaneously transform several sets of incident, reflected and transmitted waves, providing that they are independent from each other. Consequently, there are three main methods that may be considered to solve the inverse synthesis problem: reducing the number of independent unknowns, increasing the number of transformations or a combination of these two methods.

In order to reduce the number of unknowns, one may, for instance, enforce conditions on the susceptibilities so that they depend on each other. These conditions may include the reciprocity conditions in (2.10), or the passivity and losslessness conditions in (2.13). If these conditions are imposed on the susceptibilities, then the number of independent variables is reduced since several susceptibility components are related to each other. For instance, the reciprocity conditions reduce the number of independent tangential susceptibilities from 16 to 10. However, this method may not be the most appropriate since the conditions that are imposed on the susceptibilities may not be compatible with the specified transformation.

In general, the most appropriate approach to solve the system (2.15) is to match the number of unknown susceptibilities to the number of specified transformations. In many cases, only one transformation is required and thus only 4 susceptibilities are used to synthesize the metasurface. With 4 susceptibilities to select out of 16, the number of different possible combinations is very large. However, most of these combinations of susceptibilities lead to nonphysical or unpractical designs. As an illustration, we will present in Sec. 2.7.1 how rotation of polarization can be achieved by considering different combinations of susceptibilities. It is then obvious that the choice of susceptibilities depends on the requirements of the specified problem. Note that these considerations are naturally extendable to the cases where more than one transformation is desired.

In the forthcoming discussions, we will only present a limited number of combinations of susceptibilities for the sake of conciseness but without loss of generality. First, we will start by considering the synthesis of a birefringent metasurface, which is one of the most commonly used types of structure. Then, we will present an illustrative example of multiple transformations.

Note that a single transformation between specified incident, reflected and transmitted waves requires 4 susceptibilities only in the general case where these waves exhibit both x and y polarization states. However, if only one of these two polarization states is considered, then the system (2.15) reduces to 2 equations. In this scenario, only 2 susceptibilities instead of 4 are required to synthesize the metasurface.

2.3.1 Synthesis of Birefringent Metasurfaces

We now consider the most simple and conventional case of metasurface synthesis. It consists in synthesizing a monoanisotropic ($\overline{\overline{\chi}}_{\mathrm{em}} \equiv \overline{\overline{\chi}}_{\mathrm{me}} = 0$) metasurface possessing only diagonal nonzero susceptibility components, which corresponds to a birefringent structure [159]. For such a metasurface, the system (2.15) reduces to

$$\begin{pmatrix} \Delta H_y \\ \Delta H_x \\ \Delta E_y \\ \Delta E_x \end{pmatrix} = \begin{pmatrix} \widetilde{\chi}_{\mathrm{ee}}^{xx} & 0 & 0 & 0 \\ 0 & \widetilde{\chi}_{\mathrm{ee}}^{yy} & 0 & 0 \\ 0 & 0 & \widetilde{\chi}_{\mathrm{mm}}^{xx} & 0 \\ 0 & 0 & 0 & \widetilde{\chi}_{\mathrm{mm}}^{yy} \end{pmatrix} \cdot \begin{pmatrix} E_{x,\mathrm{av}} \\ E_{y,\mathrm{av}} \\ H_{x,\mathrm{av}} \\ H_{y,\mathrm{av}} \end{pmatrix}, \tag{2.17}$$

which may be straightforwardly solved and yields, using (2.16), the following simple relations for the 4 susceptibilities:

$$\chi_{\mathrm{ee}}^{xx} = \frac{-\Delta H_y}{j\omega\epsilon_0 E_{x,\mathrm{av}}}, \tag{2.18a}$$

$$\chi_{\mathrm{ee}}^{yy} = \frac{\Delta H_x}{j\omega\epsilon_0 E_{y,\mathrm{av}}}, \tag{2.18b}$$

$$\chi_{\mathrm{mm}}^{xx} = \frac{\Delta E_y}{j\omega\mu_0 H_{x,\mathrm{av}}}, \tag{2.18c}$$

$$\chi_{\mathrm{mm}}^{yy} = \frac{-\Delta E_x}{j\omega\mu_0 H_{y,\mathrm{av}}}, \tag{2.18d}$$

where, according to (2.5) and (2.8), $\Delta H_y = H_{y,\mathrm{t}} - (H_{y,\mathrm{i}} + H_{y,\mathrm{r}})$, $E_{x,\mathrm{av}} = (E_{x,\mathrm{t}} + E_{x,\mathrm{i}} + E_{x,\mathrm{r}})/2$, and so on. By synthesis, a metasurface with the susceptibilities in (2.18) will exactly produce the specified reflected and transmitted transverse components of the fields when the metasurface is illuminated by the specified incident field. Since the longitudinal fields are completely determined from the transverse components, according to the uniqueness theorem, the complete specified electromagnetic fields are exactly generated by the metasurface.

Due to the orthogonality between x- and y-polarized waves, the susceptibilities in (2.18) can be separated into two subsets corresponding to equations (2.18a) and (2.18d), and equations (2.18b) and (2.18c), respectively. These two sets of susceptibilities are able to independently and simultaneously transform x- and y-polarized waves. Consequently, each subset allows one to perform the simplest example of single transformation. If the two electric and the two magnetic susceptibilities in (2.18) are equal to each other ($\chi_{\mathrm{ee}}^{xx} = \chi_{\mathrm{ee}}^{yy}$ and $\chi_{\mathrm{mm}}^{xx} = \chi_{\mathrm{mm}}^{yy}$), then the metasurface is monoisotropic and accordingly performs the same operation for both x- and y-polarized waves. If this is not the case, then the metasurface is monoanisotropic (birefringent) and can perform the simplest case of double transformation. Note that we will

see in the next section a more general case of multiple transformation that is not based on the orthogonal separation of x- and y-polarized waves as it is the case here.

The system in (2.17) represents the most conventional way of synthesizing metasurfaces performing single (or double by birefringence) transformation, but it is obviously not the only one possible. One may for instance imagine a monoanisotropic metasurface with nonzero *off-diagonal* components, which would be solved in the exact same fashion while performing a different kind of electromagnetic transformation since it would correspond to a gyrotropic structure. An example of such a gyrotropic metasurface will be presented in Sec. 2.7.1.

2.3.2 Multiple Transformations

We have just seen how a metasurface can be synthesized to perform a single transformation, if the structure is monoisotropic, or a very particular case of double transformations, if the structure is monoanisotropic. However, as mentioned in Sec. 2.3, the general system of equations (2.15) has the capability to perform multiple transformations given its large number of degrees of freedom, i.e. its 16 susceptibility components. Here, we will see how the system (2.15) can be solved for several transformations including incident waves coming from one side only or both sides of the metasurface. To accommodate for the additional degrees of freedom, three additional wave transformations are added, so that (2.15) transforms to

$$\begin{pmatrix} \Delta H_{y1} & \Delta H_{y2} & \Delta H_{y3} & \Delta H_{y4} \\ \Delta H_{x1} & \Delta H_{x2} & \Delta H_{x3} & \Delta H_{x4} \\ \Delta E_{y1} & \Delta E_{y2} & \Delta E_{y3} & \Delta E_{y4} \\ \Delta E_{x1} & \Delta E_{x2} & \Delta E_{x3} & \Delta E_{x4} \end{pmatrix} = \begin{pmatrix} \widetilde{\chi}_{\mathrm{ee}}^{xx} & \widetilde{\chi}_{\mathrm{ee}}^{xy} & \widetilde{\chi}_{\mathrm{em}}^{xx} & \widetilde{\chi}_{\mathrm{em}}^{xy} \\ \widetilde{\chi}_{\mathrm{ee}}^{yx} & \widetilde{\chi}_{\mathrm{ee}}^{yy} & \widetilde{\chi}_{\mathrm{em}}^{yx} & \widetilde{\chi}_{\mathrm{em}}^{yy} \\ \widetilde{\chi}_{\mathrm{me}}^{xx} & \widetilde{\chi}_{\mathrm{me}}^{xy} & \widetilde{\chi}_{\mathrm{mm}}^{xx} & \widetilde{\chi}_{\mathrm{mm}}^{xy} \\ \widetilde{\chi}_{\mathrm{me}}^{yx} & \widetilde{\chi}_{\mathrm{me}}^{yy} & \widetilde{\chi}_{\mathrm{mm}}^{yx} & \widetilde{\chi}_{\mathrm{mm}}^{yy} \end{pmatrix} \cdot \begin{pmatrix} E_{x1,\mathrm{av}} & E_{x2,\mathrm{av}} & E_{x3,\mathrm{av}} & E_{x4,\mathrm{av}} \\ E_{y1,\mathrm{av}} & E_{y2,\mathrm{av}} & E_{y3,\mathrm{av}} & E_{y4,\mathrm{av}} \\ H_{x1,\mathrm{av}} & H_{x2,\mathrm{av}} & H_{x3,\mathrm{av}} & H_{x4,\mathrm{av}} \\ H_{y1,\mathrm{av}} & H_{y2,\mathrm{av}} & H_{y3,\mathrm{av}} & H_{y4,\mathrm{av}} \end{pmatrix}, \tag{2.19}$$

where the subscripts 1, 2, 3 and 4 indicate the electromagnetic fields corresponding to four distinct and *independent* sets of waves. As previously done, the susceptibilities can be obtained by matrix inversion conjointly with (2.16).

In order to illustrate the concept, we now consider a specific example of double transformations, which consists of synthesizing a monoanisotropic metasurface with full electric and magnetic tangential susceptibility tensors. The corresponding system is, from (2.19), given

by

$$\begin{pmatrix} \Delta H_{y1} & \Delta H_{y2} \\ \Delta H_{x1} & \Delta H_{x2} \\ \Delta E_{y1} & \Delta E_{y2} \\ \Delta E_{x1} & \Delta E_{x2} \end{pmatrix} = \begin{pmatrix} \widetilde{\chi}_{\mathrm{ee}}^{xx} & \widetilde{\chi}_{\mathrm{ee}}^{xy} & 0 & 0 \\ \widetilde{\chi}_{\mathrm{ee}}^{yx} & \widetilde{\chi}_{\mathrm{ee}}^{yy} & 0 & 0 \\ 0 & 0 & \widetilde{\chi}_{\mathrm{mm}}^{xx} & \widetilde{\chi}_{\mathrm{mm}}^{xy} \\ 0 & 0 & \widetilde{\chi}_{\mathrm{mm}}^{yx} & \widetilde{\chi}_{\mathrm{mm}}^{yy} \end{pmatrix} \cdot \begin{pmatrix} E_{x1,\mathrm{av}} & E_{x2,\mathrm{av}} \\ E_{y1,\mathrm{av}} & E_{y2,\mathrm{av}} \\ H_{x1,\mathrm{av}} & H_{x2,\mathrm{av}} \\ H_{y1,\mathrm{av}} & H_{y2,\mathrm{av}} \end{pmatrix}. \tag{2.20}$$

We assume that the two transformations that we are considering possess fields with both x and y polarizations. The solution of (2.20) is readily found by matrix inversion and, after using (2.16), the resulting susceptibilities are

$$\chi_{\mathrm{ee}}^{xx} = \frac{j}{\epsilon_0\omega} \frac{(E_{y1,\mathrm{av}}\Delta H_{y2} - E_{y2,\mathrm{av}}\Delta H_{y1})}{(E_{x2,\mathrm{av}}E_{y1,\mathrm{av}} - E_{x1,\mathrm{av}}E_{y2,\mathrm{av}})}, \tag{2.21a}$$

$$\chi_{\mathrm{ee}}^{xy} = \frac{j}{\epsilon_0\omega} \frac{(E_{x2,\mathrm{av}}\Delta H_{y1} - E_{x1,\mathrm{av}}\Delta H_{y2})}{(E_{x2,\mathrm{av}}E_{y1,\mathrm{av}} - E_{x1,\mathrm{av}}E_{y2,\mathrm{av}})}, \tag{2.21b}$$

$$\chi_{\mathrm{ee}}^{yx} = \frac{j}{\epsilon_0\omega} \frac{(E_{y2,\mathrm{av}}\Delta H_{x1} - E_{y1,\mathrm{av}}\Delta H_{x2})}{(E_{x2,\mathrm{av}}E_{y1,\mathrm{av}} - E_{x1,\mathrm{av}}E_{y2,\mathrm{av}})}, \tag{2.21c}$$

$$\chi_{\mathrm{ee}}^{yy} = \frac{j}{\epsilon_0\omega} \frac{(E_{x1,\mathrm{av}}\Delta H_{x2} - E_{x2,\mathrm{av}}\Delta H_{x1})}{(E_{x2,\mathrm{av}}E_{y1,\mathrm{av}} - E_{x1,\mathrm{av}}E_{y2,\mathrm{av}})}, \tag{2.21d}$$

$$\chi_{\mathrm{mm}}^{xx} = \frac{j}{\mu_0\omega} \frac{(H_{y2,\mathrm{av}}\Delta E_{y1} - H_{y1,\mathrm{av}}\Delta E_{y2})}{(H_{x2,\mathrm{av}}H_{y1,\mathrm{av}} - H_{x1,\mathrm{av}}H_{y2,\mathrm{av}})}, \tag{2.21e}$$

$$\chi_{\mathrm{mm}}^{xy} = \frac{j}{\mu_0\omega} \frac{(H_{x1,\mathrm{av}}\Delta E_{y2} - H_{x2,\mathrm{av}}\Delta E_{y1})}{(H_{x2,\mathrm{av}}H_{y1,\mathrm{av}} - H_{x1,\mathrm{av}}H_{y2,\mathrm{av}})}, \tag{2.21f}$$

$$\chi_{\mathrm{mm}}^{yx} = \frac{j}{\mu_0\omega} \frac{(H_{y1,\mathrm{av}}\Delta E_{x2} - H_{y2,\mathrm{av}}\Delta E_{x1})}{(H_{x2,\mathrm{av}}H_{y1,\mathrm{av}} - H_{x1,\mathrm{av}}H_{y2,\mathrm{av}})}, \tag{2.21g}$$

$$\chi_{\mathrm{mm}}^{yy} = \frac{j}{\mu_0\omega} \frac{(H_{x2,\mathrm{av}}\Delta E_{x1} - H_{x1,\mathrm{av}}\Delta E_{x2})}{(H_{x2,\mathrm{av}}H_{y1,\mathrm{av}} - H_{x1,\mathrm{av}}H_{y2,\mathrm{av}})}, \tag{2.21h}$$

where the subscripts 1 and 2 stand for the first and the second wave set transformation, respectively. Applying the conditions (2.10) and (2.13) to (2.21) indicates that in most cases the metasurface will not be only active/lossy but also nonreciprocal. The same argument applies to the more general case of the fully bianisotropic metasurface described by the susceptibilities in (2.19) which may, depending on the choice of transformations, be nonreciprocal and active/lossy. Note that the choice of using the susceptibility tensors $\overline{\overline{\chi}}_{\mathrm{ee}}$ and $\overline{\overline{\chi}}_{\mathrm{mm}}$ in (2.20) was arbitrary and other sets of susceptibilities, for instance including bianisotropic components, may be better suited to perform the desired transformations. In the upcoming Sec. 2.7.2, we will present an example of the application of relations (2.21).

2.4 Relations with Scattering Parameters

So far, we have been only interested in the mathematical synthesis of metasurfaces, which consists in finding the susceptibilities in terms of specified fields. We shall now investigate how the synthesized susceptibilities may be related to the shape of the scattering particles that will constitute the metasurfaces to be realized. Here, we will only present the mathematical expressions that relate the susceptibilities to the scattering particles, while a more in depth discussion on the realization of metasurface scattering particles will be presented in Chapter 4.

The conventional method to relate the scattering particle shape to equivalent susceptibilities (or material parameters) is based on homogenization techniques. In the case of metamaterials, these techniques may be used to relate homogenized material parameters to the scattering parameters of the scatterers. From a general perspective, a single isolated scatterer is not sufficient to describe an homogenized medium. Instead, we shall rather consider a periodic array of scatterers, which takes into account the interactions and coupling between adjacent scatterers hence leading to a more accurate description of a "medium" compared to a single scatterer. The susceptibilities, which describe the macroscopic responses of a medium, are thus naturally well-suited to describe the homogenized material parameters of metasurfaces. It follows that the equivalent susceptibilities of a scattering particle may be related to the corresponding scattering parameters, conventionally obtained via full-wave simulations, of a periodic array made of an infinite repetition of that scattering particle [132,150,160,161]. Because the periodic array of scatterers is uniform with subwavelength periodicity, the scattered fields obey Snell's law. More specifically, if the incident wave propagates normally with respect to the array, then the reflected and transmitted waves also propagate normally. In most cases, the periodic array of scattering particles is excited with normally propagating waves. This allows one to rigorously obtain the 16 *tangential* susceptibility components in (2.19). However, it does not provide any information about the normal susceptibility components of the scattering particles. This is because normally propagating waves do *not* excite the normal susceptibilities due to the purely tangential nature of their electromagnetic fields. Nevertheless, this method allows one to match the tangential susceptibilities of the scattering particle to the susceptibilities found from the metasurface synthesis performed following the procedure in Sec. 2.3 and that precisely yields the ideal tangential susceptibility components. It is clear that the scattering particles may, in addition to their tangential susceptibilities, possess nonzero normal susceptibility components. In that case, the scattering response of the metasurface, when illuminated with obliquely propagating waves, will differ from the expected ideal behavior prescribed in the synthesis. Consequently, the homogenization technique only serve as an initial guess to describe the scattering behavior of the metasurface. Note that

is possible to obtain all 36 susceptibility components (4 susceptibility tensors, each with 9 components) of a scattering particle but this would required solving the 4 GSTCs relations for 9 independent sets of incident, reflected and transmitted waves, which is particularity tedious and is thus avoided.

We will now derive the explicit expressions relating the tangential susceptibilities to the scattering parameters in the general case of a fully bianisotropic uniform metasurface surrounded by different media and excited by normally incident plane waves. Let us first write the system (2.19) in the following compact form:

$$\overline{\overline{\Delta}} = \overline{\overline{\chi}} \cdot \overline{\overline{A}}_v, \tag{2.22}$$

where the matrices $\overline{\overline{\Delta}}$, $\overline{\overline{\chi}}$ and $\overline{\overline{A}}_v$ correspond to the field differences, the normalized susceptibilities and the field averages, respectively. In order to obtain the 16 tangential susceptibility components in (2.19), we will now define four transformations by specifying the fields on both sides of the metasurface. Let us consider that the metasurface is illuminated from the left with an x-polarized normally incident plane wave. The corresponding incident, reflected and transmitted electromagnetic fields read

$$\boldsymbol{E}_{\mathrm{i}} = \hat{\boldsymbol{x}}, \qquad \boldsymbol{E}_{\mathrm{r}} = S_{11}^{xx}\hat{\boldsymbol{x}} + S_{11}^{yx}\hat{\boldsymbol{y}}, \qquad \boldsymbol{E}_{\mathrm{t}} = S_{21}^{xx}\hat{\boldsymbol{x}} + S_{21}^{yx}\hat{\boldsymbol{y}}, \tag{2.23a}$$

$$\boldsymbol{H}_{\mathrm{i}} = \frac{1}{\eta_1}\hat{\boldsymbol{y}}, \qquad \boldsymbol{H}_{\mathrm{r}} = \frac{1}{\eta_1}(S_{11}^{yx}\hat{\boldsymbol{x}} - S_{11}^{xx}\hat{\boldsymbol{y}}), \qquad \boldsymbol{H}_{\mathrm{t}} = \frac{1}{\eta_2}(-S_{21}^{yx}\hat{\boldsymbol{x}} + S_{21}^{xx}\hat{\boldsymbol{y}}), \tag{2.23b}$$

where the terms S_{ab}^{uv}, with $a, b = \{1, 2\}$ and $u, v = \{x, y\}$, are the scattering parameters with ports 1 and 2 corresponding to the left and right sides of the metasurface, respectively. The medium of the left of the metasurface has the intrinsic impedance η_1, while the medium on the right has the intrinsic impedance η_2. In addition to (2.23), three other cases have to be considered, i.e. y-polarized excitation incident from the left (port 1), and x- and y-polarized excitations incident from the right (port 2). Inserting these fields into (2.19), leads to the following matrix $\overline{\overline{\Delta}}$:

$$\overline{\overline{\Delta}} = \begin{pmatrix} -\overline{\overline{N}}_2/\eta_1 + \overline{\overline{N}}_2 \cdot \overline{\overline{S}}_{11}/\eta_1 + \overline{\overline{N}}_2 \cdot \overline{\overline{S}}_{21}/\eta_2 & -\overline{\overline{N}}_2/\eta_2 + \overline{\overline{N}}_2 \cdot \overline{\overline{S}}_{12}/\eta_1 + \overline{\overline{N}}_2 \cdot \overline{\overline{S}}_{22}/\eta_2 \\ -\overline{\overline{N}}_1 \cdot \overline{\overline{N}}_2 - \overline{\overline{N}}_1 \cdot \overline{\overline{N}}_2 \cdot \overline{\overline{S}}_{11} + \overline{\overline{N}}_1 \cdot \overline{\overline{N}}_2 \cdot \overline{\overline{S}}_{21} & \overline{\overline{N}}_1 \cdot \overline{\overline{N}}_2 - \overline{\overline{N}}_1 \cdot \overline{\overline{N}}_2 \cdot \overline{\overline{S}}_{12} + \overline{\overline{N}}_1 \cdot \overline{\overline{N}}_2 \cdot \overline{\overline{S}}_{22} \end{pmatrix}, \tag{2.24}$$

and, similarly, the matrix $\overline{\overline{A}}_v$ reads

$$\overline{\overline{A}}_v = \frac{1}{2}\begin{pmatrix} \overline{\overline{I}} + \overline{\overline{S}}_{11} + \overline{\overline{S}}_{21} & \overline{\overline{I}} + \overline{\overline{S}}_{12} + \overline{\overline{S}}_{22} \\ \overline{\overline{N}}_1/\eta_1 - \overline{\overline{N}}_1 \cdot \overline{\overline{S}}_{11}/\eta_1 + \overline{\overline{N}}_1 \cdot \overline{\overline{S}}_{21}/\eta_2 & -\overline{\overline{N}}_1/\eta_2 - \overline{\overline{N}}_1 \cdot \overline{\overline{S}}_{12}/\eta_1 + \overline{\overline{N}}_1 \cdot \overline{\overline{S}}_{22}/\eta_2 \end{pmatrix}, \tag{2.25}$$

where the matrices $\overline{\overline{S}}_{ab}$, $\overline{\overline{I}}$, $\overline{\overline{N}}_1$ and $\overline{\overline{N}}_2$ are defined by

$$\overline{\overline{S}}_{ab} = \begin{pmatrix} S_{ab}^{xx} & S_{ab}^{xy} \\ S_{ab}^{yx} & S_{ab}^{yy} \end{pmatrix}, \qquad \overline{\overline{I}} = \begin{pmatrix} 1 & 0 \\ 0 & 1 \end{pmatrix}, \qquad \overline{\overline{N}}_1 = \begin{pmatrix} 0 & -1 \\ 1 & 0 \end{pmatrix}, \qquad \overline{\overline{N}}_2 = \begin{pmatrix} 1 & 0 \\ 0 & -1 \end{pmatrix}. \quad (2.26)$$

Now, the procedure to obtain the susceptibilities of a given scattering particle is as follows: firstly, the scattering particle is simulated with periodic boundary conditions and normal excitation. Secondly, the resulting scattering parameters are used to define the matrices in (2.24) and (2.25). Finally, the corresponding susceptibilities are obtained by matrix inversion of (2.22).

Alternatively, it is possible to express the scattering parameters (for normal wave propagation) of a uniform metasurface with known susceptibilities by solving (2.22) for the scattering parameters. This leads to the following matrix equation:

$$\overline{\overline{S}} = \overline{\overline{M}}_1^{-1} \cdot \overline{\overline{M}}_2, \quad (2.27)$$

where the scattering parameter matrix, $\overline{\overline{S}}$, is defined as

$$\overline{\overline{S}} = \begin{pmatrix} \overline{\overline{S}}_{11} & \overline{\overline{S}}_{12} \\ \overline{\overline{S}}_{21} & \overline{\overline{S}}_{22} \end{pmatrix}, \quad (2.28)$$

and the matrices $\overline{\overline{M}}_1$ and $\overline{\overline{M}}_2$ are obtained from (2.22), (2.24) and (2.25) by expressing the scattering parameters in terms of the normalized susceptibility tensors. The resulting matrix $\overline{\overline{M}}_1$ reads

$$\overline{\overline{M}}_1 = \begin{pmatrix} \overline{\overline{N}}_2/\eta_1 - \tilde{\overline{\overline{\chi}}}_{\mathrm{ee}}/2 + \tilde{\overline{\overline{\chi}}}_{\mathrm{em}} \cdot \overline{\overline{N}}_1/(2\eta_1) & \overline{\overline{N}}_2/\eta_2 - \tilde{\overline{\overline{\chi}}}_{\mathrm{ee}}/2 - \tilde{\overline{\overline{\chi}}}_{\mathrm{em}} \cdot \overline{\overline{N}}_1/(2\eta_2) \\ -\overline{\overline{N}}_1 \cdot \overline{\overline{N}}_2 - \tilde{\overline{\overline{\chi}}}_{\mathrm{me}}/2 + \tilde{\overline{\overline{\chi}}}_{\mathrm{mm}} \cdot \overline{\overline{N}}_1/(2\eta_1) & \overline{\overline{N}}_1 \cdot \overline{\overline{N}}_2 - \tilde{\overline{\overline{\chi}}}_{\mathrm{me}}/2 - \tilde{\overline{\overline{\chi}}}_{\mathrm{mm}} \cdot \overline{\overline{N}}_1/(2\eta_2) \end{pmatrix}, \quad (2.29)$$

and the matrix $\overline{\overline{M}}_2$ reads

$$\overline{\overline{M}}_2 = \begin{pmatrix} \tilde{\overline{\overline{\chi}}}_{\mathrm{ee}}/2 + \overline{\overline{N}}_2/\eta_1 + \tilde{\overline{\overline{\chi}}}_{\mathrm{em}} \cdot \overline{\overline{N}}_1/(2\eta_1) & \tilde{\overline{\overline{\chi}}}_{\mathrm{ee}}/2 + \overline{\overline{N}}_2/\eta_2 - \tilde{\overline{\overline{\chi}}}_{\mathrm{em}} \cdot \overline{\overline{N}}_1/(2\eta_2) \\ \tilde{\overline{\overline{\chi}}}_{\mathrm{me}}/2 + \overline{\overline{N}}_1 \cdot \overline{\overline{N}}_2 + \tilde{\overline{\overline{\chi}}}_{\mathrm{mm}} \cdot \overline{\overline{N}}_1/(2\eta_1) & \tilde{\overline{\overline{\chi}}}_{\mathrm{me}}/2 - \overline{\overline{N}}_1\overline{\overline{N}}_2 - \tilde{\overline{\overline{\chi}}}_{\mathrm{mm}} \cdot \overline{\overline{N}}_1/(2\eta_2) \end{pmatrix}. \quad (2.30)$$

We now provide the expressions relating the susceptibilities to the scattering parameters (and vice-versa) in the particular case of the monoanisotropic diagonal metasurface discussed in Sec. 2.3.1. Moreover, we assume that the media on both sides of the metasurface are the same and correspond to vacuum, i.e. $\eta_1 = \eta_2 = \eta_0$. By definition, we know that this metasurface is nongyrotropic and reciprocal. Therefore, we have that $S_{ab}^{xy} = S_{ab}^{yx} = 0$ and that $\overline{\overline{S}}_{21} = \overline{\overline{S}}_{12}^{\mathrm{T}}$.

Solving (2.22) along with (2.16) leads to the following susceptibilities:

$$\chi_{\mathrm{ee}}^{xx} = \frac{2j\left(T_x + R_x - 1\right)}{k_0\left(T_x + R_x + 1\right)}, \tag{2.31a}$$

$$\chi_{\mathrm{ee}}^{yy} = \frac{2j\left(T_y + R_y - 1\right)}{k_0\left(T_y + R_y + 1\right)}, \tag{2.31b}$$

$$\chi_{\mathrm{mm}}^{xx} = \frac{2j\left(T_y - R_y - 1\right)}{k_0\left(T_y - R_y + 1\right)}, \tag{2.31c}$$

$$\chi_{\mathrm{mm}}^{yy} = \frac{2j\left(T_x - R_x - 1\right)}{k_0\left(T_x - R_x + 1\right)}, \tag{2.31d}$$

where, for convenience, we have that $T_x = S_{21}^{xx}$ and $R_x = S_{11}^{xx}$, and so on. Reversing these relations so as to express the scattering parameters in terms of the susceptibilities leads to

$$T_x = \frac{4 + \chi_{\mathrm{ee}}^{xx}\chi_{\mathrm{mm}}^{yy}k_0^2}{(2 + jk_0\chi_{\mathrm{ee}}^{xx})(2 + jk_0\chi_{\mathrm{mm}}^{yy})}, \tag{2.32a}$$

$$R_x = \frac{2jk_0\left(\chi_{\mathrm{mm}}^{yy} - \chi_{\mathrm{ee}}^{xx}\right)}{\left(2 + jk_0\chi_{\mathrm{ee}}^{xx}\right)\left(2 + jk_0\chi_{\mathrm{mm}}^{yy}\right)}, \tag{2.32b}$$

for x-polarized waves, and

$$T_y = \frac{4 + \chi_{\mathrm{ee}}^{yy}\chi_{\mathrm{mm}}^{xx}k_0^2}{(2 + jk_0\chi_{\mathrm{ee}}^{yy})(2 + jk_0\chi_{\mathrm{mm}}^{xx})}, \tag{2.33a}$$

$$R_y = \frac{2jk_0\left(\chi_{\mathrm{mm}}^{xx} - \chi_{\mathrm{ee}}^{yy}\right)}{\left(2 + jk_0\chi_{\mathrm{ee}}^{yy}\right)\left(2 + jk_0\chi_{\mathrm{mm}}^{xx}\right)}, \tag{2.33b}$$

for y-polarized waves. It is interesting to note the reflectionless conditions that are revealed from Eqs. (2.32b) and (2.33b) and which are respectively given by $\chi_{\mathrm{mm}}^{yy} = \chi_{\mathrm{ee}}^{xx}$ and $\chi_{\mathrm{mm}}^{xx} = \chi_{\mathrm{ee}}^{yy}$. In order to illustrate the utilization of the relations between susceptibilities and scattering parameters, we will see several examples where they are put into practice in the forthcoming sections and chapters.

At this stage, one may wonder whether the expressions obtained above *only* apply to metasurfaces synthesized to transform incident, reflected and transmitted waves that are normally propagating with respect to the metasurface, or whether they also apply for arbitrary field transformations, which generally involves nonuniform metasurfaces? To answer this question, let us consider the following four cases: 1) the metasurface is synthesized only for normally propagating waves, 2) the metasurface is synthesized for obliquely propagating waves but without changing the direction of wave propagation, i.e. the metasurface is uniform, 3) the metasurface is synthesized to change the direction of wave propagation (e.g. refraction, collimation, etc) but, at least, one of the specified wave propagates normally to the metasurface,

and 4) the metasurface is synthesized to change the direction of wave propagation but none of the specified waves propagate normally (e.g. negative refraction).

Case 1: the expressions derived above perfectly apply and the realized metasurface response will be in exact agreement with the specified one.

Case 2: for illustration, let us consider the synthesis of a reflectionless uniform metasurface that rotates the polarization of the incident wave, which impinges the metasurface at an angle $\theta_\mathrm{i} = \theta_\mathrm{t} = 30^\circ$ from broadside. If the expressions above are used and the scattering particle simulated with normal wave propagation, then the response of the realized metasurface for the specified incidence angle of 30° will *not* correspond to the expected result. Indeed, as said above, simulating all the scattering parameters with normally propagating waves and solving (2.22) yields the exact tangential susceptibility components but does not provide any information about the normal susceptibility components. Therefore, an obliquely impinging wave may excite these normal polarizations, thus affecting the scattering response of the metasurface. The second reason is due to non-negligible coupling between adjacent scattering particles, which depends on the angle incidence of the excitation (spatial dispersion). This coupling is thus different for normal and oblique wave propagation. In order to correctly synthesize this metasurface, one should change relations (2.23) so as to include the angle of wave propagation. Accordingly, the scattering particles must be simulated with the same specified angle of wave propagation. Only then, would the metasurface yield the expected scattering response.

Case 3: for illustration, let us consider the synthesis of a reflectionless metasurface that refracts a normally incident plane wave at a given refraction angle θ_t. In that case, the metasurface is nonuniform and the susceptibilities are thus functions of x and y on the metasurface. Inserting these susceptibilities into the relations above will yield scattering parameters that are themselves spatially varying. It is important to understand that these scattering parameters *do not* represent the overall scattering behavior of the metasurface but rather correspond to the *local* scattering parameters. Due to the nonuniformity of the structure, several different scattering particles have to be realized, each one of them exhibiting the local scattering parameters corresponding to their position (x, y) on the metasurface. This is achieved by simulating each scattering particle *individually* with periodic boundary conditions (PBC). Consequently, once they are all implemented and combined together to form the final metasurface, the coupling between them differs from when they were simulated with PBC. This leads to a scattering response that is different from the expected one, irrespectively of whether the relations above (assuming normal wave propagation) are used or any other one (assuming oblique wave propagation). In that case, the relations between

the susceptibilities and the scattering parameters only serve as an initial guess to realize the scattering particles, which then usually require to be further optimized so that the final metasurface performs the expected response. In addition to this, the realized scattering particles may also exhibit nonzero normal susceptibilities, which further degrades the scattering behavior of the metasurface. Since, in the example that is considered here, the incident wave is normally impinging on the metasurface, the relations derived above provide a relatively good initial guess to realize the metasurface scattering particles because the excitation of the normal susceptibility components is limited.

Case 4: this case is a combination of the two previous ones since all the waves propagate obliquely (and at different angles) with respect to the metasurface that is thus nonuniform. If the specified incident, reflected and transmitted fields are all plane waves, then it would be adequate to adjust the direction of wave propagation, to that of the specified incident wave, in (2.23) as well as in the full-wave simulations. However, if the specified incident, reflected and transmitted fields are not plane waves but arbitrary fields, then the relations derived above are sufficient to obtain an initial approximation of the specified scattering behavior that may require further optimization. This is because metasurfaces are usually synthesized by assuming that the normal susceptibility components are zero, as was done in Sec. 2.3. Therefore, simulating the scattering particles with normally propagating waves ensures that their resulting tangential susceptibilities correspond to the desired ones obtain from the synthesis. Then, the discrepancies in the final metasurface response may only come from the presence of nonzero normal polarizations and coupling with adjacent unit cells. But at least their tangential polarizations are the expected ones, which minimizes the errors in the scattering behavior of the metasurface.

We point out the fact that, in general, the susceptibilities obtained from the synthesis are complex quantities. According to the discussion in Sec. 2.2, we know that these complex quantities may be related to loss and gain. More specifically, the susceptibilities in (2.18) correspond to dissipation if their imaginary parts are negative, and gain if their imaginary parts are positive. This is relevant to the implementation of metasurfaces because, in some cases, the realization of the scattering particles is simplified by considering ideal structures made of purely lossless dielectric material and metallic inclusions made of perfect electric conductor (PEC). In that scenario, the susceptibilities retrieved with (2.31) are necessarily purely real. Consequently, it would be impossible to realize the exact complex susceptibilities obtain from the synthesis with such kind of “ideal” scattering particles.

There are, at least, three solutions to overcome this issue. The first one consists in using lossy materials to approach, as closely as possible, the required susceptibility values, which

is generally difficult since it would require precise control of the dissipation as function of the position on the metasurface. The second solution consists in simply setting to zero the imaginary parts of the synthesized susceptibilities and implementing only their remaining real parts. In that case, the metasurface response will differ from the expected one as undesired scattering will appear, which, depending on the application, may or may not be an issue. The third solution is similar to the second one, in the sense that the imaginary parts of the synthesized susceptibilities are set to zero, but the remaining real parts are optimized so as to minimize the discrepancies between the expected response of the metasurface and the approximated one. Typically, the optimization procedure consists in minimizing a cost function of the following form [132]:

$$F = \left|T_{\text{spec}} - T_{\text{approx}}\right|^2 + \left|R_{\text{spec}} - R_{\text{approx}}\right|^2, \tag{2.34}$$

where the scattering parameters T_{spec} and R_{spec} are obtained from (2.32) or (2.33) using the synthesized susceptibilities. While the parameters T_{approx} and R_{approx} are obtained from the same equations but with the purely real susceptibilities that have to be optimized. The cost function (2.34) is naturally extendable to the more general case of full scattering parameter matrices.

2.5 Metasurfaces with Nonzero Normal Polarization Densities

The metasurface synthesis relations derived in Sec. 2.3 have been obtained with the assumption that the considered metasurfaces do not possess normal susceptibility components. This restriction was imposed to simplify the GSTCs since the spatial derivatives in (2.4) vanish in the case of the absence of normal polarization densities. We will now discuss the case of metasurfaces with nonzero normal polarization densities.

The general bianisotropic system of equations (2.4) consists of a total number of 36 unknown susceptibilities for only 4 equations when full susceptibility tensors are considered, instead of 16 unknown as was previously the case. This corresponds to a heavily under-determined system, where these additional susceptibility components largely increase the number of degrees of freedom available to control electromagnetic fields.

The synthesis of metasurfaces with nonzero normal polarization densities may be performed following similar procedures as those already discussed in Sec. 2.3. As before, one needs to balance the number of unknown susceptibilities to the number of available equations provided by the GSTCs. Depending on the specifications, this may become more difficult with the addition of normal susceptibility components since more transformations may be required to

obtain a full-rank system. Additionally, if the specified transformations involve changing the direction of wave propagation, then the system (2.4) becomes a coupled system of partial differential equations in terms of the susceptibilities. This generally prevents the derivation of closed-form solutions of the susceptibilities, which should rather be obtained numerically. However, we will provide an example of a synthesis problem in Sec. 3.4 for the case of a refractive metasurface, where the susceptibilities are obtainable in closed form.

Relations between susceptibilities and scattering parameters can also be obtained by following the procedure discussed in Sec. 2.4. If the susceptibilities are spatially varying in the plane of the metasurface, then the scattering parameters are obtained by solving relations (2.4), which, as said above, form a set of coupled differential equations that may be solved numerically. However, if the metasurface susceptibility functions are not spatially varying, then Snell's law applies and the scattering parameters can thus be obtained in closed form. In that case, it is possible to derive relations similar to those in (2.24) and (2.25), and (2.29) and (2.30), that apply for the most general case where the 36 susceptibilities are considered. In Sec. 2.4, we were able to express the 16 susceptibilities in terms of scattering parameters by considering the 4 GSTCs equations along with 4 wave transformations: x- and y-polarized excitations from port 1, and x- and y-polarized excitations from port 2. Now, if 36 susceptibilities are considered, we would need to specify 9 independent wave transformations so as to form a full rank system with the 4 GSTCs equations. Although, this is feasible, it is particularly cumbersome and is thus omitted here. Alternatively, we can express the scattering parameters as functions of the susceptibilities. This is easier since, in this scenario, the system of equations is always a full rank system made of 16 unknown scattering parameters distributed among 4 wave transformations, as was the case for the derivation of (2.29) and (2.30). Unfortunately, even if expressing the scattering parameters in terms of the susceptibilities is easier than doing the opposite, the resulting relations cannot be concisely written and are thus not reported here.

Instead, we provide the expressions of the reflection and transmission coefficients for the particular case of a monoanisotropic diagonal and uniform metasurface [162]. Its susceptibility tensors are

$$\overline{\overline{\chi}}_{\mathrm{ee}} = \begin{pmatrix} \chi_{\mathrm{ee}}^{xx} & 0 & 0 \\ 0 & \chi_{\mathrm{ee}}^{yy} & 0 \\ 0 & 0 & \chi_{\mathrm{ee}}^{zz} \end{pmatrix}, \qquad \overline{\overline{\chi}}_{\mathrm{mm}} = \begin{pmatrix} \chi_{\mathrm{mm}}^{xx} & 0 & 0 \\ 0 & \chi_{\mathrm{mm}}^{yy} & 0 \\ 0 & 0 & \chi_{\mathrm{mm}}^{zz} \end{pmatrix}. \tag{2.35}$$

We illuminate the metasurface such that the scattering occurs only in the xz-plane. Inser-

ting (2.35) into (2.4) leads to the following reduced GSTCs relations:

$$-\Delta H_y = j\omega\epsilon_0\chi_{\rm ee}^{xx}E_x, \tag{2.36a}$$

$$\Delta H_x = j\omega\epsilon_0\chi_{\rm ee}^{yy}E_y - \chi_{\rm mm}^{zz}\partial_x H_z, \tag{2.36b}$$

$$\Delta E_y = j\omega\mu_0\chi_{\rm mm}^{xx}H_x, \tag{2.36c}$$

$$-\Delta E_x = j\omega\mu_0\chi_{\rm mm}^{yy}H_y + \chi_{\rm ee}^{zz}\partial_x E_z. \tag{2.36d}$$

Note that the partial derivatives in (2.36b) and (2.36d) are only in the x-direction since the scattering from this metasurface takes place in the xz-plane, and that they only apply to the fields and not to the susceptibilities since the latter are not functions of space.

If this particular metasurface was illuminated by a normally incident plane wave, then the susceptibilities $\chi_{\rm ee}^{zz}$ and $\chi_{\rm mm}^{zz}$ would not be excited since $E_z = H_z = 0$ for normal propagation. In that case, the scattering parameters are exactly the same as those in (2.32) and (2.33). Therefore, we provide the reflection and transmission coefficients in the case of oblique incidence. Making use of the fact that $\partial_x \to -jk_x$ and using relations similar to those in (2.23) for the specification of the fields, the scattering parameters for p-polarized waves are

$$T_p = \frac{k_z(4 + \chi_{\rm ee}^{xx}\chi_{\rm mm}^{yy}k_0^2 + \chi_{\rm ee}^{xx}\chi_{\rm ee}^{zz}k_x^2)}{(2j - \chi_{\rm ee}^{xx}k_z)(\chi_{\rm mm}^{yy}k_0^2 + \chi_{\rm ee}^{zz}k_x^2 - 2jk_z)}, \tag{2.37a}$$

$$R_p = \frac{2j(\chi_{\rm mm}^{yy}k_0^2 + \chi_{\rm ee}^{zz}k_x^2 - \chi_{\rm ee}^{xx}k_z^2)}{(2j - \chi_{\rm ee}^{xx}k_z)(\chi_{\rm mm}^{yy}k_0^2 + \chi_{\rm ee}^{zz}k_x^2 - 2jk_z)}, \tag{2.37b}$$

and their counterparts for s-polarized waves are

$$T_s = \frac{k_z(4 + \chi_{\rm mm}^{xx}\chi_{\rm ee}^{yy}k_0^2 + \chi_{\rm mm}^{xx}\chi_{\rm mm}^{zz}k_x^2)}{(2j - \chi_{\rm mm}^{xx}k_z)(\chi_{\rm ee}^{yy}k_0^2 + \chi_{\rm mm}^{zz}k_x^2 - 2jk_z)}, \tag{2.38a}$$

$$R_s = -\frac{2j(\chi_{\rm ee}^{yy}k_0^2 + \chi_{\rm mm}^{zz}k_x^2 - \chi_{\rm mm}^{xx}k_z^2)}{(2j - \chi_{\rm mm}^{xx}k_z)(\chi_{\rm ee}^{yy}k_0^2 + \chi_{\rm mm}^{zz}k_x^2 - 2jk_z)}. \tag{2.38b}$$

It can be easily verified that, for normal incidence, relations (2.37) and (2.38) respectively reduce to (2.32) and (2.33) since, in that case, $k_z = k_0$ and $k_x = 0$. Alternatively, by setting $\chi_{\rm ee}^{zz} = \chi_{\rm mm}^{zz} = 0$, relations (2.37) and (2.38) may be used to generalize relations (2.32) and (2.33) so as to express the reflection and transmission coefficients of a uniform metasurface as functions of the incidence angle.

2.6 Equivalence Between Surface and Volume Susceptibilities

The metasurface synthesis technique that has been developed so far uses the GSTCs relations in (2.4) to obtain the susceptibilities of an idealized metasurface with exactly zero thickness. The question that may arise is: can these ideal mathematical surface susceptibilities apply to a real physical structure that necessarily has a nonzero thickness? The short answer to that question is yes, as long as the thickness of the structure remains deeply subwavelength. As the thickness increases, the electromagnetic response of the metasurface deviates more and more from the expected response. To provide a more elaborate answer, we will evaluate the discrepancies between the scattering response of a zero-thickness metasurface and that of a thin metasurface. To do that, we shall first derive the approximate expressions that relate the ideal surface susceptibilities to volumetric ones.

For simplicity but without loss of generality, let us consider the case of an isotropic and uniform metasurface possessing an electric scalar susceptibility, χ_{ee}. The corresponding Maxwell-Ampère equation reads

$$\nabla \times \boldsymbol{H} = j\omega\epsilon_0(1 + \chi_{\text{ee}})\boldsymbol{E}. \tag{2.39}$$

Let us now consider the two following cases: where the metasurface is perfectly zero-thickness, in which case we have that $\chi_{\text{ee}} = \chi_{\text{2D}}\delta(z)$; and where the metasurface has a nonzero subwavelength thickness t, in which case we have that $\chi_{\text{ee}} = \chi_{\text{3D}}\Pi(z/t)$, where $\Pi(z)$ is the rectangular function. These two cases are respectively depicted in Figs. 2.2a and 2.2b.

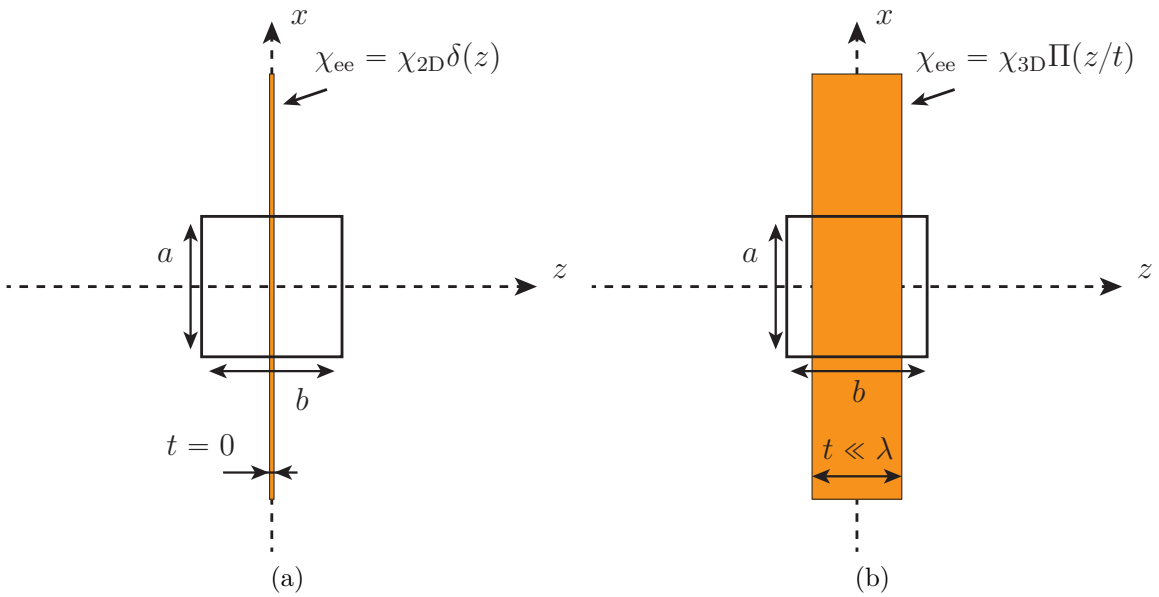

Figure 2.2 Representations of: (a) a zero-thickness metasurface and (b) a metasurface with subwavelength thickness.

Applying the Stokes' theorem to (2.39) for the case in Fig. 2.2a gives

$$\oint_C \boldsymbol{H} \cdot \boldsymbol{dl} = j\omega\epsilon_0 \iint_S \left[1 + \chi_{2\mathrm{D}}\delta(z)\right] \boldsymbol{E} \cdot \boldsymbol{dS}. \tag{2.40}$$

Evaluating the integrals over the highlighted rectangle of dimensions $a \times b$ in Fig. 2.2a leads to

$$(H_x^+ - H_x^-)a \approx j\omega\epsilon_0 \left(b + \chi_{2\mathrm{D}}\right) E_y a, \tag{2.41}$$

where it is assumed that a and b are very small compared to the wavelength. Applying again the Stokes' theorem to (2.39) for the case in Fig. 2.2b gives

$$\oint_C \boldsymbol{H} \cdot \boldsymbol{dl} = j\omega\epsilon_0 \iint_S \left[1 + \chi_{3\mathrm{D}}\Pi(z/t)\right] \boldsymbol{E} \cdot \boldsymbol{dS}, \tag{2.42}$$

which, after integration, reduces to

$$(H_x^+ - H_x^-)a \approx j\omega\epsilon_0 \left(b + \chi_{3\mathrm{D}}t\right) E_y a. \tag{2.43}$$

By comparing the expressions obtained in (2.41) and in (2.43), we can easily deduce that the relation between $\chi_{2\mathrm{D}}$ and $\chi_{3\mathrm{D}}$ is

$$\chi_{3\mathrm{D}} = \frac{\chi_{2\mathrm{D}}}{t}. \tag{2.44}$$

We can now define the approximate expressions for the material parameters of the volumetric metasurface given in terms of the synthesized surface susceptibilities, $\chi_{2\mathrm{D}}$. For instance, the relative permittivity is given by

$$\epsilon_r = 1 + \chi_{3\mathrm{D}} \approx 1 + \frac{\chi_{2\mathrm{D}}}{t}, \tag{2.45}$$

where the division by the thickness t has the effect of "diluting the strength" of the susceptibility over the longitudinal extent of the metasurface. Note that the term $\chi_{2\mathrm{D}}/t$ is dimensionless since the surface susceptibilities are expressed in meters. The developments provided above are naturally extendable to all other cases of scalar and tensorial susceptibilities.

The fact that it is possible to relate the ideal surface susceptibilities obtained from the synthesis to volumetric material parameters shows that this mathematical synthesis may also be used to describe the behavior of thin metasurfaces. However, one should keep in mind that the relation (2.45) is an approximation and is valid only when $t \ll \lambda$. In Chapter 6, we will come back to this issue and analyze the effect of a nonzero thickness on the scattering behavior of metasurfaces.

One direct application of the possibility to associate zero-thickness susceptibilities to volumetric material parameters is the simulation of the metasurface scattering behavior, which may now be performed in commercial software simply by implementing the metasurface as a material slab. Note that certain simulation software offer the option to simulate zero-thickness structures, for instance by using impedance boundary conditions or other sorts of transition conditions, but they are usually not general enough to account for fields discontinuities produced by fully bianisotropic metasurfaces. In the upcoming Sections 2.7.2, 5.8 and 6.2, we will use this thin slab metasurface approximation to simulate the scattering behavior of different metasurfaces.

Note that we have also developed more rigorous full-wave simulation tools to analyze the response of metasurfaces [3, 163, 164]. These simulation tools consists of finite-difference frequency- and time-domain (FDFD/FDTD) and spectral domain homemade codes that emulate the presence of an exactly zero-thickness metasurface, thus allowing an accurate evaluation of its scattering behavior.

2.7 Illustrative Examples

We will now illustrate the metasurface synthesis principles with three different examples. The first one presents different combinations of susceptibilities performing the same operation of polarization rotation, as an illustration of the single transformation technique addressed in Sec. 2.3.1. The second example illustrates the application of the multiple transformation technique discussed in Sec. 2.3.2 in the synthesis of a nonreciprocal metasurface. Finally, the third example combines the concept of multiple transformations with nonzero normal susceptibility components to realize a reciprocal metasurface with controllable angular scattering.

In addition to the these examples, Chapter 3 discusses in details the topic of refractive metasurfaces and Chapter 5 provides several other transformation examples that may lead to potential metasurface applications.

2.7.1 Reciprocal and Nonreciprocal Polarization Rotations

Let us consider the following synthesis problem: find the susceptibilities of a reflectionless metasurface that rotates the polarization of a normally incident plane wave by an angle of $\pi/3$. We specify that the incident wave is linearly polarized with an electric field making a $\pi/8$ angle with respect to the x-axis, as shown in Fig. 2.3. The resulting transmitted wave is thus polarized with an electric field making an angle of $11\pi/24$. We assume that the metasurface is surrounded on both sides by vacuum, i.e. $\eta_1 = \eta_2 = \eta_0$.

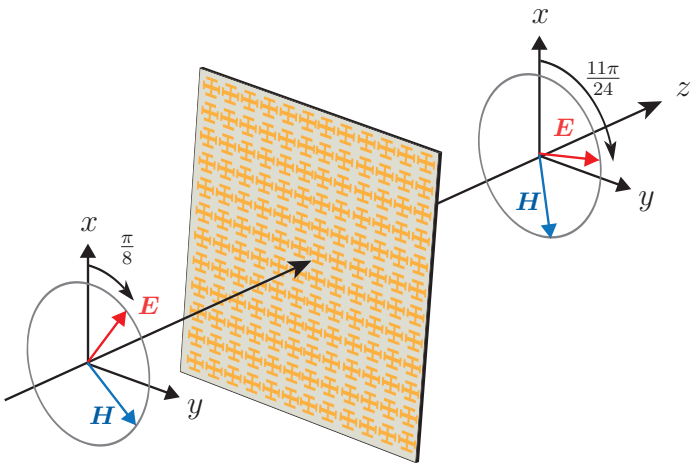

Figure 2.3 The polarization of a normally incident plane wave, linearly polarized at a $\pi/8$ angle with respect to the x-axis, is rotated by $\pi/3$. In the reciprocal case, the fields retrieve their initial polarization upon propagation along the negative z-direction, while in the nonreciprocal case the fields experience a round-trip rotation of $2\pi/3$.

The incident and transmitted electromagnetic fields corresponding to these specifications at $z = 0$, respectively, read

$$\boldsymbol{E}_{\mathrm{i}}(x,y) = \hat{\boldsymbol{x}}\cos(\pi/8) + \hat{\boldsymbol{y}}\sin(\pi/8), \tag{2.46a}$$

$$\boldsymbol{H}_{\mathrm{i}}(x,y) = \frac{1}{\eta_0}\left[-\hat{\boldsymbol{x}}\sin(\pi/8) + \hat{\boldsymbol{y}}\cos(\pi/8)\right], \tag{2.46b}$$

and

$$\boldsymbol{E}_{\mathrm{t}}(x,y) = \hat{\boldsymbol{x}}\cos(11\pi/24) + \hat{\boldsymbol{y}}\sin(11\pi/24), \tag{2.47a}$$

$$\boldsymbol{H}_{\mathrm{t}}(x,y) = \frac{1}{\eta_0}\left[-\hat{\boldsymbol{x}}\sin(11\pi/24) + \hat{\boldsymbol{y}}\cos(11\pi/24)\right]. \tag{2.47b}$$

We will now consider three different combinations of susceptibilities to realize the specified transformation. This will illustrate how the same transformation may be achieved with different sets of susceptibilities.

The first synthesis is performed with the susceptibilities of a birefringent metasurface given in (2.18). From the definition of the difference of the fields in (2.5) and the average of the fields in (2.8), the susceptibilities are readily obtained and read

$$\chi_{\mathrm{ee}}^{xx} = \chi_{\mathrm{mm}}^{yy} = -\frac{1.5048}{k_0}j, \tag{2.48a}$$

$$\chi_{\mathrm{ee}}^{yy} = \chi_{\mathrm{mm}}^{xx} = \frac{0.88063}{k_0}j. \tag{2.48b}$$

As can be seen, the susceptibilities are not functions of position since the specified transformation does not affect the direction of wave propagation but only rotates the polarization angle. We know from the discussion in Sec. 2.3.1 and also from relations (2.10) that the susceptibilities in (2.48) correspond to a reciprocal metasurface. However, we also know from (2.12) that, for the diagonal susceptibilities in (2.48), the presence of negative imaginary parts correspond to absorption while the presence positive imaginary parts correspond to gain. As a result, even though the synthesized metasurface is *not* gyrotropic, since only the diagonal components of the monoanisotropic susceptibility tensors are considered, it is still able to perform the specified rotation of polarization by reducing the amplitudes of $E_{x,\mathrm{i}}$ and $H_{y,\mathrm{i}}$ while amplifying the amplitudes of $E_{y,\mathrm{i}}$ and $H_{x,\mathrm{i}}$. Moreover, this metasurface is *only* able to rotate the polarization angle by $\pi/3$ when the incident wave is polarized at a $\pi/8$ angle. If, for instance, the incident was only polarized along x, then only the susceptibilities in (2.48a) would be excited and the resulting transmitted field would still be polarized along x but with a reduced amplitude with respect to that of the incident wave due to the loss induced by these susceptibilities. Consequently, the susceptibilities in (2.48) may not correspond to the most practical implementation of a polarization rotating metasurface.

We shall now synthesize the same rotation of polarization transformation but, this time, with a gyrotropic metasurface. To do so, we now consider the off-diagonal elements of a monoanisotropic metasurface. Solving (2.15) by setting all the susceptibilities to zero at the exception of χ_{ee}^{xy}, χ_{ee}^{yx}, χ_{mm}^{xy} and χ_{mm}^{yx} yields the following closed-form relations:

$$\chi_{\mathrm{ee}}^{xy} = \frac{-\Delta H_y}{j\omega\epsilon_0 E_{y,\mathrm{av}}}, \tag{2.49a}$$

$$\chi_{\mathrm{ee}}^{yx} = \frac{\Delta H_x}{j\omega\epsilon_0 E_{x,\mathrm{av}}}, \tag{2.49b}$$

$$\chi_{\mathrm{mm}}^{xy} = \frac{\Delta E_y}{j\omega\mu_0 H_{y,\mathrm{av}}}, \tag{2.49c}$$

$$\chi_{\mathrm{mm}}^{yx} = \frac{-\Delta E_x}{j\omega\mu_0 H_{x,\mathrm{av}}}, \tag{2.49d}$$

which, upon substitution of the fields in (2.46) and (2.47), become

$$\chi_{\mathrm{ee}}^{xy} = \chi_{\mathrm{mm}}^{xy} = -\frac{1.1547}{k_0} j, \tag{2.50a}$$

$$\chi_{\mathrm{ee}}^{yx} = \chi_{\mathrm{mm}}^{yx} = \frac{1.1547}{k_0} j. \tag{2.50b}$$

It is important to note that, contrary to the susceptibilities in (2.48), the ones in (2.50) perform the specified $\pi/3$-rotation of polarization *irrespectively* of the initial polarization of the

incident wave due to the gyrotropic nature of this metasurface. Additionally, the susceptibilities in (2.50) correspond to a nonreciprocal metasurface, as can be verified using the reciprocity conditions in (2.10). Therefore, the metasurface is a Faraday rotating surface [165,166], which exhibits the same absolute direction of polarization rotation irrespectively of the direction of wave propagation. However, contrary to conventional Faraday rotators [157], this metasurface is also reflectionless due to the presence of both electric and magnetic gyrotropic susceptibility components. Interestingly, we can see that this metasurface is also lossy and active by applying the relations (2.12). This combination of gain and loss is such that the overall operation is fully efficient, i.e. the loss is compensated by the gain. This metasurface is more practical than the previously synthesized one but it requires the implementation of nonreciprocal electric and magnetic materials, which may not be trivial to realize.

Finally, we now synthesize the metasurface by considering the full system in (2.19). To solve this system, we do not specify the transformation by using fields, as done for the two previous cases, but rather by using scattering parameters. The utilization of the scattering parameters is here justified by the fact that all the waves are propagating normally with respect to the metasurface, which exactly corresponds to the prescription of the scattering parameters in (2.23). We assign ports 1 and 2 to the left- and right-hand sides of the metasurface, respectively. Since the metasurface is reflectionless, we have that $\overline{\overline{S}}_{11} = \overline{\overline{S}}_{22} = 0$. Moreover, we require it to be also reciprocal which leads to $\overline{\overline{S}}_{21} = \overline{\overline{S}}_{12}^{\mathrm{T}}$. The matrix $\overline{\overline{S}}_{21}$ is straightforwardly defined from the specified $\pi/3$-polarization rotation angle and reads

$$\overline{\overline{S}}_{21} = \begin{pmatrix} \cos(\pi/3) & \sin(\pi/3) \\ -\sin(\pi/3) & \cos(\pi/3) \end{pmatrix} = \begin{pmatrix} 1/2 & \sqrt{3}/2 \\ -\sqrt{3}/2 & 1/2 \end{pmatrix}. \tag{2.51}$$

Upon insertion of these definitions of the scattering parameters into (2.24) and (2.25), the metasurface susceptibilities are directly obtained by matrix inversion of (2.22). This leads to following nonzero susceptibilities:

$$\chi_{\mathrm{em}}^{xx} = \chi_{\mathrm{em}}^{yy} = -\frac{2}{\sqrt{3}k_0} j, \tag{2.52a}$$

$$\chi_{\mathrm{me}}^{xx} = \chi_{\mathrm{me}}^{yy} = \frac{2}{\sqrt{3}k_0} j. \tag{2.52b}$$

From these relations, we see that these susceptibilities correspond to a chiral bianisotropic metasurface. As the previously synthesized gyrotropic metasurface, it performs the specified $\pi/3$-rotation of polarization irrespectively of the incident wave polarization state. Moreover, it has the additional advantage of being reciprocal, passive and lossless, as can be verified with (2.13). This makes this chiral metasurface probably the most practical candidate for

the realization of a polarization rotator.

Note that, in this section, we have considered only three different sets of susceptibilities to perform the same transformation. There are other possible combinations of susceptibilities that may be considered to perform this operation. However, most of them correspond to unpractical structures that may be lossy, active, nonreciprocal and/or only perform the specified transformation for the specified polarization state of the incident wave.

2.7.2 Multiple Nonreciprocal Transformations

Let us now look at an example of the application of the multiple transformation technique presented in Sec. 2.3.2. We will consider a double transformation with a monoanisotropic metasurface whose susceptibilities are given in (2.21) in terms of the specified fields.

The two transformations that are used to synthesize the metasurface are depicted in Figs. 2.4. The first transformation, shown in Fig. 2.4a, consists of a normally incident plane wave being

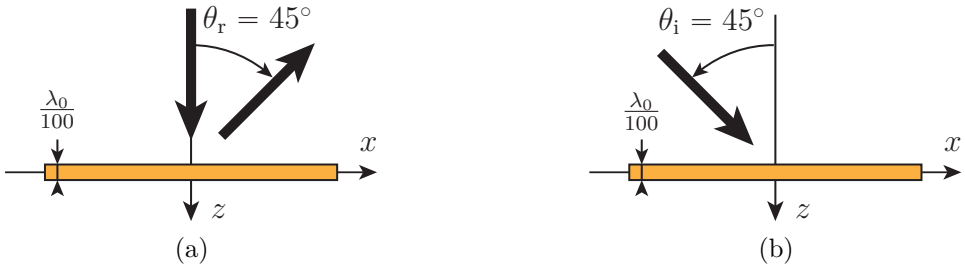

Figure 2.4 Illustrations of the two specified transformations. (a) The normally incident plane wave is fully reflected at a 45° angle. (b) The obliquely incident plane wave is fully absorbed.

fully reflected at a 45° angle. The second transformation, shown in Fig. 2.4b, consists in the full absorption of an incident wave impinging on the metasurface at a 45° angle. For these two transformations, the transmitted field is set to zero, while all the specified nonzero transverse components of the electric fields at $z = 0$ are

$$\boldsymbol{E}_{\mathrm{i},1} = \frac{\sqrt{2}}{2}(\hat{\boldsymbol{x}} + \hat{\boldsymbol{y}}), \tag{2.53a}$$

$$\boldsymbol{E}_{\mathrm{r},1} = \frac{\sqrt{2}}{2}(-\cos\theta_\mathrm{r}\hat{\boldsymbol{x}} + \hat{\boldsymbol{y}})e^{-jk_x x}, \tag{2.53b}$$

$$\boldsymbol{E}_{\mathrm{i},2} = \frac{\sqrt{2}}{2}(\cos\theta_\mathrm{i}\hat{\boldsymbol{x}} + \hat{\boldsymbol{y}})e^{-jk_x x}. \tag{2.53c}$$

For the sake of conciseness, the susceptibility functions are not shown here. Nevertheless,

we point out that the resulting susceptibilities correspond to a nonreciprocal structure which exhibits complicated spatial variations of electric and magnetic loss and gain.

We now present full-wave simulations demonstrating the double transformation control capability of the synthesized metasurface. The simulations are performed in COMSOL in which

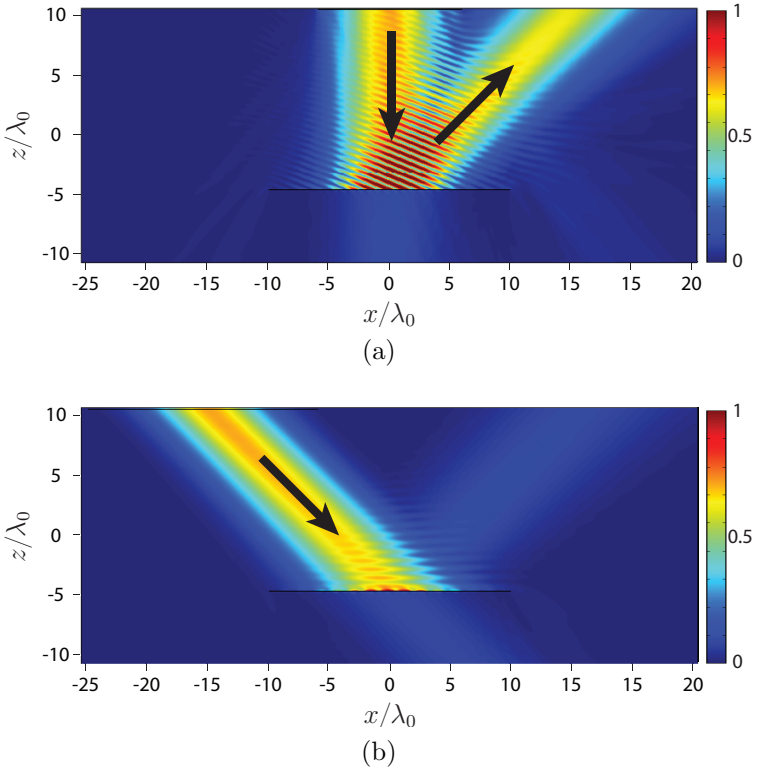

Figure 2.5 COMSOL simulated absolute value of the total electric field (V/m) corresponding to: (a) the transformation in Fig. 2.4a, and (b) the transformation in Fig. 2.4b.

the metasurface is implemented as a thin material slab of thickness $t = \lambda_0/100$ with "diluted" susceptibilities, as explained in Sec. 2.6. The simulation corresponding to the transformation of Fig. 2.4a is shown in Fig. 2.5a, while the simulation corresponding to the transformation of Fig. 2.4b is shown in Fig. 2.5b. As can be seen from the simulations, the metasurface scattering behavior is in good agreement with the expected results, at the exception of some negligible undesired scattering due to the non-ideal thickness of the metasurface.

In order to verify the nonreciprocal nature of this metasurface, we excite it with an incident wave impinging on it at an angle $\theta_\mathrm{i} = -45^\circ$, which corresponds to the reciprocal transformation of that in Fig. 2.5a. The corresponding simulation is shown in Fig. 2.6. A comparison of the ratio of the power transfer between the normally incident wave and the obliquely reflected wave in Fig. 2.5a and the power transfer between the obliquely incident wave and the normally reflected wave in Fig. 2.6, clearly shows that the metasurface is nonreciprocal as it

exhibits more dissipation in the simulation depicted in Fig. 2.6 compared to that in Fig. 2.5a.

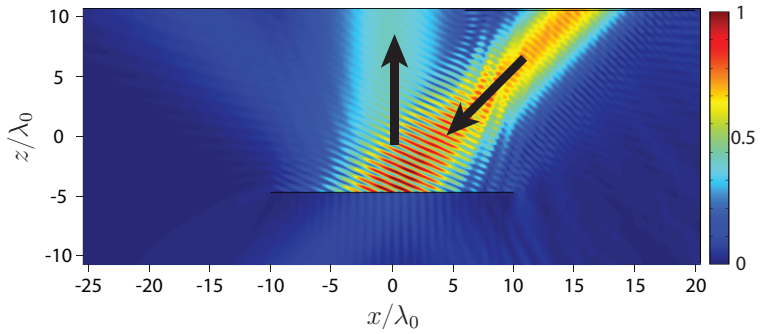

Figure 2.6 COMSOL simulated absolute value of the total electric field (V/m) corresponding to the reciprocal transformation of the one in Fig. 2.4a.

2.7.3 Controllable Angular Scattering

In this last example, we will look at another case of multiple transformations. More specifically, we will discuss the synthesis and analysis of a metasurface with controllable angle-dependent scattering [167–169].

For simplicity, we consider the case of a uniform metasurface, only transforming the phase and the amplitude of the scattered waves. The metasurface is synthesized by specifying the reflection and transmission coefficients for three different incidence angles which, by continuity, allows a relative smooth control of the angular scattering as function of the incidence angle. The synthesis of a metasurface performing three transformations requires a number of degrees of freedom which are here obtained by leveraging bianisotropy and making use of normal susceptibilities.

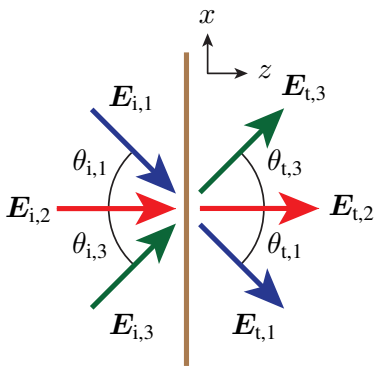

Figure 2.7 Multiple scattering from a uniform bianisotropic metasurface.

Let us now consider the electromagnetic transformations depicted in Fig. 2.7 where p-polarized incident plane waves are scattered, without rotation of polarization, by a bianisotropic reflectionless metasurface. In this transformation, the only electromagnetic field components that are not zero are E_x, E_z and H_y and therefore only a few susceptibility components will by excited by such fields. Consequently, the only susceptibilities that are relevant to the problem of Fig. 2.7 are

$$\overline{\overline{\chi}}_{\rm ee} = \begin{pmatrix} \chi_{\rm ee}^{xx} & 0 & \chi_{\rm ee}^{xz} \\ 0 & 0 & 0 \\ \chi_{\rm ee}^{zx} & 0 & \chi_{\rm ee}^{zz} \end{pmatrix}, \qquad \overline{\overline{\chi}}_{\rm em} = \begin{pmatrix} 0 & \chi_{\rm em}^{xy} & 0 \\ 0 & 0 & 0 \\ 0 & \chi_{\rm em}^{zy} & 0 \end{pmatrix}, \tag{2.54a}$$

$$\overline{\overline{\chi}}_{\rm me} = \begin{pmatrix} 0 & 0 & 0 \\ \chi_{\rm me}^{yx} & 0 & \chi_{\rm me}^{yz} \\ 0 & 0 & 0 \end{pmatrix}, \qquad \overline{\overline{\chi}}_{\rm mm} = \begin{pmatrix} 0 & 0 & 0 \\ 0 & \chi_{\rm mm}^{yy} & 0 \\ 0 & 0 & 0 \end{pmatrix}, \tag{2.54b}$$

where all the susceptibilities that are not excited by the fields have been set to zero for simplicity. The susceptibility tensors in (2.54) contain a total number of 9 unknown components. However, we are here interested in synthesizing a *reciprocal* metasurface, which reduces the number of unknowns to 6 since, from the reciprocity conditions in (2.10), we have that $\chi_{\rm ee}^{xz} = \chi_{\rm ee}^{zx}$, $\chi_{\rm em}^{xy} = -\chi_{\rm me}^{yx}$ and $\chi_{\rm em}^{zy} = -\chi_{\rm me}^{yz}$.

In order to simplify the synthesis and the analysis, we specify that the metasurface is uniform in the xy-plane. Accordingly, the susceptibilities are not functions of x and y and hence the spatial derivatives on the right-hand sides of (2.4a) and (2.4b) only apply to the fields and not to the susceptibilities through (2.7). This restriction means that the reflection and transmission angles follow conventional Snell's law, i.e. $\theta_{\rm r} = -\theta_{\rm i}$ and $\theta_{\rm t} = \theta_{\rm i}$.

Let us now substitute the susceptibilities (2.54) into (2.4a) and (2.4b) with (2.7) and enforce reciprocity. This leads to the two following equations:

$$\Delta H_y = -j\omega\epsilon_0(\chi_{\rm ee}^{xx} E_{x,\rm av} + \chi_{\rm ee}^{xz} E_{z,\rm av}) - jk_0\chi_{\rm em}^{xy} H_{y,\rm av}, \tag{2.55a}$$

$$\begin{aligned} \Delta E_x = &-j\omega\mu_0\chi_{\rm mm}^{yy} H_{y,\rm av} + jk_0(\chi_{\rm em}^{xy} E_{x,\rm av} + \chi_{\rm em}^{zy} E_{z,\rm av}) \\ &- \chi_{\rm ee}^{xz}\partial_x E_{x,\rm av} - \chi_{\rm ee}^{zz}\partial_x E_{z,\rm av} - \eta_0\chi_{\rm em}^{zy}\partial_x H_{y,\rm av}. \end{aligned} \tag{2.55b}$$

The system (2.55) contains 6 unknown susceptibilities. In order to solve it, we apply the multiple transformation concept discussed in Sec. 2.3.2, which consists in specifying three independent sets of incident, reflected and transmitted waves. Moreover, since the metasurface is perfectly uniform, we synthesize the metasurface using scattering parameters instead of fields, as done for the chiral metasurface in Sec. 2.7.1. Thus, the reflection (R) and transmis-

sion (T) coefficients of the metasurface in Fig. 2.7 may be specified for three different angles of incidence. By specifying the reflection and transmission coefficients for three specific angles, one can achieve controllable quasi-continuous angular scattering since the response of the metasurface for non-specified angles de facto corresponds to an interpolation of the three specified responses.

To illustrate the concept, let us consider a reflectionless transformation ($R = 0$) where three incident plane waves, impinging on the metasurface at $\theta_{\mathrm{i},1} = -45^\circ$, $\theta_{\mathrm{i},2} = 0^\circ$ and $\theta_{\mathrm{i},3} = +45^\circ$, are transmitted with transmission coefficients $T_1 = 0.75$, $T_2 = 0.5e^{j45^\circ}$ and $T_3 = 0.25$ and transmission angles $\theta_\mathrm{t} = \theta_\mathrm{i}$. The expressions relating the susceptibilities to the reflection and transmission coefficients being extensively long, we do not provide them here. However, the susceptibilities corresponding to the these specified scattering parameters are given by

$$\overline{\overline{\chi}}_{\mathrm{ee}} = \frac{1}{k_0}\begin{pmatrix} -2.46 - 0.08j & 0 & 0.64j \\ 0 & 0 & 0 \\ 0.64j & 0 & 0.42 + 0.88j \end{pmatrix}, \quad \overline{\overline{\chi}}_{\mathrm{em}} = \frac{1}{k_0}\begin{pmatrix} 0 & 1.74 - 0.68j & 0 \\ 0 & 0 & 0 \\ 0 & 0.39 - 0.68j & 0 \end{pmatrix}, \tag{2.56a}$$

$$\overline{\overline{\chi}}_{\mathrm{me}} = \frac{1}{k_0}\begin{pmatrix} 0 & 0 & 0 \\ -1.74 + 0.68j & 0 & -0.39 + 0.68j \\ 0 & 0 & 0 \end{pmatrix}, \quad \overline{\overline{\chi}}_{\mathrm{mm}} = \frac{1}{k_0}\begin{pmatrix} 0 & 0 & 0 \\ 0 & 1.02 - 1.45j & 0 \\ 0 & 0 & 0 \end{pmatrix}. \tag{2.56b}$$

It can be easily verified that these susceptibility tensors satisfy the reciprocity conditions (2.10), but the complex values of the susceptibilities indicate the presence of both gain and loss.

Now, to verify that the scattered waves have the specified amplitude and phase at the three specified incidence angles and also to see the response at non-specified angles, we mathematically analyze the scattering from the synthesized metasurface versus the incidence angle. For this purpose, and as previously mentioned, relations (2.55) are solved to determine the reflection and transmission coefficients versus θ_i. The resulting amplitude and phase of the reflection and transmission coefficients are plotted in Figs. 2.8a and 2.8b, respectively. As may be seen in these graphs, the metasurface exhibits the specified response in terms of both coefficients at the three specified angles. Moreover, the transmission exhibits a continuous amplitude decrease as θ_i increases beyond -50°.

Using the exact same synthesis procedure, we shall now look at another interesting example which consists in the synthesis of a spatial angular phaser. In that case, the metasurface is reflectionless, passive and lossless and exhibits a transmission phase shift, ϕ, that is function of the incidence angle, i.e. $T = e^{j\phi(\theta_\mathrm{i})}$. Similarly as before, the three incident plane waves

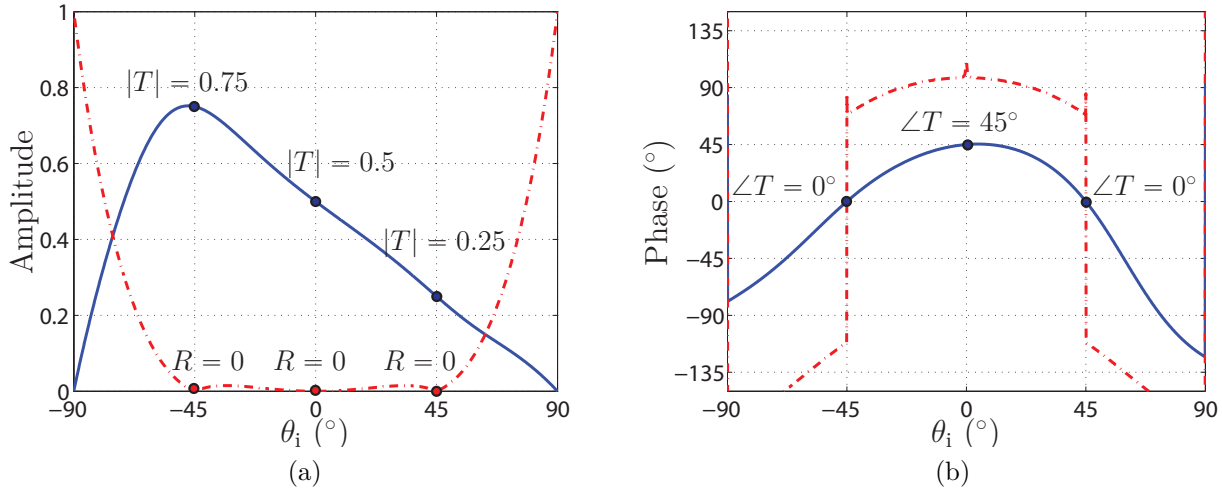

Figure 2.8 Reflection (dashed red line) and transmission (solid blue line) amplitude (a) and phase (b) as functions of the incidence angle for a metasurface synthesize for the transmission coefficients $T = \{0.75; 0.5e^{j45^\circ}; 0.25\}$ (and $R = 0$) at the respective incidence angles $\theta_i = \{-45^\circ; 0^\circ; +45^\circ\}$.

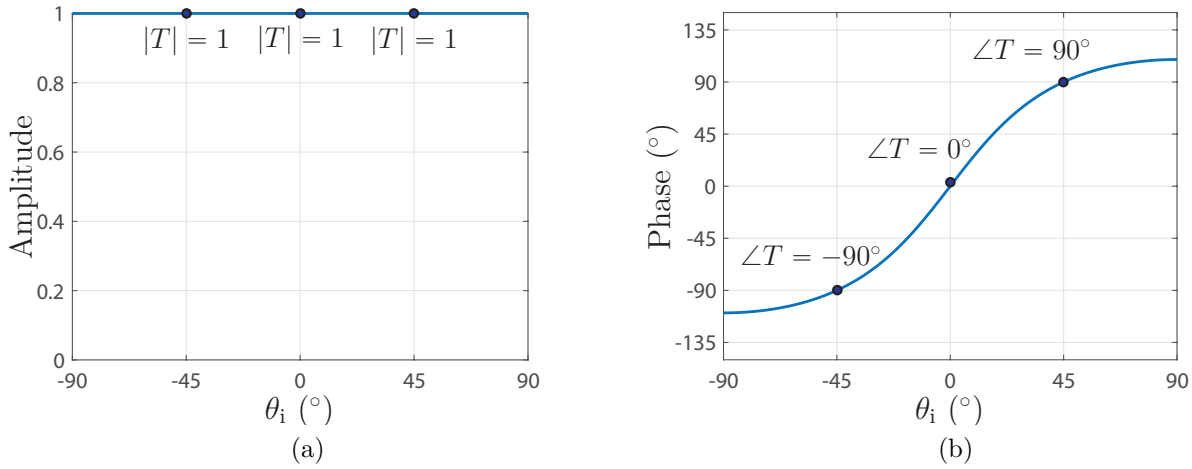

Figure 2.9 Transmission amplitude (a) and phase (b) as functions of the incidence angle for a metasurface synthesize for the transmission coefficients $T = \{e^{-j90^\circ}; 1; e^{j90^\circ}\}$ (and $R = 0$) at the respective incidence angles $\theta_i = \{-45^\circ; 0^\circ; +45^\circ\}$.

impinge on the metasurface at $\theta_{i,1} = -45^\circ$, $\theta_{i,2} = 0^\circ$ and $\theta_{i,3} = +45^\circ$ and are transmitted with transmission coefficients $T_1 = e^{-j\alpha}$, $T_2 = 1$ and $T_3 = e^{j\alpha}$, where α is a given phase shift.

Solving relations (2.55) with these specifications yields the following nonzero susceptibilities:

$$\chi_{\mathrm{ee}}^{xz} = \chi_{\mathrm{ee}}^{zx} = \frac{2\sqrt{2}}{k_0} \tan\left(\frac{\alpha}{2}\right). \tag{2.57}$$

Since the metasurface only possesses these two susceptibilities, it is possible to obtain the following simple angular dependent transmission coefficient:

$$T(\theta_{\mathrm{i}}) = -1 + \frac{2}{1 - j\sqrt{2}\sin(\theta_{\mathrm{i}})\tan\left(\frac{\alpha}{2}\right)}, \tag{2.58}$$

while the reflection coefficient is $R(\theta_{\mathrm{i}}) = 0$.

In order to illustrate the angular behavior of the transmission coefficient in (2.58), it is plotted in Figs. 2.9 for a specified phase shift of $\alpha = 90°$. As expected, the transmission amplitude remains unity for all incidence angles while the transmission phase is asymmetric around broadside and covers about a 220°-phase range. It is interesting to note that the susceptibilities χ_{ee}^{xz} and χ_{ee}^{zx} exhibit such kind of angular asymmetric behavior.

2.8 Synthesis and Analysis of Nonlinear Metasurfaces

So far, we have been only interested in purely linear metasurfaces, i.e. where the polarization densities are linear functions of the electric and magnetic fields. Let us now investigate the case of a metasurface with nonzero second-order nonlinear electric and magnetic susceptibility tensors [100, 153, 170–172][3]. Second-order nonlinearity is a weak effect that is present in non-centrosymmetric structures. For instance, we may find electric nonlinearities in certain crystals [173], while non-negligible magnetic nonlinearities may be found in certain ferrofluids [174].

In the case that is considered here, the polarization densities in (2.7), which correspond to a linear bianisotropic medium, transform into

$$\boldsymbol{P} = \epsilon_0 \overline{\overline{\chi}}_{\mathrm{ee}}^{(1)} \cdot \boldsymbol{E}_{\mathrm{av}} + \epsilon_0 \overline{\overline{\chi}}_{\mathrm{ee}}^{(2)} : \boldsymbol{E}_{\mathrm{av}}\boldsymbol{E}_{\mathrm{av}}, \tag{2.59a}$$

$$\boldsymbol{M} = \overline{\overline{\chi}}_{\mathrm{mm}}^{(1)} \cdot \boldsymbol{H}_{\mathrm{av}} + \overline{\overline{\chi}}_{\mathrm{mm}}^{(2)} : \boldsymbol{H}_{\mathrm{av}}\boldsymbol{H}_{\mathrm{av}}, \tag{2.59b}$$

where $\overline{\overline{\chi}}^{(1)}$ and $\overline{\overline{\chi}}^{(2)}$ correspond to the first-order (linear) and second-order (nonlinear) susceptibility tensors, respectively. In order to simplify the synthesis and analysis of nonlinear metasurfaces, we assume here that the metasurfaces are isotropic and that their corresponding susceptibility tensors in (2.59) are of rank zero.

[3]This section is based on a slightly modified version of [153].

To proceed with the metasurface synthesis, we substitute (2.59) into the time-domain counterparts of the GSTCs in (2.4). We consider the time-domain instead of the frequency-domain GSTCs because nonlinear materials generate new frequencies [173], which obviously cannot be taken into account with a frequency-domain formulation. Let us now consider x-polarized wave excitation, in which case the time-domain GSTCs become

$$-\Delta H = \epsilon_0 \chi_{\mathrm{ee}}^{(1)} \frac{\partial}{\partial t} E_{\mathrm{av}} + \epsilon_0 \chi_{\mathrm{ee}}^{(2)} \frac{\partial}{\partial t} E_{\mathrm{av}}^2, \tag{2.60a}$$

$$-\Delta E = \mu_0 \chi_{\mathrm{mm}}^{(1)} \frac{\partial}{\partial t} H_{\mathrm{av}} + \mu_0 \chi_{\mathrm{mm}}^{(2)} \frac{\partial}{\partial t} H_{\mathrm{av}}^2, \tag{2.60b}$$

where E and H are, respectively, the x-component of the electric field and the y-component of the magnetic field. Note that we assume that the susceptibilities are not functions of time and that they are dispersion-less[4]. This means that the time derivatives in (2.4), which apply to the polarization densities, only affect the fields in (2.60) and not the susceptibilities.

The synthesis procedure consists in solving (2.60) so as to obtain the susceptibilities in terms of the specified fields. As can be seen, the system (2.60) is a system of 2 equations in 4 unknown susceptibilities. To solve it, we may proceed as in Sec. 2.3.2 where we considered two arbitrary transformations. The system in (2.60) may thus be transformed into the following matrix system:

$$\begin{bmatrix} -\Delta H_1 \\ -\Delta H_2 \\ -\Delta E_1 \\ -\Delta E_2 \end{bmatrix} = \frac{\partial}{\partial t} \begin{bmatrix} \epsilon_0 E_{\mathrm{av},1} & \epsilon_0 E_{\mathrm{av},1}^2 & 0 & 0 \\ \epsilon_0 E_{\mathrm{av},2} & \epsilon_0 E_{\mathrm{av},2}^2 & 0 & 0 \\ 0 & 0 & \mu_0 H_{\mathrm{av},1} & \mu_0 H_{\mathrm{av},1}^2 \\ 0 & 0 & \mu_0 H_{\mathrm{av},2} & \mu_0 H_{\mathrm{av},2}^2 \end{bmatrix} \cdot \begin{bmatrix} \chi_{\mathrm{ee}}^{(1)} \\ \chi_{\mathrm{ee}}^{(2)} \\ \chi_{\mathrm{mm}}^{(1)} \\ \chi_{\mathrm{mm}}^{(2)} \end{bmatrix}, \tag{2.61}$$

where the subscripts 1 and 2 refer to the fields of two arbitrary independent transformations.

[4]While this condition may seem a priori unrealistic, we point out the fact that a nonlinear medium generates all multiples of the excitation frequency, ω_0. Therefore, the dispersion-less condition reduces to having $\chi(\omega_0) = \chi(2\omega_0) = \chi(3\omega_0) = ...$, which may be achieved with properly designed metamaterial structures (at least for the first equality). Note that this condition is equivalent to the phase matching condition conventionally used in nonlinear optics [173].

By matrix inversion of (2.61), the susceptibilities are

$$\chi_{\mathrm{ee}}^{(1)} = -\frac{\Delta H_2 \frac{\partial}{\partial t} E_{\mathrm{av},1}^2 - \Delta H_1 \frac{\partial}{\partial t} E_{\mathrm{av},2}^2}{\epsilon_0 (\frac{\partial}{\partial t} E_{\mathrm{av},1}^2 \frac{\partial}{\partial t} E_{\mathrm{av},2} - \frac{\partial}{\partial t} E_{\mathrm{av},1} \frac{\partial}{\partial t} E_{\mathrm{av},2}^2)}, \tag{2.62a}$$

$$\chi_{\mathrm{mm}}^{(1)} = -\frac{\Delta E_2 \frac{\partial}{\partial t} H_{\mathrm{av},1}^2 - \Delta E_1 \frac{\partial}{\partial t} H_{\mathrm{av},2}^2}{\mu_0 (\frac{\partial}{\partial t} H_{\mathrm{av},1}^2 \frac{\partial}{\partial t} H_{\mathrm{av},2} - \frac{\partial}{\partial t} H_{\mathrm{av},1} \frac{\partial}{\partial t} H_{\mathrm{av},2}^2)}, \tag{2.62b}$$

$$\chi_{\mathrm{ee}}^{(2)} = \frac{\Delta H_2 \frac{\partial}{\partial t} E_{\mathrm{av},1} - \Delta H_1 \frac{\partial}{\partial t} E_{\mathrm{av},2}}{\epsilon_0 (\frac{\partial}{\partial t} E_{\mathrm{av},1}^2 \frac{\partial}{\partial t} E_{\mathrm{av},2} - \frac{\partial}{\partial t} E_{\mathrm{av},1} \frac{\partial}{\partial t} E_{\mathrm{av},2}^2)}, \tag{2.62c}$$

$$\chi_{\mathrm{mm}}^{(2)} = \frac{\Delta E_2 \frac{\partial}{\partial t} H_{\mathrm{av},1} - \Delta E_1 \frac{\partial}{\partial t} H_{\mathrm{av},2}}{\mu_0 (\frac{\partial}{\partial t} H_{\mathrm{av},1}^2 \frac{\partial}{\partial t} H_{\mathrm{av},2} - \frac{\partial}{\partial t} H_{\mathrm{av},1} \frac{\partial}{\partial t} H_{\mathrm{av},2}^2)}. \tag{2.62d}$$

These relations may a priori seem to be valid irrespectively of the specified fields. However, this is not true in most cases. Indeed, let us consider a simple example where the specified incident, reflected and transmitted fields are given by $E_{\mathrm{i}} = E_0 e^{j(\omega_{\mathrm{i}} t - k_{\mathrm{i}} z)}$, $E_{\mathrm{r}} = R e^{j(\omega_{\mathrm{r}} t - k_{\mathrm{r}} z)}$ and $E_{\mathrm{t}} = T e^{j(\omega_{\mathrm{t}} t - k_{\mathrm{t}} z)}$ with different values of ω_{i}, ω_{r} and ω_{t} for the two transformations. Upon substitution of these fields into (2.62), the resulting susceptibilities become functions of time. This result is incompatible with the assumption, made above to obtain (2.60), that the susceptibilities were not time varying. Therefore, we cannot specify the fields of the two transformations in (2.62) in a completely arbitrary fashion. We should rather find the appropriate way to specify these fields such that the synthesized susceptibilities are time independent. The question that one may ask is how should we specify these fields? To answer this question, we will tackle the problem from a different perspective. Instead of performing a synthesis, we will analyze the scattered fields from a known nonlinear metasurface. From this analysis, we will be able to deduce the proper way to specify the fields in the synthesis.

We are now interested in analyzing the fields scattered from a nonlinear metasurface. To computed these scattered fields, we assume for simplicity that the metasurface is uniform and that it is illuminated by a normally incident plane wave. In that case, the metasurface produces normally reflected and transmitted plane waves with reflection and transmission coefficients that can be found by solving (2.60). However, the system in (2.60) is a set of nonlinear nonhomogeneous first-order coupled differential equations which is difficult to solve analytically. As will be shown shortly, we will solve it numerically but first, we will simplify it so as to find an approximate analytical solution. In order to simplify the problem, we assume that the metasurface to be analyzed has known susceptibilities such that the metasurface is reflectionless. If the metasurface is known to be reflectionless, then the system (2.60) reduces to a single equation which dramatically simplifies the resolution of the problem. For this purpose, we need to find the reflectionless conditions in the case of a nonlinear metasurface.

These conditions may be obtained from (2.62) by specifying that $E_\mathrm{r} = H_\mathrm{r} = 0$ and using $E = \pm\eta_0 H$ since normal plane wave propagation is considered, where $+$ corresponds to waves propagating in the positive z-direction and vice-versa for $-$. As said above, we have to consider two transformations to be able to solve the system (2.62). Therefore, let us consider the two transformations illustrated in Figs. 2.10, where the two sets of waves propagate either both in the positive z-direction, as in Fig. 2.10a, or both in the negative z-direction, as in Fig. 2.10b. Note that a third case is also possible, where the waves Ψ_1 and Ψ_2 would

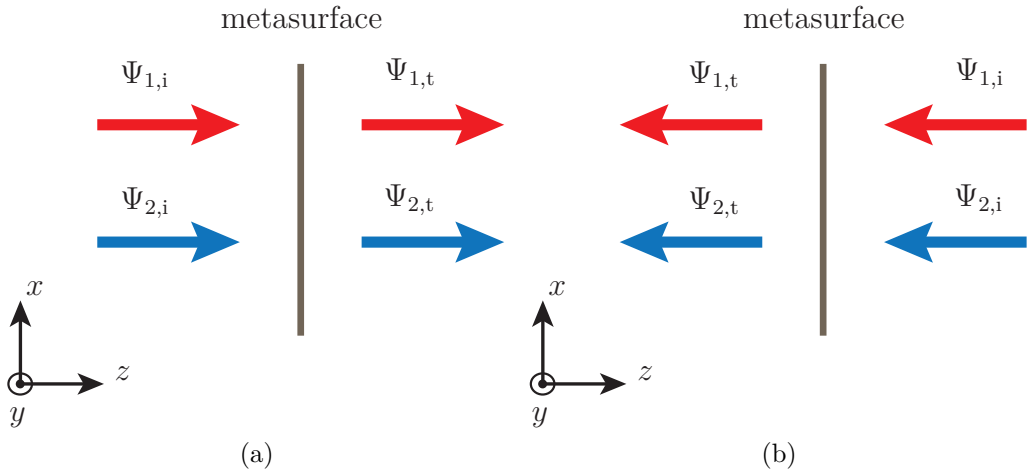

Figure 2.10 Two different approaches to synthesize a nonlinear metasurface. (a) Two incident waves (Ψ_1 and Ψ_2), propagating in the positive z-direction, are transmitted by the metasurface. (b) Two incident waves, propagating in the negative z-direction, are transmitted by the metasurface.

propagate in opposite directions. This scenario is not considered here since, in that case, it is not possible to obtain the reflectionless conditions, as will be explained shortly. Solving (2.62) for the case depicted in Fig. 2.10a and comparing the expressions of the electric and magnetic susceptibilities reveals the following reflectionless conditions:

$$\chi_\mathrm{ee}^{(1)} = \chi_\mathrm{mm}^{(1)}, \tag{2.63a}$$

$$\eta_0\chi_\mathrm{ee}^{(2)} = \chi_\mathrm{mm}^{(2)}. \tag{2.63b}$$

By the same token, the reflectionless conditions for the case depicted in Fig. 2.10b read

$$\chi_\mathrm{ee}^{(1)} = \chi_\mathrm{mm}^{(1)}, \tag{2.64a}$$

$$-\eta_0\chi_\mathrm{ee}^{(2)} = \chi_\mathrm{mm}^{(2)}. \tag{2.64b}$$

Note that the only difference between (2.63) and (2.64) is the minus sign in the relation

between the second-order susceptibilities. It may come as a surprise that different reflectionless conditions are obtained for different directions of wave propagation. This is due to the nonreciprocal nature of this metasurface, which is both nonlinear and asymmetric. This asymmetry is due to the presence of the square of the fields in (2.60) and by considering the relation between the electric and magnetic fields ($E = \pm\eta_0 H$), which depends on the direction of wave propagation. It is this asymmetry that explains the difference between (2.63) and (2.64), and thus, the nonreciprocal response of this metasurface.

Now that the reflectionless conditions have been obtained, we can proceed with the analysis of the scattered fields from the nonlinear metasurface. For this purpose, we use the reflectionless conditions in (2.63) which correspond to the transformation depicted in Fig. 2.10a. This reduces the system (2.60) to a single independent equation, which upon substitution of the difference of the fields, $\Delta E = E_\mathrm{t} - E_\mathrm{i}$, the average of the fields, $E_\mathrm{av} = \frac{1}{2}(E_\mathrm{t} + E_\mathrm{i})$, and the average square of the fields, $E_\mathrm{av}^2 = E_\mathrm{av}E_\mathrm{av}^* = \frac{1}{4}(E_\mathrm{i}^2 + E_\mathrm{i}E_\mathrm{t}^* + E_\mathrm{t}E_\mathrm{i}^* + E_\mathrm{t}^2)$ becomes

$$2\chi_\mathrm{ee}^{(1)}\frac{\partial}{\partial t}E_\mathrm{t} + \chi_\mathrm{ee}^{(2)}\frac{\partial}{\partial t}(E_\mathrm{i}E_\mathrm{t}^* + E_\mathrm{t}E_\mathrm{i}^* + E_\mathrm{t}^2) + \frac{4\eta_0}{\mu_0}E_\mathrm{t} = \frac{4\eta_0}{\mu_0}E_\mathrm{i} - \chi_\mathrm{ee}^{(2)}\frac{\partial}{\partial t}E_\mathrm{i}^2 - 2\chi_\mathrm{ee}^{(1)}\frac{\partial}{\partial t}E_\mathrm{i}, \quad (2.65)$$

where we assume that $E_\mathrm{i} = E_0\cos(\omega_0 t)$ is a known excitation and E_t is the transmitted field that we are solving for. If E_0, $\chi_\mathrm{ee}^{(1)}$ and $\chi_\mathrm{ee}^{(2)}$ are real quantities, the relation (2.65) becomes

$$\begin{aligned}&\chi_\mathrm{ee}^{(2)}\frac{\partial}{\partial t}E_\mathrm{t}^2 + \left(2\chi_\mathrm{ee}^{(1)} + 2E_0\cos(\omega_0 t)\chi_\mathrm{ee}^{(2)}\right)\frac{\partial}{\partial t}E_\mathrm{t} + \left(\frac{4\eta_0}{\mu_0} - 2\omega_0\chi_\mathrm{ee}^{(2)}E_0\sin(\omega_0 t)\right)E_\mathrm{t} = \\ &\frac{4\eta_0}{\mu_0}E_0\cos(\omega_0 t) + \omega_0\chi_\mathrm{ee}^{(2)}E_0\sin(2\omega_0 t) + 2\omega_0\chi_\mathrm{ee}^{(1)}E_0\sin(\omega_0 t).\end{aligned} \quad (2.66)$$

This differential equation may now be solved to obtain the transmitted field. But first, let us recall the assumptions that were made to obtain Eq. (2.66). We have considered an isotropic reflectionless and uniform nonlinear metasurface with purely real second-order nonlinear electric and magnetic susceptibilities illuminated by a normally incident plane wave. This reveals how difficult it is to analyze nonlinear metasurfaces and, despite all of these assumptions, Eq. (2.66) does not possess any exact analytical solution.

Since it is not possible to find an exact solution to (2.66), we will now try to find an approximate solution for the transmitted field using perturbation analysis [175]. This is justified if we assume that the second-order susceptibilities are very small compared to the first-order ones. Typically, assuming nonresonant excitation, we have that $\chi^{(2)} \approx 10^{-12}\chi^{(1)}$ [173]. As a consequence of this assumption, we can approximate the expression of the transmitted field

using a power series such that

$$E_{\mathrm{t}} \approx E_{\mathrm{t},0} + \varepsilon E_{\mathrm{t},1} + \varepsilon^2 E_{\mathrm{t},2} + ... \tag{2.67}$$

where ε is a small quantity which also applies to the susceptibilities as follows

$$\chi_{\mathrm{ee}}^{(1)} \gg \chi_{\mathrm{ee}}^{(2)} \approx \varepsilon. \tag{2.68}$$

We can now solve recursively and individually each term of (2.67). Substituting (2.67) and (2.68) into (2.66) and removing all terms containing ε, leads to the following equation

$$2\chi_{\mathrm{ee}}^{(1)} \frac{\partial}{\partial t} E_{\mathrm{t},0} + \frac{4\eta_0}{\mu_0} E_{\mathrm{t},0} = \frac{4\eta_0}{\mu_0} E_0 \cos(\omega_0 t) + 2\omega_0 \chi_{\mathrm{ee}}^{(1)} E_0 \sin(\omega_0 t), \tag{2.69}$$

which is only expressed in terms of the unknown $E_{\mathrm{t},0}$ and does not contain any nonlinear susceptibility. This equation thus corresponds to a linear reflectionless metasurface, whose complex steady-state solution is

$$E_{\mathrm{t},0} = E_0 \frac{2 - jk_0\chi_{\mathrm{ee}}^{(1)}}{2 + jk_0\chi_{\mathrm{ee}}^{(1)}} e^{j\omega_0 t}, \tag{2.70}$$

which exactly corresponds to the expected transmitted field as previously found in (2.32) if $\chi_{\mathrm{ee}}^{xx} = \chi_{\mathrm{mm}}^{yy}$. Note that the frequency of $E_{\mathrm{t},0}$ is the same as that of the incident wave. Now that the expression for $E_{\mathrm{t},0}$ has been found, we can proceed by deriving the expression for $E_{\mathrm{t},1}$. This is achieved by inserting $E_{\mathrm{t}} \approx E_{\mathrm{t},0} + \varepsilon E_{\mathrm{t},1}$ into (2.66) along with (2.70), and removing all terms proportional to ε^2 (or higher powers). This operation transforms (2.66) into

$$\begin{aligned} &\chi_{\mathrm{ee}}^{(2)} \frac{\partial}{\partial t} E_{\mathrm{t},0}^2 + \left(2\chi_{\mathrm{ee}}^{(1)} + 2E_0 \cos(\omega_0 t)\chi_{\mathrm{ee}}^{(2)}\right) \frac{\partial}{\partial t} E_{\mathrm{t},0} + \left(\frac{4\eta_0}{\mu_0} - 2\omega_0 \chi_{\mathrm{ee}}^{(2)} E_0 \sin(\omega_0 t)\right) E_{\mathrm{t},0} \\ &+ 2\chi_{\mathrm{ee}}^{(1)} \frac{\partial}{\partial t} E_{\mathrm{t},1} + \frac{4\eta_0}{\mu_0} E_{\mathrm{t},1} = \frac{4\eta_0}{\mu_0} E_0 \cos(\omega_0 t) + \omega_0 \chi_{\mathrm{ee}}^{(2)} E_0 \sin(2\omega_0 t) + 2\omega_0 \chi_{\mathrm{ee}}^{(1)} E_0 \sin(\omega_0 t), \end{aligned} \tag{2.71}$$

which is a differential equation in $E_{\mathrm{t},1}$ and contains the nonlinear susceptibility $\chi_{\mathrm{ee}}^{(2)}$. As before, this equation can be easily solved and leads to the following steady-state solution

$$E_{\mathrm{t},1} = E_0 k_0 \chi_{\mathrm{ee}}^{(2)} \left[\frac{4 + 12E_0 - 4j\chi_{\mathrm{ee}}^{(1)} k_0 (E_0 - 1) + (\chi_{\mathrm{ee}}^{(1)} k_0)^2 (E_0 - 1)}{4(\chi_{\mathrm{ee}}^{(1)} k_0 - j)(\chi_{\mathrm{ee}}^{(1)} k_0 - 2j)^2} \right] e^{j2\omega_0 t}, \tag{2.72}$$

which, as can be seen, is at a frequency $2\omega_0$ corresponding to a second-harmonic generation.

We can now apply the same method that was used to obtain $E_{\mathrm{t},0}$ and $E_{\mathrm{t},1}$ to find the expression of $E_{\mathrm{t},2}$. We do not provide the differential equation that apply to $E_{\mathrm{t},2}$ because it is too lengthy. Instead, we only provide the corresponding steady-state solution which is

$$E_{\mathrm{t},2} = C_{\mathrm{t},2}\left[(2j - 3\chi_{\mathrm{ee}}^{(1)}k_0)e^{j\omega_0 t} + 3(2j + \chi_{\mathrm{ee}}^{(1)}k_0)e^{j3\omega_0 t}\right], \tag{2.73}$$

where $C_{\mathrm{t},2}$ is given by

$$C_{\mathrm{t},2} = \frac{j(\chi_{\mathrm{ee}}^{(2)}k_0E_0)^2\left[4 + 12E_0 + \chi_{\mathrm{ee}}^{(1)}k_0(\chi_{\mathrm{ee}}^{(1)}k_0 - 4j)(E_0 - 1)\right]}{2(\chi_{\mathrm{ee}}^{(1)}k_0 - 2j)^3(\chi_{\mathrm{ee}}^{(1)}k_0 - j)(\chi_{\mathrm{ee}}^{(1)}k_0 + 2j)(3\chi_{\mathrm{ee}}^{(1)}k_0 - 2j)}. \tag{2.74}$$

Contrary to $E_{\mathrm{t},0}$, which is at frequency ω_0, and $E_{\mathrm{t},1}$, which is at frequency $2\omega_0$, we see that $E_{\mathrm{t},2}$ is a superposition of two waves at frequencies ω_0 and $3\omega_0$. At this stage, it is important to note that to ensure the validity of (2.70), (2.72) and (2.73), the following relations must be satisfied: $E_{\mathrm{t},0} \gg E_{\mathrm{t},1} \gg E_{\mathrm{t},2}$ and $\chi_{\mathrm{ee}}^{(1)} \gg \chi_{\mathrm{ee}}^{(2)}$ according to the prescription of perturbation theory. If we look at the dependence of $E_{\mathrm{t},0}$, $E_{\mathrm{t},1}$ and $E_{\mathrm{t},2}$ on E_0 and $\chi_{\mathrm{ee}}^{(2)}$, we see that the transmitted field expressions are only valid for specific values of E_0 and $\chi_{\mathrm{ee}}^{(2)}$, which limits the generality of these expressions.

From these results, we can predict that the general scattering behavior of nonlinear metasurfaces corresponds to a superposition of waves with all multiples of ω_0. Consequently, the scattered field may be expressed as

$$E_{\mathrm{s}} = \sum_{n=1}^{\infty} E_{\mathrm{s,n}}e^{jn\omega_0 t}, \tag{2.75}$$

where E_{s} may represent the reflected or the transmitted electric field and where $E_{\mathrm{s,n}}$ are complex constants. This analysis of the scattering from nonlinear metasurfaces reveals the form that the specified fields should take while performing the synthesis of such metasurfaces. More specifically, the specified fields should contain all harmonics, according to (2.75), so that the synthesized susceptibilities in (2.62) do not depend on time.

Now that the approximate solutions of the transmitted field have been obtained mathematically, we will perform numerical simulations to validate our results. Let us consider a metasurface designed with the reflectionless conditions given in (2.63), and the following arbitrary parameters: $E_0 = 1.5$ V/m, $\chi_{\mathrm{ee}}^{(1)} = 0.1$ m and $\chi_{\mathrm{ee}}^{(2)} = 0.04$ m^2/V. To perform the numerical simulations, we use a 1D FDTD scheme that was specifically designed to simulate zero-thickness metasurfaces [3]. This code was adapted to take into account second-order

nonlinear susceptibilities, as explained in Appendix D[5].

We start by exciting the metasurface with a plane wave propagating in the positive z-direction. The corresponding simulation results are shown in Fig. 2.11a. The simulation

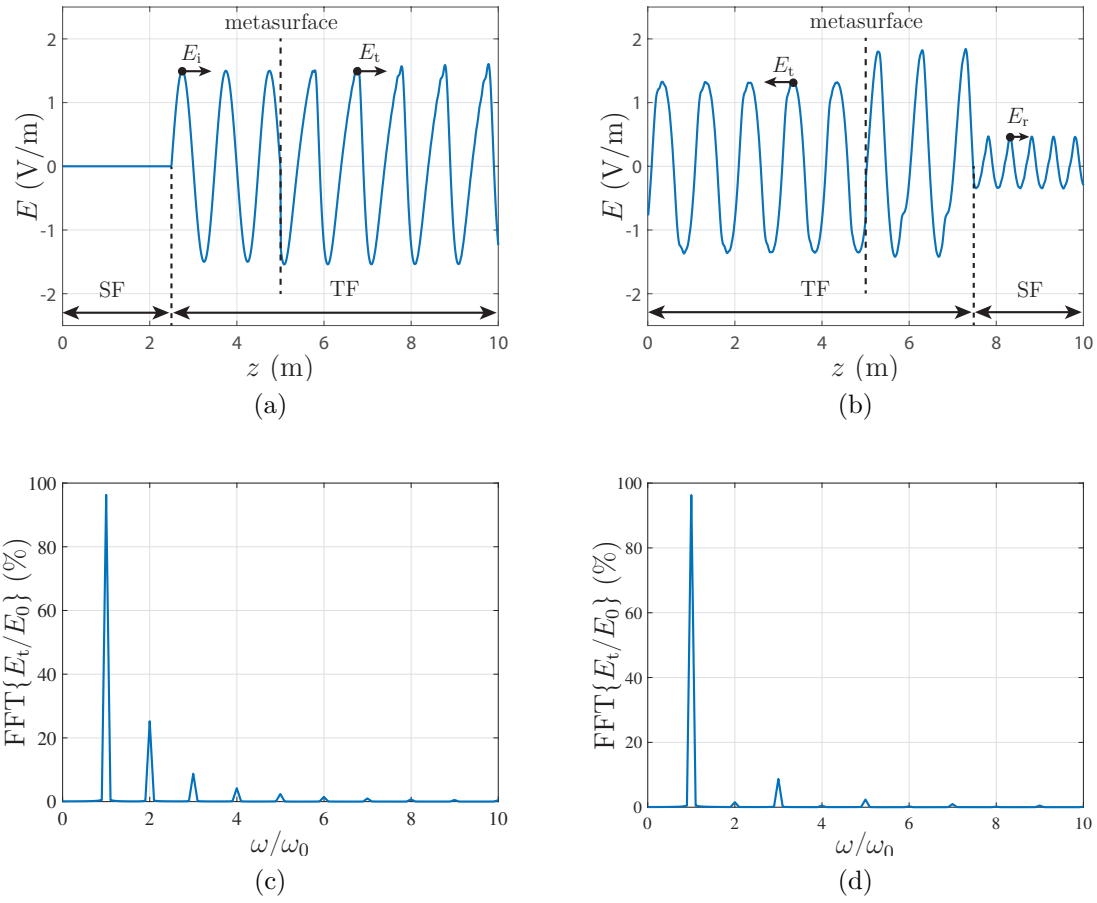

Figure 2.11 FDTD simulations of a nonlinear metasurface assuming the following parameters: $E_0 = 1.5$ V/m, $\chi_{ee}^{(1)} = 0.1$ m and $\chi_{ee}^{(2)} = 0.04$ m^2/V. In (a), the metasurface is illuminated from the left, while in (b) it is illuminated from the right. The normalized Fourier transform of the transmitted field of (a) is plotted in (c), while the one corresponding to (b) is plotted in (d).

is performed using a scattered-field region (SF) and a total-field region (TF) and the source is placed at the boundary between these two regions, while the metasurface lies in the center of the simulation window. If we look at the SF region in Fig. 2.11a, we see that the reflected electric field is zero, which demonstrates the expected reflectionless nature of this metasurface. Figure 2.11c presents the time-domain Fourier transform of the transmitted field in Fig. 2.11a, which is normalized to E_0. We can clearly see the predicted generation of

[5]Note that normalized constants are used in all following simulations and thus $c_0 = \epsilon_0 = \mu_0 = f_0 = 1$.

harmonics whose amplitudes decrease as ω increases.

To evaluate the nonreciprocal response of this metasurface, we perform another simulation where the incident plane wave is now impinging on the metasurface from its right-hand side. Accordingly, we have changed the position of the SF and TF regions. The corresponding simulation result is plotted in Fig. 2.11b. The presence of a nonzero electric field in the SF region confirms that this metasurface is only reflectionless from one side but not from the other. Moreover, the time-domain Fourier transform of the corresponding transmitted field, which is shown in Fig. 2.11d, reveals that the frequencies that are odd multiples of ω_0 are transmitted, while the even multiples of ω_0 are strongly suppressed. Since the metasurface is lossless (purely real susceptibilities), we can infer that the frequencies that are even multiples of ω_0 are thus mostly reflected. The generation of transmitted waves, with corresponding frequencies that are even multiples of the excitation frequency, is thus a nonreciprocal process since $S_{21}^{\omega_0 \to 2n\omega_0} \neq S_{12}^{\omega_0 \to 2n\omega_0}$, where $n = 1, 2, 3, ...$

Next, we are interested in comparing the theoretical results obtained in Eqs. (2.70), (2.72) and (2.73) to FDTD simulations. To perform this comparison, we consider two different metasurfaces that are both reflectionless with conditions as in (2.63). For these two metasurfaces, we compare the amplitudes of the three first harmonics, corresponding to frequencies ω_0, $2\omega_0$ and $3\omega_0$, that are found from (2.70), (2.72) and (2.73) to those obtained from the time-domain Fourier transforms of FDTD simulations. We point out that, to compute the theoretical amplitude of the harmonic at frequency ω_0, we have to consider both Eqs. (2.70) and (2.73). To these two metasurfaces, we attribute specific values of E_0 and $\chi_{ee}^{(1)}$ while the value of $\chi_{ee}^{(2)}$ is swept over a specified range. Note that the values of these different terms cannot be selected arbitrarily because the FDTD simulation equations may lead to nonphysical results, as explained in Appendix D. We have consequently chosen values that lead to physical responses and also made sure that $\chi_{ee}^{(1)} > \chi_{ee}^{(2)}$ so as to satisfy the prescription of perturbation theory in (2.68).

In the case of the first metasurface, we specify that $E_0 = 1.5$ V/m and $\chi_{ee}^{(1)} = 0.1$ m while $\chi_{ee}^{(2)}$ is swept between $[0, 0.04]$ m^2/V. The resulting amplitudes of the three first harmonics are plotted in Fig. 2.12a, where the solid blue lines correspond to perturbation analysis approximations and the red dashed lines correspond to FDTD simulations. For the second metasurface, we specify that $E_0 = 10$ V/m and $\chi_{ee}^{(1)} = 0.3$ m while $\chi_{ee}^{(2)}$ is swept between $[0, 0.01]$ m^2/V; the corresponding results are plotted in Fig. 2.12b. For the two metasurfaces, we see that the theoretical results are in good agreement with those of the FDTD simulations. We also note that large values of $\chi_{ee}^{(2)}$ increase the discrepancies between the two methods, which is expected since perturbation theory leads to inaccurate results if the conditions that

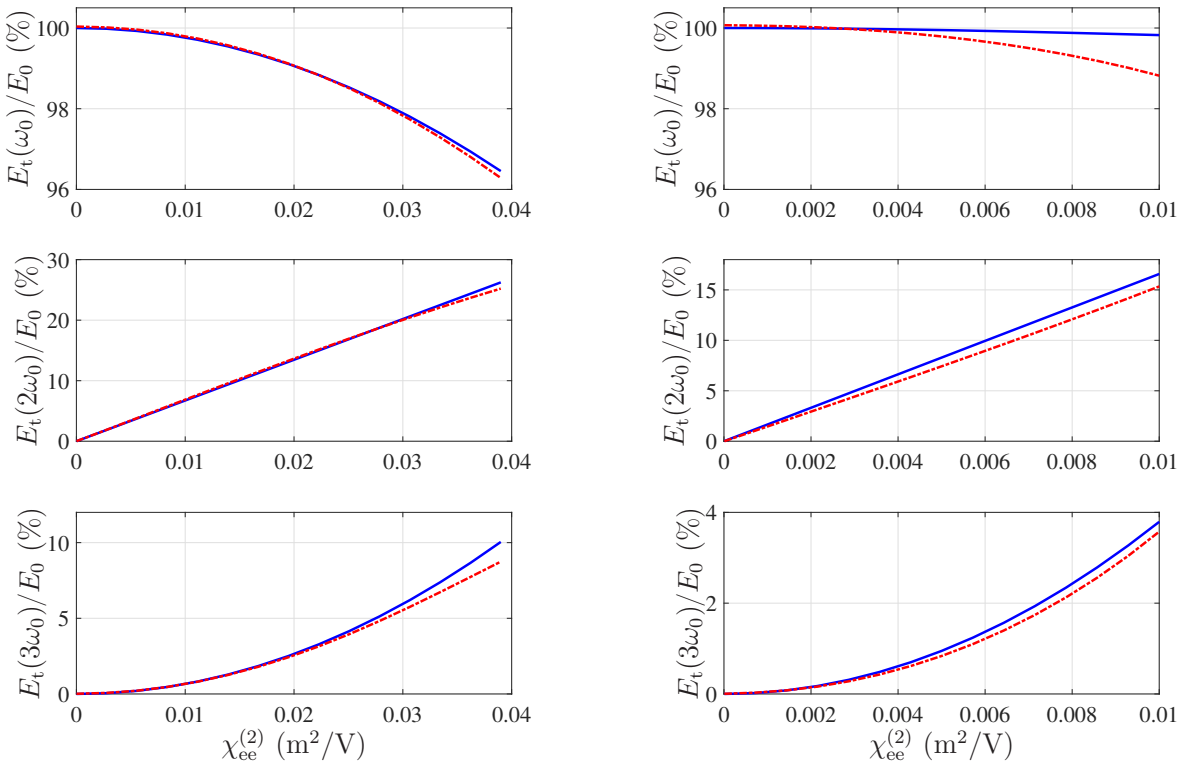

Figure 2.12 Comparisons between the amplitude of the three first normalized harmonics computed from the analytical expressions found using perturbation analysis (solid blue lines) and FDTD simulations (dashed red lines). The following parameters are used: (a) $E_0 = 1.5$ V/m, $\chi_{ee}^{(1)} = 0.1$ m and (b) $E_0 = 10$ V/m, $\chi_{ee}^{(1)} = 0.3$ m.

$\chi_{ee}^{(1)} \gg \chi_{ee}^{(2)}$ is not respected. Additionally, the theoretical results are necessarily affected by the fact that Eq. (2.67) is truncated such that all terms beyond $E_{t,2}$ are not taken into consideration.

It should be noted that the FDTD simulations in both Figs. 2.11 and 2.12 show that the metasurface is lossless and passive as evidenced by power conservation, i.e $\sum_{n=1}^{\infty} |E(\omega_n)|^2 = |E_0|^2$. However, this is not the case for the perturbation analysis expressions due to their truncation, as can be notably seen in Fig. 2.12b where $\sum_{n=1}^{3} |E(\omega_n)|^2 > |E_0|^2$ for values of $\chi_{ee}^{(2)}$ that are close to 0.01.

2.9 Comparison with Other Metasurface Synthesis Techniques

In parallel to the work developed in this thesis, other metasurface synthesis techniques were being investigated, as already pointed out in Chapter 1. We will here briefly compare these techniques to the one presented in this document.

We shall start with the synthesis techniques developed by Grbic [131–134] and Eleftheriades [135–137,176], which are essentially equivalent to each other. They treat the metasurface discontinuity as an excitable sheet of electric and magnetic surface currents. In that case, the electromagnetic fields on both sides of the metasurface can be related to each other using impedance boundary conditions (IBC). Using the same notation as in (2.4), the IBC read

$$\hat{\boldsymbol{z}} \times \Delta \boldsymbol{H} = \overline{\overline{Z}}_{\mathrm{e}}^{-1} \cdot \boldsymbol{E}_{\mathrm{av}}, \tag{2.76a}$$

$$\Delta \boldsymbol{E} \times \hat{\boldsymbol{z}} = \overline{\overline{Z}}_{\mathrm{m}} \cdot \boldsymbol{H}_{\mathrm{av}}, \tag{2.76b}$$

where $\overline{\overline{Z}}_{\mathrm{e}}$ and $\overline{\overline{Z}}_{\mathrm{m}}$ are the metasurface electric and magnetic impedance tensors, respectively. These relations were later extended to include bianisotropy in the form of magnetoelectric coupling tensors. A comparison between the bianisotropic extensions of (2.76) and the GSTCs based boundary conditions in (2.14), reveals that these two sets of relations are essentially equivalent to each other besides the convention used for the material parameters. It should be noted that the IBC relate the transverse components of the fields, accordingly the tensors $\overline{\overline{Z}}_{\mathrm{e}}$ and $\overline{\overline{Z}}_{\mathrm{m}}$ are 2×2 matrices. However, the susceptibility tensors in (2.7) are 3×3 matrices since they include normal components. Consequently, the GSTCs relations (2.4), which include the spatial derivatives of the normal polarization densities, are more general to describe the discontinuities of the fields in the presence of a metasurface than the IBC. The fact that normal components are not taken into account in the IBC reduces the number of available degrees of freedom, as discussed in Sec. 2.5, and thus prevents the implementation of certain transformation specifications such as, for instance, the metasurface with controllable angular scattering presented in Sec. 2.7.3. Moreover, the use of polarization densities and susceptibilities, instead of impedances, allows a more direct extension of the GSTCs so as to include nonlinearities, as done in Sec. 2.8.

Let us now discuss the synthesis technique that was developed by Tretyakov [138,139]. This synthesis technique is distinct from the GSTCs based technique developed here because it relates the fields scattered by the metasurface to the polarizabilities of single scattering particles instead of material parameters like the susceptibilities. This makes this synthesis technique particularly interesting since the polarizabilities can be related to the physical dimensions of scattering particles, at least when the latter present relatively simple geometries. Therefore,

it is possible, to some extent, to relate the fields scattered by the metasurface to the shapes of its scatterers.

Now, we briefly summarize the main steps of the synthesis technique in [138, 139] so as to compare it to the GSTCs based technique of this thesis. In the most general case, the metasurface is formed by a periodic array of bianisotropic scattering particles described in terms of polarizability tensors. When the metasurface is illuminated, the effect of each scattering particle can be associated to electric and magnetic dipole moments, which are given by

$$\boldsymbol{p} = \overline{\overline{\alpha}}_{\mathrm{ee}} \cdot \boldsymbol{E}_{\mathrm{loc}} + \overline{\overline{\alpha}}_{\mathrm{em}} \cdot \boldsymbol{H}_{\mathrm{loc}}, \tag{2.77a}$$

$$\boldsymbol{m} = \overline{\overline{\alpha}}_{\mathrm{me}} \cdot \boldsymbol{E}_{\mathrm{loc}} + \overline{\overline{\alpha}}_{\mathrm{mm}} \cdot \boldsymbol{H}_{\mathrm{loc}}, \tag{2.77b}$$

where $\boldsymbol{E}_{\mathrm{loc}}$ and $\boldsymbol{H}_{\mathrm{loc}}$ are the local fields acting on each individual scattering particle. These local fields may be expressed as functions of the incident field by considering the coupling between adjacent scattering particles, which leads to

$$\boldsymbol{E}_{\mathrm{loc}} = \boldsymbol{E}_{\mathrm{inc}} + \overline{\overline{\beta}}_{\mathrm{e}} \cdot \boldsymbol{p}, \tag{2.78a}$$

$$\boldsymbol{H}_{\mathrm{loc}} = \boldsymbol{H}_{\mathrm{inc}} + \overline{\overline{\beta}}_{\mathrm{m}} \cdot \boldsymbol{m}, \tag{2.78b}$$

where $\overline{\overline{\beta}}_{\mathrm{e}}$ and $\overline{\overline{\beta}}_{\mathrm{m}}$ are electric and magnetic coupling tensors [138]. Inserting (2.78) into (2.77) and solving for the dipole moments, leads to

$$\boldsymbol{p} = \overline{\overline{\hat{\alpha}}}_{\mathrm{ee}} \cdot \boldsymbol{E}_{\mathrm{inc}} + \overline{\overline{\hat{\alpha}}}_{\mathrm{em}} \cdot \boldsymbol{H}_{\mathrm{inc}}, \tag{2.79a}$$

$$\boldsymbol{m} = \overline{\overline{\hat{\alpha}}}_{\mathrm{me}} \cdot \boldsymbol{E}_{\mathrm{inc}} + \overline{\overline{\hat{\alpha}}}_{\mathrm{mm}} \cdot \boldsymbol{H}_{\mathrm{inc}}, \tag{2.79b}$$

where the dipole moments are only expressed in terms of the incident fields and where the terms $\overline{\overline{\hat{\alpha}}}$ correspond to effective polarizability tensors. Next, the reflected and transmitted fields from the metasurface may be found by considering that the metasurface is a periodic array of electric and magnetic dipole moments. In the far-field, the reflected and transmitted waves can thus be respectively expressed as

$$\boldsymbol{E}_{\mathrm{r}} = -\frac{j\omega}{2S} \cdot [\eta_0 \boldsymbol{p} - \hat{\boldsymbol{z}} \times \boldsymbol{m}], \tag{2.80a}$$

$$\boldsymbol{E}_{\mathrm{t}} = \boldsymbol{E}_{\mathrm{inc}} - \frac{j\omega}{2S} \cdot [\eta_0 \boldsymbol{p} + \hat{\boldsymbol{z}} \times \boldsymbol{m}], \tag{2.80b}$$

where S is the surface area of the array unit cells. Finally, the relations between the scattered fields from the metasurface and the effective polarizabilities are obtained by combining (2.80)

with (2.79) and making use of the fact that $\boldsymbol{H}_{\text{inc}} = \hat{\boldsymbol{z}} \times \boldsymbol{E}_{\text{inc}}/\eta_0$ for plane waves. The synthesis procedure then consists in specifying the desired incident, reflected and transmitted electric fields and then solving for the polarizabilities. Alternatively, it is straightforward to find the scattered fields from a metasurface with known scattering particles since the reflected and transmitted fields are already decoupled in (2.80), which is not the case of the GSTCs relations. Computing the scattered fields from a known metasurface using the GSTCs usually requires to resort to involved numerical analyses since the reflected and transmitted fields cannot be conveniently decoupled from each other, except when the metasurface is uniform in which case we can use the method discussed in Sec. 2.4.

To illustrate how the particle dimensions can be related to the scattered fields, we shall consider the case of a metasurface composed of omega scattering particles like the one depicted in Fig. 2.13. This structure is made of a thin conducting wire and its overall size is subwavelength. It is possible to find approximate polarizabilities corresponding to this scattering

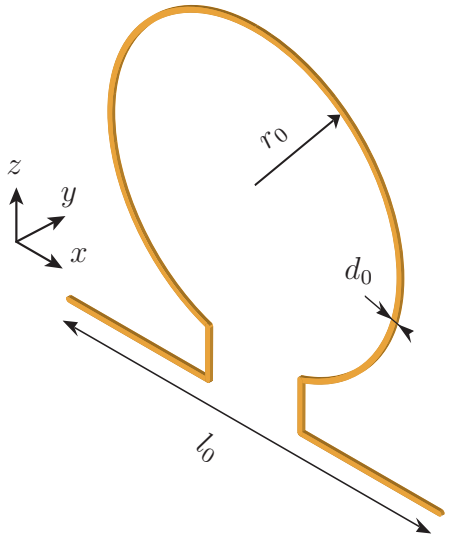

Figure 2.13 Representation of an omega particle.

particle if we assume that the wire diameter d_0 is very small such that $d_0 \ll l_0, r_0$. In that case, the polarizabilities are given by [158]

$$\overline{\overline{\alpha}}_{\text{ee}} = \alpha_{\text{ee}}^{xx} \hat{\boldsymbol{x}}\hat{\boldsymbol{x}} + \alpha_{\text{ee}}^{zz} \hat{\boldsymbol{z}}\hat{\boldsymbol{z}}, \tag{2.81a}$$

$$\overline{\overline{\alpha}}_{\text{mm}} = \alpha_{\text{mm}}^{yy} \hat{\boldsymbol{y}}\hat{\boldsymbol{y}}, \tag{2.81b}$$

$$\overline{\overline{\alpha}}_{\text{me}} = \alpha_{\text{me}}^{yx} \hat{\boldsymbol{y}}\hat{\boldsymbol{x}}, \tag{2.81c}$$

$$\overline{\overline{\alpha}}_{\text{em}} = -\overline{\overline{\alpha}}_{\text{me}}^{\text{T}}. \tag{2.81d}$$

Further analysis, which are detailed in [158], allows one to find approximate expressions

relating the terms in (2.81) to the parameters r_0 and d_0 of the omega particle. Now, we see how the desired scattered fields can be easily specified in (2.80) and then directly related to the parameters r_0 and d_0, providing of course that the specified transformation is compatible with the available degrees of freedom of the omega particle.

Both the GSTCs based synthesis technique and the polarizability based synthesis technique, which was briefly presented here, have their own advantages and disadvantages. The polarizability based synthesis technique has the advantage of being able to relate, in a relative simple fashion, the specified fields to the scattering particle shapes. Which would be more complicated to achieve with the GSTCs technique. However, the latter is more rigorous than the former. Indeed, the coupling tensors $\overline{\overline{\beta}}$ in (2.78) are approximate and only apply in the case of normal plane wave incidence [177]. Similarly, relations (2.80) correspond to the approximate electric fields, radiated by an array of electric and magnetic dipole moments, that are obtained by neglecting near-field contributions. In contrast, the GSTCs apply for all directions of wave propagation and the near-field contributions are not neglected. Finally, the GSTCs technique has the advantage that the susceptibilities resulting from the synthesis can be directly related to material parameters like the permittivity and the permeability. This allows one to easily simulate the behavior of the metasurface under any illumination and especially for incident waves that deviate from the specified one. Such kind of metasurface scattering analysis would be more difficult to achieve with the polarizability based technique.

Even though these two synthesis techniques are relatively distinct from each other, it is possible to relate the effective polarizabilities to the susceptibilities that are used in this work. The corresponding relations are provided in Appendix C.

2.10 Summary

In this chapter, we have developed and discussed the mathematical synthesis of metasurfaces. We started by simplifying the metasurface inverse problem by assuming that the metasurface is a zero-thickness electromagnetic discontinuity. This allows the derivation of rigorous boundary conditions, the GSTCs, from which stems the metasurface synthesis procedure.

We have seen how the susceptibilities may be expressed in terms of the specified fields and how this led to the conclusion that a fully bianisotropic metasurface has the capability to perform several wave transformations. The relations between fields and susceptibilities enabled us to then derive the relations between the scattering parameters and the susceptibilities, which is a crucial step towards the physical realization of metasurfaces.

A few examples have been presented to illustrate the implementation of the synthesis techni-

que, and many more will be presented in the forthcoming chapters. Notably, the next chapter proposes an extensive discussion on the particular case of refractive metasurfaces.

Next, we have extended the range of possible metasurface electromagnetic transformations by taking into account the presence of second-order nonlinearities. We have seen how the reflectionless conditions can be obtained and how they differ depending on the direction of wave propagation, which is related to the nonreciprocal nature of nonlinear materials. The topic of nonlinear metasurfaces is vast and definitively requires further investigation, as this work only scratched the surface.

Finally, we have compared different synthesis techniques that have been develop mostly in parallel to the work that is presented here. In general, the GSTCs synthesis technique is more rigorous as it does not require any assumption in terms of field specifications. However, this synthesis technique may be more complicated for the practical realization of metasurfaces since it is generally more difficult to relate the scattering particle shapes to the susceptibilities.

CHAPTER 3 Fundamental Theory of Refractive Metasurfaces

We have seen, in the previous chapter, how a metasurface can be synthesized from the specified electromagnetic fields using the susceptibilities. We will now discuss various aspects of the synthesis technique and also present an alternative approach to the mathematical design of metasurfaces. As a basis for the discussion, we will consider the topic of refractive metasurfaces. As we will see, this type of electromagnetic transformation is a perfect candidate to illustrate how the synthesis method works as well as to put into practice several of the concepts developed previously.

In the first two sections, we will discuss the synthesis of a monoanisotropic (i.e. only described by the susceptibility tensors $\overline{\overline{\chi}}_{\mathrm{ee}}$ and $\overline{\overline{\chi}}_{\mathrm{mm}}$) refractive metasurface and evaluate its transmission efficiency. It will be demonstrated that the efficiency of such a kind of transformation is inherently limited and leads to the design of a lossy structure.

Then, we will present an alternative approach to the design of refractive metasurfaces that has the advantage of being fully efficient. We will see that only an asymmetric, and consequently bianisotropic, metasurface can allow "perfect" refraction[1]. Finally, we will discuss a more exotic case where the metasurface possesses nonzero normal susceptibility components.

3.1 Monoanisotropic Refractive Metasurfaces: Two Synthesis Approaches

For the purpose of this discussion let us assume that the refraction transformation involves x-polarized waves and takes place in the xz-plane with a monoanisotropic metasurface, the relevant susceptibilities, repeated from (2.18), are given by

$$\chi_{\mathrm{ee}}^{xx} = \frac{-\Delta H_y}{j\omega\epsilon_0 E_{x,\mathrm{av}}}, \tag{3.1a}$$

$$\chi_{\mathrm{mm}}^{yy} = \frac{-\Delta E_x}{j\omega\mu_0 H_{y,\mathrm{av}}}. \tag{3.1b}$$

These susceptibilities correspond to a rigorous description of the material parameters that perform the specified transformation between the incident, reflected and transmitted waves. It is however interesting to note that the susceptibilities may also be defined from reflection and transmission coefficients, as discussed in Sec. 2.4. In that case, the susceptibilities,

[1]Here the term "perfect" refers to a fully efficient transformation and which does not produce spurious diffraction.

repeated from (2.31), are given by

$$\chi_{\mathrm{ee}}^{xx} = \frac{2j\left(T_x + R_x - 1\right)}{k_0\left(T_x + R_x + 1\right)}, \tag{3.2a}$$

$$\chi_{\mathrm{mm}}^{yy} = \frac{2j\left(T_x - R_x - 1\right)}{k_0\left(T_x - R_x + 1\right)}. \tag{3.2b}$$

We see that with relations (3.1) and (3.2), there are two different ways of synthesizing a metasurface. The metasurface can be rigorously synthesized in terms of tangential electromagnetic fields with relations (3.1), or approximatively synthesized in terms of transmission and reflection coefficients with relations (3.2).

Since the susceptibilities may be obtained from relations (3.1) or from relations (3.2), one may ask the question: what is the difference between these two synthesis methods? To answer the question, we will compare them in three different ways. First, we will compare how the resulting susceptibility functions differ from each other in the case of a refractive metasurface. Then, from the synthesized susceptibilities, we will compare the corresponding reflection and transmissions coefficients. Finally, we will compare their scattering response by performing full-wave simulations.

For the purpose of this discussion, the metasurface is specified to be reflectionless. The electric and magnetic fields at the metasurface ($z = 0$) have the general following form:

$$\boldsymbol{E}_{\mathrm{a}} = A_{\mathrm{a}}\left(\hat{\boldsymbol{x}}\frac{k_{z,\mathrm{a}}}{k_0} - \hat{\boldsymbol{z}}\frac{k_{x,\mathrm{a}}}{k_0}\right)e^{-jk_{x,\mathrm{a}}x} \quad \text{and} \quad \boldsymbol{H}_{\mathrm{a}} = \frac{A_{\mathrm{a}}}{\eta_0}\hat{\boldsymbol{y}}e^{-jk_{x,\mathrm{a}}x}, \tag{3.3}$$

where $\mathrm{a} = \mathrm{i}, \mathrm{t}, \mathrm{r}$ denotes the incident, transmitted and reflected waves, respectively, A is their amplitude and η_0 is the intrinsic impedance of the surrounding medium (considered here to be vacuum) associated with the wavenumber k_0. The transverse and longitudinal wavenumbers are defined by $k_{x,\mathrm{a}} = k_0 \sin\theta_{\mathrm{a}}$ and $k_{z,\mathrm{a}} = k_0 \cos\theta_{\mathrm{a}}$, respectively. In this example, the reflected wave is specified to be zero so $A_{\mathrm{r}} = 0$. In order to obtain the metasurface susceptibilities with the first metasurface synthesis method, which is based on relations (3.1), the fields in (3.3) are inserted into (3.1). This leads to

$$\chi_{\mathrm{ee}}^{xx} = 2j\left(\frac{A_{\mathrm{t}}e^{jk_{x,\mathrm{i}}x} - A_{\mathrm{i}}e^{jk_{x,\mathrm{t}}x}}{A_{\mathrm{i}}k_{z,\mathrm{i}}e^{jk_{x,\mathrm{t}}x} + A_{\mathrm{t}}k_{z,\mathrm{t}}e^{jk_{x,\mathrm{i}}x}}\right), \tag{3.4a}$$

$$\chi_{\mathrm{mm}}^{yy} = \frac{2j}{k_0^2}\left(\frac{A_{\mathrm{t}}k_{z,\mathrm{t}}e^{jk_{x,\mathrm{i}}x} - A_{\mathrm{i}}k_{z,\mathrm{i}}e^{jk_{x,\mathrm{t}}x}}{A_{\mathrm{t}}e^{jk_{x,\mathrm{i}}x} + A_{\mathrm{i}}e^{jk_{x,\mathrm{t}}x}}\right). \tag{3.4b}$$

We will now use the second synthesis method, which is based on relations (3.2), to synthesize the same refraction transformation. However, the relations (3.2) were initially derived in

Sec. 2.4 to relate the susceptibilities to the scattering parameters of normally propagating waves. Therefore, it may then seem inappropriate to use such relations for the synthesis of a metasurface that changes the direction of wave propagation. While these relations are rigorous for the case of normal wave propagation, they may nevertheless be applied in the case of oblique wave propagation. In that latter case, these relations lead to approximate material parameters because they do not rigorously describe the electromagnetic transformation corresponding to a change in the direction of wave propagation, especially when large refraction angles are required.

To define the reflection and transmission coefficients in (3.2), we may resort to the complex amplitude transmittance method [159], if the reflection coefficient is zero, or alternatively to the momentum transformation technique [130], if the reflection coefficient is not zero. In our case, the metasurface is specified to be reflectionless meaning that $R_x = 0$ in (3.2), which leads to $\chi_{\mathrm{ee}}^{xx} = \chi_{\mathrm{mm}}^{yy}$. Making use of the complex amplitude transmittance method, the transmission coefficient is defined as

$$T_x = \frac{\Psi_{\mathrm{t}}}{\Psi_{\mathrm{i}}}, \tag{3.5}$$

where Ψ_{i} and Ψ_{t} are respectively the phase profiles of the incident and the transmitted waves on the metasurface plane. The phase profile of the incident wave is $\Psi_{\mathrm{i}} = e^{-jk_{x,\mathrm{i}}x}$, while that of the transmitted wave is $\Psi_{\mathrm{t}} = e^{-jk_{x,\mathrm{t}}x}$. Inserting these definitions into (3.5) reduces (3.2) to

$$\chi_{\mathrm{ee}}^{xx} = \chi_{\mathrm{mm}}^{yy} = \frac{2}{k_0} \tan\left(\frac{k_{x,\mathrm{t}} - k_{x,\mathrm{i}}}{2} x\right). \tag{3.6}$$

We will now compare the differences between the synthesized susceptibilities obtained with the rigorous relations (3.4) to those obtained with the approximate relations (3.6). We assume that the incident and transmission angles are $\theta_{\mathrm{i}} = 20^\circ$ and $\theta_{\mathrm{t}} = 45^\circ$, respectively. For this set of angles, we heuristically specify that $A_{\mathrm{i}} = A_{\mathrm{t}} = 1$. The corresponding real (solid blue lines) and imaginary (dashed red lines) parts of the electric and magnetic susceptibilities are plotted in Figs. 3.1, where Figs. 3.1a and 3.1c correspond to the first synthesis method while Figs. 3.1b and 3.1d correspond to the second synthesis method. There are two main differences between these two synthesis methods. The first one lies in the fact that both electric and magnetic susceptibilities are equal to each other in (3.6), which is not the case with the rigorous relations in (3.4). The second important difference is that the susceptibilities in (3.6) are purely real, while those in (3.4) are complex. We know from the discussion in Sec. 2.2, that the imaginary parts of the susceptibilities are responsible for loss or gain. Therefore, the approximate synthesis method leads to a purely passive and lossless metasurface, which is not the case of the rigorous method. In the next section, we will explain why

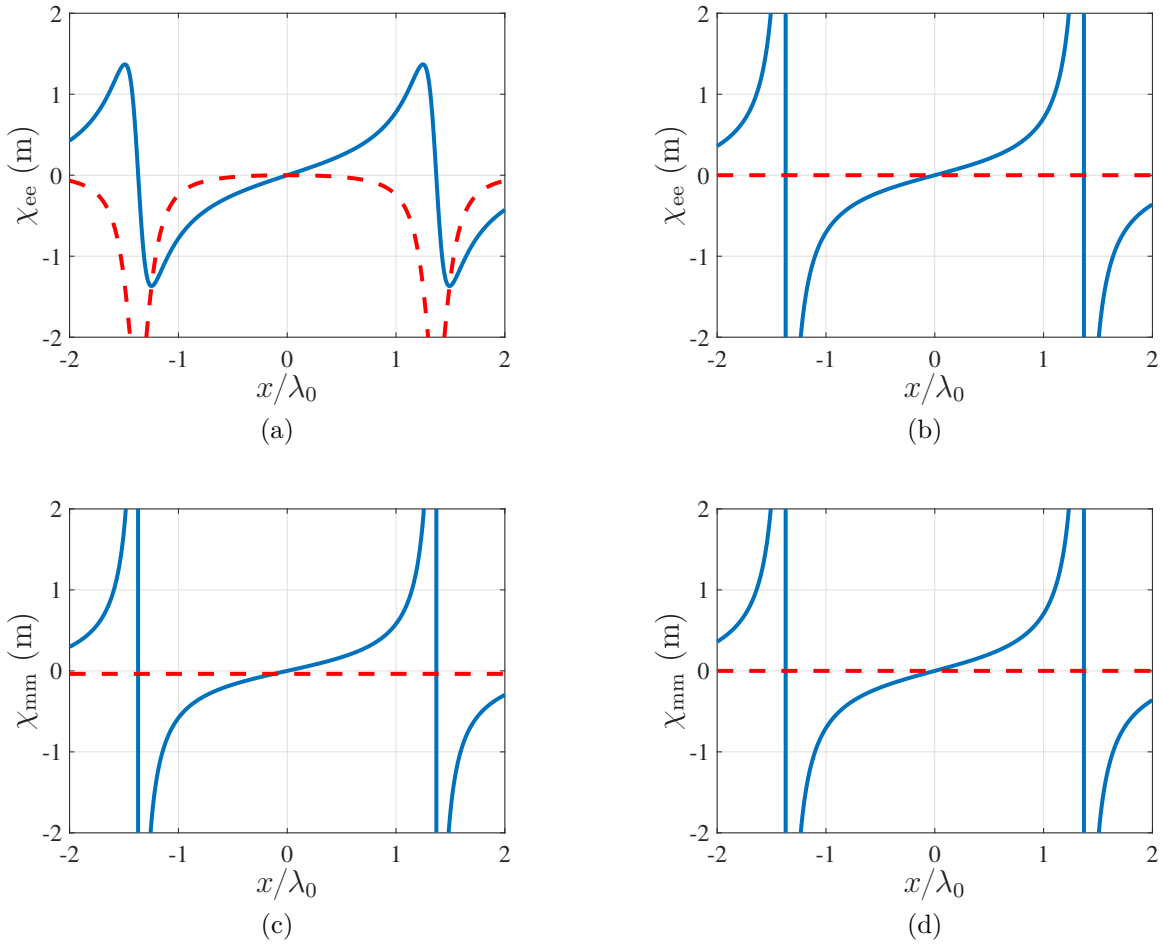

Figure 3.1 Susceptibilities of a refractive metasurface transformation with an incidence angle of $\theta_\mathrm{i} = 20^\circ$ and a refraction angle of $\theta_\mathrm{t} = 45^\circ$. The solid blue lines correspond to real parts while the dashed red lines correspond to imaginary parts. The susceptibilities in the left are obtained with the first method, while those in the right are obtained with the second method.

the susceptibilities of the rigorous method in (3.4) present nonzero imaginary parts. We will notably see that the incident power flow through the metasurface is not equal to the transmitted power flow [178, 179], leading to undesired absorbtion. Also note that the periodicity of the susceptibilities in the x-direction is larger than λ_0, suggesting that this metasurface should be easily implementable with simple scattering particles.

Now that the susceptibilities found from the two methods have been compared, let us compare their corresponding scattering parameters. It was found in the previous chapter that the transmission and reflection coefficients for a monoanisotropic metasurface can be expressed

as

$$T_x = \frac{4 + \chi_{\mathrm{ee}}^{xx}\chi_{\mathrm{mm}}^{yy}k^2}{(2 + jk\chi_{\mathrm{ee}}^{xx})(2 + jk\chi_{\mathrm{mm}}^{yy})}, \tag{3.7a}$$

$$R_x = \frac{2jk\,(\chi_{\mathrm{mm}}^{yy} - \chi_{\mathrm{ee}}^{xx})}{(2 + jk\chi_{\mathrm{ee}}^{xx})\,(2 + jk\chi_{\mathrm{mm}}^{yy})}. \tag{3.7b}$$

To obtain the scattering parameters of the first synthesis method, we substitute the susceptibilities in (3.4) into (3.7). The resulting amplitude and phase of the transmission and reflection coefficients are respectively plotted in Figs 3.2a and 3.2c, where the solid blues lines correspond to the transmission coefficient and the dashed red lines to the reflection coefficient. For the second synthesis method, the transmission and reflection coefficients are those already specified in (3.5) and are given by $T_x = e^{j(k_{x,\mathrm{i}} - k_{x,\mathrm{t}})x}$ and $R_x = 0$, respectively. For comparison, their corresponding amplitude and phase are plotted in Figs. 3.2b and 3.2d.

From these plots, it is worth noting that the scattering behavior of these refractive metasurfaces can be associated to that of equivalent amplitude and phase gratings. Notably, the first synthesis method leads to a metasurface whose scattering behavior may be described by the combined effect of a nonuniform amplitude and phase grating, while the second synthesis method leads to a phase-gradient metasurface with uniform unit transmission. The fact that the reflection coefficient that is plotted in Fig. 3.2a is nonzero may a priori appear contradictory given the prescription of zero reflection specified to obtain relations (3.4). However, remember that the scattering parameters are computed based on the assumption of rectilinear propagation, which obviously does not correspond to the present example. The actual reflection produced by the susceptibilities in (3.4) is *rigorously zero*, and the nonzero reflection parameter in Fig. 3.2a is an artifact of the mapping between the rectilinear scattering parameters and the physical problem. It is important to understand that the reflection and transmission coefficients *only* apply locally and thus do not rigorously describe the overall scattering behavior of the metasurface when the latter is nonuniform. This is because finding the scattered fields from a nonuniform metasurface necessarily implies solving a differential system of equations since, in Maxwell equations, the electric and the magnetic fields are related to each other via spatial derivatives. Therefore, looking at the metasurface as an equivalent amplitude and phase grating may only be used as a rough approximation to evaluate its responses, except in the specific case where the metasurface is uniform. However, it may still be deduced from Fig. 3.2a that the metasurface is lossy, as evidenced by the fact that $|T_x|^2 + |R_x|^2 < 1$. In the next section, we will explain why the metasurface is lossy, while it was initially synthesized with the prescription that the amplitude of the transmitted wave

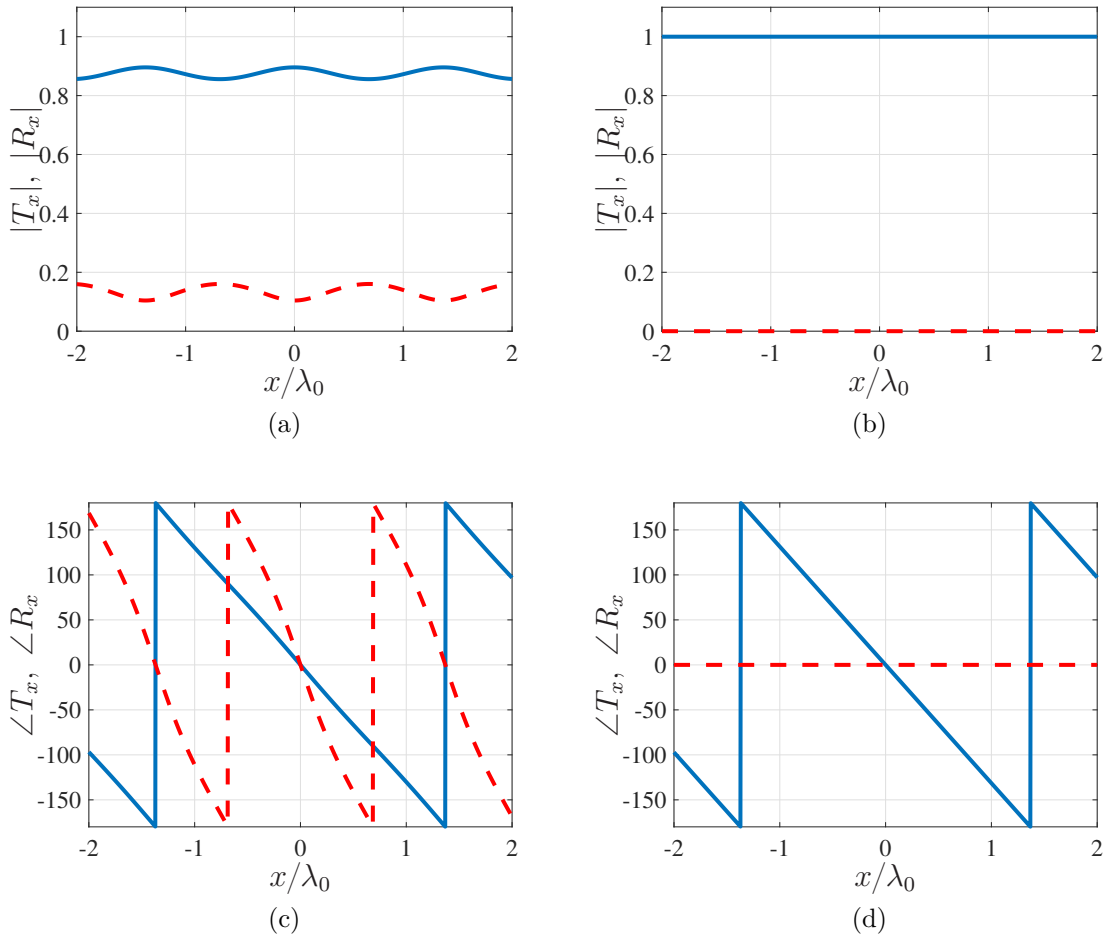

Figure 3.2 Transmission (solid blue line) and reflection (dashed red line) coefficients for a refractive metasurface transformation with an incidence angle of $\theta_\mathrm{i} = 20°$ and a refraction angle of $\theta_\mathrm{t} = 45°$. The top and bottom plots correspond to the amplitude and phase of these coefficients, respectively. The plots on the left are obtained with the first method, while the ones on the right are obtained with the second method.

is the same as the amplitude of the incident wave.

The last comparison between the two synthesis methods consists in analyzing their respective scattering behavior via full-wave simulations. For this purpose, we use a finite-difference frequency-domain (FDFD) scheme that we have developed for the specific objective of simulating zero-thickness metasurfaces [163]. The full-wave simulation corresponding to the first synthesis method is shown in Fig. 3.3a, while that of the second method is shown in Fig. 3.3b. As can be seen, both metasurfaces refract the incident beam at a 45° angle without any reflection. In Fig. 3.3b, we see the presence of an undesired diffraction order, which is due to the non-rigorousness of relations (3.6) to synthesize this refractive transformation. Thus, one may think that the result in Fig. 3.3a is necessarily better than the one in Fig. 3.3b.

However, this is not the case. Indeed, the transmission efficiency, which is defined as the ratio between the power transmitted in the desired direction (here at 45°) and the incident power, is not the same for the two methods. The transmission efficiencies are computed by measuring the field right before and after the metasurfaces in Figs. 3.3, which leads to about 75% for the first method and 97% for the second one. It may come as a surprise that the

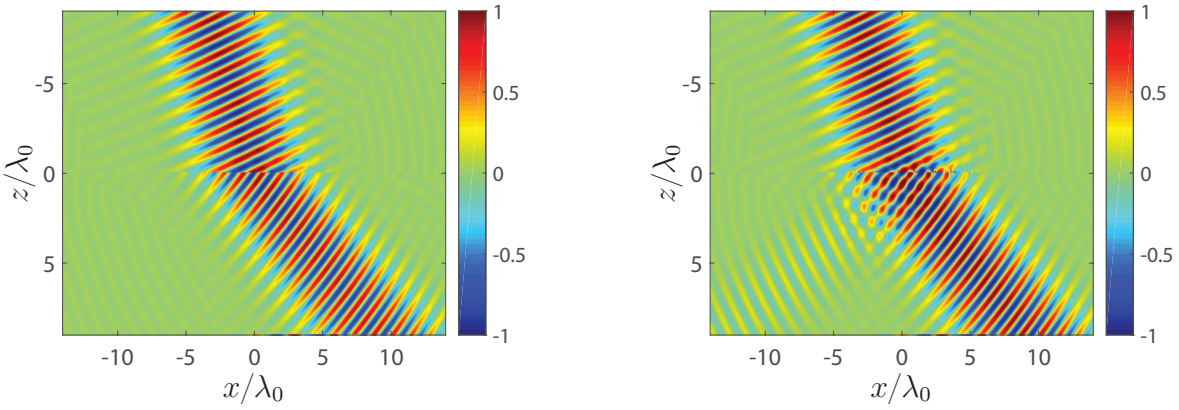

Figure 3.3 Full-wave simulated real part of the $H_z\eta_0$ component obtained using: (a) the first synthesis method with susceptibilities as in (3.4), (b) the second synthesis method with susceptibilities as in (3.6).

rigorous synthesis method leads to a worse efficiency than the approximate method, but this may be explained by the fact that the metasurface in Fig. 3.3a is lossy, as said above.

From the three comparisons between the two synthesis methods presented above, we can conclude that the second synthesis is in many cases preferred over the first one for its implementation simplicity and better efficiency, even though the latter is more rigorous than the former. There are two reasons that make the physical implementation of the second synthesis method easier: the fact that the metasurface is passive and lossless and that the transmission coefficient has a unit amplitude and only a phase variation. Therefore the only purpose of the scattering particles is to provide specific phase shifts. The rigorous synthesis technique requires the implementation of nonuniform loss, which is practically difficult to achieve. Note that several of the metasurfaces that will be presented in Chapter 5 have been synthesized based on this second synthesis technique.

3.2 Inefficiency of Monoanisotropic Refractive Metasurfaces

We will now investigate in more details the reasons that make monoanisotropic refractive metasurfaces inherently inefficient, if synthesized with either of the two methods, and lossy,

if synthesized using the first method. As can be seen in Figs. 3.1a and 3.1c, both electric and magnetic susceptibilities are complex functions and their respective imaginary parts is negative indicating a lossy structure according to the discussion in Sec. 2.2. It can be easily verified that the required transformation is lossy by considering relations (2.12). While relations (2.12d) and (2.12e) are zero due to the monoanisotropic and diagonal nature of the metasurface susceptibility tensors, relations (2.12b) and (2.12c) are not zero indicating the presence of power dissipation (or generation). Relations (2.12b) and (2.12c) are plotted in Fig. 3.4 versus the x-direction on the metasurface plane for the specified fields of the refractive transformation discussed above. Figure 3.4 shows the electric (solid blue line), magnetic

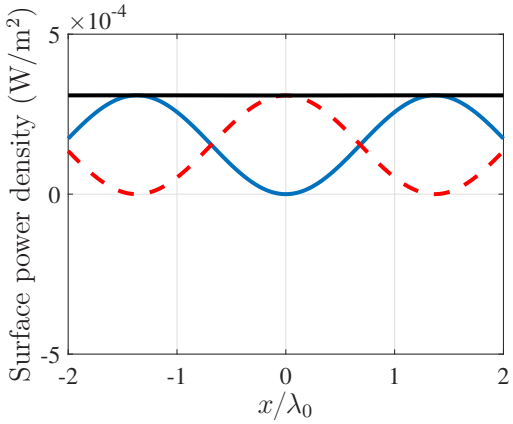

Figure 3.4 Metasurface surface power density including the electric (solid blue line) and magnetic (dashed red line) contributions (corresponding to eqs. (2.12b) and (2.12c), respectively) when $A_\mathrm{i} = A_\mathrm{t} = 1$. Note that positive values correspond to loss and negative values to gain.

(dashed red line) and total (solid black line) surface power density on the metasurface. The fact that all curves in Fig. 3.4 are real and positive reveals that the metasurface is purely lossy. The presence of the observed loss might come as a surprise especially when considering that the specified incident and transmitted fields have the same amplitude ($A_\mathrm{i} = A_\mathrm{t} = 1$).

In this transformation, the presence of loss can be explained [178] by considering the simple geometrical description shown in Fig. 3.5. What might be confusing when considering plane waves is obvious when considering finite size beams: the beamwidth of the incident beam, L_i, is not the same as the beamwidth of the transmitted beam, L_t, except in the trivial case where $\theta_\mathrm{i} = \theta_\mathrm{t}$. Additionally, the Poynting vector of the incident wave, S_i, and that of the transmitted wave, S_t, are the same since $A_\mathrm{i} = A_\mathrm{t}$. The fact that the beamwidths are different but the Poynting vectors are the same means that the total incident power, defined[2] as $P_\mathrm{i} = S_\mathrm{i} L_\mathrm{i}$, is generally not the same as the transmitted power, P_t. This translates into a

[2]Since we are considering a 2D problem, we omit the dimension of the metasurface in the y-direction, as it is the same for the incident and transmitted waves.

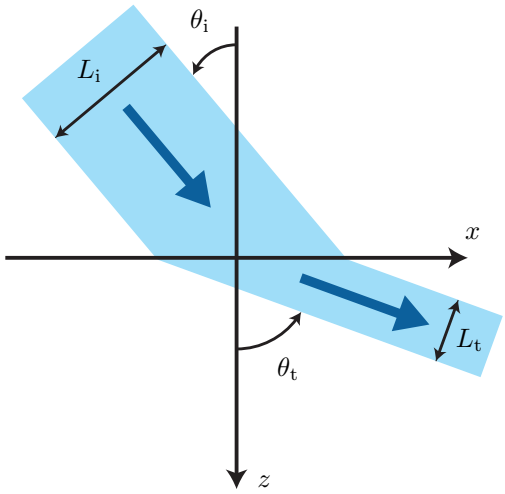

Figure 3.5 Representation of the different beamwidths between the incident and transmitted waves.

transmission efficiency, η, given by

$$\eta = \frac{P_t}{P_i} = \frac{S_t L_t}{S_i L_i} = |t|^2 \frac{\cos\theta_t}{\cos\theta_i}. \tag{3.8}$$

where the coefficient t is the amplitude ratio defined as $t = A_t/A_i$. The power dissipated or produced by the metasurface, P_m, is easily obtained as the difference of the incident power and the transmitted power

$$P_m = P_i - P_t = |A_i|^2 \cos\theta_i - |A_t|^2 \cos\theta_t, \tag{3.9}$$

which can also be written as

$$P_m = P_i(1 - \eta). \tag{3.10}$$

It is clear, from equation (3.8), that the coefficient t as well as the angles θ_i and θ_t play a major role in determining the transmission efficiency of the metasurface. If $\theta_t > \theta_i$ (as in the example considered here), the metasurface remains purely lossy (both electrically and magnetically) as long as the coefficient t is limited to the range $0 \leqslant |t| \leqslant 1$. The metasurface is naturally more and more lossy as $|t|$ decreases to 0.

In our example, $t = 1$ which gives a power efficiency of $\eta = 75.25\%$ and the total dissipated power by the metasurface can be obtained by integrating both electric and magnetic contributions (corresponding to the black line in Fig. 3.4) over the size of the metasurface. Note that this efficiency is exactly the same as the one that was computed in the simulation of Fig. 3.3a. Increasing the value of t beyond 1 will increase the efficiency but at the cost of having a partially active metasurface. In the particular case where $t = \sqrt{\cos\theta_i/\cos\theta_t}$, the

efficiency (3.8) is always equal to $\eta = 1$ and consequently $P_{\mathrm{m}} = 0$. But even if the total dissipated or produced power by the metasurface is zero, the metasurface is actually a combination of alternating electric gain and loss and magnetic loss and gain such that electric and magnetic contributions perfectly cancel each other, as illustrated in Fig. 3.6. It is therefore wrong to assume that, because $P_{\mathrm{m}} = 0$, the metasurface is passive and lossless because, as illustrated here, the metasurface would actually be simultaneously active and lossy. It is

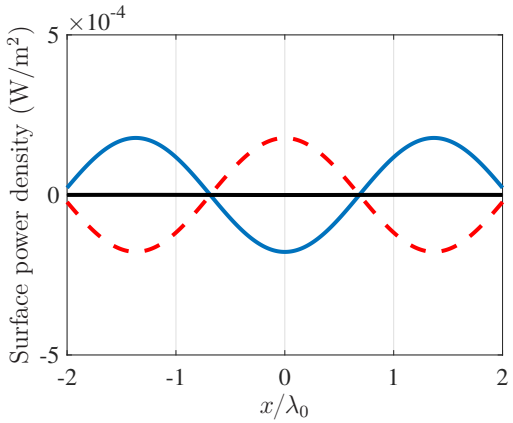

Figure 3.6 Metasurface surface power density including the electric (solid blue line) and magnetic (dashed red line) contributions (corresponding to eqs. (2.12b) and (2.12c), respectively) when $t = \sqrt{\cos\theta_{\mathrm{i}}/\cos\theta_{\mathrm{t}}}$. Note that positive values correspond to loss and negative values to gain.

important to note that, in the case where $\theta_{\mathrm{t}} < \theta_{\mathrm{i}}$, the metasurface is purely passive (but lossy) when $t = \cos\theta_{\mathrm{i}}/\cos\theta_{\mathrm{t}}$ [178].

Now, let us come back to the transmission and reflection coefficients that are plotted in Fig. 3.2. As may be seen in Fig. 3.2a, the absolute value of the transmission coefficient oscillates around 87%, which, converted in terms of transmitted power, is very close to the previously calculated power efficiency of $\eta = 75.25\% \approx (87\%)^2$. In the same figure, the absolute value of the reflection coefficient oscillates around 13%.

There is a last point that we would like to address. At the end of Sec. 2.4, we have proposed to simplify the realization of metasurfaces by setting the imaginary parts of the synthesized susceptibilities to zero. This has the effect of ignoring the loss (or gain) that would normally be induced by the susceptibilities. The question that may be asked is how would this affect the efficiency of the metasurface? Assume that only the real values of the susceptibilities were to be realized instead of the complex ones shown in Figs. 3.1a and 3.1c. In that case, the amplitude of the new transmission coefficient (which is not shown here) would be very close to full and quasi-uniform transmission while the phase profile of the transmission coefficient would remain unaltered compared to that computed from the exact susceptibilities presented

in Figs. 3.2c. Since the transmission phase has not been changed from the exact one, the approximate metasurface performs a transformation that essentially follows the specification, with the exception of undesired diffraction orders due to the nullification of the imaginary parts of the susceptibilities. In fact, the scattering behavior of such a metasurface would resemble that of a metasurface synthesized with the second synthesis method. It results that, whether a lossy structure is implemented or an altered version of it where only the real values of the susceptibilities are implemented, the total power being transmitted into the desired direction may change substantially. In practice, it is often the latter case that is preferred as it corresponds to an easier structure to realize because the metasurface is essentially only affecting the phase of the incident wave while keeping its amplitude constant.

3.3 Perfectly Refracting Bianisotropic Metasurfaces

Up to now, we have seen how the efficiency of a monoanisotropic refractive metasurface is limited due to the inherent presence of loss or undesired scattering. There exists, however, an alternative approach to realize passive, lossless and fully efficient refractive metasurfaces [180–185]. As shown notably in [180], a monoanisotropic metasurface is a symmetric structure (with respect to the longitudinal direction) and thus, exhibits the same impedance matching from both sides. But since the waves on both sides of the metasurface propagate in different directions, the metasurface can only be matched for one of these two waves. By reciprocity, this limits the overall efficiency of the structure. The alternative approach is to consider a bianisotropic metasurface, which is asymmetric due its nonzero magnetoelectric coupling coefficients. This asymmetry is due to the fact that a bianisotropic medium is spatially dispersive [158]. Consequently, waves propagating in opposite directions induce different responses from the medium. In that case, the waves on both sides of the metasurface can both be matched, which maximizes the efficiency of the transformation.

In the following lines, we will synthesize a bianisotropic refractive metasurface and show that it allows perfect refraction, i.e. a power transmission efficiency of $\eta = 1$. Let us consider the bianisotropic GSTCs relations in (2.15). For a refractive metasurface, rotation of polarization is not required, thus the nonzero susceptibility components considered for the synthesis are the diagonal components of $\overline{\overline{\chi}}_{\mathrm{ee}}$ and $\overline{\overline{\chi}}_{\mathrm{mm}}$ and the off-diagonal components of $\overline{\overline{\chi}}_{\mathrm{em}}$ and $\overline{\overline{\chi}}_{\mathrm{me}}$. The introduction of nonzero magnetoelectric coupling coefficients doubles the number of unknown susceptibilities. This means that the multiple wave transformation technique described in Sec. 2.3.2 is used here to obtain the following fully determined system

of equations:

$$\begin{pmatrix} \Delta H_{y1} & \Delta H_{y2} \\ \Delta H_{x1} & \Delta H_{x2} \\ \Delta E_{y1} & \Delta E_{y2} \\ \Delta E_{x1} & \Delta E_{x2} \end{pmatrix} = \begin{pmatrix} \widetilde{\chi}_{\mathrm{ee}}^{xx} & 0 & 0 & \widetilde{\chi}_{\mathrm{em}}^{xy} \\ 0 & \widetilde{\chi}_{\mathrm{ee}}^{yy} & \widetilde{\chi}_{\mathrm{em}}^{yx} & 0 \\ 0 & \widetilde{\chi}_{\mathrm{me}}^{xy} & \widetilde{\chi}_{\mathrm{mm}}^{xx} & 0 \\ \widetilde{\chi}_{\mathrm{me}}^{yx} & 0 & 0 & \widetilde{\chi}_{\mathrm{mm}}^{yy} \end{pmatrix} \cdot \begin{pmatrix} E_{x1,\mathrm{av}} & E_{x2,\mathrm{av}} \\ E_{y1,\mathrm{av}} & E_{y2,\mathrm{av}} \\ H_{x1,\mathrm{av}} & H_{x2,\mathrm{av}} \\ H_{y1,\mathrm{av}} & H_{y2,\mathrm{av}} \end{pmatrix}, \tag{3.11}$$

where the second transformation is the reciprocal of the first one. Assuming that the refraction takes places in the xz-plane and that the waves are all p-polarized, the system (3.11) reduces to

$$\begin{pmatrix} \Delta H_{y1} & \Delta H_{y2} \\ \Delta E_{x1} & \Delta E_{x2} \end{pmatrix} = \begin{pmatrix} \widetilde{\chi}_{\mathrm{ee}}^{xx} & \widetilde{\chi}_{\mathrm{em}}^{xy} \\ \widetilde{\chi}_{\mathrm{me}}^{yx} & \widetilde{\chi}_{\mathrm{mm}}^{yy} \end{pmatrix} \cdot \begin{pmatrix} E_{x1,\mathrm{av}} & E_{x2,\mathrm{av}} \\ H_{y1,\mathrm{av}} & H_{y2,\mathrm{av}} \end{pmatrix}. \tag{3.12}$$

An illustration of the first and second transformations is presented in Figs. 3.7a and 3.7b, respectively. Note that the subscripts i and t respectively refer to the incident and transmit sides of the metasurface rather than the incident and transmitted waves. The electromagnetic

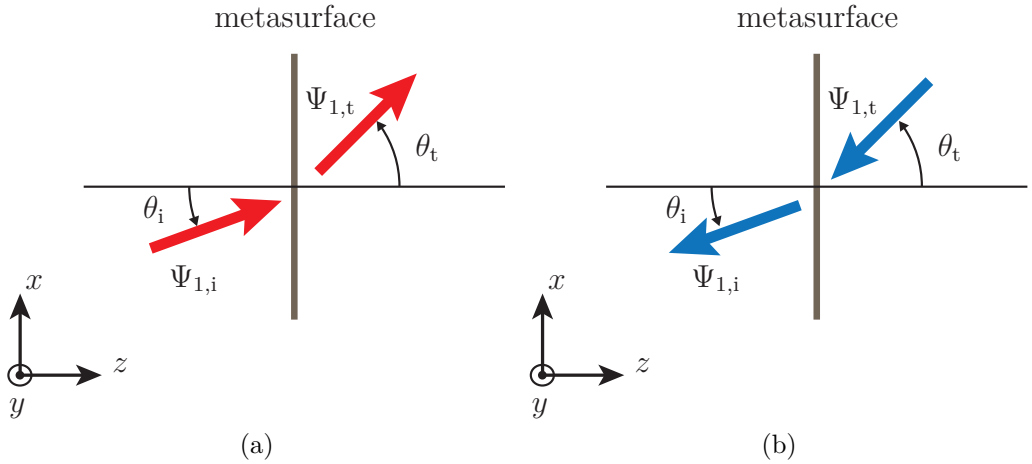

Figure 3.7 Representation of the two transformations used to solve system (3.12). (a) First transformation corresponding to the fields in (3.13), (b) second transformation corresponding to the fields in (3.14).

fields on the incident and transmit sides of the metasurface, assuming that the medium on both sides is vacuum, and that correspond to the first transformation read

$$E_{x1,\mathrm{i}} = \frac{k_{z,\mathrm{i}}}{k_0} e^{-jk_{x,\mathrm{i}}x}, \qquad E_{x1,\mathrm{t}} = A_{\mathrm{t}} \frac{k_{z,\mathrm{t}}}{k_0} e^{-jk_{x,\mathrm{t}}x}, \tag{3.13a}$$

$$H_{y1,\mathrm{i}} = e^{-jk_{x,\mathrm{i}}x}/\eta_0, \qquad H_{y1,\mathrm{t}} = A_{\mathrm{t}} e^{-jk_{x,\mathrm{t}}x}/\eta_0, \tag{3.13b}$$

where A_{t} is the amplitude of the wave on the transmit side. The fields corresponding to the

second transformation read

$$E_{x2,\mathrm{i}} = -\frac{k_{z,\mathrm{i}}}{k_0} e^{jk_{x,\mathrm{i}}x}, \qquad E_{x2,\mathrm{t}} = -A_\mathrm{t}\frac{k_{z,\mathrm{t}}}{k_0} e^{jk_{x,\mathrm{t}}x}, \tag{3.14a}$$

$$H_{y2,\mathrm{i}} = e^{jk_{x,\mathrm{i}}x}/\eta_0, \qquad H_{y2,\mathrm{t}} = A_\mathrm{t} e^{jk_{x,\mathrm{t}}x}/\eta_0. \tag{3.14b}$$

Now the metasurface susceptibilities can be obtained by substituting (3.13) and (3.14) into (3.12) and considering (2.16). Solving for the susceptibilities yields

$$\chi_{\mathrm{ee}}^{xx} = -\frac{4A_\mathrm{t}\sin(x(k_{x,\mathrm{i}}-k_{x,\mathrm{t}}))}{A_\mathrm{t}\cos(x(k_{x,\mathrm{i}}-k_{x,\mathrm{t}}))(k_{z,\mathrm{i}}+k_{z,\mathrm{t}})+k_{z,\mathrm{i}}+k_{z,\mathrm{t}}A_\mathrm{t}^2}, \tag{3.15a}$$

$$\chi_{\mathrm{mm}}^{yy} = -\frac{4k_{z,\mathrm{i}}k_{z,\mathrm{t}}A_\mathrm{t}\sin(x(k_{x,\mathrm{i}}-k_{x,\mathrm{t}}))}{k_0^2\left(A_\mathrm{t}\cos(x(k_{x,\mathrm{i}}-k_{x,\mathrm{t}}))(k_{z,\mathrm{i}}+k_{z,\mathrm{t}})+k_{z,\mathrm{i}}+k_{z,\mathrm{t}}A_\mathrm{t}^2\right)}, \tag{3.15b}$$

$$\chi_{\mathrm{em}}^{xy} = \frac{2j}{k_0}\left[\frac{A_\mathrm{t}\cos(x(k_{x,\mathrm{i}}-k_{x,\mathrm{t}}))(k_{z,\mathrm{i}}-k_{z,\mathrm{t}})-k_{z,\mathrm{i}}+k_{z,\mathrm{t}}A_\mathrm{t}^2}{A_\mathrm{t}\cos(x(k_{x,\mathrm{i}}-k_{x,\mathrm{t}}))(k_{z,\mathrm{i}}+k_{z,\mathrm{t}})+k_{z,\mathrm{i}}+k_{z,\mathrm{t}}A_\mathrm{t}^2}\right], \tag{3.15c}$$

$$\chi_{\mathrm{me}}^{yx} = -\frac{2j}{k_0}\left[\frac{A_\mathrm{t}\cos(x(k_{x,\mathrm{i}}-k_{x,\mathrm{t}}))(k_{z,\mathrm{i}}-k_{z,\mathrm{t}})+k_{z,\mathrm{i}}-k_{z,\mathrm{t}}A_\mathrm{t}^2}{A_\mathrm{t}\cos(x(k_{x,\mathrm{i}}-k_{x,\mathrm{t}}))(k_{z,\mathrm{i}}+k_{z,\mathrm{t}})+k_{z,\mathrm{i}}+k_{z,\mathrm{t}}A_\mathrm{t}^2}\right]. \tag{3.15d}$$

Comparing the values for χ_{em}^{xy} and χ_{me}^{yx}, we see that the metasurface is nonreciprocal[3] for an arbitrary value of A_t. However, we are here interested in the synthesis of a reciprocal metasurface, which is the case only when $A_\mathrm{t} = \sqrt{k_{z,\mathrm{i}}/k_{z,\mathrm{t}}} = \sqrt{\cos\theta_\mathrm{i}/\cos\theta_\mathrm{t}}$. Note that this condition on A_t is equivalent to equalizing the normal power flow ($P_\mathrm{i} = P_\mathrm{t}$) for the waves on both sides of the metasurface and also corresponds to the case discussed above where the monoanisotropic metasurface has an efficiency $\eta = 1$ with a combination of active and lossy elements, as was shown in Fig. 3.6. With this definition of A_t, relations (3.15) reduce to

$$\chi_{\mathrm{ee}}^{xx} = \frac{4\sin(\alpha x)}{\beta\cos(\alpha x)+\sqrt{\beta^2-\gamma^2}}, \tag{3.16a}$$

$$\chi_{\mathrm{mm}}^{yy} = \frac{\beta^2-\gamma^2}{4k_0^2}\frac{4\sin(\alpha x)}{\beta\cos(\alpha x)+\sqrt{\beta^2-\gamma^2}}, \tag{3.16b}$$

$$\chi_{\mathrm{em}}^{xy} = -\chi_{\mathrm{me}}^{yx} = \frac{2j}{k_0}\frac{\gamma\cos(\alpha x)}{\beta\cos(\alpha x)+\sqrt{\beta^2-\gamma^2}}, \tag{3.16c}$$

where $\beta = k_{z,\mathrm{i}} + k_{z,\mathrm{t}}$, $\gamma = k_{z,\mathrm{i}} - k_{z,\mathrm{t}}$ and $\alpha = k_{x,\mathrm{t}} - k_{x,\mathrm{i}}$. It can be easily verified that the bianisotropic refractive metasurface with the susceptibilities in (3.16) corresponds to a reciprocal, passive and lossless structure based on the conditions (2.13). As an illustration, the susceptibilities in (3.16) are plotted in Figs. 3.8 for the same incident and transmitted angles as in the previous sections, i.e. $\theta_\mathrm{i} = 20^\circ$ and $\theta_\mathrm{t} = 45^\circ$, respectively. Because χ_{ee}^{xx} and

[3]The reciprocity conditions given in (2.10) stipulate that $\chi_{\mathrm{em}}^{xy} = -\chi_{\mathrm{me}}^{yx}$.

χ_{mm}^{yy} are proportional to each other only the electric susceptibility is presented in Fig. 3.8a, similarly only χ_{em}^{xy} is plotted in Fig. 3.8b.

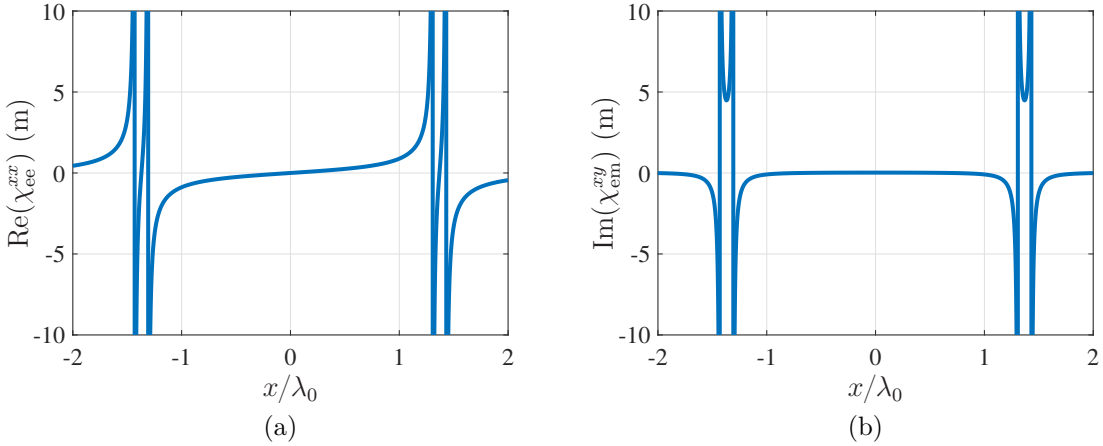

Figure 3.8 Bianisotropic refractive metasurface susceptibilities: (a) χ_{ee}^{xx} and (b) χ_{em}^{xy} for an incidence angle of $\theta_{\mathrm{i}} = 20°$ and a refraction angle of $\theta_{\mathrm{t}} = 45°$.

Now that the susceptibilities for bianisotropic refractive metasurfaces have been obtained, we are interested in their conversion into scattering parameters, which is a necessary step for the physical implementation of metasurfaces. The scattering parameters for a bianisotropic metasurface surrounded by vacuum, with susceptibilities as in (3.11) and for x-polarized waves are obtained from (2.27) and read

$$S_{21} = \frac{\chi_{\mathrm{ee}}^{xx}\chi_{\mathrm{mm}}^{yy}k_0^2 - (2j + \chi_{\mathrm{em}}^{xy}k_0)(2j + \chi_{\mathrm{me}}^{yx}k_0)}{2jk_0(\chi_{\mathrm{ee}}^{xx} + \chi_{\mathrm{mm}}^{yy}) + \chi_{\mathrm{em}}^{xy}\chi_{\mathrm{me}}^{yx}k_0^2 + 4 - \chi_{\mathrm{ee}}^{xx}\chi_{\mathrm{mm}}^{yy}k_0^2}, \tag{3.17a}$$

$$S_{12} = \frac{\chi_{\mathrm{ee}}^{xx}\chi_{\mathrm{mm}}^{yy}k_0^2 - (2j - \chi_{\mathrm{em}}^{xy}k_0)(2j - \chi_{\mathrm{me}}^{yx}k_0)}{2jk_0(\chi_{\mathrm{ee}}^{xx} + \chi_{\mathrm{mm}}^{yy}) + \chi_{\mathrm{em}}^{xy}\chi_{\mathrm{me}}^{yx}k_0^2 + 4 - \chi_{\mathrm{ee}}^{xx}\chi_{\mathrm{mm}}^{yy}k_0^2}, \tag{3.17b}$$

$$S_{11} = \frac{2jk_0\left(\chi_{\mathrm{mm}}^{yy} - \chi_{\mathrm{ee}}^{xx} + \chi_{\mathrm{me}}^{yx} - \chi_{\mathrm{em}}^{xy}\right)}{2jk_0\left(\chi_{\mathrm{ee}}^{xx} + \chi_{\mathrm{mm}}^{yy}\right) + \chi_{\mathrm{em}}^{xy}\chi_{\mathrm{me}}^{yx}k_0^2 + 4 - \chi_{\mathrm{ee}}^{xx}\chi_{\mathrm{mm}}^{yy}k_0^2}, \tag{3.17c}$$

$$S_{22} = \frac{2jk_0\left(\chi_{\mathrm{mm}}^{yy} - \chi_{\mathrm{ee}}^{xx} + \chi_{\mathrm{em}}^{xy} - \chi_{\mathrm{me}}^{yx}\right)}{2jk_0\left(\chi_{\mathrm{ee}}^{xx} + \chi_{\mathrm{mm}}^{yy}\right) + \chi_{\mathrm{em}}^{xy}\chi_{\mathrm{me}}^{yx}k_0^2 + 4 - \chi_{\mathrm{ee}}^{xx}\chi_{\mathrm{mm}}^{yy}k_0^2}. \tag{3.17d}$$

It is interesting to note that a bianisotropic metasurface has different reflection coefficients for its two sides, i.e. $S_{11} \neq S_{22}$, which is not the case of a monoanisotropic metasurface, as can be verified by setting to zero χ_{em}^{xy} and χ_{me}^{yx} in (3.17). The fact that $S_{11} \neq S_{22}$ means that bianisotropy is related to longitudinal asymmetry, i.e. the metasurface does not "look" the same from both sides. Thus, the scattering particles composing the metasurface will be required to present such kind of asymmetry. Now the scattering parameters corresponding to the bianisotropic refractive metasurface are obtained by inserting (3.16) into (3.17), which

leads to

$$S_{21} = S_{12} = \frac{jk_0\sqrt{\beta^2 - \gamma^2}}{jk_0\beta\cos(\alpha x) - (k_0^2 + k_{z,i}k_{z,t})\sin(\alpha x)}, \tag{3.18a}$$

$$S_{11} = \frac{jk_0\gamma\cos(\alpha x) + (k_0^2 - k_{z,i}k_{z,t})\sin(\alpha x)}{jk_0\beta\cos(\alpha x) - (k_0^2 + k_{z,i}k_{z,t})\sin(\alpha x)}, \tag{3.18b}$$

$$S_{22} = -\frac{jk_0\gamma\cos(\alpha x) - (k_0^2 - k_{z,i}k_{z,t})\sin(\alpha x)}{jk_0\beta\cos(\alpha x) - (k_0^2 + k_{z,i}k_{z,t})\sin(\alpha x)}. \tag{3.18c}$$

As expected, the metasurface scattering parameters are reciprocal ($S_{21} = S_{12}$) and the two reflection coefficients are different from each other ($S_{11} \neq S_{22}$). The scattering parameters in (3.18) are plotted for illustration in Figs. 3.9. As can be seen in Fig. 3.9a, the amplitudes

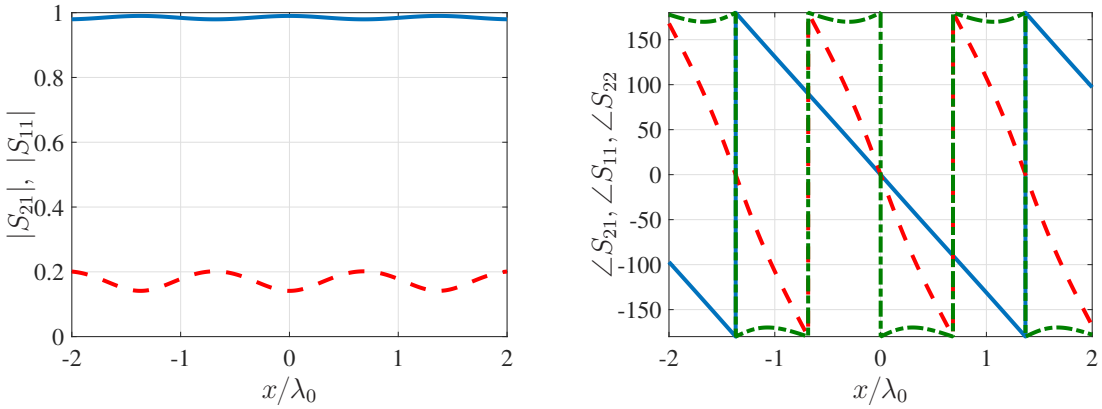

Figure 3.9 (a) Amplitude and (b) phase of the transmission $S_{21} = S_{12}$ (solid blue lines) and reflection S_{11} (dashed red lines) and S_{22} (dotted green line) coefficients from (3.18) for an incidence angle of $\theta_i = 20°$ and a refraction angle of $\theta_t = 45°$.

of both reflection coefficients are the same ($|S_{11}| = |S_{22}|$), hence the reason why only $|S_{11}|$ is displayed in the figure, and are not zero. Note that in Fig. 3.9a we have that $|S_{21}|^2 + |S_{11}|^2 = 1$, which, as expected, shows that the bianisotropic metasurface is lossless.

Finally, to close the loop, one may compare the scattering parameters in Figs. 3.2 to those in Figs. 3.9. As can be seen in Fig. 3.9a, the transmission coefficient is almost 1 like the one in Fig. 3.2b. Moreover, both transmission phases are the exactly the same. Therefore, the bianisotropic metasurface has almost the same scattering parameters as those of a monoanisotropic metasurface synthesized with the second method. In fact, if the reflection coefficient in Fig. 3.2a is ignored, these two metasurfaces would essentially behave identically. We now see that the second synthesis method, in addition to being easier to realize compared to the first method and to the bianisotropic one, also provides a very good response that is very

close to that of the bianisotropic structure, which is the best that is possible to achieve.

We have realized two different bianisotropic refractive metasurfaces to validate the results developed above. However, since this project involves several other people, the details are not reported here but may be found in [186].

3.4 Refractive Metasurfaces with Normal Susceptibility Components

Let us finally investigate a fourth metasurface synthesis approach to implement a refractive transformation. We consider the case of a monoanisotropic metasurface with nonzero normal susceptibilities. With the electromagnetic fields of the refractive transformation given by (3.3), the only relevant susceptibility components are

$$\overline{\overline{\chi}}_{\mathrm{ee}} = \begin{pmatrix} \chi_{\mathrm{ee}}^{xx} & 0 & \chi_{\mathrm{ee}}^{xz} \\ 0 & 0 & 0 \\ \chi_{\mathrm{ee}}^{zx} & 0 & \chi_{\mathrm{ee}}^{zz} \end{pmatrix}, \qquad \overline{\overline{\chi}}_{\mathrm{mm}} = \begin{pmatrix} 0 & 0 & 0 \\ 0 & \chi_{\mathrm{mm}}^{yy} & 0 \\ 0 & 0 & 0 \end{pmatrix}, \tag{3.19}$$

where the susceptibilities components that do not play a role in this transformation have been set to zero. As already explained in Sec. 2.5, normal susceptibility components involve the spatial derivatives in the GSTCs relations (2.4). The GSTCs thus form a system of coupled differential equations. In most cases, this system requires numerical analysis to be solved, however, in the particular case of a refractive metasurface, we can solve it analytically and obtain closed-form solutions of the susceptibilities. In this example, we also require the metasurface to be reciprocal, which, from (2.10), means that $\chi_{\mathrm{ee}}^{zx} = \chi_{\mathrm{ee}}^{xz}$.

Inserting (3.19) into (2.4) with $\chi_{\mathrm{ee}}^{zx} = \chi_{\mathrm{ee}}^{xz}$ leads, after simplification, to

$$\Delta H_y = -j\omega\epsilon_0(\chi_{\mathrm{ee}}^{xx} E_{x,\mathrm{av}} + \chi_{\mathrm{ee}}^{xz} E_{z,\mathrm{av}}), \tag{3.20a}$$

$$\Delta E_x = -j\omega\mu_0\chi_{\mathrm{mm}}^{yy} H_{y,\mathrm{av}} - \partial_x[\chi_{\mathrm{ee}}^{xz} E_{x,\mathrm{av}} + \chi_{\mathrm{ee}}^{zz} E_{z,\mathrm{av}}]. \tag{3.20b}$$

Similarly to the case of the bianisotropic metasurface discussed before, we have a system of 2 equations in 4 unknowns. In order to solve this system of equations, we proceed by considering 2 wave transformations, exactly as done in Figs. 3.7. This transforms (3.20) into

$$\Delta H_{y1} = -j\omega\epsilon_0(\chi_{\mathrm{ee}}^{xx}E_{x1,\mathrm{av}} + \chi_{\mathrm{ee}}^{xz}E_{z1,\mathrm{av}}), \tag{3.21a}$$

$$\Delta H_{y2} = -j\omega\epsilon_0(\chi_{\mathrm{ee}}^{xx}E_{x2,\mathrm{av}} + \chi_{\mathrm{ee}}^{xz}E_{z2,\mathrm{av}}), \tag{3.21b}$$

$$\Delta E_{x1} = -j\omega\mu_0\chi_{\mathrm{mm}}^{yy}H_{y1,\mathrm{av}} - \partial_x[\chi_{\mathrm{ee}}^{xz}E_{x1,\mathrm{av}} + \chi_{\mathrm{ee}}^{zz}E_{z1,\mathrm{av}}], \tag{3.21c}$$

$$\Delta E_{x2} = -j\omega\mu_0\chi_{\mathrm{mm}}^{yy}H_{y2,\mathrm{av}} - \partial_x[\chi_{\mathrm{ee}}^{xz}E_{x2,\mathrm{av}} + \chi_{\mathrm{ee}}^{zz}E_{z2,\mathrm{av}}]. \tag{3.21d}$$

We can now directly obtain χ_{ee}^{xx} and χ_{ee}^{xz} by linearly solving Eqs. (3.21a) and (3.21b). These susceptibilities are thus given by

$$\chi_{\mathrm{ee}}^{xx} = \frac{j}{\omega\epsilon_0}\frac{(\Delta H_{y,2}E_{z1,\mathrm{av}} - \Delta H_{y,1}E_{z2,\mathrm{av}})}{(E_{x2,\mathrm{av}}E_{z1,\mathrm{av}} - E_{x1,\mathrm{av}}E_{z2,\mathrm{av}})}, \tag{3.22a}$$

$$\chi_{\mathrm{ee}}^{xz} = \frac{j}{\omega\epsilon_0}\frac{(\Delta H_{y,1}E_{x2,\mathrm{av}} - \Delta H_{y,2}E_{x1,\mathrm{av}})}{(E_{x2,\mathrm{av}}E_{z1,\mathrm{av}} - E_{x1,\mathrm{av}}E_{z2,\mathrm{av}})}. \tag{3.22b}$$

In order to obtain the two remaining unknown susceptibilities, we start by expressing χ_{mm}^{yy} from (3.21d), which leads to

$$\chi_{\mathrm{mm}}^{yy} = -\frac{\Delta E_{x2} + \partial_x[\chi_{\mathrm{ee}}^{xz}E_{x2,\mathrm{av}} + \chi_{\mathrm{ee}}^{zz}E_{z2,\mathrm{av}}]}{j\omega\mu_0 H_{y2,\mathrm{av}}}. \tag{3.23}$$

Then, substituting (3.23) into (3.21c) gives the following differential equation in χ_{ee}^{zz}:

$$\begin{aligned}\left(\frac{H_{y1,\mathrm{av}}}{H_{y2,\mathrm{av}}}E_{z2,\mathrm{av}} - E_{z1,\mathrm{av}}\right)\partial_x\chi_{\mathrm{ee}}^{zz} + \left(\frac{H_{y1,\mathrm{av}}}{H_{y2,\mathrm{av}}}\partial_x E_{z2,\mathrm{av}} - \partial_x E_{z1,\mathrm{av}}\right)\chi_{\mathrm{ee}}^{zz} = \Delta E_{x1} \\ + \partial_x[\chi_{\mathrm{ee}}^{xz}E_{x1,\mathrm{av}}] - \Delta E_{x2}\frac{H_{y1,\mathrm{av}}}{H_{y2,\mathrm{av}}} - \partial_x[\chi_{\mathrm{ee}}^{xz}E_{x2,\mathrm{av}}]\frac{H_{y1,\mathrm{av}}}{H_{y2,\mathrm{av}}},\end{aligned} \tag{3.24}$$

where χ_{ee}^{xz} is known from (3.22b). Even though this differential equation is rather complicated, it is possible to obtain a closed-form solution in the case of a refractive transformation. Let us use the definition of the fields for the 2 wave transformations that are respectively given in (3.13) and (3.14) with $A_{\mathrm{i}} = A_{\mathrm{t}} = 1$. In that case, the resulting susceptibilities are given by

$$\chi_{\mathrm{ee}}^{xx} = 2\frac{k_{x,\mathrm{t}} - k_{x,\mathrm{i}}}{k_{x,\mathrm{i}}k_{z,\mathrm{t}} - k_{x,\mathrm{t}}k_{z,\mathrm{i}}}\tan\left(\frac{k_{x,\mathrm{i}} - k_{x,\mathrm{t}}}{2}x\right), \tag{3.25a}$$

$$\chi_{\mathrm{ee}}^{xz} = 2\frac{k_{z,\mathrm{t}} - k_{z,\mathrm{i}}}{k_{x,\mathrm{i}}k_{z,\mathrm{t}} - k_{x,\mathrm{t}}k_{z,\mathrm{i}}}\tan\left(\frac{k_{x,\mathrm{i}} - k_{x,\mathrm{t}}}{2}x\right), \tag{3.25b}$$

$$\chi_{\mathrm{ee}}^{zz} = \sec\left(\frac{k_{x,\mathrm{i}} - k_{x,\mathrm{t}}}{2}x\right)^2\left[C - 2x\frac{(k_{z,\mathrm{i}} - k_{z,\mathrm{t}})}{(k_{x,\mathrm{i}} + k_{x,\mathrm{t}})} - \frac{\sin[(k_{x,\mathrm{i}} - k_{x,\mathrm{t}})x](k_{z,\mathrm{i}}^2 - k_{z,\mathrm{t}}^2)}{(k_{x,\mathrm{i}} + k_{x,\mathrm{t}})(k_{x,\mathrm{i}}k_{z,\mathrm{t}} - k_{x,\mathrm{t}}k_{z,\mathrm{i}})}\right], \tag{3.25c}$$

$$\begin{aligned}\chi_{\mathrm{mm}}^{yy} = &-\frac{\sec\left(\frac{k_{x,\mathrm{i}}-k_{x,\mathrm{t}}}{2}x\right)^4}{4(k_{x,\mathrm{i}}+k_{x,\mathrm{t}})k_0^2}\Big\{2(k_{x,\mathrm{i}}^2-k_{x,\mathrm{i}}k_{x,\mathrm{t}}+k_{x,\mathrm{t}}^2)[C(k_{x,\mathrm{i}}+k_{x,\mathrm{t}})+2x(k_{z,\mathrm{t}}-k_{z,\mathrm{i}})]\\ &+2k_{x,\mathrm{i}}k_{x,\mathrm{t}}[C(k_{x,\mathrm{i}}+k_{x,\mathrm{t}})+2x(k_{z,\mathrm{t}}-k_{z,\mathrm{i}})]\cos[(k_{x,\mathrm{i}}-k_{x,\mathrm{t}})x]\\ &-(4k_{x,\mathrm{i}}k_{z,\mathrm{i}}-6k_{x,\mathrm{t}}k_{z,\mathrm{i}}-6k_{x,\mathrm{i}}k_{z,\mathrm{t}}+4k_{x,\mathrm{t}}k_{z,\mathrm{t}})\sin[(k_{x,\mathrm{i}}-k_{x,\mathrm{t}})x]\\ &+(k_{x,\mathrm{t}}k_{z,\mathrm{i}}+k_{x,\mathrm{i}}k_{z,\mathrm{t}})\sin[2(k_{x,\mathrm{i}}-k_{x,\mathrm{t}})x]\Big\},\end{aligned} \tag{3.25d}$$

where C is an integration constant. We see an unexpected result: the susceptibilities χ_{ee}^{zz} and χ_{mm}^{yy} are both linearly dependent on x. This is due to the fact that the 2 transformations in Figs. 3.7 are the reciprocal of each other and also to the integration operation required to solve (3.24). This result may a priori seem wrong and contradictory since the specified fields are plane waves while two of the resulting susceptibilities are linearly varying along x. However, the correct way to evaluate the interaction of an incident plane wave with a metasurface possessing the susceptibilities in (3.25) is through the GSTCs relations in (3.20). More specifically, the linear dependencies on x of the susceptibilities χ_{mm}^{yy} and χ_{ee}^{zz} cancel each other when inserted into (3.20b).

Using relations (2.13), we see that the metasurface is perfectly passive and lossless since the susceptibilities in (3.25) are purely real. This is unexpected since the electromagnetic fields were specified with $A_{\mathrm{i}} = A_{\mathrm{t}} = 1$, which means that the power flow through the metasurface is not conserved and thus that the efficiency is limited by relation (3.8). Therefore, we can assert that the susceptibilities in (3.25) are not physically consistent since energy conservation is not satisfied. Note that if the amplitude of the transmitted wave was increased so as to satisfy the conservation of power, as done in Sec. 3.3, then it can easily be shown that the metasurface becomes active. At this point, we have to conclude that, while the steps followed to obtain the result provided by relations (3.25) seem mathematically correct, the final susceptibilities are physically wrong. We can thus ask the question: is it physically possible to synthesize a refractive metasurface with normal susceptibility components? And if yes, what susceptibilities components should be considered?

3.5 Summary

In this chapter, we have applied several of the concepts that were first developed in Chapter 2. As a basis for the discussion, we have selected the particular topic of refractive metasurfaces, which provides a simple but nonetheless rich and insightful study case.

We have seen that a monoanisotropic metasurface can be synthesized rigorously, by specifying the exact fields, or approximatively, by specifying the scattering parameters. The rigorous synthesis method leads to a lossy design that performs the expected transformation with a

reduced transmission efficiency. The approximate synthesis method leads to a lossless design that presents undesired scattering but an overall better transmission efficiency. In terms of practical realization, the approximate synthesis method has the advantage of being easier to implement since it is lossless and exhibits a flat amplitude transmission.

Next, we have seen that the only way to synthesize a perfectly efficient refractive metasurface is by using bianisotropy. In that case, the metasurface is not only passive, lossless and reciprocal but it also presents a "pure" refractive transformation, i.e. without undesired scattering.

Finally, we have discussed the case of a monoanisotropic refractive metasurface with nonzero normal susceptibility components. We have realized that the resulting susceptibilities are not physically consistent, which casts doubt on whether or not it is possible to synthesize refractive metasurfaces with normal susceptibility components.

CHAPTER 4 Practical Realization & Measurement

In the two previous chapters, we have been interested in the mathematical description and synthesis of metasurfaces, which allow one to find the metasurface susceptibilities and corresponding scattering parameters from the specified electromagnetic transformation(s) given in terms of incident, reflected and transmitted fields. In this chapter[1], we will discuss the physical realization of metasurfaces, which is the second main step in the general framework of metasurface synthesis.

The conventional procedure to realize a metasurface, which is not trivial, may be decomposed into four main steps. Firstly, the metasurface susceptibilities are obtained from the initial specified fields. They are then usually simulated using commercial software or FDFD/FDTD codes to verify that they perform the expected transformation. In some cases, it is required to adjust the susceptibilities by changing the initial specified fields so as to achieve the most optimal transformation. Once the optimal susceptibilities are obtained, the corresponding scattering parameters are computed using (2.32) and (2.33), for birefringent metasurfaces, or (2.22) in a more general case.

Secondly, the scattering parameter functions (which are continuous functions) are spatially discretized using a square lattice in the xy-plane with subwavelength resolution and where each discrete point corresponds to a scattering particle (or unit cell) to be implemented. This step requires to either choose a specific unit cell size, which is generally in a range between $\lambda_0/2$ and $\lambda_0/10$, or to know a priori the lateral size of the unit cells, which may be the case when one has already a database of scattering particle responses[2]. In all cases, it is important that the unit cell lateral size be less than λ_0 to avoid generating undesired diffraction orders [159], ensuring the homogeneity of the metasurface and also properly sampling the scattering parameter functions according to the Nyquist criterion. Ideally, the smaller the unit cells, the better. But the smaller they are, the less the interact with the exciting field, which limits their minimum size to about $\lambda_0/10$. Below that limit, it is difficult to achieve resonance and thus the control of the electromagnetic field is limited because of the limited range of values that the metasurface material parameters may take.

Thirdly, full-wave simulations of unit cells, whose shapes will be discussed later, are performed using commercial software, which yield their scattering parameters. For each lattice site, the shapes of the unit cells are tuned until their scattering parameters match those found from

[1] This chapter is based on [151, 187].

[2] For instance, we have been using the same type of unit cell (with $\lambda_0/5$ lateral size) for several different metasurfaces.

the previous step. These simulations are done assuming periodic boundary conditions (PBC) even if the metasurface to be implemented is nonuniform (scattering parameters are varying functions of x and/or y). In this latter case, local periodicity is assumed meaning that the metasurface must exhibit slowly varying spatial features and that consequently the coupling between adjacent unit cells in the final structure is comparable to that in the perfectly periodic environment of the simulation software. However, when the metasurface exhibits very rapid spatial variations compared to the free-space wavelength, the assumption of local periodicity is not valid anymore and the coupling between adjacent unit cells may be very different when the unit cell is inserted into the final nonuniform metasurface compared to when it is simulated with PBC. In such a case, the electromagnetic response of the realized metasurface will not correspond to the expected result. Therefore, it is in general difficult (or even impossible) to realize metasurfaces with very rapid spatial variations compared to the size of the unit cells.

Finally, once all unit cells have been obtained from the full-wave simulations, one can simulate the entire structure (or only a part of it if the scattering parameters are periodic functions) to analyze the electromagnetic response of the metasurface. In most cases, the response will slightly differ from the expected result, which is likely to be due to the error induced because of the local periodicity assumption. In such a case, the unit cells may be further tuned via parametric analysis or standard optimization techniques to improve the response of the metasurface and achieve a better agreement with the initial specifications.

In the following two sections, we present two different unit cell structures that may be used to realize metasurfaces. The first one consists in cascaded metallic layers, while the second one is based on dielectric resonators.

4.1 Scattering Particles Based on Cascaded Metallic Layers

In this section, we present the design of unit cells based on cascaded metallic layers. It must be noted that the following developments are based on well known microwave theory concepts already used since the 1950s, notably for the implementation of frequency selective surfaces (FSS) [32]. More recently, these concepts have been adopted for the realization of metasurfaces [85, 133, 134, 146, 188–190] and they are concisely reported here for the sake of completeness of this work.

Most metasurfaces designed to be used in the microwave regime are composed of one or several layers of metallic patterns separated by dielectric substrates. This technology may also be considered at optical frequencies but the additional plasmonic loss due to the metallic parts

as well as the complexity of fabrication make it less attractive compared to other alternatives like the fully dielectric unit cell structure that will be discussed in the next section. The condition, to be able to realize a fully functional metasurface, is that its unit cell scattering parameters cover a 2π-phase range while being able to maintain a constant transmission (or reflection) amplitude, which is usually equal to 1 to maximize efficiency. However, it was shown that metasurfaces using one single metallic layer cannot fundamentally achieve full transmission and 2π-phase coverage [148]. This limitation is due to the limited number of degrees of freedom that are provided by a single-layer structure. It naturally follows that increasing the number of metallic layers increases the number of degrees of freedom, which may contribute to improve the bandwidth as well as the achievable transmission or reflection phase coverage. A remarkable and important case is that of a three metallic layer structure, and more specifically the particular case where the two outer layers are the same. This three-layer structure is the simplest one that provides a full transmission and a 2π-phase coverage[3] [85, 133, 134, 146, 188–190]. This kind of structure is symmetric with respect to the longitudinal direction and is therefore limited to the implementation of monoanisotropic metasurfaces. A unit cell with three different layers would be asymmetric and thus would allow the realization of bianisotropic metasurfaces, as discussed in Sec. 3.3, at the cost of a more complicated design. Note that the overall thickness of the three-layer structure remains deeply subwavelength. For most practical applications, this kind of three metallic layer structure is sufficient but more layers may be considered as a mean to increase the bandwidth [32] at the cost of extra loss, weight and implementation complexity.

It can be easily verified, using microwave theory concepts, that cascading three metallic layers (with similar outer layers) is sufficient to realize a transmission coefficient of $0 \leqslant |T| \leqslant 1$ with a 2π-phase coverage. For a given polarization, each metallic layer can be described by an impedance layer and each of the two dielectric spacers by an equivalent transmission line. The entire structure can then be analyzed using the ABCD matrix technique [191] as such

$$\begin{pmatrix} A & B \\ C & D \end{pmatrix} = \begin{pmatrix} 1 & 0 \\ Y_1 & 1 \end{pmatrix} \cdot \begin{pmatrix} \cos(\beta d) & j\eta_d \sin(\beta d) \\ \frac{j\sin(\beta d)}{\eta_d} & \cos(\beta d) \end{pmatrix} \cdot \begin{pmatrix} 1 & 0 \\ Y_2 & 1 \end{pmatrix} \cdot \begin{pmatrix} \cos(\beta d) & j\eta_d \sin(\beta d) \\ \frac{j\sin(\beta d)}{\eta_d} & \cos(\beta d) \end{pmatrix} \cdot \begin{pmatrix} 1 & 0 \\ Y_1 & 1 \end{pmatrix}, \tag{4.1}$$

where β is the propagation constant along the z-direction and d and η_d are the thickness and the impedance of the dielectric substrates, respectively. The terms Y_1 and Y_2 correspond to the admittances of the outer layers and the middle layer, respectively. Finally, the ABCD

[3] Similar considerations naturally apply for the reflection coefficient if the metasurface is used in reflection.

matrix (4.1) can be converted into scattering parameters using the following relation [191]

$$\begin{pmatrix} S_{11} & S_{12} \\ S_{21} & S_{22} \end{pmatrix} = \frac{1}{2A + B/\eta_0 + C\eta_0} \begin{pmatrix} B/\eta_0 - C\eta_0 & 2 \\ 2 & B/\eta_0 - C\eta_0 \end{pmatrix}. \tag{4.2}$$

To illustrate how the transmission coefficient, S_{21}, changes as function of Y_1 and Y_2, we plot it in Figs. 4.1. These two figures are obtained by substituting (4.1) into (4.2) and plotting the amplitude and phase of S_{21} versus the imaginary parts of Y_1 and Y_2 for arbitrary values of β, η_d and d. We assume here that the unit cell is perfectly lossless and passive, thus $\mathrm{Re}(Y_1) = \mathrm{Re}(Y_2) = 0$. These figures reveal that it is possible to cover a 2π-phase range while maintaining full transmission (see the solid black line in the two figures).

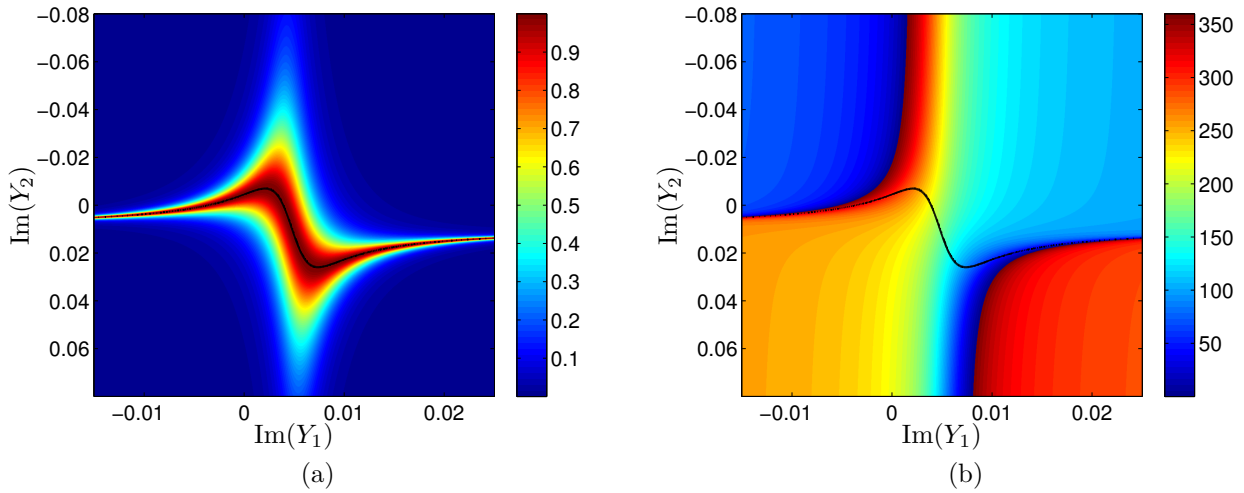

Figure 4.1 (a) Transmitted power ($|S_{21}|^2$) and (b) phase for the three cascaded metallic layers versus the imaginary parts of the impedance of Y_1 and Y_2. The black line indicates that full transmission can be achieved and that the corresponding phase varies between 0 and 2π.

The question that arises now is what kind of shape should the metallic layers have to realize the unit cells? There are several different shapes that have been investigated over time [32] but the one we have used for the vast majority of our metasurfaces is the Jerusalem cross. A generic Jerusalem cross with all its tunable dimensions is shown in Fig. 4.2a, while an illustration of a unit cell made with three cascaded crosses is shown in Fig. 4.2b.

The characteristic shape of the Jerusalem cross provides a relatively independent control of x and y polarizations, which simplifies the realization of the scattering particles. More specifically, the independent control of both x and y polarization is achieved by considering that tuning the parameters B_x, W_x and L_y mostly affects y-polarized waves and, parameters B_y, W_y and L_x mostly affects x-polarized waves. With this kind of shape, there is an

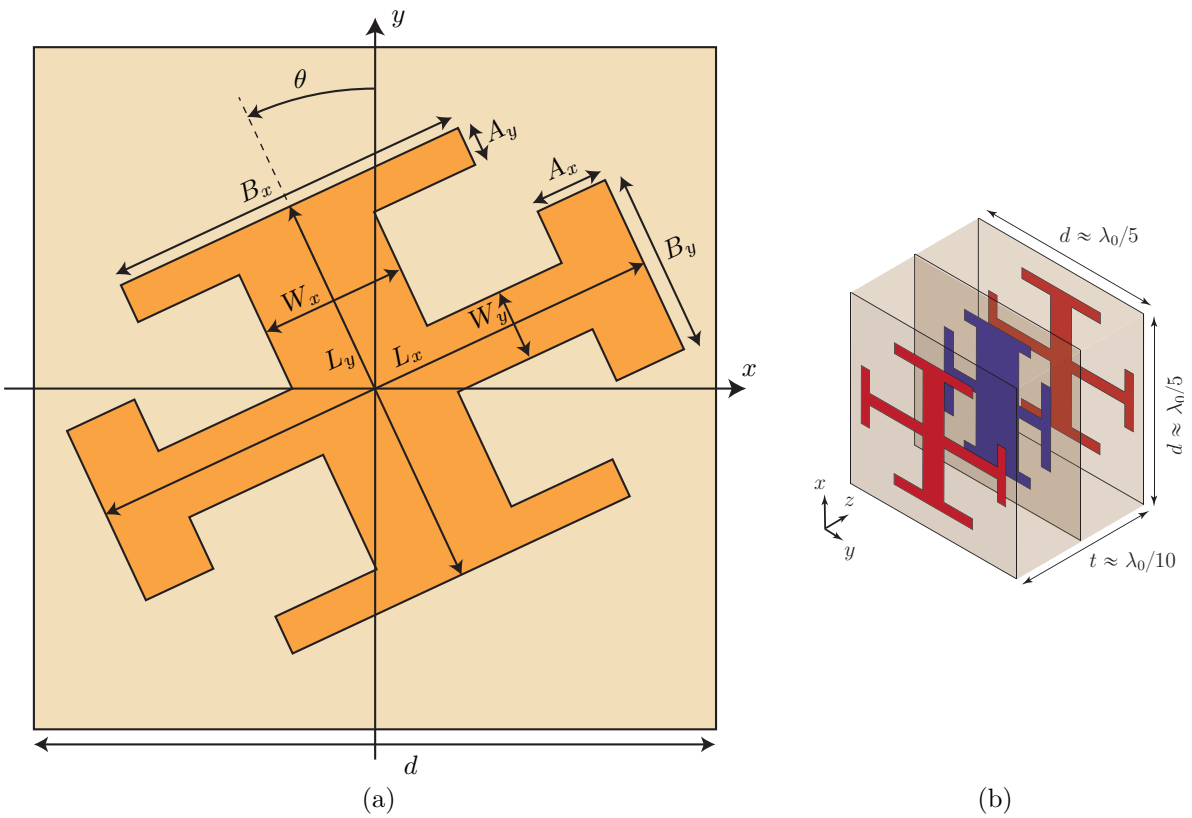

Figure 4.2 Representations of (a) a generic Jerusalem cross with the dimensions that can be modified. (b) A unit cell with three metallic (PEC) Jerusalem crosses separated by dielectric slabs, the outer layers are identical.

important capacitive coupling between adjacent unit cells. This coupling has the effect of increasing the response of the scattering particles, thus enabling the implementation of unit cells with smaller transverse and longitudinal dimensions with respect to the operating wavelength [32, 192]. However, this comes at the cost of a more complex structure to realize due to the large number of tunable parameters. The coupling between adjacent unit cells also has the disadvantage of making the implementation of nonuniform metasurfaces more difficult because the overall response of the metasurface is more sensitive to the variations of shape of adjacent unit cells.

We are now interested in finding the exact dimensions, shown in Fig. 4.2a, of the Jerusalem cross of the outer and middle layers, to which we will now refer to as layers 1 and 2, respectively. There are two main methods that are considered here to design these layers. The first method consists in inserting the required scattering parameters found from the synthesis into Eqs. (4.1) and (4.2) and solving these relations so as to obtain the corresponding required admittance of each layer.

However, even if it is possible to obtain the admittance of each individual layer, there is unfortunately no direct and analytical method to relate the dimensions of layers 1 and 2 to the admittances Y_1 and Y_2. The conventional method consists in simulating each layer *individually* using PBC to obtain its corresponding scattering parameters. From the simulated scattering parameters, the corresponding admittance of the layer can be found using (4.2) with $[A, B; C, D] = [1, 0; Y, 1]$ and solving for Y. Then, by iterative tuning, the Jerusalem cross dimensions are modified until the layer admittance matches the required one found from the previous steps. While this method is useful because it simplifies the realization of the unit cells by allowing one to design each layer separately, it is rigorous *only* in absence of longitudinal evanescent coupling between the metallic layers since the ABCD matrix method only takes into account zeroth-order propagating waves[4]. And, unfortunately, the unit cell total thickness is in the order of $\lambda_0/10$, which means that the longitudinal coupling between the layers is non-negligible. Nevertheless, this method may still be used to obtain an initial structure, which would then require further numerical optimizations to achieve the specified response.

In order to evaluate the effect of coupling between the metallic layers, we have compared the error between the scattering parameters obtained from simulations of the entire three-layer unit cells and the scattering parameters obtained by first simulating each layer individually (to obtain admittances Y_1 and Y_2) and then combining them together using Eqs. (4.1) and (4.2) to obtain the overall scattering parameters of the three layer structure. This error is computed from the difference between the scattering parameters of these two methods obtained from thousands of simulations. The corresponding normalized mean error is plotted in Fig. 4.3 versus the total unit cell thickness which ranges between $\lambda_0/10$ and $10\lambda_0$ and for three different relative permittivity of commercially available dielectric substrates ($\epsilon_r = 3,\ 6.15$ and 10.2). The results in Fig. 4.3 reveal that the error due to the coupling may generally be lowered by decreasing the relative permittivity of the dielectric substrate and/or by increasing its thickness.

Instead of trying to realize the unit cells by using the admittances of individual layers, we may alternatively consider another method, which consists in simulating the entire three-layer structure and tuning the dimensions of the layers until the required scattering parameters, found from the synthesis, are obtained. From an electromagnetic perspective, we can consider that the interactions between the exciting wave and the three metallic layers generate equivalent electric and magnetic responses. In the frequency range of interest, the unit cell is small compared to the wavelength and thus only presents dipolar electric and magnetic re-

[4]Higher diffraction orders or evanescent waves are not considered in the ABCD method.

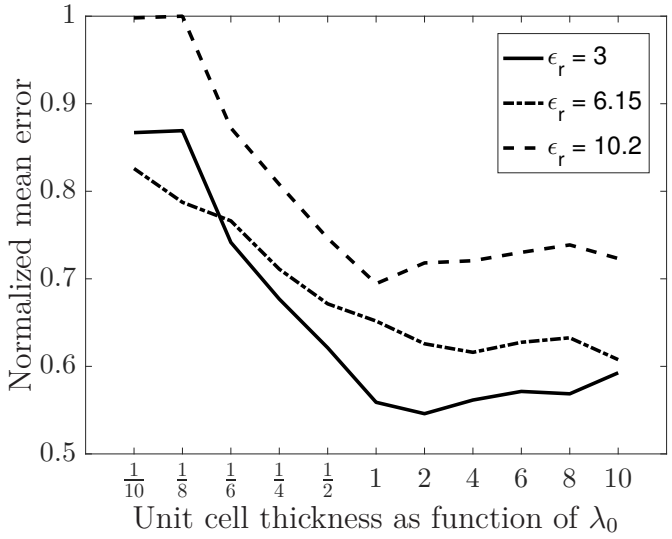

Figure 4.3 Normalized mean error between scattering parameters obtained by simulating entire three-layer unit cells and scattering parameters obtained by simulating each layer individually. The error is given versus the unit cell thickness and the relative permittivity of commercially available dielectric substrates.

sonances. Higher-order multipolar resonances occur at higher frequencies where the unit cell size approaches that of the wavelength. Thus, the metasurface can be seen as an equivalent array of electric and magnetic dipole moments. The complete control of the transmission amplitude and phase that the unit cell provides is achieved by the superposition of the fields scattered by the electric and magnetic dipolar resonances, as formulated in (2.80). In the case of the three-layer unit cell, the structure is symmetric in the longitudinal direction. We can thus analyze the behavior of the structure using even/odd mode analysis. The odd mode resonance is achieved when the surface currents induced by the incident wave are equal and opposite on the outer layers. In that case, the total current is zero on the middle layer. Such a current distribution corresponds to an equivalent magnetic dipole moment. Since the current is null on the middle layer, this layer does not play a role in the magnetic response of the structure [133]. The even mode resonance is achieved when the same current distribution is excited on the three layers, thus corresponding to an equivalent electric dipole moment. Practically speaking, this means that layers 1 are modified first, to tune the magnetic response, and then layer 2 is modified to adjust the electric response of the structure. Usually, a few optimization iterations are required to design one unit cell.

We will now illustrate the effects of changing the physical dimensions of layers 1 and 2 on the unit cell scattering parameters. For this purpose, we consider a unit cell whose dimensions correspond to those of "Cell 3" that are provided in Table 5.4. To see how changing layers 1

and 2 affects the scattering parameters of this unit cell, we perform three different simulations whose results are reported in Figs. 4.4. The first simulation is performed with the exact same

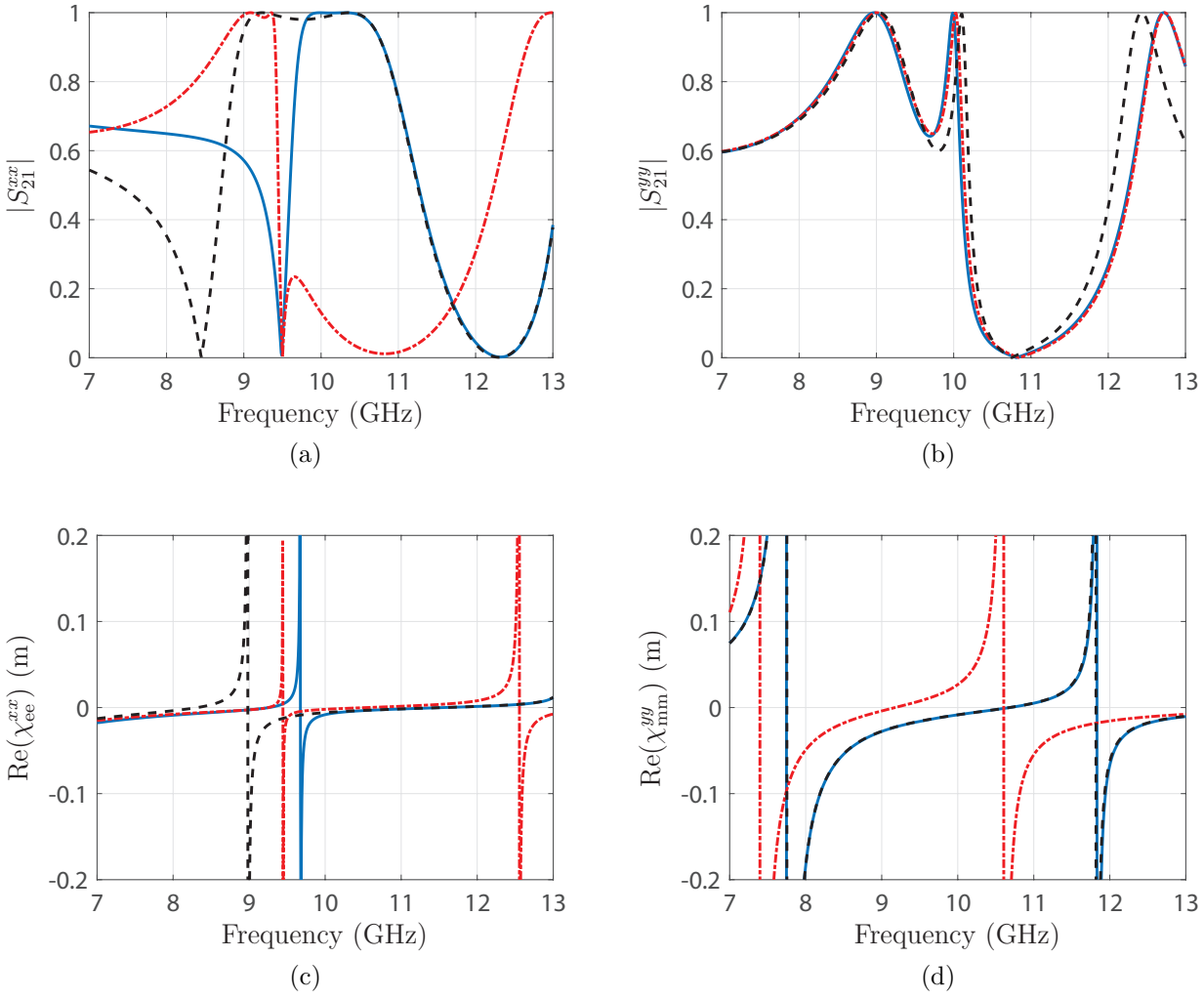

Figure 4.4 CST simulations of three different unit cells. The solid blue lines correspond to the simulations of "Cell 3", whose dimensions are given in Table 5.4. The plots (a) and (b) correspond to the amplitude of S_{21}^{xx} and S_{21}^{yy}, respectively. The plots (c) and (d) are the real parts of χ_{ee}^{xx} and χ_{mm}^{yy}, respectively. For the dotted red lines, L_x of layers 1 is change to 5 mm. For the dashed black lines, L_x of layer 2 is change to 4.4 mm.

dimensions as those in Table 5.4, and the corresponding results are plotted in solid blue lines in the figures. For the second simulation, the dimensions L_x of the layers 1 are increased from 4.25 mm to 5 mm, the corresponding results are plotted in dotted red lines in the figures. For the third simulation, the dimension L_x of layer 2 is increased from 3.75 mm to 4.4 mm, the corresponding results are plotted in dashed black lines in the figures.

We expect that these variations of dimensions will mostly affect the x-polarized transmission

coefficient, S_{21}^{xx}, while leaving unchanged the y-polarized transmission coefficient, S_{21}^{yy}. The amplitudes of these scattering parameters are plotted in Figs. 4.4a and 4.4b, respectively. We see that the scattering parameters of this unit cell, which was originally realized to exhibit full transmission ($|S_{21}^{xx}| \approx |S_{21}^{yy}| \approx 1$) at 10 GHz, have experienced very different variations. As expected, the parameter S_{21}^{xx} has drastically changed, while the parameter S_{21}^{yy} remains almost unaffected over the selected frequency range. To reveal the effects of these dimensional changes on the electric and magnetic responses of the unit cell, we convert the scattering parameters in Fig. 4.4a into the corresponding electric and magnetic susceptibilities using relations (2.31a) and (2.31d). For the three simulations, the resulting real parts of χ_{ee}^{xx} are plotted in Fig. 4.4c, while the real parts of χ_{mm}^{yy} are plotted in Fig 4.4d. We clearly see that changing layers 1 has a strong effect on the magnetic resonance and a non-negligible effect on the electric resonance (see the red dotted lines). On the other hand, changing layer 2 only affects the electric resonance, which is expected due to the longitudinal symmetry of the structure. In both cases, we have increased the dimensions L_x of the middle and outer layers, which translates in an increase of the capacitive coupling between adjacent unit cells and thus a decreases in the corresponding electric and/or magnetic resonance frequency.

Most of the metasurfaces made with metallic scattering particles that will be presented in Chapter 5 have been realized for an operating frequency around 10 GHz. At this frequency, the transverse dimension of the unit cell is $d = 6$ mm ($\approx \lambda_0/5$). For the fabrication, we are using a commercially available dielectric substrate: Rogers RO3003 with a relative permittivity of $\epsilon_r = 3$ and a loss tangent of $\tan\delta = 0.001$. The unit cells are made by gluing together two substrates with a thickness of 1.52 mm each, leading to an overall metasurface thickness of 3.04 mm ($\approx \lambda_0/10$). For the gluing process, we use a 3M 9458 adhesive tape with an approximate thickness of 25,4 micrometers and a relative permittivity of 3 that is deposited on one of the two dielectric substrates. Then, the substrates are pressed together for about 30 minutes at a temperature of 40° C. Note that, due to the very approximate thickness and permittivity of the glue, it is not taken into account in the numerical simulations of the unit cells.

4.2 Scattering Particles Based on Dielectric Resonators

In addition to the aforementioned metallic unit cells, the realization of the metasurface scattering particles may be achieved by considering purely dielectric resonators without any metallic part. As previously discussed, one essential requirement to achieve full transmission (or reflection) and a 2π-phase coverage, is the presence of both electric and magnetic resonances, which are naturally occurring in dielectric resonators [193, 194]. For this rea-

son, dielectric resonators have been widely used to realize metasurfaces [115, 116, 195, 196]. A dielectric metasurface is, as before, a uniform (or nonuniform) two-dimensional array of dielectric resonators, where the thickness of the metasurface and the period of the unit cells in the array are both subwavelength.

Dielectric unit cells are particularly attractive in the optical regime, where they are more easily realizable compared to the cascaded metallic layer structure discussed above and also exhibit no plasmonic loss thanks to the absence of metallic inclusions. A typical unit cell is shown in Fig. 4.5a where the resonator is a dielectric cylinder of circular cross section with permittivity $\epsilon_{r,1}$ placed on a dielectric slab with permittivity $\epsilon_{r,2}$ (usually silica) for mechanical support [118, 196–199]. Other types of particle shapes are naturally also possible. This

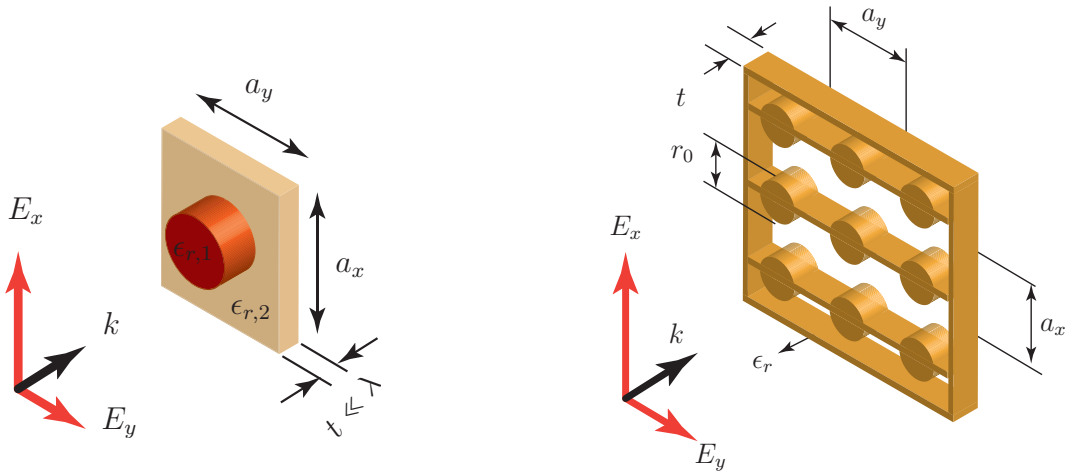

Figure 4.5 Representations of two dielectric metasurface unit cell designs. In (a), the conventional optical regime design, where a dielectric resonator of permittivity $\epsilon_{r,1}$ is placed on a dielectric substrate of permittivity $\epsilon_{r,2}$. In (b), our unit cell design for the microwave region, where the resonators are held together by dielectric connections.

includes 90°-symmetric shapes like squares, which (like cylinders) present the same behavior for x- and y-polarized waves. But also 90°-asymmetric shapes, such as ellipses and rectangles, which allow a complete and independent control of the two orthogonal polarizations [116]. An additional advantage of dielectric unit cells is that they have much less physical parameters to adjust compared to the Jerusalem cross, which effectively simplifies the optimization procedure to achieve a specified response but comes at the cost of less degrees of freedom.

We have also proposed an alternative implementation of dielectric metasurfaces, which is designed to be used in the microwave regime [200, 201]. In the proposed design, the resonators are not placed on a substrate, they are rather held together with dielectric connections, as

depicted in Fig. 4.5b. This design has the advantage of being easy to fabricate since the fabrication process essentially consists in laser cutting a pattern mask. An additional advantage of this structure is that it is immune to the presence of multiple reflections occurring inside the supporting slab, as it is the case of the structure in Fig. 4.5a. In general and for simplicity, we assume that all resonators have the same thickness, which can be achieved by gluing together several slabs of commercially available dielectric substrates. The gluing process is the same as the one explained in the previous section. An example of such structure is depicted in Fig. 4.6, which shows a fabricated metasurface made of several patterned dielectric slabs. The disadvantage of the dielectric connections is that they affect the elec-

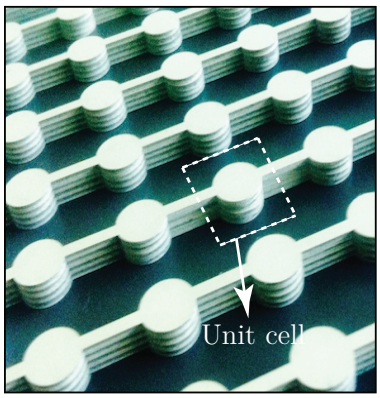

Figure 4.6 Example of a fabricated dielectric metasurface with interconnected resonators made of four stacked dielectric slabs glued together.

tromagnetic behavior of the resonators. In order to minimize these effects, these connections are made very small with respect to the operating wavelength. In that case, their presence has negligible effect on the polarization that is orthogonal to them, e.g. E_x in Fig. 4.5b. However, their effects on the polarization that is parallel to them cannot be ignored but can be compensated by numerical optimizations.

For both structures in Figs. 4.5, the physical dimensions of the unit cells are obtained using the same approach as for the cascaded metallic layer structure discussed above. Each unit cell is simulated assuming PBC. Its dimensions are tuned until the desired scattering parameters are obtained, which in general requires a few optimization iterations.

The various advantages of dielectric metasurfaces may play an important role in the development of metasurfaces designed to work at multiple frequencies or over extended frequency bands. Traditionally, the bandwidth of transmit arrays or FSS may be increased by cascading several layers [32] at the cost of having thicker, more complex and more lossy structures. A potential alternative lies in the use of highly coupled dielectric resonators, which are easier to design and less lossy compared to metallic structures. The idea consists in placing resonating

particles close to each other so as to increase mutual coupling and consequently generate new resonant frequencies. Thus, the coupling between the resonators can be used as an additional degree of freedom to tune the frequency response of metasurfaces [112].

A disadvantage of dielectric resonators is that, to achieve a small unit cell lateral size and thickness, a high difference between the dielectric permittivity of the particle and that of the surrounding medium is required. This means that metasurfaces with rapid spatial variations compared to the free-space wavelength can only be realized using high permittivity resonators, which may not be easily available. As a comparison, the lateral size and thickness of the metallic unit cells used in this work are about $\lambda_0/5$ and $\lambda_0/10$, respectively; while the dielectric unit cell counterparts are about $\lambda_0/1.1$ and $\lambda_0/3.3$, respectively, for resonators of relative permittivity $\epsilon_r = 10.2$ surrounded by air.

4.3 Measurement Setup

In order to measure the responses of metasurfaces, we use the home-made measurement setup that is show in Fig. 4.7. It consists of a rotating arm used to attach the exciting horn antenna. The arm can rotate from $-90°$ to $90°$ around the center where the metasurface is

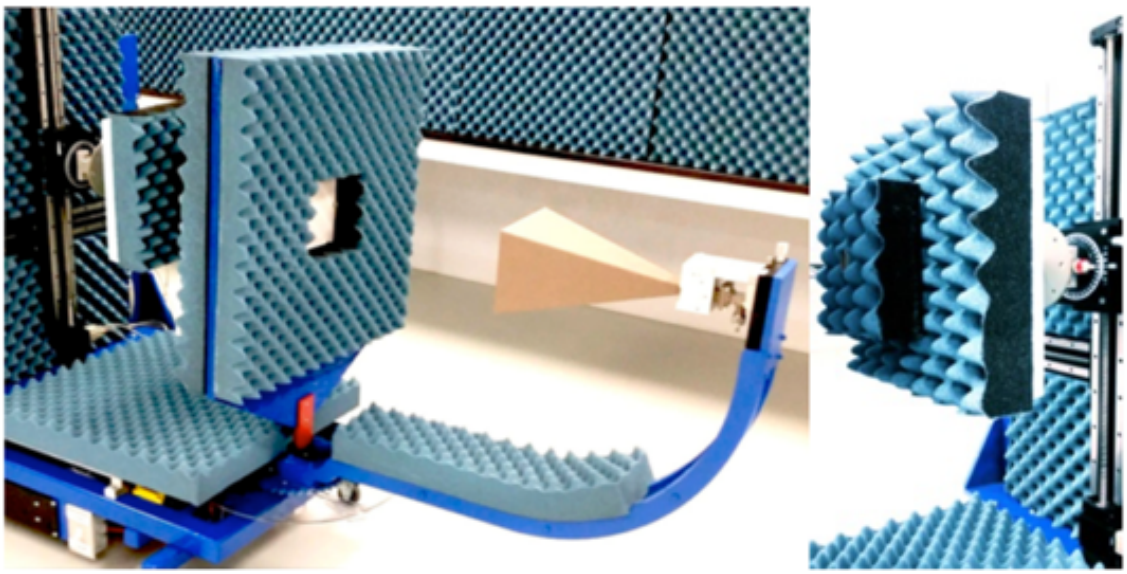

Figure 4.7 Metasurface measurement setup. The photograph on the left shows the rotating arm with a horn antenna, the metasurface holder with a metasurface in the middle and, on the left-hand side, we see the three-axis stage. The photograph on the right is a close-up view of the scanning waveguide probe mounted on the three-axis stage with absorbers to reduce scattering from metallic parts.

placed. The arm is long enough so that the metasurface lies in the far-field of the antenna.

The metasurface holder is covered with microwave absorbers at the exception of a small aperture in the center where the metasurface is screwed, with plastic screws, to a plastic frame. On the other side of the setup, a three-axis (x, y and z) stage allows a waveguide probe to scan the entire space in the transmit side of the metasurface. Additionally, the exciting antenna and the scanning probe are both attach onto rotary stages that allow an easy control of the transmitter and receiver polarizations, respectively. The measurements are performed by scanning with a waveguide probe rather than simply measuring the line-of-sight scattering parameters with two conventional antennas because most metasurfaces that have been realized are nonuniform and thus change the direction of wave propagation. Scanning the transmit side of the metasurface thus allows one to effectively obtain all important information about the transmitted waves directions of propagation, amplitude, phase and polarizations through plane wave expansion methods [202, 203]. Note that the waveguide probe, that is used to measure the transmitted field, has a specific directivity. It is generally recommended to compensate for the effect of the waveguide probe transfer function, which distorts the measured fields. In most cases, it is possible to use probe corrections techniques that are notably detailed in [203][5]

The rotating arm as well as the three-axis stage are both connected to a vector network analyzer (VNA) that measures the scattering from the metasurface. The motions of the rotating arm and the three-axis stage are controlled with an home-made Visual Basic software that is also connected to the VNA to acquire data. The overall measurement process is completely automatic.

Note that all metasurfaces that will be presented in the next chapter have been measured with this measurement setup.

4.4 Summary

In this chapter, we have first discussed the physical realization of metasurfaces. We propose two main methods to implement the scattering particles. The first one consists in using metallic unit cells made by cascading metallic layers, which have the shape of Jerusalem crosses. The second on consists in using dielectric resonators which typically take the shape of cylinders with elliptical cross section. In both cases, the metasurface can be seen as an array of electric and magnetic dipole moments. Finding the exact shape of the unit cells thus requires controlling the resonance frequencies of both the electric and magnetic resonances so that the unit cell exhibits the required reflection/transmission amplitude and phase. This

[5] See section 17.2.4B.

is achieved by iterative full-wave simulations and optimizations.

Finally, we have described the metasurface measurement setup. Since most metasurfaces, that will be presented in the next chapter, are changing the direction of wave propagation, a simple line-of-sight measurement is not sufficient to properly investigate the scattering behavior of these structures. Consequently, we measure the near-field on a plane on the transmit side of the metasurface using a waveguide probe. This provides an accurate evaluation of the scattering response of these metasurfaces.

CHAPTER 5 Advanced Concepts and Applications

In this chapter, we present several metasurface concepts and applications that have been realized or investigated during the course of this PhD program. The metasurfaces presented here have been synthesized and realized using the synthesis framework developed from Chapter 2 to Chapter 4, which are themselves based on previously published works [128, 151, 187].

We will start by discussing the implementation of dielectric metasurfaces for temporal dispersion engineering [200, 201]. Then, birefringent metasurfaces [204, 205], able to independently control orthogonally polarized waves, will be presented [187, 206]. Different birefringent wave transformers are proposed which include: a half-wave plate [115, 207, 208], a quarter-wave plate [209, 210], a polarization beam splitter [211–213] and an orbital angular momentum [66, 84, 85, 214, 215] generator. These different operations are illustrated in Figs. 5.1.

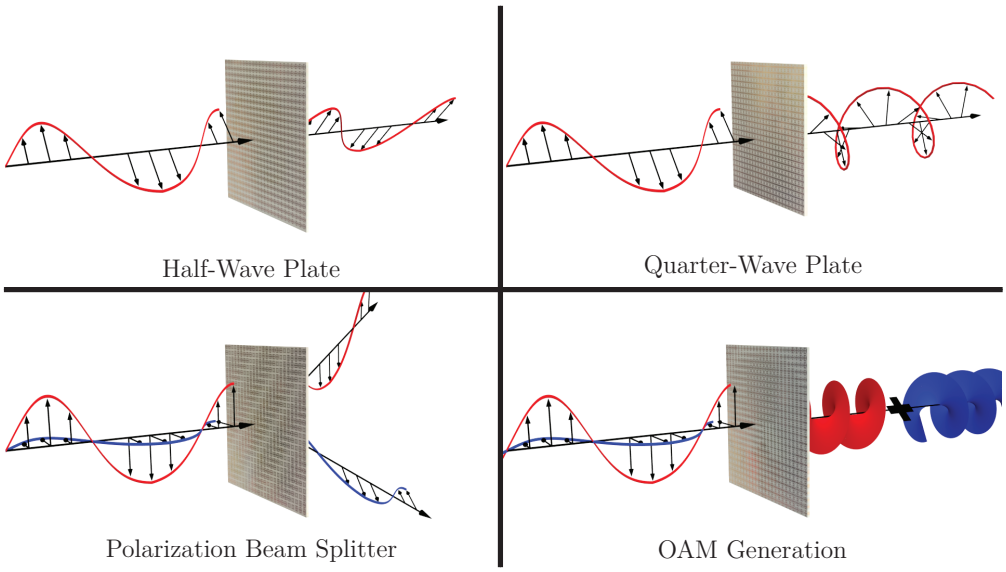

Figure 5.1 Illustrations of some birefringent metasurface transformations.

We next present the implementations of two coherent spatial processors [216, 217] and of a metasurface system that transforms space waves into surface waves [218, 219]. The mathematical synthesis of a nonreciprocal and nongyrotropic metasurface is also discussed [220, 221] and the conceptual emission enhancement of light-emitting diodes (LEDs) is briefly addressed [2, 222]. Finally, we will investigate the capabilities of metasurfaces to control radiation pressure in order produce repulsive, attractive lateral and rotational optical forces.

5.1 Temporal Dispersion Engineering

Dispersion engineering consists in manipulating the temporal content of time-domain signals and thus requires the capability to control the frequency response of materials or systems [223]. A direct application of dispersion engineering is real-time analog signal processing (R-ASP) [224]. A typical example of a R-ASP system is that of phasers [225], which are integrated guided-wave components. Metasurfaces performing real-time signal processing could therefore be the spatial counterparts of integrated phaser [151, 200, 201][1]. For such an application, the metasurface should exhibit a broadband flat transmission amplitude (ideally close to full-transmission) and a controllable frequency-dependent phase response or, equivalently, a frequency-dependent group delay[2]. The idea of using metasurfaces for dispersion engineering stems from the recent developments of broadband metasurfaces able to perform, for instance, broadband: wavefront manipulations [89], dispersion compensation [118, 226], matching [227] and quarter and half-wave operations [228, 229].

Here, we propose the concept of a broadband all-dielectric metasurface for real-time analog signal processing, as discussed in [151,200,201], which is implemented in the microwave region using the design approach discussed in Sec. 4.2. This concept is inspired by previous works on all-dielectric metasurfaces in the optical regime [115, 118, 196–199, 230–233].

From the discussion in Sec. 4.2, we know that dielectric resonators exhibit both electric and magnetic resonances. In general, these two resonances do not occur at the same frequency and the overall response of the dielectric resonator metasurface is not broadband, as will be shown shortly. However, by varying the physical dimensions of the resonators as well as the ratio between the relative permittivity of the resonators and that of the surrounding medium, it is possible to tune these resonances so that they occur at the same frequency. In which case, if the two resonances have the same strength and dispersion and are associated with orthogonal dipole moments in the transverse plane of the metasurface, reflection may be totally suppressed. This is due to perfect destructive interference of the waves scattered by the electric and magnetic resonances in the incident side of the metasurface, and their constructive interference at the transmit side of it [194]. In this case, if lossless material is considered, the transmission is theoretically 100% and flat over a wide bandwidth. Moreover, the transmission phase covers a full 2π range around the resonance frequency. It must be noted that, in general, the electric and magnetic resonances have different dispersions [227], which leads to non-ideal constructive/destructive interferences on both sides of the metasur-

[1] This section is based on a slight modified version of [201].

[2] The group delay is defined as $\tau = -\partial\phi(\omega)/\partial\omega$, where $\phi(\omega)$ is the transmission phase-shift across the metasurface.

face and thus the transmission amplitude is not perfectly flat over the bandwidth of interest. If the dielectric loss of the resonators is neglected, this small variation in transmission does not drop below -2 dB, as can be seen in Fig. 5.2, which represents the transmission, reflection and group delay responses of a typical broadband dielectric metasurface tuned such that its electric and magnetic resonances occur at around the same frequency.

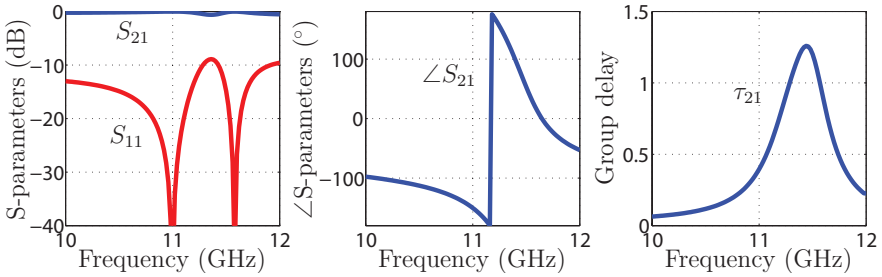

Figure 5.2 Rigorous coupled wave analysis (RCWA) of a typical broadband dielectric metasurface. The plots show the transmission and reflection coefficients as well as the transmission phase and the transmission group delay, respectively.

5.1.1 Matched Dispersion Response

We now investigate the frequency response of broadband metasurfaces by considering that its electric and magnetic resonances can be modeled using a Lorentzian model [159]. For the purpose of this study, we assume that the metasurface is made of a uniform array of isotropic dielectric resonators and without dielectric connections used for mechanical support. In that case, a normally incident plane wave impinging on the metasurface is normally reflected and transmitted with reflection and transmission coefficients, as obtained in (2.32), which are

$$R(\omega) = \frac{2jk_0\left(\chi_{\mathrm{mm}}(\omega) - \chi_{\mathrm{ee}}(\omega)\right)}{\left(2 + jk_0\chi_{\mathrm{ee}}(\omega)\right)\left(2 + jk_0\chi_{\mathrm{mm}}(\omega)\right)}, \tag{5.1a}$$

$$T(\omega) = \frac{4 + \chi_{\mathrm{ee}}(\omega)\chi_{\mathrm{mm}}(\omega)k_0^2}{(2 + jk_0\chi_{\mathrm{ee}}(\omega))(2 + jk_0\chi_{\mathrm{mm}}(\omega))}, \tag{5.1b}$$

where $\chi_{\mathrm{ee}}(\omega)$ and $\chi_{\mathrm{mm}}(\omega)$ are the frequency-dependent electric and magnetic susceptibilities, respectively, and k_0 is the free-space wavenumber. From (5.1a), we know that the metasurface is reflectionless if $\chi_{\mathrm{mm}}(\omega) = \chi_{\mathrm{ee}}(\omega)$ for all ω. We may now assume that the susceptibilities follow a Lorentzian dispersion profile [159] such that

$$\chi_{\mathrm{ee}}(\omega) = \frac{2A\omega_{\mathrm{p}}^2}{(\omega_0^2 - \omega^2) + j\gamma\omega}, \tag{5.2}$$

where A is the amplitude, γ is a damping factor, ω_0 is the resonance frequency and ω_p is the plasma frequency. Substituting (5.2) into (5.1b) leads to the following transmission coefficient:

$$T(\omega) = \frac{(\omega_0^2 - \omega^2) - j(Ak_0\omega_\mathrm{p}^2 - \omega\gamma)}{(\omega_0^2 - \omega^2) + j(Ak_0\omega_\mathrm{p}^2 + \omega\gamma)}, \tag{5.3}$$

and the reflection coefficient is $R(\omega) = 0$.

It can be easily verified that if the dielectric metasurface is perfectly lossless ($\gamma = 0$), then the amplitude of the transmission coefficient in (5.3) is 100% and flat over a broad bandwidth. Additionally, the transmission phase, $\phi(\omega)$, exhibits a 2π variation around the resonance frequency.

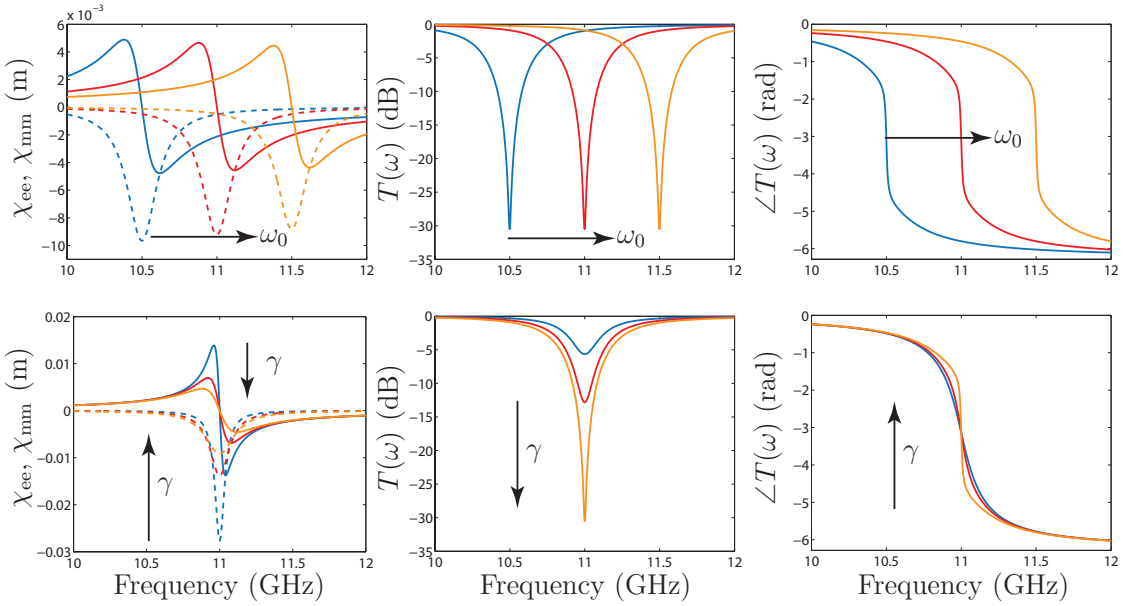

Figure 5.3 Effect of the resonance frequency and loss on the real and imaginary parts of the susceptibilities as well as the amplitude and phase transmission of a metasurface formed by a 2D square array of dispersion-matched Lorentz oscillators. Top row, varying resonance frequencies ($\gamma = 15\times10^8$ rad/s, $\omega_0 = 2\pi[10.5\ 11\ 11.5]\times10^9$ rad/s), and, bottom row, varying loss coefficient γ ($\gamma = [5\ 10\ 15]\times10^8$ rad/s, $\omega_0 = 2\pi11\times10^9$ rad/s). In all cases, $A = 10^{-4}$ and $\omega_\mathrm{p} = 2\pi11\times10^9$ rad/s.

In order to illustrate the effects of changing the resonance frequency, ω_0, and the absorption coefficient, γ, on the susceptibilities in (5.2) and the coefficient in (5.3), we perform several simulations, whose corresponding results are plotted in Fig. 5.3. In the two figures on the left, the solid lines correspond to the real parts of the susceptibilities, while the dashed lines correspond to their imaginary parts. The amplitude of the transmission coefficient is plotted in the two middle figures, while the corresponding transmission phase is plotted in the two

remaining ones. We see that as γ increases, the transmission amplitude decreases around the resonance frequency. Moreover, the frequency variation of the transmission phase becomes sharper as γ is increased.

5.1.2 Simulations and Experimental Demonstrations

In order to analyze the scattering response of a dielectric metasurface, we have first simulated a metasurface with unmatched electric and magnetic resonances, i.e. $\chi_{\rm ee}(\omega) \neq \chi_{\rm mm}(\omega)$. The specified frequency range is from 10 to 12 GHz, which corresponds to that in Fig. 5.3. Referring to the dimensions in Fig. 4.5b, the metasurface is designed with the following parameters: thickness $t = 5.08$ mm ($\approx \lambda_0/5.4$), radius $r_0 = 5.5$ mm ($\approx \lambda_0/5$) and unit cell period $a_x = a_y = 21.5$ mm ($\approx \lambda_0/1.2$). We have chosen a commercially available dielectric substrate which is Rogers RO3210 with a relative permittivity of $\epsilon_r = 10.2$ and a loss tangent of $\tan\delta = 0.0027$. Note that the dielectric connections holding the resonators together are not considered here.

The corresponding simulation results are shown in Figs. 5.4. The amplitude and phase of the transmission and reflection coefficients are plotted on the top of Figs. 5.4a, while the corresponding susceptibilities, obtained with (2.31), are plotted at the bottom. We see that

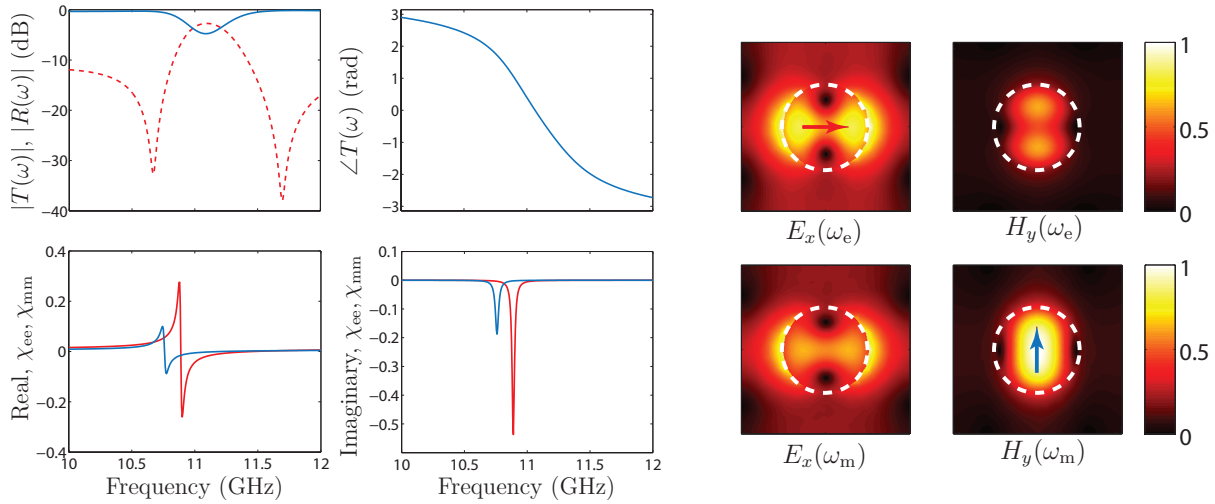

Figure 5.4 Simulated unmatched metasurface. (a) Top, transmission (solid blue line) and reflection (dashed red line) coefficients on the left and, transmission phase on the right. Bottom, real part of the retrieved electric (red line) and magnetic (blue line) susceptibilities on the left and corresponding imaginary parts on the right. (b) Electric and magnetic field distributions in the electric and magnetic resonances, respectively. All results are computed using HFSS.

the susceptibilities effectively follow a Lorentzian type resonance model and that the electric and magnetic resonances do not occur at the same frequency. A closer inspection reveals that the corresponding resonances are at $\omega_e = 2\pi 10.9 \times 10^9$ rad/s and $\omega_m = 2\pi 10.8 \times 10^9$ rad/s, respectively. Moreover, note that the two susceptibilities do not exhibit the same dispersion response. In that case, the metasurface is unmatched and thus presents relatively low transmission in the frequency range of interest. To see the responses of the resonators, the electric and magnetic fields are shown in Fig. 5.4b at frequencies ω_e and ω_m, where we can clearly see that the fields are unbalanced.

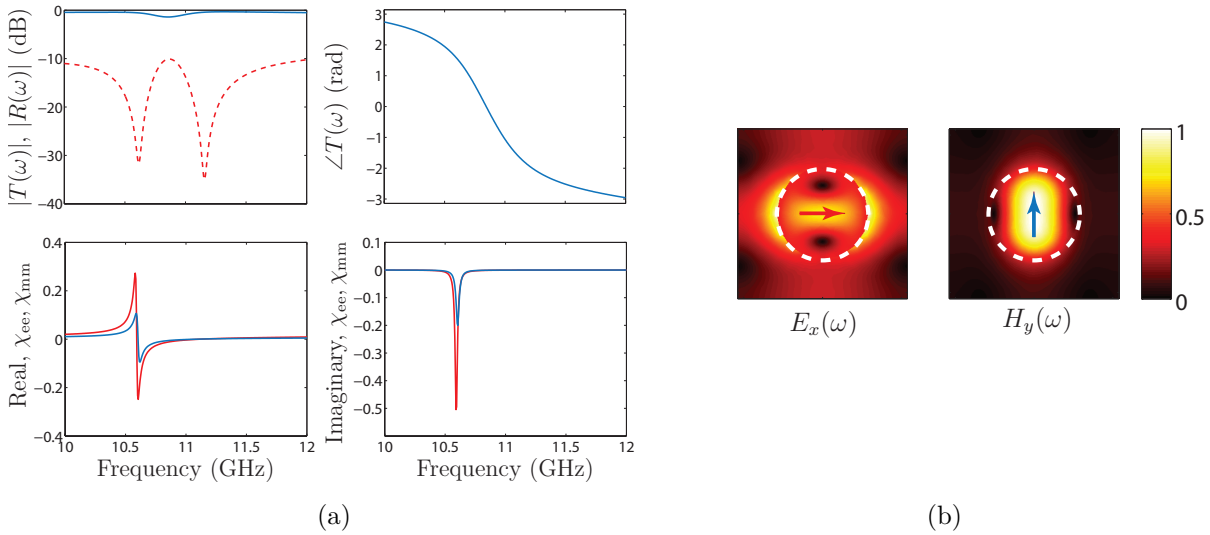

Figure 5.5 Simulated matched metasurface. (a) Top, transmission (solid blue line) and reflection (dashed red line) coefficients on the left and, transmission phase on the right. Bottom, real part of the retrieved electric (red line) and magnetic (blue line) susceptibilities on the left and corresponding imaginary parts on the right. (b) Electric and magnetic field distributions when the electric and magnetic resonances overlap ($\omega = \omega_e = \omega_m = 10.6 \times 10^9$ rad/s). All results are computed using HFSS.

Let us now investigate the case of a metasurface with overlapping electric and magnetic resonances. To achieve this result, the radius of the resonators has been increased to $r_0 = 5.775$ mm ($\approx \lambda_0/4.7$). The corresponding simulations are shown in Figs. 5.5, where, as before, the transmission and reflection coefficients are plotted on top of Figs. 5.5a, while the corresponding susceptibilities are plotted at the bottom. As can be seen, the resonance occurs at $\omega = \omega_e = \omega_m = 2\pi 10.6 \times 10^9$ rad/s. Despite the fact that the dispersion of the electric and magnetic resonances are slightly different, the matching is good and the transmission coefficient is almost flat over a large bandwidth. The presence of the dip in the transmission at the resonance frequency can be explained by the inherent dielectric loss and the unequal dispersion of the two resonances. Note that, even without loss, it is generally difficult to

achieve perfect matching because of the different dispersions [227].

The simulations presented so far, notably in Figs. 5.5, illustrate that a dielectric resonator metasurface can achieve a broadband transmission (close to unity) while covering a 2π-phase range. Such a dielectric metasurface, with matched resonances, has been realized based on the microwave design discussed in Sec. 4.2 and whose structure is depicted in Fig. 4.5b. The fabricated metasurface has essentially the same parameters as those of the previously designed dielectric structures, at the exception that $r_0 = 4.95$ mm ($\approx \lambda_0/4.95$) and $a_x = a_y = 20$ mm ($\approx \lambda_0/1.4$). Additionally, the resonators of this metasurface are held together by dielectric connections of width $w = 2.54$ mm ($\approx \lambda_0/11$). The metasurface thickness $t = 5.08$ mm is achieved by stacking together four 1.27-mm thick Rogers RO3210 dielectric slabs. This metasurface has been optimized to factor in the presence of the dielectric connections, hence the reason why it has different dimensions than the metasurface whose simulations are plotted in Fig. 5.5. A picture of the fabricated metasurface is shown in Fig. 4.6.

This metasurface has been simulated with two different techniques and measured so as to evaluate its scattering response. One simulation was performed with CST, while the other one with a home-made rigorous coupled-wave analysis (RCWA) code [1, 234]. The resulting transmission and reflection coefficients amplitude and phase are plotted in Figs. 5.6a and 5.6b, respectively. In all cases, the excitation is x-polarized, i.e. perpendicular to the dielectric connections. From these results, we can deduce that the matching is good leading to a high

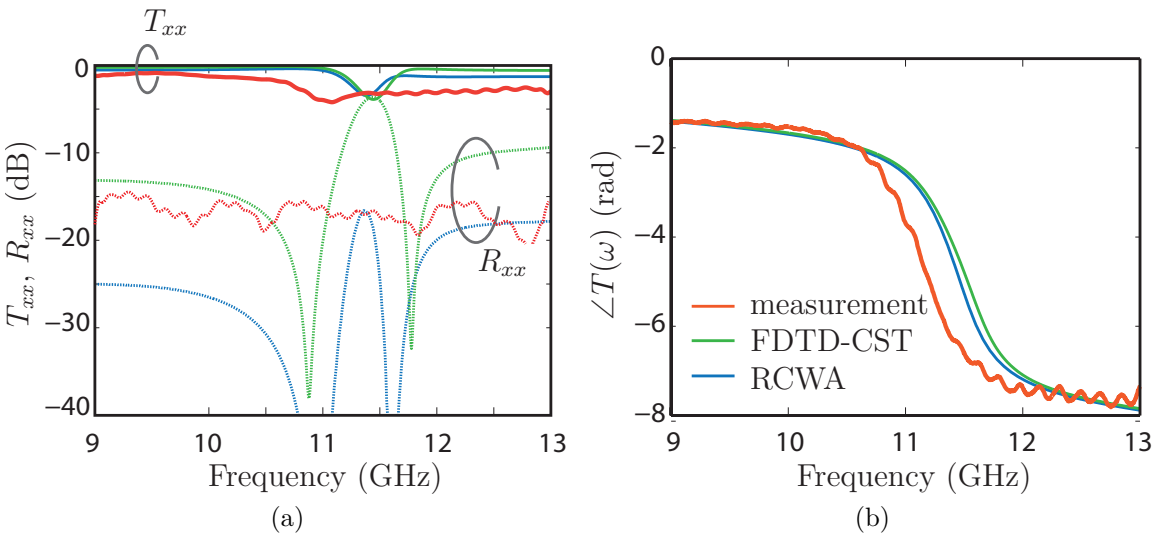

Figure 5.6 Transmission amplitude and phase of the metasurface in Fig. 5.40. Full-wave results are also shown for comparison, computed using CST Microwave Studio and Rigorous Coupled-Wave Analysis Technique [1], where an infinite 2D array is assumed.

transmission extending over the entire frequency band. The presence of a -4 dB dip in the

transmission, at the resonance frequency $\omega_e \approx \omega_m = 2\pi 10.8 \times 10^9$ rad/s, is caused by the combined effects of dielectric loss and unequal dispersions. Comparing the simulated results to the measured response, we see that the resonance frequency is down-shifted by about 3%. This small discrepancy may be explained by errors introduced in the fabrication of the structure.

Overall, the fabricated metasurface demonstrates that the design in Fig. 4.5b can effectively achieve the expected broadband response that is required to achieve dispersion engineering. This is the case when the excitation polarization is perpendicular to the dielectric connections, in which case, the latter have negligible effects on the response of the metasurface.

The capability to control the dispersion and thus the group delay, in order to realize real-time processors, may be achieved by cascading several dielectric metasurfaces with different resonators exhibiting different Lorentzian responses [151, 200, 201]. An example is illustrated in Fig. 5.7, where three metasurfaces with different dispersion are cascaded to shape the overall frequency response of the system.

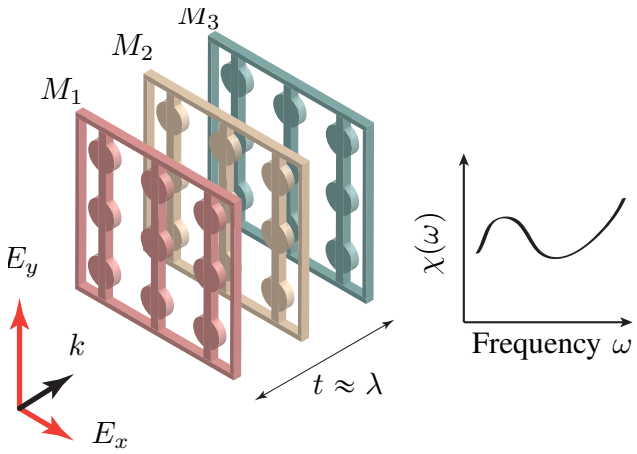

Figure 5.7 Conceptual idea of cascading several dielectric metasurfaces for dispersion engineering.

The concept of metasurface based dispersion engineering presented here has been demonstrated, in the microwave regime, with the simple dielectric design of Fig. 4.5b. This concept can naturally be implemented in the optical regime with the more conventional type of dielectric structure of Fig. 4.5a. It is worthwhile noting that a more sophisticated control of the transmission can be obtained by using more complex shapes for the resonators such as, for instance, elliptical resonators that would allow an anisotropic control of the dispersion.

5.2 Electromagnetic Wave plates

An electromagnetic wave plate is a structure that can be described by nonzero monoanisotropic diagonal susceptibility tensors, which corresponds to birefringence. This kind of structure induces different phase shifts for orthogonal polarizations. We will consider the case of normal wave propagation with respect to the metasurface which exhibits phase retardations of ϕ_x and ϕ_y for x and y polarizations, respectively. It is common to characterize wave plates by the phase shift difference, $\Delta\phi = |\phi_x - \phi_y|$, that they induce. In this section[3], we will present the implementations of half-wave plates, $\Delta\phi = \pi$, and quarter-wave plates, $\Delta\phi = \pi/2$. Figures 5.8 illustrate the operation of these two wave plates when illuminated by a linearly polarized plane wave. The half-wave plate rotates by 90° the polarization of linearly polarized waves, or changes the handedness of circularly polarized waves. The quarter-wave plate is a linear-to-circular polarization converter [159].

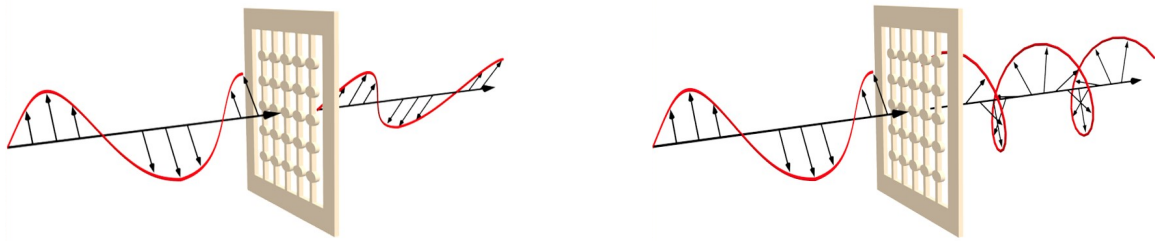

(a) (b)

Figure 5.8 Operation of (a) a half-wave plate and (b) a quarter-wave plate.

It is important to note that we are not specifying any change in the direction of wave propagation. This means that the metasurfaces are perfectly uniform structures. Consequently, their implementation is drastically simplified since only one unit cell has to be realized and repeated periodically. We will present the realization of half- and quarter-wave plates designed with the dielectric unit cell structure discussed in Sec. 4.2 as well as the metallic unit cell structure discussed in Sec. 4.1.

5.2.1 Dielectric Implementation

In Sec. 5.1, dielectric metasurfaces were used to perform dispersion engineering and it was demonstrated that such structures can control the phase while maintaining a good transmission efficiency over a large bandwidth. We now use the same kind of unit cell to achieve an anisotropic control of the transmission phase for x and y polarizations. The cylindrical

[3]This section is based on a slight modified version of [187, 201].

resonators used so far are not well suited for such kind of transformations since they are isotropic structures due to their inherent geometrical symmetries. We will instead use dielectric resonators with elliptical cross-section, which provides enough degrees of freedom to perform the required transformations. However, this comes at the cost of reduced bandwidth due to the impossibility to control both polarizations while matching the electric and magnetic resonances at the same frequency.

The dielectric half- and quarter-wave plates have been designed for an operating frequency of 18 GHz. After numerical optimizations in CST to take into account the presence of the dielectric connections, the dimensional parameters common to the two structures are: a unit cell size of 14.9 mm ($\approx \lambda_0/1.1$), a thickness of 5.08 mm ($\approx \lambda_0/3.3$) obtained by stacking together two Rogers RO3210 substrates of thickness 2.54 mm each, and a connection width of 1.25 mm ($\approx \lambda_0/13.3$). In what follows, the dimensions of the ellipses are specified in terms of their major axis (a) and minor axis (b) that are in the x- and y-direction, respectively. The resonators are held together with dielectric connections that extend in the y-direction. For both structures, the resonators are tuned such that the transmission coefficients for x- and y-polarized waves have equal amplitude and specific phase shift difference as given above.

The realized half-wave plate metasurface is shown in Fig. 5.9a. After full-wave optimizations, it was found that the dimensions of the elliptical resonators are: $a = 4.5$ mm ($\approx \lambda_0/3.7$) and $b = 3.7$ mm ($\approx \lambda_0/4.5$). The metasurface was then measured and the resulting normalized[4] transmitted power for x and y polarizations are respectively plotted, in solid blue line and dashed red line, in Fig. 5.9b. The measured phase difference between the two polarizations is plotted in Fig. 5.9c. From these results, we can see that at 18.4 GHz, the amplitude of both transmission coefficients is the same and is equal to -1 dB, while the phase shift difference is $\Delta\phi \approx \pi$. This means that the metasurface effectively performs the half-wave plate operation with a small frequency up-shift with respect to the initial specification.

The realized quarter-wave plate metasurface is shown in Fig. 5.10a. After full-wave optimizations, it was found that the dimensions of the elliptical resonators are: $a = 5.4$ mm ($\approx \lambda_0/3.1$) and $b = 3.7$ mm ($\approx \lambda_0/4.5$). The metasurface was then measured and the resulting normalized transmitted power for x and y polarizations are respectively plotted, in solid blue line and dashed red line, in Fig. 5.10b. The measured phase difference between the two polarizations is plotted in Fig. 5.10c. From these results, we can see that at 18.1 GHz, the amplitude of both transmission coefficients is the same and is equal to -1 dB, while the phase shift difference is $\Delta\phi \approx \pi/2$. This means that the metasurface effectively performs

[4]The normalization is computed by dividing the measured transmission with the metasurface by the measured transmission without the metasurface.

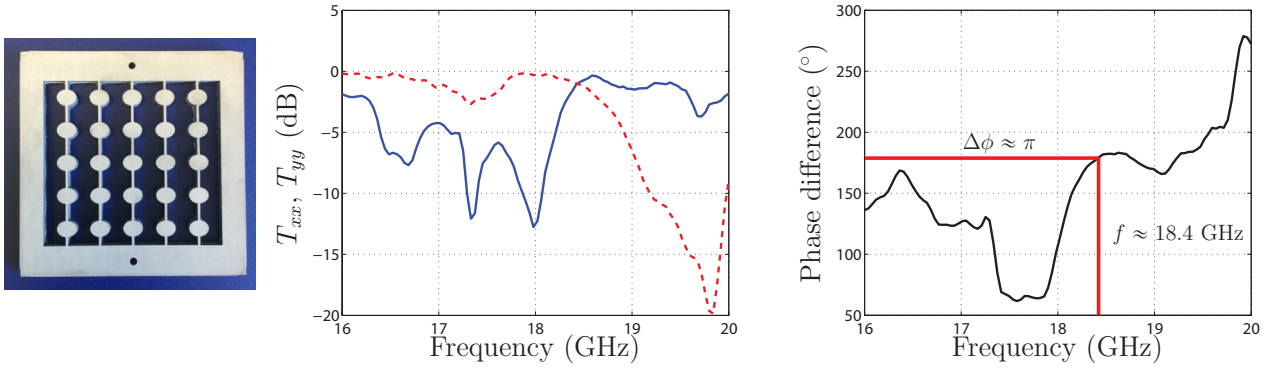

(a) (b) (c)

Figure 5.9 Half-wave plate dielectric metasurface (a) picture of the structure. Measurements for (b) normalized transmitted power T_{xx} (solid blue line) and T_{yy} (dashed red line), and (c) phase difference between the two polarizations.

the quarter-wave plate operation with a small frequency up-shift with respect to the initial specification.

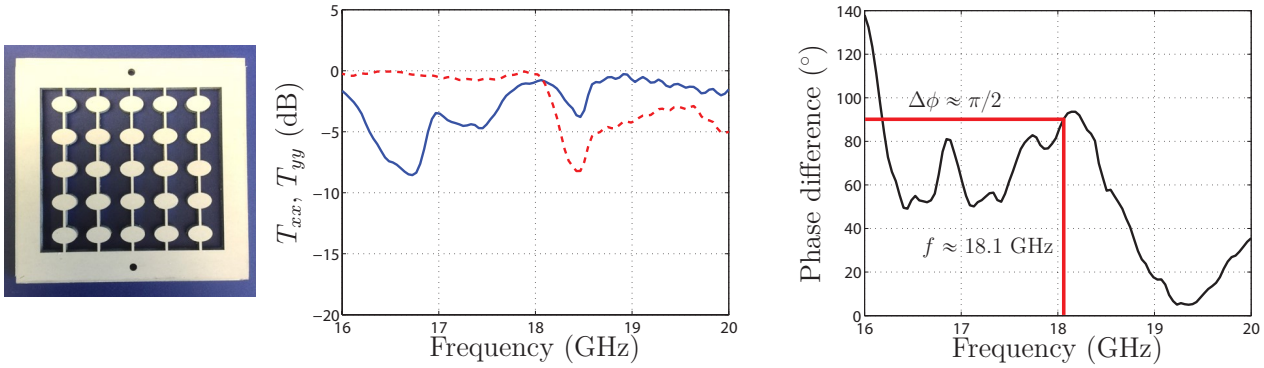

(a) (b) (c)

Figure 5.10 Quarter-wave plate dielectric metasurface (a) picture of the structure. Measurements for (b) normalized transmitted power T_{xx} (solid blue line) and T_{yy} (dashed red line), and (c) phase difference between the two polarizations.

In the two realized metasurfaces of Figs. 5.9 and 5.10, we see that the transmission coefficients are not flat in the selected frequency band, contrary to the dielectric metasurface with cylindrical resonators discussed in the previous section. This is because it is in general impossible to tune the dimensions of the elliptical resonators such that the electric and magnetic resonances overlap at the same frequency for both polarizations. Notice also how the x- and y-polarized transmission coefficients differ from each other due to the anisotropy

of the resonators and also to the presence of the dielectric connections in the y-direction.

5.2.2 Metallic Implementation

Wave plates performing the same operations are now realized with metallic scattering particles with a specified operation frequency of 10 GHz. Following the procedure described in Sec. 4.1, the dimensions of the Jerusalem crosses of the half-wave plate metasurface unit cell are given in Table 5.1, where OL denotes the dimensions of the outer layers and ML the dimensions of the middle layer according to Fig. 4.2a. The corresponding fabricated

Table 5.1 Geometrical dimensions (in mm) for the unit cell of the metasurface in Fig. 5.11a. OL denotes the outer layers and ML the middle layer.

Layer	Lx	Ly	Wx	Wy	Ax	Ay	Bx	By
OL	4	4.75	0.5	0.5	0.5	0.5	3.25	2.25
ML	5	5	0.5	0.25	0.25	0.75	2.25	3.5

metasurface is shown in Fig. 5.11a. It is made of 24×24 unit cells, which corresponds to an aperture of about $5\lambda_0 \times 5\lambda_0$. The holes on the left- and right-hand sides of the metasurface are used to screw it to the measurement setup as discussed in Sec. 4.3.

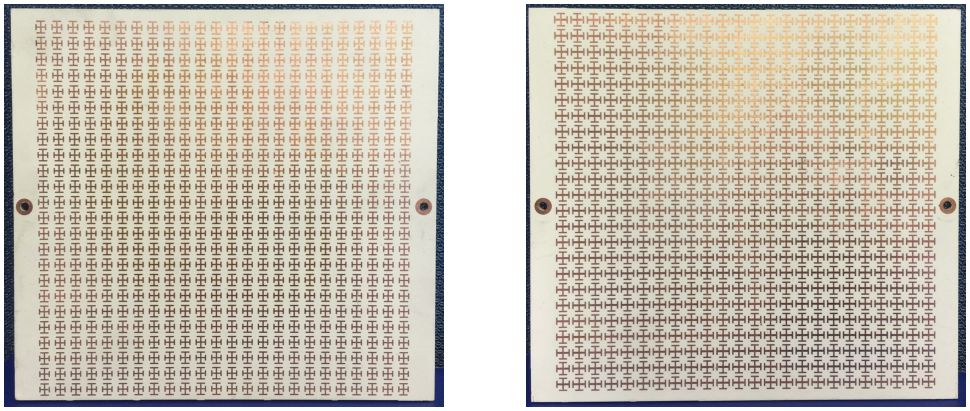

(a) (b)

Figure 5.11 Fabricated (a) half-wave plate and (b) quarter-wave plate.

To evaluate the transmission properties of this metasurface, we have measured the x- and y-polarized transmission coefficients that are plotted in Fig. 5.12a in solid blue line and dashed red line, respectively. In these figures, the measured transmission coefficients are normalized with respect to a reference transmission measurement performed without metasurface. The corresponding transmission phase difference between the two polarization is shown in

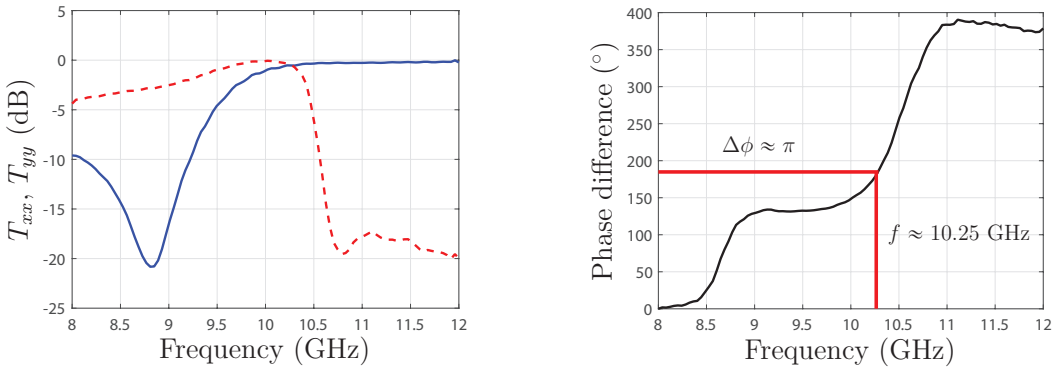

(a) (b)

Figure 5.12 Half-wave plate metasurface measurements for (a) normalized transmitted power T_{xx} (solid blue line) and T_{yy} (dashed red line), and (b) phase difference between the two polarizations.

Fig 5.12b. From these measurements, we see that the amplitudes of the transmission coefficients are very close to unity around the desired frequency of operation, revealing the very good transmission efficiency of this structure. The required $\Delta\phi = \pi$ phase-shift difference occurs at 10.25 GHz, which is slightly up-shifted with respect to the desired operating frequency of 10 GHz. From Figs. 5.12a and 5.12b, we can deduce that the cross-polarization conversion efficiency of this metasurface is about 95% at 10.25 GHz for a -3-dB bandwidth of about 10%.

The fabricated quarter-wave plate metasurface which is shown in Fig. 5.11b has been realized with the same procedure as that of the previous metasurface. The physical dimensions of its Jerusalem crosses are reported in Table 5.2.

Table 5.2 Geometrical dimensions (in mm) for the unit cell of the metasurface in Fig. 5.11b. OL denotes the outer layers and ML the middle layer.

Layer	Lx	Ly	Wx	Wy	Ax	Ay	Bx	By
OL	5	5	0.5	0.75	0.5	0.5	3	2.75
ML	2.75	5	0.5	0.75	0.25	0.5	2.75	1.75

To evaluate the scattering response of this metasurface, we have performed the exact same measurements that we did for the half-wave plate metasurface. Accordingly, the normalized x- and y-polarized transmission coefficients are plotted in Figs. 5.13a in solid blue line and dashed red line, respectively, while the phase-shift difference between the two polarizations is plotted in Fig. 5.13b. As was the case for the half-wave plate metasurface, the transmission coefficients of the quarter-wave plate metasurface approach unity at 10 GHz which exactly

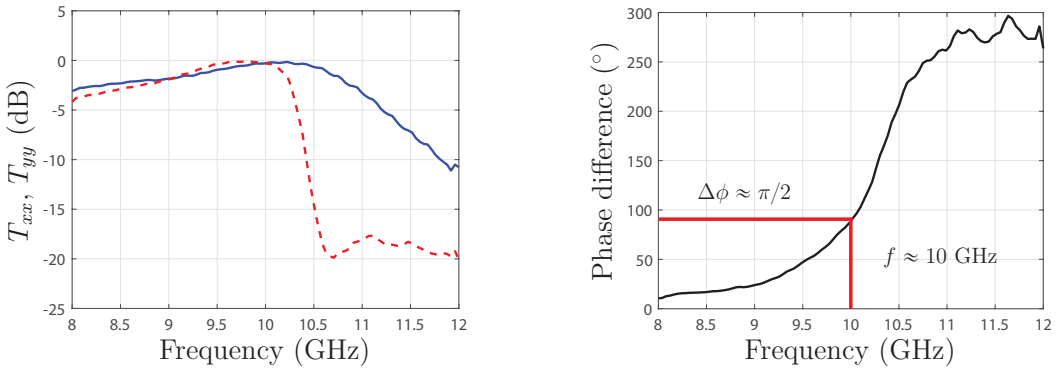

(a) (b)

Figure 5.13 Quarter-wave plate metasurface measurements for (a) normalized transmitted power T_{xx} (solid blue line) and T_{yy} (dashed red line), and (b) phase difference between the two polarizations.

corresponds to the specified frequency of operation. At the same frequency, the phase-shift difference is $\Delta\phi = \pi/2$, which confirms the quarter-wave plate operation of this metasurface. From the results presented in Figs. 5.13, it is possible to evaluate the linear-to-circular conversion efficiency which is 94% at 10 GHz with a -3-dB bandwidth of about 12%.

5.3 Polarization Beam Splitter

The polarization beam splitting (PBS) metasurface that is discussed here is part of the more general framework of generalized birefringent reflecting and refracting structures which perform independent control of the reflection and transmission angles and amplitudes of orthogonally polarized waves [187,206][5]. As an example, the case of reflectionless birefringent refraction is illustrated in Fig. 5.14, where two incident plane waves with perpendicular and parallel polarization, respectively, are refracted to arbitrary independent directions. The general case of reflectionless refraction that is illustrated in Fig. 5.14 is not simple to realize since the periodicity of the susceptibility functions for both polarizations is not same if the incidence and refraction angles are different for the two polarizations. We will therefore consider a simplified problem where x- and y-polarized incident waves are normally impinging on the metasurface, which refracts them in the xz-plane at angles $\pm\theta_t$. This beam splitting operation is thus perfectly symmetric leading to the same susceptibility periodicity for the two polarizations. In order to implement this metasurface, we have used the second synthesis technique following the procedure elaborated in Sec. 3.1, which consists in synthesizing the metasurface using transmission coefficients. In that case, the transmissions coefficients for x

[5]This section is based on a slight modified version of [187].

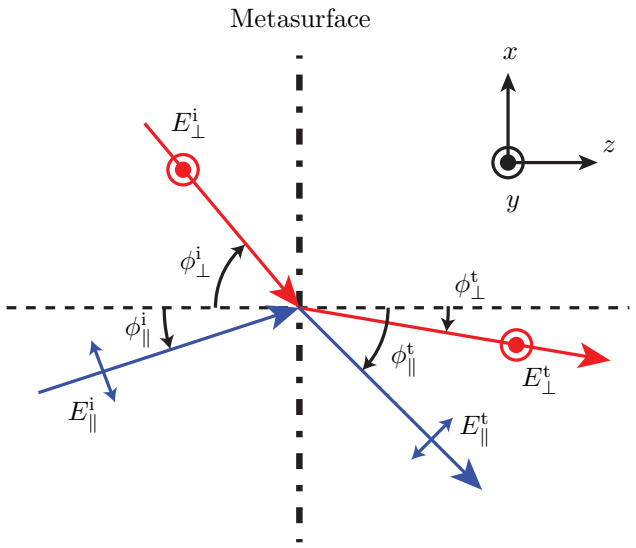

Figure 5.14 Birefringent reflectionless refraction operation.

and y polarizations are obtained using (3.5), which leads to $T_x(x) = e^{-jk_0 \sin\theta_{\mathrm{t}} x}$ and $T_y(x) = e^{jk_0 \sin\theta_{\mathrm{t}} x}$. The metasurface is thus a double phase-gradient structure with periods $P_x = P_y = \lambda_0/\sin\theta_{\mathrm{t}}$. In order to realize the metasurface, the periodic susceptibility functions are discretized to form 8 unit cells that will be implemented with the metallic scattering particles of Sec. 4.1. We have chosen the operating frequency to be 10 GHz for which the unit cell transverse size is $\lambda_0/5$. The size and the number of unit cells per period directly dictate the achievable refraction angle, which, in our case, is $\theta_{\mathrm{t}} = \arcsin(5/8) \approx 38.7°$.

According to the specified transmission coefficients, each of the 8 unit cells forming a period of the susceptibility functions, must exhibit unit transmission amplitudes and different phase retardations for x and y polarizations, which are respectively denoted as ϕ_x and ϕ_y. The corresponding transmission phases are given in Table 5.3 for the 8 unit cells. Note that the absolute phase shift of a single unit cell is irrelevant, only the phase shift difference between adjacent unit cells (here 45°) matters. As can be seen in Table 5.3, the supercell (formed by

Table 5.3 Transmission phase shifts (in degrees) for x and y polarizations of the 8 unit cells forming the PBS metasurface.

	1	2	3	4	5	6	7	8
ϕ_x	0	45	90	135	180	225	270	315
ϕ_y	315	270	225	180	135	90	45	0

the 8 unit cells) has an asymmetric phase progression meaning that the unit cells number 5, 6, 7 and 8 have opposite x and y phase shifts as the unit cells number 4, 3, 2 and 1, respectively. This means that the 4 last unit cells are simply the 90°-rotated versions of

the first 4 unit cells. Consequently, the realization of this metasurface is greatly simplified because only half of the unit cells need to be found by full-wave simulations.

These 4 unit cells have been realized following the procedure in Sec. 4.1 and their corresponding dimensions are given in Table 5.4.

Table 5.4 Geometrical dimensions (in mm) for the first four unit cells of the PBS metasurface. OL denotes the outer layers and ML the middle layers.

		Lx	Ly	Wx	Wy	Ax	Ay	Bx	By
Cell 1	OL	5.5	4	0.5	0.625	0.5	0.5	4.875	2.25
	ML	5.5	5.5	0.375	1.125	0.5	0.5	1.375	2.875
Cell 2	OL	5.25	4.25	0.625	0.5	0.5	0.5	4.125	3
	ML	5.75	3.5	0.5	0.375	0.5	0.5	0.5	1.375
Cell 3	OL	4.25	4.75	0.625	0.25	0.5	0.5	4.25	3
	ML	3.75	5.25	0.5	0.375	0.5	0.5	2.25	4.5
Cell 4	OL	3.75	3.5	0.125	0.125	0.5	0.5	2.25	4.375
	ML	5.5	5.25	0.375	1.125	0.5	0.5	4.75	0.125

In order to verify the beam splitting operation of the PBS metasurface, full-wave simulations are performed. The supercell is simulated in CST assuming periodic boundary conditions and normally incident plane wave illumination polarized along x or y. The simulation results are presented in Figs. 5.15a and 5.15b for the two respective polarizations. As can be observed, the x-polarized refraction result agrees well with the expected response. However, the y-polarized transformation does not agree well with the expectation as evidenced by the presence of an interference pattern on the transmit side of the metasurface caused by undesired diffraction orders. This effect may be explained by the presence of spurious coupling between adjacent unit cells. While the coupling affects both polarizations, it turns out that it is more damaging to the y polarization than the x polarization. It has to be noted that the metasurface is nonuniform only in the x-direction while being perfectly uniform in the y-direction, this asymmetry in the structure is hypothesized to be the cause of the different behavior of the two polarizations.

To reduce the damaging effect that the coupling has on the y-polarized wave and thus achieve a better response, we have modified the metasurface such that the same nonuniformity is present in both x- and y-directions. Consequently, the metasurface is now periodic in these two directions instead of being periodic only in the x-direction. Accordingly, the supercell is now made of 8×8 unit cells instead of 1×8. Because of this modification, the beam splitting operation does not occur in the xz-plane anymore but on a plane rotated by 45° with respect

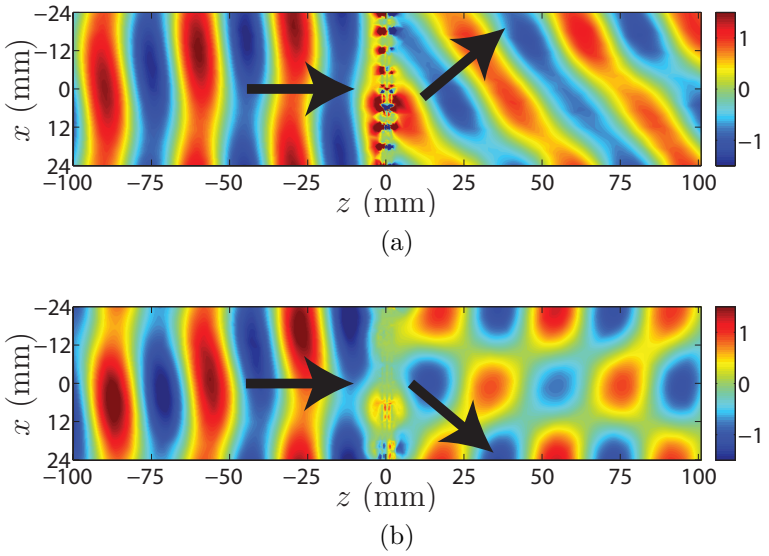

Figure 5.15 Full-wave simulations, assuming periodic boundary conditions, of the PBS metasurface supercell. (a) An x-polarized normally incident plane wave is impinging from left to right on the metasurface that refracts it upward. (b) A y-polarized normally incident plane wave is impinging from left to right on the metasurface that refracts it downward.

to the z-axis. Moreover, the period of the phase gradients is reduced to $P = 8\lambda_0/(5\sqrt{2})$, which changes the transmission angle to $\theta_t \approx 62.1^\circ$ for an operating frequency of 10 GHz.

The realized metasurface is shown in Fig. 5.16 where the supercell is highlighted by the black square. Note the sinusoidally varying pattern in the diagonal direction indicating the

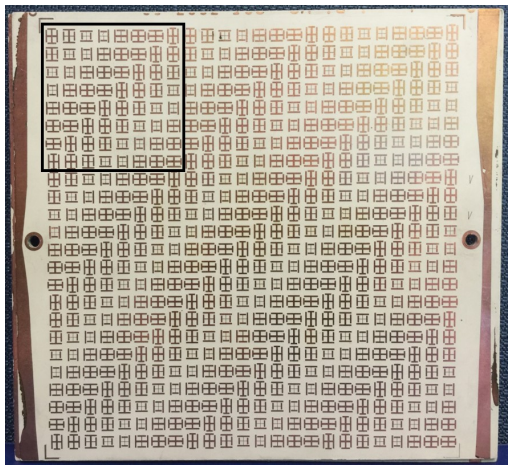

Figure 5.16 Fabricated polarization beam splitting metasurface. The supercell made of 8×8 unit cells is highlighted by the black square.

direction of the phase gradients and thus the direction of beam splitting. The metasurface is made of 24×24 unit cells, which corresponds to a repetition of 9 supercells. Even though

the supercell is now made of 64 unit cells, it is still made of a repetition (and/or rotation) of the same 4 unit cells given in Table 5.4.

Due to the large electrical size of the supercell, it was not practically possible to perform full-wave simulations. The metasurface was instead characterized only via measurements. A horn antenna was used to generate the normally incident waves while a probe was scanning the near-field over a plane parallel to the metasurface in the transmission region. Near-field to far-field transformation [203] was then used to evaluate the transmission response of the metasurface. The measured x and y polarization transmissions, in the diagonal plane of the metasurface, are plotted in Fig. 5.17a as a dashed blue line and a solid red line, respectively. Note that the curves have been normalized with respect to the y-polarized transmission.

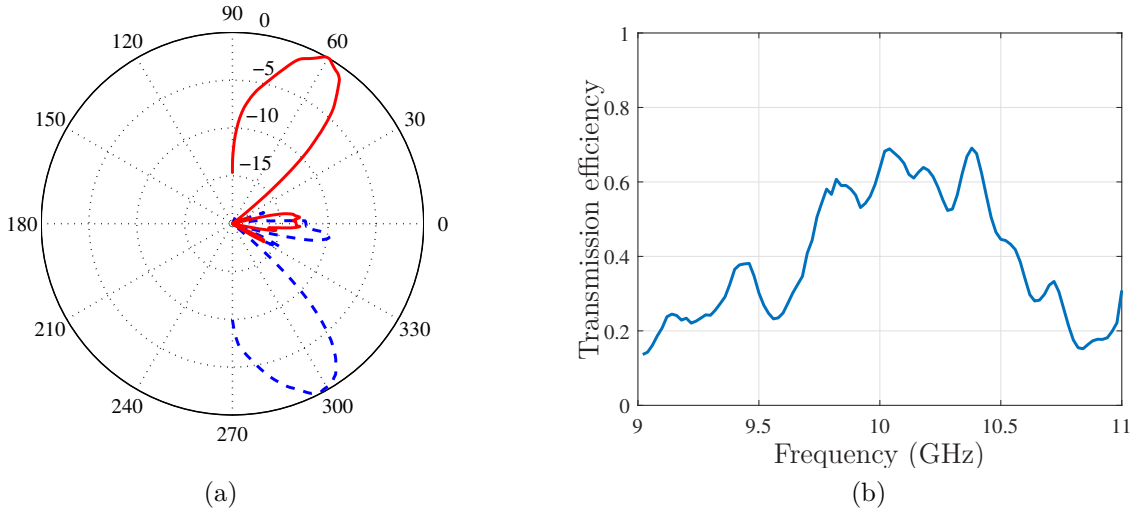

Figure 5.17 PBS metasurface (a) measured normalized transmitted power (dB) for x-polarization (dashed blue line) and y-polarization (solid red line), and (b) transmission power efficiency.

As can be seen, the metasurface effectively separates the two polarizations which are refracted, with almost identical amplitude, at about $+60°$ and $-60°$ from broadside, respectively. The frequency corresponding to the results in Fig. 5.17a is about 10.4 GHz and the transmission power efficiency, defined as the ratio between the transmitted power in the desired direction and the incident power, is about 70%. The efficiency of the metasurface versus frequency is plotted in Fig. 5.17b. The reasons for which the metasurface efficiency does not exceed 70% can be explained partly by the presence of dielectric and ohmic loss in the unit cells as well as from undesired refraction orders (either in reflection or in transmission) that are due to the spurious coupling of the unit cells. For instance, zeroth diffraction orders are clearly visible in the measurements shown in Fig. 5.17a.

5.4 Orbital Angular Momentum Generator

There are two kinds of angular momentum of light, the most familiar one is spin angular momentum, which is related to circular or elliptical polarization, and the second one is orbital angular momentum (OAM), which is related to the spatial distribution of the field taking the form of a helical wavefront [235,236]. Typically, a light beam possessing OAM as a phase profile, in the transverse plane, that is proportional to $e^{jm\phi}$, where ϕ is the azimuthal angle in cylindrical coordinates and $m \in \mathbb{Z}$ is the topological charge. OAM beams have attracted attention due to their capabilities to manipulate nanoparticles [237] as well as their potential application for telecommunications [238]. In that latter case, OAM light has the advantage of possessing a virtually infinite number of states (topological charges) compared to circular polarization which exhibits only two possible states (LHCP and RHCP).

We present here a metasurface that is able to generate OAM beams when illuminated by a normally incident linearly polarized plane wave[6]. Depending on the polarization of the incident wave, OAM beams with opposite topological charges are generated. There exists several types of OAM beams that could be generated and the most common one is the Bessel beam, which corresponds to the solution of the wave equation in cylindrical coordinates. However, Bessel beams have the disadvantage of being either radially or azimuthally polarized making the generation of two OAM beams with a single metasurface difficult. For this reason, the OAM beams that are generated by the metasurface are not Bessel beams but rather Hypergeometric Gaussian (HyG) beams which are solutions of the paraxial wave equation and are linearly polarized [239].

The metasurface is synthesized so as to transform an x-polarized normally incident plane wave into an HyG wave of topological charge $m = +1$ and y-polarized normally incident plane wave into an HyG wave of topological charge $m = -1$. The electric field of an HyG wave, in cylindrical coordinates, reads [239]

$$E(\rho,\phi,z) = \frac{\Gamma\left(1+|m|+\frac{p}{2}\right)}{\Gamma(|m|+1)} \frac{j^{|m|+1}\zeta^{|m|/2}\xi^{p/2}}{[\xi+j]^{1+|m|/2+p/2}} e^{jm\phi-j\zeta} \times \ {}_1F_1\left(-\frac{p}{2}, |m|+1; \frac{\zeta[\xi+j]}{\xi[\xi-j]}\right), \quad (5.4)$$

where ${}_1F_1(a,b;x)$ is the confluent hypergeometric function, $\Gamma(x)$ is the gamma function, $p \geqslant -|m|$ is a real parameter, and where $\zeta = \rho^2/(w_0^2[\xi+j])$, $\xi = z/z_R\ w_0$, with w_0 being the beam waist and z_r the Rayleigh range given by $z_r = \pi w_0^2/\lambda$.

As an illustration, the amplitude and phase of the HyG beam, for $m = -1$, are plotted in Figs. 5.18a and 5.18b, respectively.

[6]This section is based on a slight modified version of [187].

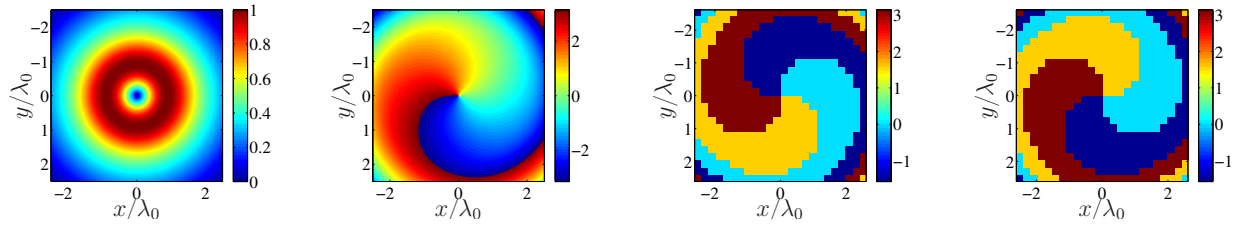

Figure 5.18 Hypergeometric Gaussian wave (a) amplitude and (b) phase for parameters $p = 1$, $m = -1$, $w_0 = \lambda$ and $\xi = 1$. The metasurface simplified phase patterns for x and y polarizations are given in (c) and (d) for topological charges $m = +1$ and $m = -1$, respectively.

Because the spatial distribution of the HyG field is not periodic in the transverse plane, a large number of unit cells has to be implemented contrary to the PBS metasurface, discussed in the previous section, which was realized with a repetition of only 4 unit cells. Moreover, the amplitude of the HyG wave is nonuniform which further complicates the realization of the unit cells.

In order to overcome these difficulties, we discretize the phase profiles of the two OAM beams with only four phase samples for simplicity. For a metasurface made of 24×24 unit cells, the corresponding transmission phase shifts for x and y polarizations are respectively plotted in Figs. 5.18c and 5.18d. Moreover, we assume that the metasurface transmission coefficients for x and y polarizations are given by $|T_x(x, y)| = |T_y(x, y)| = 1$ instead of following the profile in Fig. 5.18a. Despite the fact that this approximation might a priori seem extreme, it turns out that the main properties of an HyG beam may be obtained by only implementing its phase evolution. For instance, the null amplitude at the center of the wave is achieved by destructive interferences due to the phase rotation around the center. Moreover, the orbital angular momentum information is contained not in the amplitude but rather in the phase of the beam. These considerations justify the assumption that only the phase profile of the transmitted waves should be implemented while their respective amplitude can be assumed to be uniform and equal to 1.

In order to know how many unit cells are required to realize the metasurface, we combine together the phase shifts in Figs. 5.18c and 5.18d. This results in the pattern presented in Fig. 5.19a, which represents the 24×24 unit cells of the metasurface and where each color corresponds to a specific unit cell having unique phase shift for x and y polarizations. Figure 5.19a reveals that the total number of different unit cells composing the metasurface is 16. It is interesting to note that the unit cells in the highlighted regions 1, 2 and 3 are quarter-wave plates, half-wave plates and isotropic wave plates (where $\phi_x = \phi_y$), respectively.

Table 5.5 Geometrical dimensions (in mm) for 10 of the unit cells of the metasurface in Fig. 5.19b. OL denotes the outer layers and ML the middle layers. The numbers in the first column correspond to the phase shifts (ϕ_x, ϕ_y) for x and y polarizations, respectively.

(ϕ_x, ϕ_y)	Layer	Lx	Ly	Wx	Wy	Ax	Ay	Bx	By
(45,45)	OL	5	5	0.5	0.5	0.5	0.5	3.5	3.5
	ML	4.75	4.75	0.75	0.75	0.5	0.5	3.5	3.5
(45,135)	OL	5	4.75	0.5	0.5	0.5	0.5	3.25	3.25
	ML	4.75	4.75	0.25	1	1	0.5	2.5	3.75
(45,225)	OL	4.75	5	0.75	0.5	0.25	0.25	2.75	4.25
	ML	4.5	2.75	0.25	0.5	0.5	0.75	1.75	3.25
(45,315)	OL	4.75	4	0.5	0.5	0.5	0.5	2.25	3.75
	ML	4.75	5	0.25	0.5	0.5	0.5	3	2.75
(135,135)	OL	4.75	4.75	0.5	0.5	0.5	0.5	3.25	3.25
	ML	4.75	4.75	0.5	0.5	0.75	0.75	2.75	2.75
(135,225)	OL	4.75	5	0.5	0.75	0.5	0.5	3	3
	ML	2.75	4.5	0.5	0.75	0.25	0.75	3.25	1.75
(135,315)	OL	4	4.75	0.5	0.5	0.5	0.5	3.25	2.25
	ML	5	4.75	0.5	0.25	0.5	0.75	2.5	3
(225,225)	OL	4.75	4.75	0.75	0.75	0.5	0.5	3.25	3.25
	ML	2.75	2.75	0.75	0.75	0.25	0.25	1.75	1.75
(225,315)	OL	4	4.75	0.5	0.5	0.5	0.5	2.75	1.5
	ML	5	2.75	0.75	0.25	0.5	0.25	1.75	4.25
(315,315)	OL	4	4	0.5	0.5	0.5	0.5	2.25	2.25
	ML	5	5	0.25	0.25	0.5	0.5	3	3

A closer inspection of the phase profiles reveals that 6 out of the 16 unit cells correspond to rotated version of each other and thus the metasurface requires the implementation of only 10 unique unit cells. The dimensions of these 10 unit cells are given in Table 5.5 and the fabricated metasurface is shown in Fig. 5.19b.

The OAM multiplexing metasurface has an electrical size that is too large to be practically simulated, as was the case for the PBS metasurface discussed in the previous section. To be able to objectively assess the performance of the fabricated metasurface, we have compared the metasurface measured transmitted fields to the expected transmitted fields produced by an ideal metasurface illuminated by the horn antenna. This was achieved by first measuring the radiated reference field of the exciting horn antenna at the position of the metasurface (but without metasurface). Then, the expected ideal transmitted fields of the metasurface were calculated using the antenna reference field and assuming ideal transmission of flat and

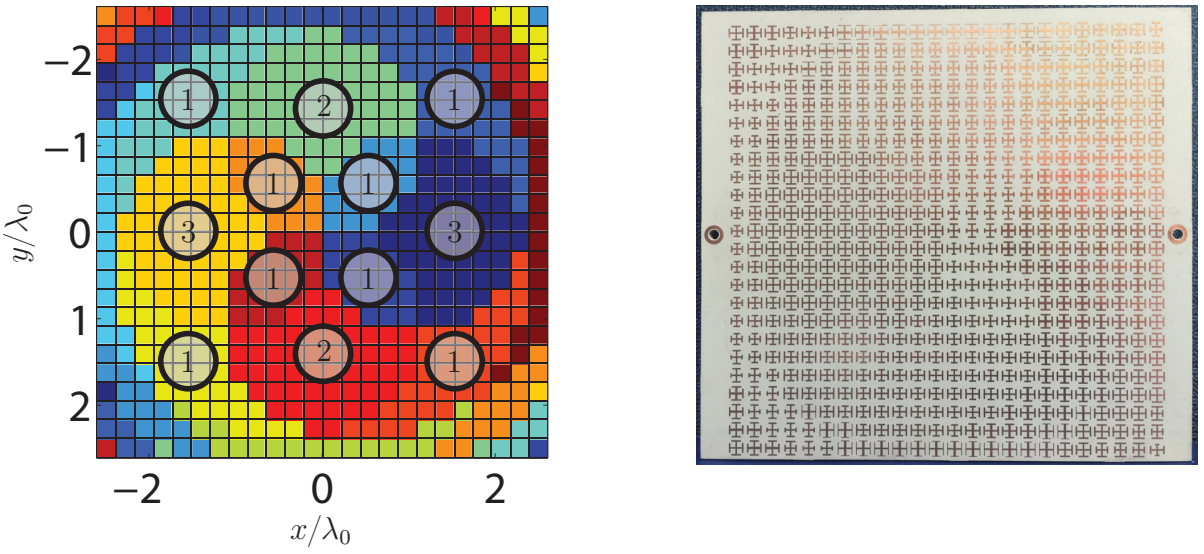

(a) (b)

Figure 5.19 (a) Representation of the 16 different types of unit cells composing the OAM generator metasurface. Each color represents a unit cell with specific phase shifts for x and y polarizations. The unit cells in regions 1 are quarter-wave plates, the ones in regions 2 are half-wave plates and the ones in regions 3 are isotropic. (b) Fabricated metasurface.

unity amplitude and phase profiles as in Figs. 5.18c and 5.18d. The results are reported in Figs. 5.20 and 5.21 which respectively correspond to x and y polarizations. In these two figures, plots (a) and (b) are the expected transmitted fields amplitude and phase and the corresponding measured transmissions, with the metasurface, are shown in plots (c) and (d).

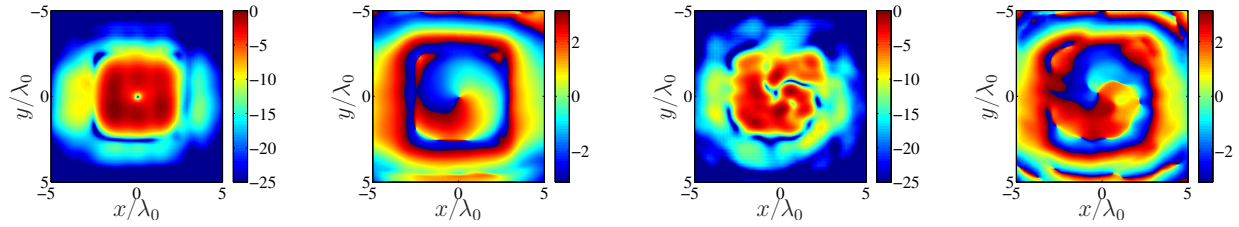

(a) (b) (c) (d)

Figure 5.20 x-polarized simulated (a) amplitude and (b) phase of the expected metasurface scattered field by taking into account the radiation of the horn antenna. Corresponding measured (c) amplitude and (d) phase of the metasurface scattered field.

The measured results are in good agreements with the simulated results. The topological charges of $m = +1$ and $m = -1$ are achieved with a power transmission efficiency near 80% at 10 GHz. Finally, the transmission efficiency of the metasurface was evaluated for

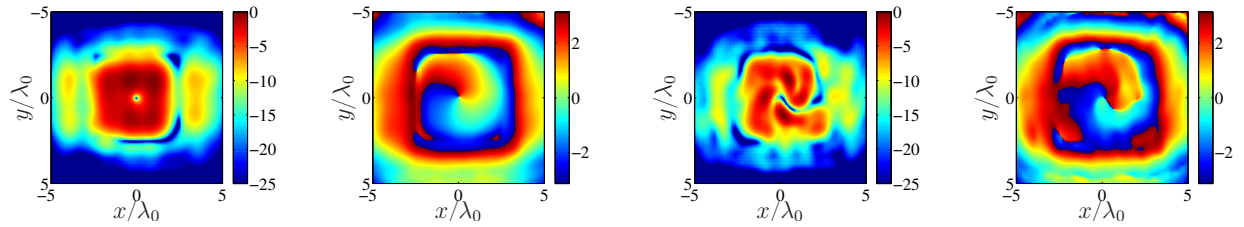

Figure 5.21 y-polarized simulated (a) amplitude and (b) phase of the expected metasurface scattered field by taking into account the radiation of the horn antenna. Corresponding measured (c) amplitude and (d) phase of the metasurface scattered field.

a frequency band between 8 and 12 GHz. The result is reported in Fig. 5.22. The results

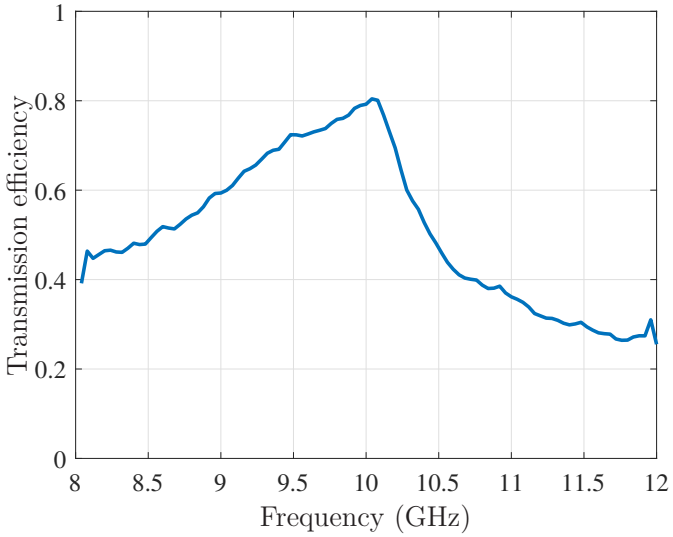

Figure 5.22 OAM multiplexing metasurface transmission efficiency.

presented in Figs. 5.21 and 5.20 as well as in Fig. 5.22 indicate that the response of the OAM is in good agreement with the expected results.

5.5 Coherent Spatial Light Processors

We now present the concept of metasurface spatial processors [151][7] that may be seen as a functional extension of both the Mach-Zehnder interferometer [159] and the transistor [240]. As these devices, this metasurface spatial processor can perform switching and amplifying operations under the application of an external control signal. However, it additionally provides the capabilities of performing these operations remotely, using an electromagnetic

[7]This section is based on a slight modified version of [151, 216].

control wave, and of providing a whole range of metasurface spatial wave transformations such as, for instance, refraction and beam shaping.

The remote nature of the control in this metasurface device contrasts with the local control of previously reported tunable metasurfaces based on electrically tuned scattering particles [241–244], while its Mach-Zehnder and transistor functionalities are totally distinct from those of previously reported optically controlled nonlinear metasurfaces [245, 246].

The metasurface spatial processor modulates the input wave via a coherently superimposed control wave, as done in [69] where the addition of coherent wave on the transmit side of the metasurface is used to suppress undesired reflected or transmitted waves. Similarly, the devices proposed in [247, 248] are also based on coherent superposition of input and control waves. However, they require a thin absorbing plasmonic layer and contra-propagating input and control waves to achieve the required electromagnetic control, and this operation is restricted to waves propagating normally to the surface. In our case, the metasurface is a bianisotropic structure allowing arbitrary input/control waves and the metasurface has the advantage of exhibiting spatial control of the output wave.

The metasurface spatial processor concept is represented in Figs. 5.23c and 5.23d, while the operation of a conventional transistor is represented in Fig. 5.23a and that of an integrated Mach-Zehnder interferometer in Fig. 5.23b. The metasurface spatial processor is associated to the operation of a transistor in the sense that the input wave illuminating the metasurface plays the role of the DC bias (Fig. 5.23c) of the transistor. This input wave opens an "electromagnetic channel" which can be modulated by the application of a control wave (Fig. 5.23d) that modifies the wave transmitted by the metasurface, in a similar fashion as the DC bias of a transistor opens its semiconductor channel that is next modulated by the application of a dynamic voltage (Fig. 5.23a). The Mach-Zehnder interferometer may be used as an optical modulator as well as an optical switch. The operation consists in first splitting the input wave into two beams, one being the reference and the other one having a controllable phase shift (ϕ). Then, the two beams are recombined coherently to form the output wave as a modulated version of the input wave.

In addition to the previously mentioned operation, the coherent superposition of the input wave and the control wave on the metasurface allows for a sophisticated spatial control scattered waves with a great diversity of possible transformations. For instance, the application of the control wave may be used to deflects the transmitted wave, as shown in Figs. 5.23c and 5.23d. Note that the operation example in Figs. 5.23c and 5.23d only represents a particular spatial processing operation. In general, the superposition of the input and control waves can manipulate the amplitude, the phase, the polarization, and the direction of

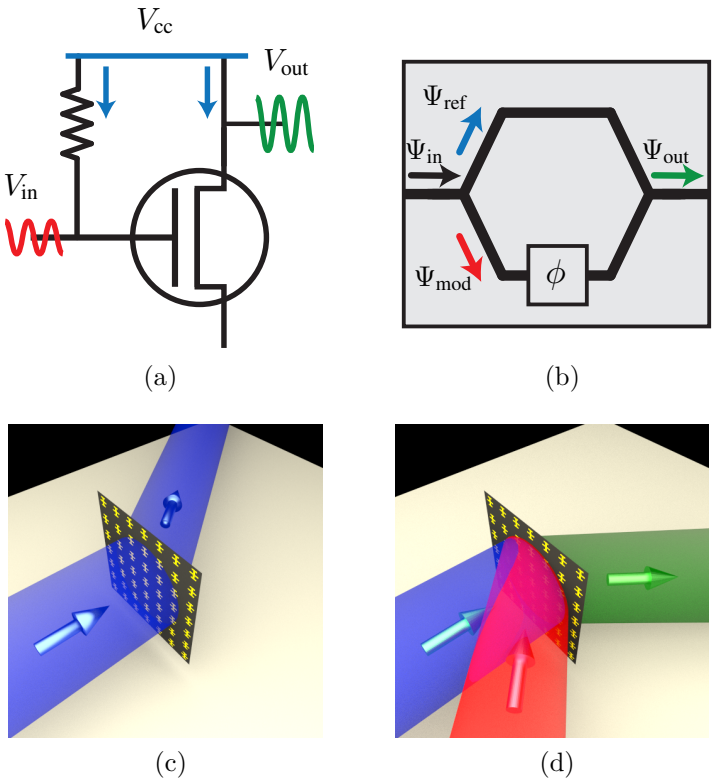

Figure 5.23 Metasurface spatial processor as a conceptual functional extension of both (a) the transistor and (b) the Mach-Zehnder interferometer. (c) Unmodulated metasurface spatial processor transforming an input wave into an arbitrary output wave. (d) Metasurface spatial processor in the modulated regime, where the output wave is modified by a control wave interfering on the metasurface with the input wave.

refraction of the reflected and transmitted waves in an almost arbitrary fashion.

5.5.1 Switch-Modulator Design

To illustrate the metasurface spatial processor concept, we present the case of a switch-modulator processor. In this device, the switching operation is achieved by destructive interference between the input wave (E_{i}) and the control wave (E_{c}) while linear modulation is obtained by tuning the phase of the control wave. In this scenario, assuming that the waves propagate along the z-direction with propagation constant k_0, the complex amplitude of the transmitted wave (E_{t}) changes according to

$$E_{\mathrm{t}} = E_{\mathrm{i}}^{+} + E_{\mathrm{c}}^{+} = e^{jk_0 z} + e^{jk_0 z + j\phi} = 2e^{jk_0 z + j\phi/2} \cos\left(\frac{\phi}{2}\right), \tag{5.5}$$

where E_{i}^{+} and E_{c}^{+}, here assumed to have both unit amplitude, are the transmitted waves due to E_{i} and E_{c}, respectively, in the transmit side of the system, and where ϕ is the phase

difference between E_{i}^{+} and E_{c}^{+}. The amplitude of the transmitted wave therefore spans the range between 0 and 2, which, in the latter limit, corresponds to a gain of 2 compared to the amplitude of the transmitted wave when only E_{i} is illuminating the metasurface.

In a very general case, the input wave and the control may impinge on the metasurface under different angles, which means that the metasurface must be able to transform the two waves independently of each other. Therefore, these two waves must have mutually orthogonal polarizations on the incident side of the metasurface. However, since they must interfere on the transmit side, their polarization must match after transmission by the metasurface. Consequently, the polarization of the control wave is rotated by the metasurface to match that of the input wave. In such circumstances, the metasurface differently affects the x and y polarizations (birefringence) and rotates one polarization without affecting the other one (anisotropic chirality).

In order to realize this operation, two metasurface configuration are considered. The first configuration, shown in Fig. 5.24a, represents the simplest case, where the input wave and the control wave are both normally incident on the metasurface. As may be seen in the figure, on the incident side of the metasurface, the control wave is p-polarized while the input wave is s-polarized. The metasurface is designed to pass both waves with the same transmission coefficient to ensure complete power extinction or maximal amplification. On the transmit side, the polarization of the control wave is rotated so that both transmitted waves are s-polarized to interfere. In this scenario, the phase difference between E_{i}^{+} and E_{c}^{+} is such that the control wave suppresses transmission by destructive interference ($\phi = \pi$). The second configuration, shown in Fig. 5.24b, performs the same operation but for the case of an obliquely impinging control wave, that spatially separates the input and control wave sources, as may be required in practical systems.

An important consequence of the designs in Figs. 5.24 is that their efficiency is inherently limited by reciprocity. This may be understood by considering a normally incident s-polarized wave impinging on the metasurface from the right in Fig. 5.24a, as shown in Fig. 5.25. Because the metasurface transforms the input and control waves with the same transmission coefficient, by design specification, the power of the incident wave in Fig. 5.25 equally splits into two orthogonally polarized waves. Therefore, using the concept of scattering parameters and denoting the left-hand side of the metasurface as port 1 and its right-hand side as port 2, the tensorial backward transmission coefficient $\overline{\overline{S}}_{12}$ reads

$$\overline{\overline{S}}_{12} = \begin{pmatrix} S_{12}^{pp} & S_{12}^{ps} \\ S_{12}^{sp} & S_{12}^{ss} \end{pmatrix} = \frac{\sqrt{2}}{2} \begin{pmatrix} 0 & -1 \\ 0 & 1 \end{pmatrix}, \tag{5.6}$$

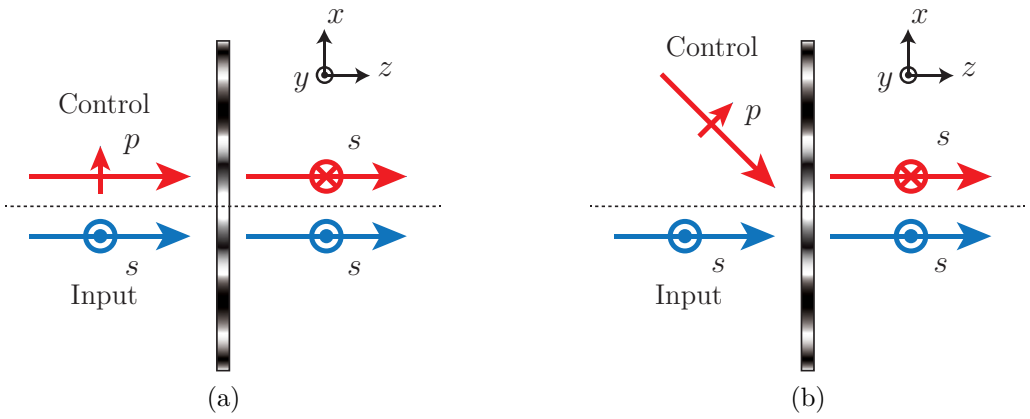

Figure 5.24 Representations of two illustrative switch-modulator metasurface spatial processors. In (a), the input and control waves are both normally incident on the metasurface. The polarization of the control wave is rotated by 90° to match the polarization of the input wave. A π-phase shift is imposed between the two transmitted waves so that they cancel out by destructive interference. In (b), the control wave is obliquely impinging on the metasurface, to avoid the unpractical collocation of the input and control wave sources.

where S_{12}^{pp} corresponds to the backward transmission coefficient from parallel to parallel polarization, S_{12}^{ps} corresponds to the backward transmission coefficient from perpendicular to parallel polarization, etc. Note that the phase difference ϕ can be either present in the control wave or induced by the metasurface, as is here the case (minus sign in S_{12}^{ps}). It follows, by reciprocity, that the transformation in Fig. 5.24a is given by

$$\overline{\overline{S}}_{21} = \overline{\overline{S}}_{12}^{T} = \begin{pmatrix} S_{21}^{pp} & S_{21}^{ps} \\ S_{21}^{sp} & S_{21}^{ss} \end{pmatrix} = \frac{\sqrt{2}}{2} \begin{pmatrix} 0 & 0 \\ -1 & 1 \end{pmatrix}, \tag{5.7}$$

where T is the transpose operator. This reveals that the device has a power efficiency that is limited to 50% and that undesired scattering is unavoidable if the metasurface is reciprocal and lossless. Similar considerations apply in the oblique incidence case of Fig. 5.24b. Note that this constraint may be alleviated in future by using nonreciprocal metasurfaces [96, 97].

Now, we will discuss the implementation of the two structures in Figs. 5.24. These metasurfaces have been simulated, realized and measured and the corresponding results are presented in the two following sections.

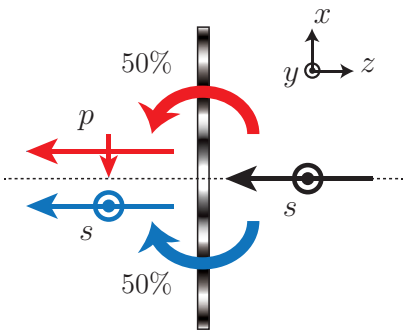

Figure 5.25 Normally incident s-polarized wave impinging on the metasurface in Fig. 5.24a from the right (negative z-direction). The incident wave is transformed, by design, into two mutually orthogonal waves with equal amplitude.

5.5.2 Normally Incident Control

For the transformation in Fig. 5.24a, the metasurface is uniform in the xy-plane since no change in the direction of wave propagation is specified. To synthesize this metasurface and find its susceptibilities, one may specify the fields or, alternatively, use the scattering parameter approach with (2.22) since the metasurface is uniform and that the waves are all propagating normally to the surface. The latter method is used here since the transmission parameters are already provided in (5.6) and (5.7). In addition to those, the reflection coefficient tensors have the form

$$\overline{\overline{S}}_{11} = \frac{\sqrt{2}}{2}\begin{pmatrix} 0 & e^{i\phi_{ps}} \\ e^{i\phi_{sp}} & 0 \end{pmatrix}, \quad \overline{\overline{S}}_{22} = \begin{pmatrix} e^{i\phi_{pp}} & 0 \\ 0 & 0 \end{pmatrix}, \tag{5.8}$$

where ϕ_{ab} $(a, b = s, p)$ are reflection phases corresponding to the specified polarizations, which may be left as free parameters since they are not essential for the required transformations. The metasurface susceptibilities can be straightforwardly found by inserting the scattering parameters (5.6), (5.7) and (5.8) into (2.22). The corresponding metasurface is fully bianisotropic, with 16 nonzero susceptibility tensor elements (or less depending on the values of ϕ_{ps}, ϕ_{sp} and ϕ_{pp}), which are omitted here for briefness.

The periodically repeated scattering particle required to satisfy the specifications has been implemented using a metallic unit cell for an operating frequency of 16 GHz. It is worth noting that because the metasurface is bianisotropic, the unit cell is necessarily asymmetric in the longitudinal direction, as discussed in Sec. 3.3. Therefore, the Jerusalem crosses of the three metallic layers are different from each other. The corresponding dimensions of the Jerusalem crosses are reported in Table 5.6 and the realized metasurface is shown in Figs. 5.26

along with a representation of a unit cell. As seen in Fig. 5.26a, the middle Jerusalem cross

Table 5.6 Geometrical dimensions (in mm) for the unit cell of the metasurface in Fig. 5.26a. The layers order goes in the positive z-direction.

	d	Lx	Ly	Wx	Wy	θ	Ax	Ay	Bx	By
Layer 1	8	4	4	1	1	0	0	0	-	-
Layer 2	8	4	6	1.5	1.5	45°	0	0	-	-
Layer 3	8	6.8	5	1.6	1.5	0	0	0	-	-

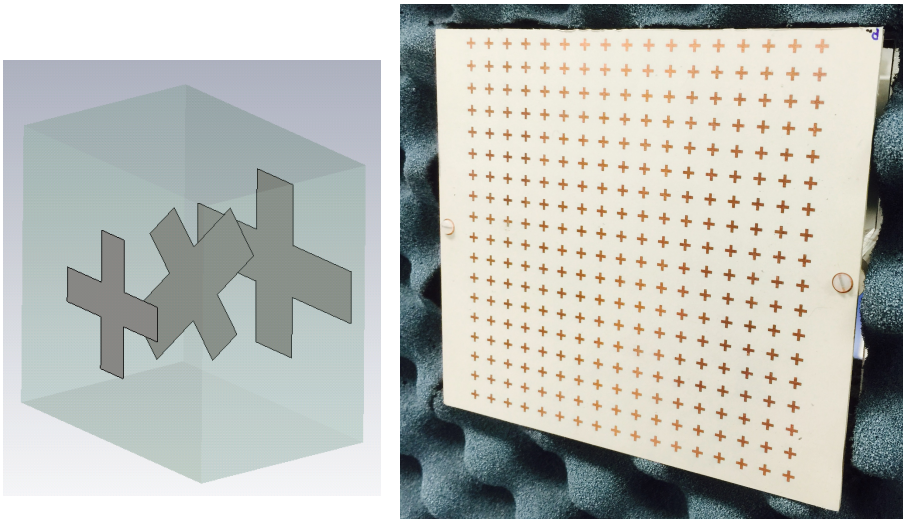

(a) (b)

Figure 5.26 Switch-modulator spatial metasurface processor with normally incident control wave (Fig. 5.24a). (a) Three-layer unit cell designed for an operating frequency of 16 GHz. (b) Fabricated structure, composed of 17 × 18 unit cells, on the measurement setup.

is rotated by 45° with respect to the outer layers so as to produce the chirality that is required to rotate the polarization of the control wave.

The numerical simulations of the metasurface in Fig. 5.26b are plotted in Fig. 5.27, where the metasurface lies at $z = 0$. In this set of figures, the plots on the left correspond to s-polarized waves, while the plots on the right correspond to p-polarized waves. In plots (a) and (b), the metasurface is illuminated only by the control wave. In plots (c) and (d), only the input wave illuminates the metasurface. And in plots (e) and (f), both input and control waves are superimposed. The arrows indicate the direction of wave propagation.

Figure 5.27b shows the control wave (initially p-polarized) that is normally incident onto the metasurface. Since the metasurface rotates the polarization of this wave by 90°, none

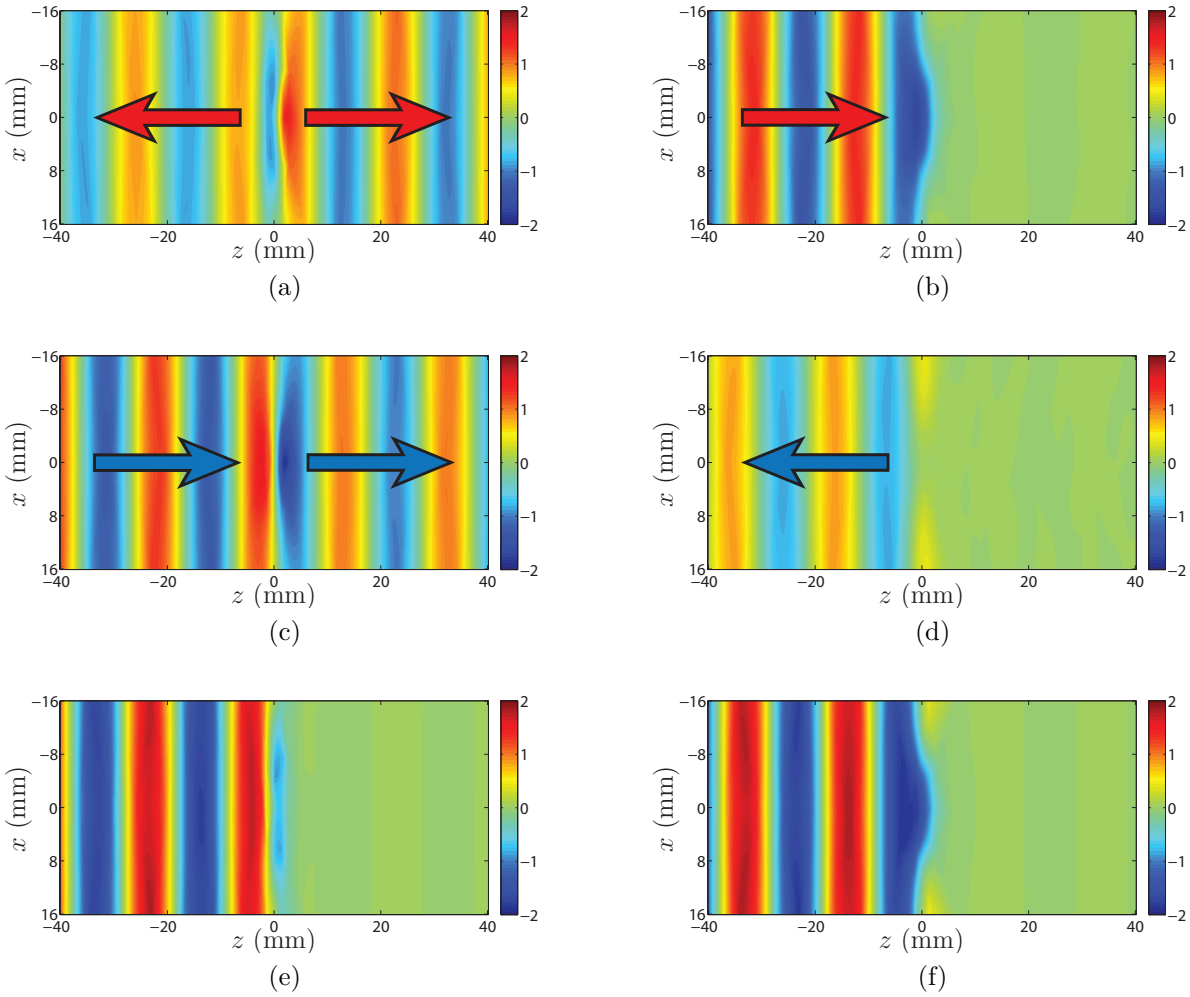

Figure 5.27 Full-wave simulation of the structure in Fig. 5.26b. S-polarized fields are plotted on the left, p-polarized fields on the right. The metasurface is located in the plane $z = 0$. In (a) and (b) only the control wave is present. In (c) and (d) only the input wave is present. In (e) and (f) both waves are superimposed.

of its p-polarized component is transmitted. We see in Fig. 5.27a that the control wave is effectively transformed into s-polarization, almost half of it being reflected and the other half being transmitted. Figure 5.27c shows the input wave (initially s-polarized) impinging on the metasurface, with half of it being transmitted without rotation of polarization and the other half being reflected with p-polarization, as shown in Fig. 5.27d. One should notice that, the input and control waves on the right-hand sides of Figs. 5.27a and 5.27c have both the same amplitude but opposite phases. As a result, as the two waves simultaneously impinge on the metasurface, they destructively interfere at the output so as to suppress power transmission, as evidenced in Fig. 5.27e. Note that, when these two waves are incident on the metasurface, the p-polarized transmission is also suppressed, as can be seen in Fig. 5.27f.

The corresponding experimental results are presented in Fig. 5.28a, where the *s*-polarized transmission is measured when the metasurface is illuminated by the input wave, the control wave and the combination of the two, respectively. The spatial metasurface switch exhibits an isolation of over 35 dB, as evidenced by the dashed-dot black line. The corresponding spatial metasurface amplification results, obtained by tuning the phase of the control signal for constructive interference at the output, is only shown here in the case of perfect constructive interference (dotted green line). In this case, a maximum gain of 2 (or 6 dB) is achieved. Figure 5.28b shows the bandwidth of this metasurface in the aforementioned three different operation states: ON state (only input wave), OFF state (destructive interference) and gain state (constructive interference). Note that the apparent asymmetric behavior of the OFF and gain states is the result of the logarithmic scale which makes the OFF state converge to $-\infty$ for an ideal destructive interference.

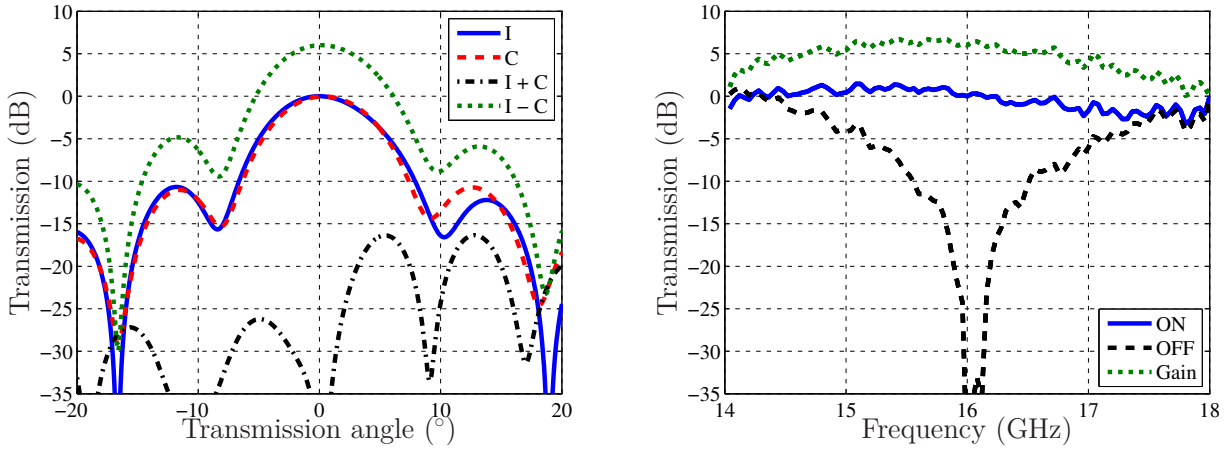

Figure 5.28 Measured *s*-polarized transmission for the metasurface of Fig. 5.26b with the metasurface illuminated by the input wave (solid blue line), the control wave (dashed red line), the destructive (dashed-dot black line) and constructive (dotted green line) superpositions of the two, respectively, at 16 GHz. (b) ON state (input wave only), OFF state (destructive interference) and gain (constructive interference). All curves are normalized with respect to the ON state at 16 GHz.

5.5.3 Obliquely Incident Control

The oblique control transformation in Fig. 5.24b can be synthesized following the same procedure as that described for the previous case. However, the design of this metasurface is more complicated since it must change the direction of propagation of the control wave

but not that of the input wave. Consequently, the metasurface is now nonuniform (but still periodic), which leads to more complicated bianisotropic susceptibility tensor functions.

In order to realize the metasurface, the spatially periodic scattering parameters corresponding to the required transformation are discretized to form a supercell made of four unit cells. Following the second synthesis approach discussed in Sec. 3.1, each of the four unit cells induces a different transmission phase shift for the control wave so that it gets normally transmitted across the metasurface. Accordingly, the phase shift between adjacent unit cells is $\pi/2$ so that the four unit cells cover a complete phase cycle. It turns out that due to symmetries, the two first unit cells correspond to the 90° counterparts of the two last unit cells, which simplifies the implementation of the metasurface. The dimensions of the two realized unit cells are given in Table 5.7, while the fabricated metasurface as well as a representation of the supercell are shown in Figs. 5.29. Note that the operation frequency is 12 GHz. At this frequency and for this unit cell size, the incidence angle of the control wave is 50°.

Table 5.7 Geometrical dimensions (in mm) for the first two unit cells of the metasurface in Fig. 5.29a. The layers order goes in the positive z-direction.

		d	Lx	Ly	Wx	Wy	θ	Ax	Ay	Bx	By
Cell 1	Layer 1	8	4.5	4.5	0.5	0.5	0	0.25	0.25	2	3
	Layer 2	8	6	8	1	1	45°	0	0	-	-
	Layer 3	8	5.5	5.5	0.5	0.5	0	0.25	0.25	2	3
Cell 2	Layer 1	8	4.5	4.5	0.5	0.5	0	0.25	0.25	2	2
	Layer 2	8	7	3	1	1	45°	0	0	-	-
	Layer 3	8	5.5	5.5	0.5	0.5	0	0.25	0.25	2	3

From Table 5.7 we can easily deduce the dimensions of the third and fourth unit cells. They respectively share the same dimensions as those of the first and second unit cells at the exception that their respective layer 2 is rotated by 90°. Thus, the dimensions of the unit cells 3 and 4 can be easily obtained by using $\theta = -45°$ (instead of $\theta = 45°$) for the layer 2 of unit cells 1 and 2, respectively. Since these unit cells are simulated in a perfectly periodic and uniform environment, it is thus expected that the final metasurface exhibits some undesired scattered fields compared to the expected ideal specifications because of spurious coupling between adjacent unit cells.

The numerical simulations of the metasurface are presented in Fig. 5.30, where the plots on the left correspond to s-polarized waves and the plots on the left correspond to p-polarized waves. As before, plots (a) and (b) correspond to control wave illumination only. Plots (c) and (d), input wave illumination only. And in plots (e) and (f), both input and control waves

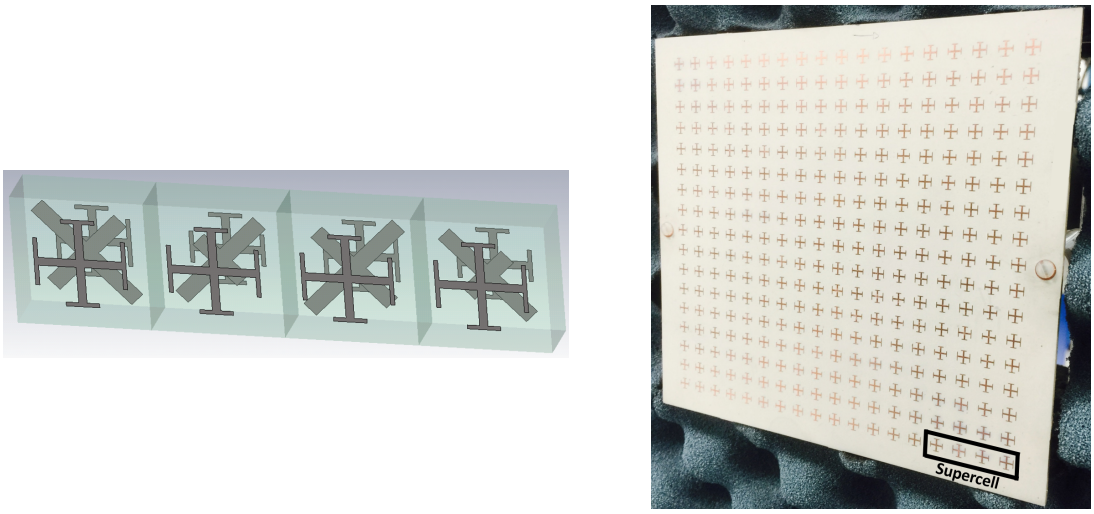

(a) (b)

Figure 5.29 Switch-modulator spatial metasurface processor with obliquely incident control wave (Fig. 5.24b). (a) Representation of the supercell composed of four unit cells, the structure is realized for an operating frequency of 12 GHz. (b) Fabricated structure, with 17×18 unit cells, on the measurement setup. The black box indicates where the supercell is on the metasurface and how it is periodically repeated.

are superimposed. The arrows indicate the direction of wave propagation.

The control wave (initially p-polarized) is obliquely incident on the metasurface with a 50° angle, as shown in Fig. 5.30b. Since the metasurface rotates the polarization of the control wave, almost no p-polarized component is transmitted (at the exception of a small parasitic transmission and reflection). In Fig. 5.30a, we see that the control wave is effectively transformed into s-polarization and that almost half of the wave is normally transmitted while the other half is normally reflected. In Fig. 5.30c, the input wave (initially s-polarized) is incident on the metasurface and half of it is transmitted without rotation of polarization. The other half of the input wave is mostly reflected at a 50° angle with p-polarization, as shown in Fig. 5.30d.

One should notice that, on the right-hand side of Figs. 5.30a and 5.30c, the input wave and the control wave have both the same amplitude but opposite phases. When the two waves are simultaneously impinging on the metasurface, the results is a cancellation of all s-polarized transmitted power, as shown in Fig. 5.30e.

Finally, the experimental results are presented in Fig. 5.31a, where the metasurface is illuminated by the input wave (solid line), the control wave (dashed line) and the combination of the two (dashed-dot line, for the destructive interference case, and dotted line, for the

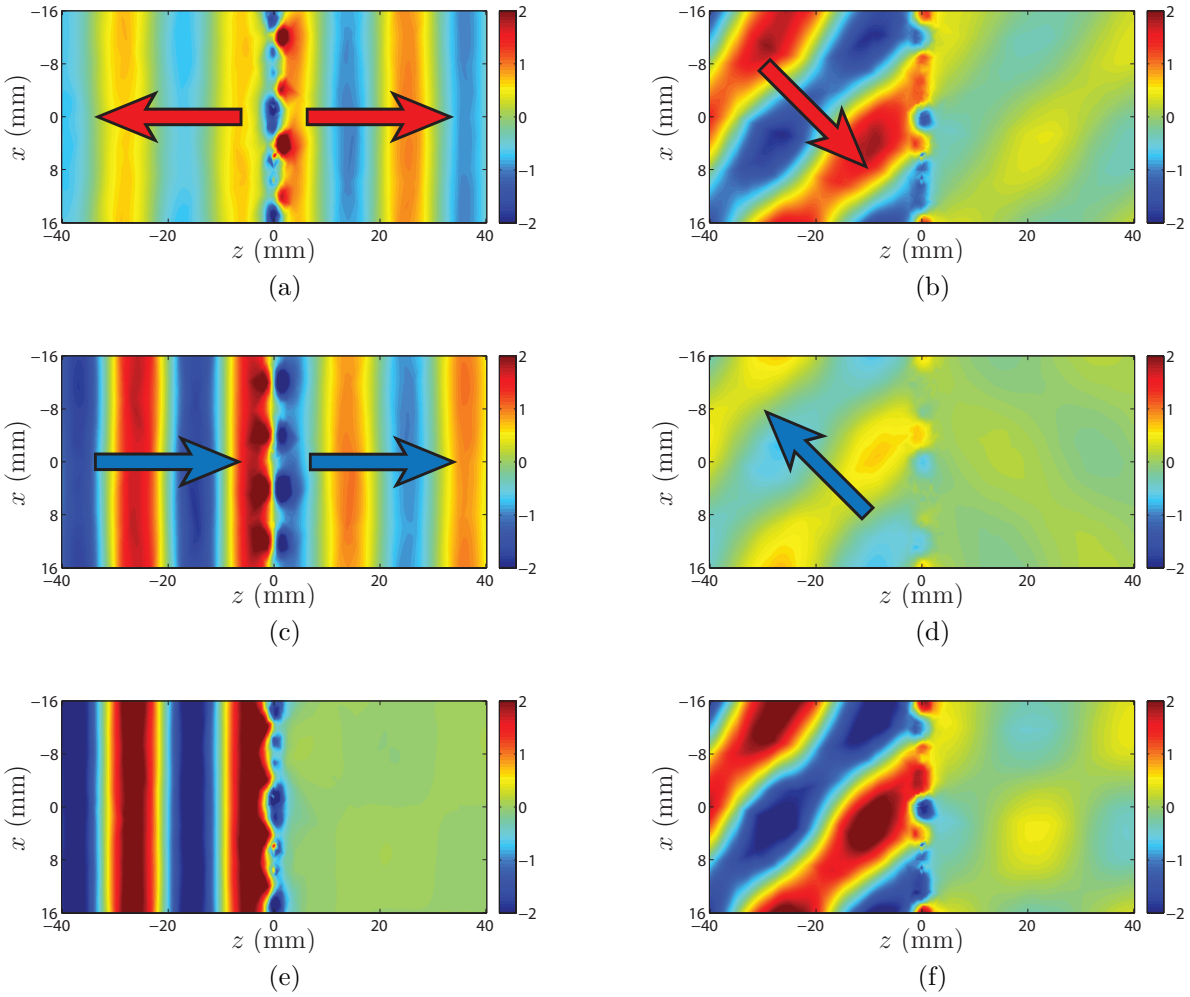

Figure 5.30 Full-wave simulation of the structure in Fig. 5.29b. S-polarized fields are plotted on the left, p-polarized fields on the right. The metasurface is located in the plane $z = 0$. In (a) and (b) only the control wave is present. In (c) and (d) only the input wave is present. In (e) and (f) both waves are superimposed.

constructive interference case). As before, an isolation of over 35 dB is obtained as well as a gain of 6 dB in the direction of propagation. Figure 5.31b shows the bandwidth of this metasurface in the three different operation states: ON state (only incident wave), OFF state (destructive interference) and gain state (constructive interference).

The expected responses of the two metasurfaces are in very good agreement with the corresponding simulated and measured responses.

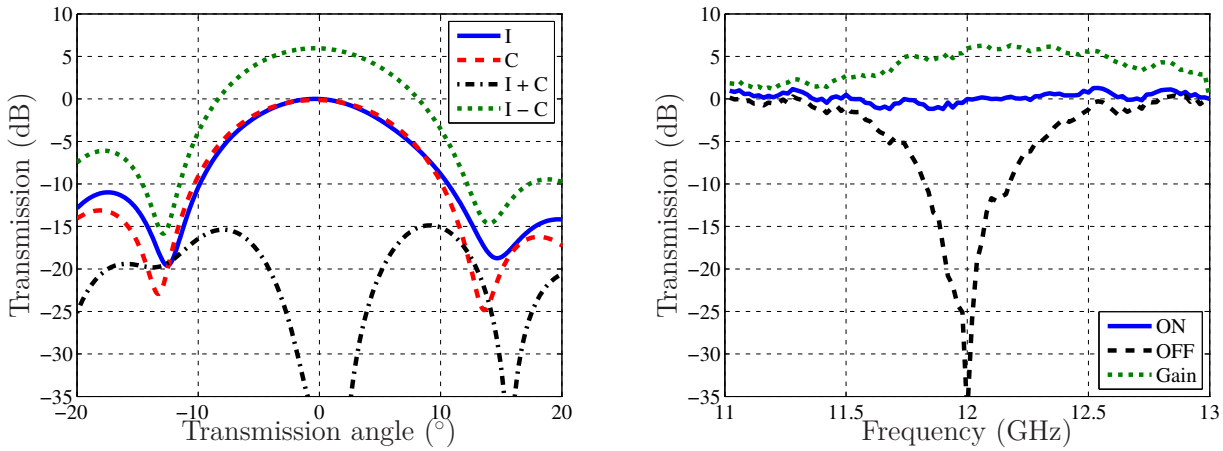

Figure 5.31 Measured *s*-polarized transmission for the metasurface of Fig. 5.29b with the metasurface illuminated by the input wave (solid blue line), the control wave (dashed red line), the destructive (dashed-dot black line) and constructive (dotted green line) superposition of the two, respectively, at 12 GHz. (b) Measured bandwidth for the ON state (only input wave), OFF state (destructive interference) and gain (constructive interference). All curves are normalized with respect to the ON state at 12 GHz.

5.6 Space-Wave Routing via Surface Waves

All the metasurface presented so far as well as the vast majority of metasurface designs and applications reported to date have been restricted to isolated metasurfaces, i.e. single metasurface structures performing specific electromagnetic transformations. In order to extend the range of these transformations, we propose the concept of a *metasurface system*, namely a combination of several metasurface structures collectively exhibiting properties that would be unattainable with a single metasurface. Specifically, we present a metasurface system composed of three juxtaposed metasurfaces, that *routes* space-wave beams, between different locations, via surface waves. Such a system may be used, for instance, to laterally shift or modulate the beamwidth of scattered waves[8].

In this section, we will first introduce the concept of space-wave routing via surface waves in a metasurface system. Then, we will discuss the synthesis technique for the design of such a system, which will be used to demonstrate system routing in an "electromagnetic periscope". Finally, two additional potential applications, namely a compact beam expander and a multi-wave refractor, will be presented.

[8]This section is based on a slightly modified version of [218].

5.6.1 Space-Wave Routing Concept

The fundamental idea, which is depicted in Fig. 5.32, consists in converting an incoming space wave into a surface wave, propagating this surface wave between two points along a desired path, and then converting it back, with possible other transformations, into an outgoing space wave. This concept may be used to laterally shift reflected or transmitted waves (electromagnetic periscope), modulate the width of beams, or enable multiple refraction, in a very compact fashion, as will be discussed thereafter. In the system depicted in Fig. 5.32, the

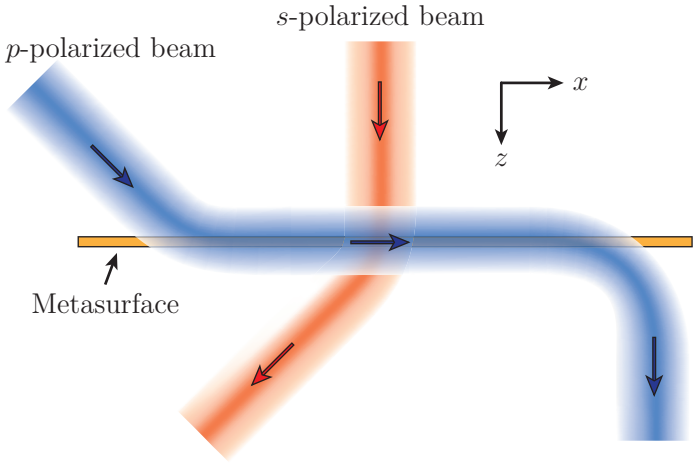

Figure 5.32 Concept of a metasurface system performing the operations of space-wave routing via surface waves for p-polarized beams and generalized refraction for s-polarized beams.

metasurface is assumed to be monoanisotropic diagonal, and hence birefringent, allowing for the independent control of s and p polarizations. The metasurface system may be designed, for instance, to route p-polarized waves and refract (or perform any another transformation on) s-polarized waves.

We shall now describe the space-wave routing concept in more details. Let us consider the optical system depicted in Fig. 5.33a, which consists of a dielectric waveguide with two prisms placed at different locations above it. This system may be used to perform the routing operation described in Fig. 5.32. Assume that an input beam Ψ_{in} is impinging on the left prism at an angle $\theta > \theta_{\text{c}}$, where θ_{c} is the angle of total internal reflection. An evanescent wave with wavenumber k_x, corresponding to that of the incident wave, is formed between the prism and the waveguide due to total internal reflection. This evanescent wave then couples to a waveguide mode with matched k_x, and the resulting wave propagates along the waveguide in the x-direction. The amount of coupling between the incident space wave and the guided wave is proportional to the distance d between the prism and the waveguide, and is usually less than unity, leading to a nonzero reflected wave Ψ_{r}. Farther along the waveguide, the guided wave is transformed back into an output space wave Ψ_{out} by the second prism by the

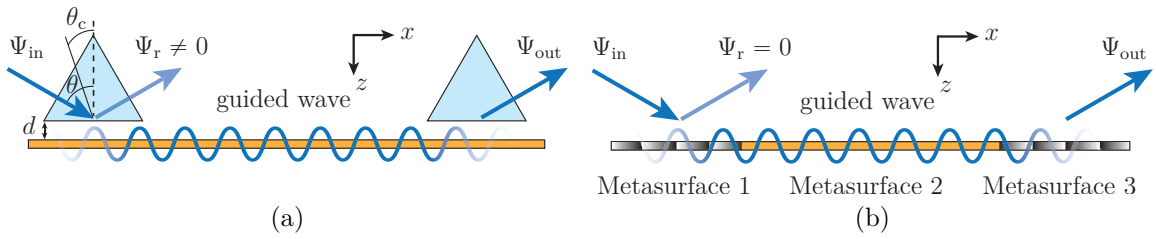

Figure 5.33 Representations of two optical systems performing the same wave routing operation. (a) Combination of two prisms and a dielectric waveguide. (b) Composite metasurface, including two spatially modulated metasurfaces placed at the ends of a guiding metasurface.

reverse mechanism.

We introduce here the metasurface system depicted in Fig. 5.33b to perform the same operation in a much more compact (purely planar) and (ideally) perfectly reflectionless fashion. This system consists of three different metasurfaces juxtaposed to each other. The input space wave is coupled into a guided surface wave by a spatially modulated metasurface. The middle metasurface is a surface-wave guiding structure that propagates the guided wave in the x-direction. Finally, another spatially modulated metasurface transforms the guided wave back into a space wave at the other end of the system.

5.6.2 Metasurface System Synthesis

Exact Synthesis Based on GSTCs

The metasurface system introduced above can be rigorously synthesized using the GSTCs method so as to provide the exact medium parameters performing the transformation depicted in Fig. 5.33b. As said above, the metasurface system is birefringent and may consequently be described by the susceptibility relations given in (2.18).

Let us now synthesize the space-wave to surface-wave transformation performed by the first metasurface in Fig. 5.33b. Let us assume a p-polarized wave ($\boldsymbol{E} \in xz$-plane and $\boldsymbol{H} \parallel \hat{y}$), to be routed (Fig. 5.32), which corresponds to the synthesis relations (2.18a) and (2.18d). In this case, the tangential electromagnetic fields, at $z = 0$, are

$$E_{x,\mathrm{a}} = A_\mathrm{a} \frac{k_{z,\mathrm{a}}}{k_0} e^{-jk_{x,\mathrm{a}}x} \quad \text{and} \quad H_{y,\mathrm{a}} = A_\mathrm{a} e^{-jk_{x,\mathrm{a}}x}/\eta_0, \tag{5.9}$$

where A is a complex constant, k_x and k_z are the tangential and longitudinal wavenumbers, respectively, η_0 and k_0 are the impedance and wavenumber of free space, respectively, and the subscript a = i, r, t denotes the incident, reflected and transmitted waves, respectively. We shall consider the transformation of an incident space wave with $A_\mathrm{i} = 1$ and $k_{x,\mathrm{i}} = k_0 \sin\theta_\mathrm{i}$,

where $\theta_\mathrm{i} = 45^\circ$ is the incidence angle, into a surface wave with $A_\mathrm{t} = 0.728$ and $k_{x,\mathrm{t}} = 1.2k_0$. The corresponding longitudinal k-component is found as $k_{z,\mathrm{a}} = \sqrt{k_0^2 - k_{x,\mathrm{a}}^2}$ which, in the case of the transmitted wave, is an imaginary quantity corresponding to wave evanescence perpendicular to the metasurface and surface-wave propagation in the x-direction. The value 0.728 was derived to ensure a purely passive (although lossy) reflectionless ($A_\mathrm{r} = 0$) metasurface[9].

Finite-difference frequency-domain (FDFD) simulations [163] are used to analyze the response of the synthesized metasurface. Figure 5.34a shows how an obliquely incident Gaussian beam is transformed into a surface wave on the transmit side of the metasurface. Note that the transformation in Fig. 5.34a is "perfect" in the sense that no parasitic diffraction order is present. However, the surface wave only exists in the region where the Gaussian beam illuminates the metasurface and does not propagate farther along the structure. This is because the metasurface was synthesized assuming an incident plane wave illuminating the entire structure and not just a small portion of it, as is the case with a Gaussian beam. Consequently, the surface wave is restricted to the region within the waist of the incident beam and cannot propagate beyond its excitation zone as it is not an eigen-mode of this metasurface. The generation of spurious diffraction orders is suppressed by the lossy nature of the metasurface.

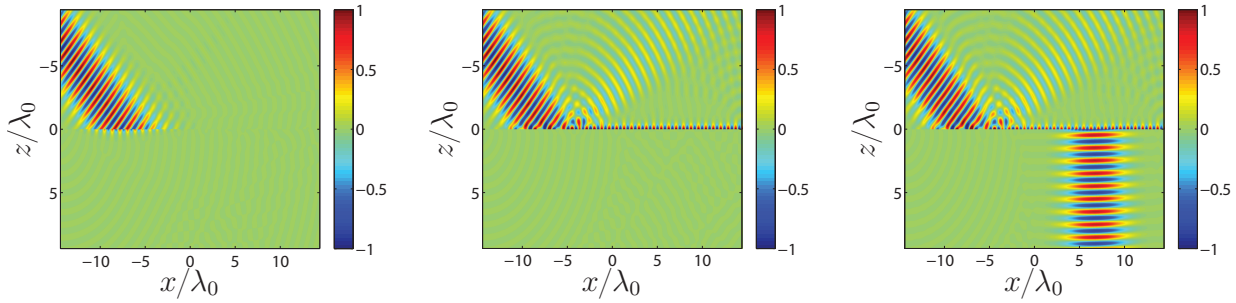

Figure 5.34 Finite-difference frequency-domain (FDFD) simulations showing the real part of H_y in the case of (a) the conversion of a space wave into a localized surface wave, (b) the coupling of the surface wave into a guided wave that propagates along a juxtaposed metasurface, and (c) the propagating surface wave is then transformed back into a space wave.

In order to propagate the surface wave farther along the surface, it is necessary to introduce a discontinuity in the metasurface or, in other words, to place a second metasurface next to

[9]This proviso was found by inserting (5.9) into (2.18) with specified parameters A_i, $k_{x,\mathrm{a}}$ and $k_{z,\mathrm{a}}$ and solving for A_t such that $\mathrm{Im}(\chi_{\mathrm{ee}}^{xx}), \mathrm{Im}(\chi_{\mathrm{mm}}^{yy}) < 0$. This shows that the space wave cannot be transformed into a surface wave without dissipation.

the first one, as shown in Fig. 5.33b. Thus, the first metasurface is synthesized as a space-wave to surface-wave transformer to convert the incident wave into a guided wave, while the second metasurface is synthesized as a surface-wave guiding structure, to route the wave along the overall structure. This operation is achieved, considering the juxtaposed (first and second) metasurface system as a composite metasurface, by specifying the fields as follows. The incident field is defined with the parameters $A_\mathrm{i} = U(-x - 5\lambda_0)$ and $k_{x,\mathrm{i}} = k_0 \sin\theta_\mathrm{i}$ ($\theta_\mathrm{i} = 45°$), where $U(x)$ is the unit step function. The unit step function is used here to create a discontinuity in the incident field at the position $-5\lambda_0$ on the metasurface. Additionally, we set $A_\mathrm{t} = 0$, $A_\mathrm{r} = 0.728$ and $k_{x,\mathrm{r}} = 1.2k_0$[10]. Inserting these field specifications into (2.18) and performing an FDFD simulation for an incident Gaussian beam impinging on the metasurface at the position $-7\lambda_0$ yields the result presented in Fig. 5.34b. As can be seen, the surface wave effectively couples into the second metasurface where it now propagates as a guided wave. Note that the presence of the discontinuity between the two metasurfaces introduces some spurious scattering of the incident wave, which could be avoided using a smooth transition. At this stage, it is important to point out the fact that a metasurface can theoretically support a guided wave that would exist only on *one* of its two sides, as seen in Fig. 5.34b. This is rather unconventional since most guided waves generally exhibit evanescent fields on both sides of the interface, as it is the case for surface plasmon polaritons [159]. It is therefore speculated that a bianisotropic metasurface could support different guided waves (with different propagation constants) on its two sides due to its longitudinal asymmetry.

Finally, the energy carried by the surface wave is extracted and transformed back into a space wave by the third metasurface in Fig. 5.33b upon specifying a nonzero transmitted wave with parameters $A_\mathrm{t} = 0.6 \cdot \exp[4(x - 6.5\lambda_0)^2/5]$ and $k_{x,\mathrm{t}} = k_0 \sin\theta_\mathrm{t}$, where the transmission angle is chosen here to be $\theta_\mathrm{t} = 0$. The simulation result is shown in Fig. 5.34c.

To synthesize the second metasurface so that it also refracts the s-polarized wave, as shown in Fig. 5.32, one would simply need to insert the s-counterpart of (5.9) into (2.18b) and (2.18c), as conventionally done for generalized refractive metasurfaces. In this case, assuming a non-zero transmission angle, the metasurface becomes globally nonuniform in the x-direction, although it is seen as perfectly uniform to the p-polarized wave (birefringence). For conciseness, we will ignore the synthesis of the s-polarized transformation in what follows to concentrate only on the synthesis of the p-polarized transformation.

The electric and magnetic susceptibilities of the composite metasurface corresponding to the simulation in Figs. 5.34c, are plotted in Fig. 5.35a and 5.35b, respectively. The conversion

[10] In this second example, the surface wave is placed on the reflection side of the metasurface to later permit an easier design of the third metasurface.

from space wave to surface wave occurs in the portion of the metasurface where $x < -5\lambda_0$. In this region, the metasurface (first metasurface) is spatially varying and exhibits nonuniform loss as evidenced by the oscillating negative imaginary parts of the susceptibilities. From $x = -5\lambda_0$ to approximatively $x = 0$, the metasurface (second metasurface) supports the propagation of a surface wave. It is interesting to note that, in this region, the metasurface is perfectly uniform, passive and lossless, with susceptibilities given by the following simple relations $\chi_{\mathrm{ee}}^{xx} = 2j/k_{z,\mathrm{r}}$ and $\chi_{\mathrm{mm}}^{yy} = 2jk_{z,\mathrm{r}}/k_0^2$, where $k_{z,\mathrm{r}}$ is the purely imaginary propagation constant of the surface wave in the longitudinal direction. Finally, starting from $x > 0$, the

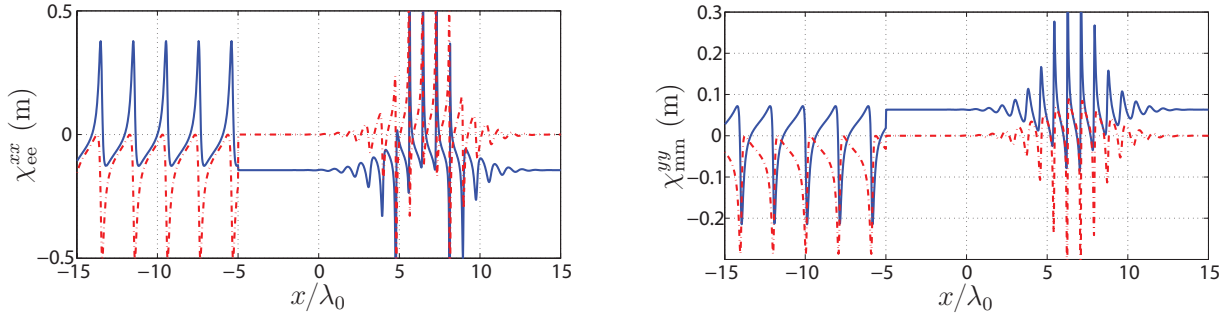

Figure 5.35 Electric (a) and magnetic (b) susceptibilities corresponding to the transformation presented in Fig. 5.34c. The solid blue lines are the real parts while the dashed red lines are the imaginary parts.

metasurface (third metasurface) becomes spatially varying again, allowing part of the energy conveyed by the surface wave to progressively leak out to form the space wave. Here, the susceptibilities have values oscillating between positive and negative imaginary parts. This indicates that the metasurface is successively varying between gain and loss. The presence of loss, as in the first part of the metasurface, is generally required to suppress undesired diffraction orders. The presence of active regions, corresponding to gain in the last part of the metasurface, is due to the way the fields were specified in the synthesis. Indeed, the surface wave (reflected wave) was specified with *constant* amplitude over the entire metasurface, including in the third region, and it is therefore not surprising that gain is required in the region where the transmitted space wave is generated and where it draws power from the surface wave. The metasurface could be made perfectly passive by specifying a surface wave with progressively decreasing amplitude as its energy is being leaked out. In that case, the third metasurface would actually act as a leaky-wave antenna.

Simplified Synthesis Based on Phase-Gradient and Guiding-Wave Structures

The GSTCs-based metasurface synthesis technique yields the exact susceptibilities performing the specified transformation. However, the resulting susceptibilities may, in some situations, be difficult to realize. For instance, the metasurface described by the susceptibilities in Figs. 5.35 presents spatially varying electric and magnetic losses which may be challenging to implement. Moreover, the generation of the transmitted space wave also requires gain as is evidenced by the positive imaginary parts of the susceptibilities on the right-hand side of Figs. 5.35. For these reasons, we next propose an alternative synthesis method for space-wave to surface-wave transformations performed by the two end metasurfaces in Fig. 5.33b. This method will result in a slightly different design that will be much easier to realize but comes at the cost of a lower efficiency.

The waveguiding structure (second metasurface in Fig. 5.33b) will be realized using the susceptibilities found previously since these susceptibilities are exact and easy to realize, as seen in Fig. 5.35. However, the structure will require some optimization to account for deviations from the ideal response due to its nonzero thickness. This may be achieved by following design procedures routinely used in the implementation of slow-wave structures [249, 250], as will be discussed thereafter.

In order to transform the incident space wave into a surface wave with a specific propagation constant along the metasurface, we will use here a simple phase-gradient structure which is equivalent to the second synthesis approach discussed in Sec. 3.1. Let us consider the generalized law of refraction [66], that can be expressed, using the transverse wavenumber of the incident and refracted waves and the effective wavenumber of the phase gradient-structure, K, as

$$k_{x,\mathrm{t}} = k_{x,\mathrm{i}} + K, \tag{5.10}$$

where $K = 2\pi/P$ with P being the phase-gradient period of the metasurface. This period is designed such that the specified incident wave is refracted at a specified angle, i.e. $P = \lambda_0/(\sin\theta_{\mathrm{t,spec}} - \sin\theta_{\mathrm{i,spec}})$. From (5.10), we express the normalized transverse wavenumber of the transmitted wave as a function of K and the incidence angle as

$$\frac{k_{x,\mathrm{t}}}{k_0} = \sin\theta_{\mathrm{i}} + \frac{K}{k_0}, \tag{5.11}$$

which allows one to determine the transverse wavenumber for *any* incidence angle θ_{i}. As an illustration, relation (5.11) is plotted in Fig. 5.36 as a function of the incidence angle for the specified angles $\theta_{\mathrm{i,spec}} = 0$ and $\theta_{\mathrm{t,spec}} = 45°$. The region in blue, where $|k_{x,\mathrm{t}}/k_0| < 1$, corresponds to space-wave modes. Outside of this region, $|k_{x,\mathrm{t}}/k_0|$ is larger than 1 and the

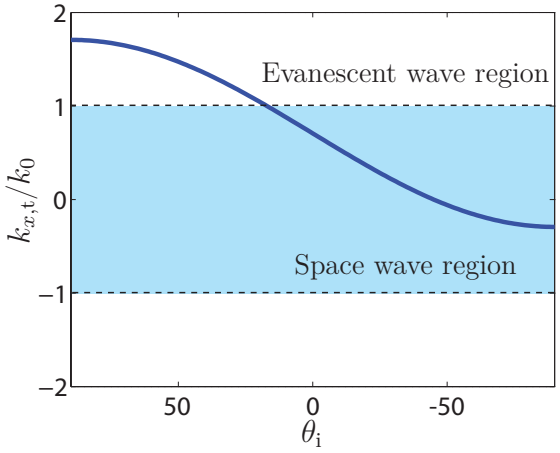

(a)

Figure 5.36 Normalized transverse wavenumber of the transmitted wave versus incidence angle according to Eq. (5.11) for a phase-gradient metasurface designed with the specified angles $\theta_{\mathrm{i,spec}} = 0$ and $\theta_{\mathrm{t,spec}} = 45°$.

longitudinal wavenumber $k_{z,\mathrm{t}} = \sqrt{k_0^2 - k_{x,\mathrm{t}}^2}$ is therefore imaginary, corresponding to evanescent waves. This shows that a simple phase-gradient metasurface can be used as a converter between a space wave and a surface wave when the metasurface wavenumber K and the incidence angle θ_i are properly chosen [251–253].

The three-metasurface system in Fig. 5.33b may therefore be realized as follows. The first metasurface is designed as a phase-gradient metasurface with increasing phase in the positive x-direction; this positive phase ramp increases the momentum of the incident wave (in the x-direction) so as to transform it into a surface wave. The second metasurface is designed to support the propagation of a surface wave with the same wavenumber. Finally, the third metasurface is again designed as a phase-gradient structure but this time with increasing phase in the negative x-direction, which reduces the momentum of the surface wave and hence transforms it back into a space wave.

5.6.3 The "Electromagnetic Periscope"

For the realization of the metasurface system, and particularly the realization of the space-wave to surface-wave converters (metasurfaces 1 and 3), we use, for simplicity, the approximate synthesis technique presented in Sec. 5.6.2, rather than the exact but more problematic technique based on GSTCs.

A schematic of the metasurface system is presented in Fig. 5.37. The figure shows the conceptual operation of the structure with momentum "push" (K_1) and momentum "pull"

(K_2) induced by the first and last metasurfaces, respectively, and the surface-wave guidance in the middle metasurface. We shall now design the metasurface system for the following specifications: input angle $\theta_{\text{in}} = 30^\circ$ and output angle $\theta_{\text{out}} = -7.2^\circ$.

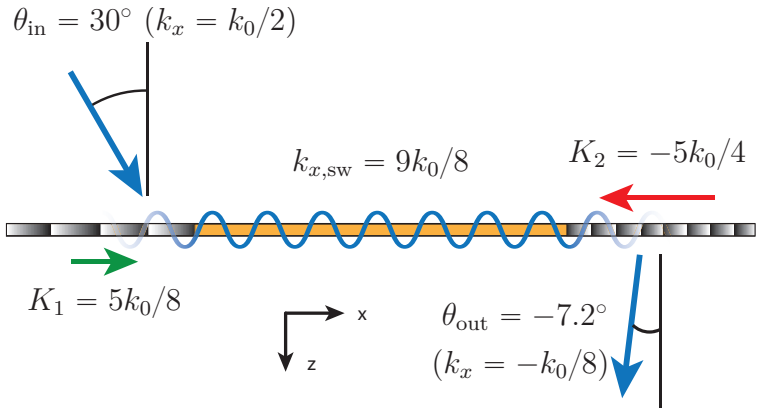

Figure 5.37 Schematic representation of the electromagnetic periscope metasurface system.

The first phase-gradient metasurface, transforming the input p-polarized space wave into a surface wave, is implemented with a supercell of 8 unit cells of size $\lambda_0/5$ with transmission phases ranging from 0 to 2π. The corresponding metasurface wavenumber is $K_1 = 2\pi/P_1 = 2\pi/(8\lambda_0/5) = 5k_0/8$. Then, for the specified input wave with $\theta_{\text{in}} = 30^\circ$, corresponding to $k_{x,\text{in}} = k_0/2$, one finds, using (5.10) with $k_{x,\text{i}} = k_{x,\text{in}}$ and $K = K_1$, the surface-wave wavenumber to be $k_{x,\text{sw}} = k_{x,\text{t}} = 9k_0/8$, which corresponds to the x-wavenumber across the entire metasurface system.

Upon this basis, the third metasurface is designed as follows. The output angle of $\theta_{\text{out}} = -7.2^\circ$ corresponds to $k_{x,\text{out}} = -k_0/8$. We apply (5.10) with $k_{x,\text{i}} = k_{x,\text{sw}} = 9k_0/8$ and $k_{x,\text{t}} = k_{x,\text{out}} = -k_0/8$, which yields $K_2 = -5k_0/4$. Since $|K_2/K_1| = 2$, $P_2 = P_1/2$, and hence, still assuming $\lambda_0/5$ unit cells, the supercell includes now 4 unit cells. This metasurface may for instance be identical to the first metasurface where every two unit-cell rows have been removed.

The p-polarization surface-wave guiding structure, in the middle of the metasurface system, may also be realized as a metasurface, for compatibility with its phase-gradient neighbours, instead of as a traditional waveguiding structure. In addition, to allow the s-polarization generalized refraction operation depicted in Fig. 5.32, this structure must be completely transparent, and could therefore not be implemented in the form of a conventional waveguide. As explained previously, the metasurface is designed using the p-polarization susceptibilities already found with the exact synthesis method. In the current design, we consider the particular case of s-polarization normal transmission, leading to global uniformity.

The overall metasurface system, composed of the three juxtaposed metasurfaces, is imple-

mented with metallic scattering particles, as discussed in Sec. 4.1. The thickness of the structure is $\lambda_0/10$ and each unit cell has a transverse size of $\lambda_0/5 \times \lambda_0/5$ for an operation frequency of $f = 10$ GHz. For the two phase-gradient metasurfaces, the scattering parameters of each unit cell are assumed to simply consist of a phase transmission coefficient, $T = e^{j\phi}$, where the phase shift ϕ depends on the unit cell position within the supercell. To realize this supercell, we use the same unit cells as those obtained for the polarization beam splitting metasurface discussed in Sec. 5.3. For this metasurface, half of the 8 unit cells are rotated versions of the remaining ones. Consequently, the dimensions of the 4 unique unit cells are already given in Table 5.4. The third metasurface is made of a supercell of 4 unit cells. The corresponding dimensions are obtained as follows: the first and second unit cells are the same as the 90°-rotated versions of cells 2 and 4 in Table 5.4, while the third and fourth unit cells correspond to cells 3 and 1 in Table 5.4, respectively.

For the waveguiding metasurface, the susceptibilities given above are first converted into scattering parameters using (2.32). Because this metasurface is uniform (as seen by a p-polarized wave), in contrast to the phase-gradient metasurfaces, only one unit cell has to be designed. Once the dimensions of the Jerusalem crosses corresponding to the susceptibilities have been found, the unit cell is optimized using an eigen-mode solver with the goal to achieve a wavenumber of $k_{x,\mathrm{sw}} = 9k_0/8$ at the operation frequency of $f = 10$ GHz. The final dimensions of the unit cell for this metasurface are given in Table 5.8.

Table 5.8 Geometrical dimensions (in mm) for the unit cell of the metasurface in Fig. 5.11b. OL denotes the outer layers and ML the middle layer.

Layer	Lx	Ly	Wx	Wy	Ax	Ay	Bx	By
OL	5.5	4	0.5	1	0.5	0.5	2.25	2.25
ML	5	5	0.25	1	0.5	0.5	3.75	-

The dispersion curve for the fundamental mode of the optimized waveguiding structure is plotted in Fig. 5.38. Note that the horizontal axis represents the x-wavenumber normalized to the free-space wavenumber, so that the figure shows only the slow-wave region ($k_{x,\mathrm{sw}}/k_0 > 1$). Comparing the two insets in the figure shows that the field distribution of this fundamental mode is essentially identical, and hence compatible, with the field distributions of the two phase-gradient metasurfaces. Since the metasurfaces have been in addition designed to all exhibit the same polarization and wavenumber, it may be inferred that the coupling between them is maximized, as desired.

The realized metasurface system is shown in Fig. 5.39. Due to limitation of our fabrication process, the three metasurfaces have been realized separately rather than as a single entity

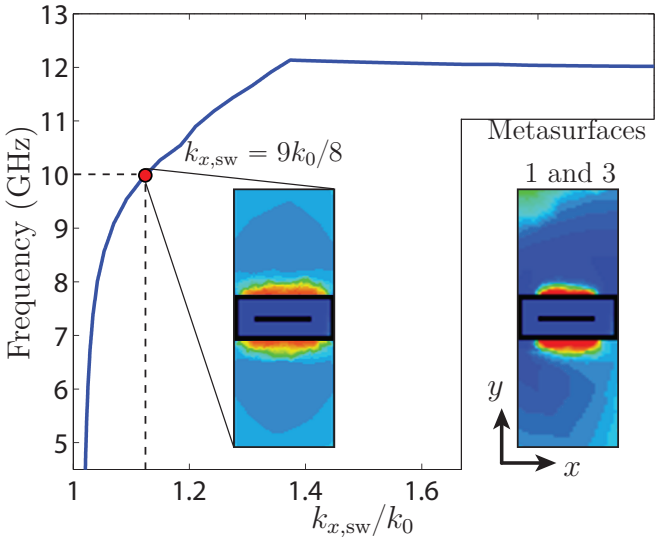

Figure 5.38 Dispersion curve and magnetic field distribution (absolute value at 10 GHz) for the fundamental mode of the waveguiding metasurface. The separate inset represents the excited fields in the surrounding phase-gradient metasurfaces (also at 10 GHz).

and have then been screwed to a plastic frame (at the back and hence not visible in Fig. 5.39) to form the overall metasurface system. Each metasurface is made of 24×24 unit cells, corresponding to a size of $4.8\lambda_0 \times 4.8\lambda_0$. The dimensions of the system are 45 cm×15 cm×3 mm.

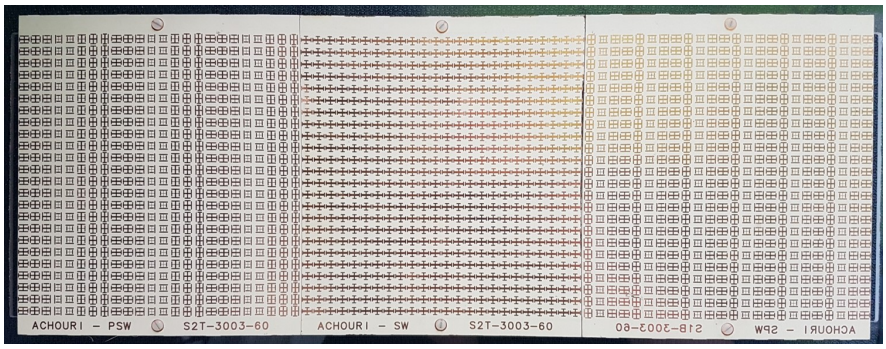

Figure 5.39 Fabricated metasurface system corresponding to Fig. 5.32. The metasurfaces from the left to the right perform the following operations on the *p*-polarized wave: space-wave to surface-wave transformation, surface-wave propagation, and surface-wave to space-wave transformation. At the same time, the central metasurface is perfectly transparent to *s*-polarized waves. The difference between the phase-gradients of the two end metasurfaces is clearly visible.

The measurement of the metasurface system was performed using the experimental setup depicted in Fig. 5.40. The input side of the metasurface system is covered everywhere by absorbers except for a small aperture allowing the illumination of the first metasurface on the left. A high-gain X-band horn antenna illuminates the structure at the input side while

a waveguide probe scans the metasurface system at the output side in the near-field region. The near-field is measured in the middle of the metasurface system in Fig. 5.39 along the x-direction. The measured near-field will be first Fourier-transformed to compute the spatial (k-domain) spectrum, and hence identify the modes excited at the output side of the system, and next propagated in the xz-plane by the angular spectrum technique [202], so as to verify the periscope operation of the system.

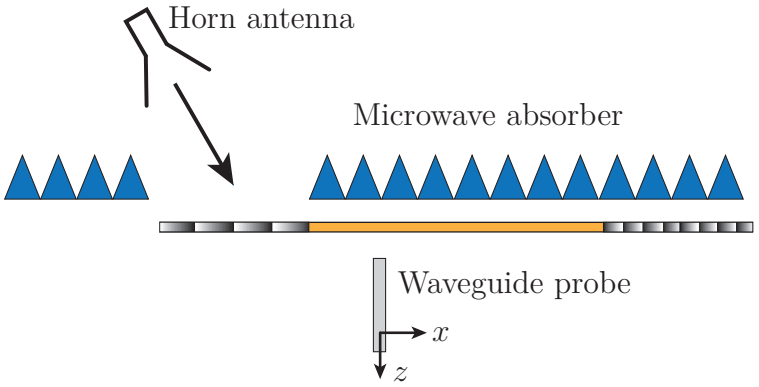

Figure 5.40 Side view of the configuration of the metasurface system measurement setup.

The modes excited along the overall structure, as the probe scans the entire x-dimension of the system, are revealed in Fig. 5.41a, which plots the normalized x-Fourier transform of the output near-field measured along the x-direction using the setup of Fig. 5.40. The mode excited at the output of the metasurface system with the highest amplitude is a surface wave of wavenumber $k_{x,\mathrm{sw}} = 9k_0/8$ corresponding to the wavenumber of the specified surface-wave mode. The reason why this mode is dominant is because it is excited along the entire structure, being first generated on the first metasurface, next guided by the second one and eventually radiated by the third one. The mode excited with the next higher intensity is the space-wave mode at $k_{x,\mathrm{t}} = k_0/2$, which corresponds to the input wave impinging the metasurface at $\theta_{\mathrm{in}} = 30°$. The third largest peak lies in the negative side of the horizontal axis and corresponds to the specified transmitted space wave with wavenumber $k_{x,\mathrm{t}} = -k_0/8$ generated by the third metasurface.

Figure 5.41b shows the modes excited only at the output side of the third metasurface, when the near-field probe scans only on that part of the system. As expected, the two strongest modes correspond to the specified transmitted space wave with $k_{x,\mathrm{t}} = -k_0/8$ and the specified surface wave with $k_{x,\mathrm{t}} = 9k_0/8$.

Next, we compute the field scattered by the metasurface system by applying the angular spectrum propagation technique [202] to the near-field measured along the entire structure. To clearly see the propagation of the expected transmitted space wave with $k_{x,\mathrm{t}} = -k_0/8$,

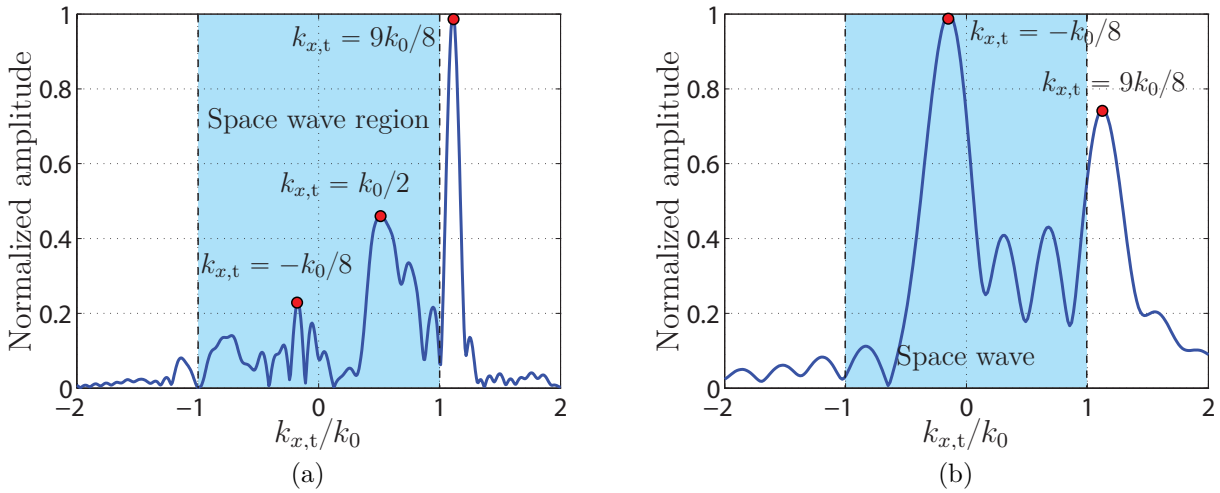

Figure 5.41 Normalized x-Fourier transform (k_x-domain) of the output near-field measured along the x-direction at 1 cm from the metasurface in the z-direction (Fig. 5.40). (a) Scanning across the entire metasurface system. (b) Scanning only across the third metasurface. The regions highlighted in blue correspond to the space wave region.

we ignore the contribution of the input wave, which generates important spurious scattering, as is visible in Fig. 5.41a around $k_{x,\mathrm{t}}/k_0 = 0.5$. This is achieved by first taking the Fourier transform of the near-field, yielding the data in Fig. 5.41a, and next setting to zero all the modes excited in the region $0.2 < k_{x,\mathrm{t}}/k_0 < 0.8$ in Fig. 5.41a to remove the contributions from the input wave. Then, the field is propagated along the z-direction following the usual procedure of the angular spectrum propagation technique. The resulting scattered field on the transmit side of the metasurface is plotted in Fig. 5.42, where the metasurface system lies at $z = 0$ and extends from $x = -22.5$ cm to $x = 22.5$ cm. In this figure, we can see the presence

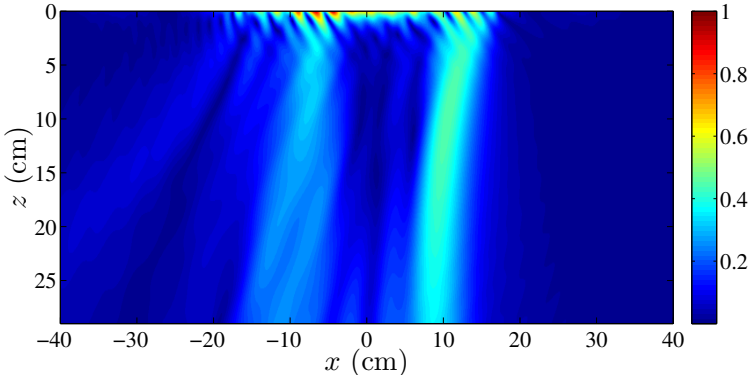

Figure 5.42 Absolute value of the transmitted electric field (E_x component) obtained by angular spectrum propagation. The metasurface system is at $z = 0$ and extends from $x = -22.5$ cm to $x = 22.5$ cm.

of a strong surface wave near the structure close to $z = 0$. In the region around $x = -10$ cm, we see some scattering which is due to the discontinuity between adjacent metasurfaces. In the region around $x = 10$ cm, we see a beam emerging from the metasurface system and being deflected towards the left. This beam corresponds to the specified transmitted space wave with $\theta_{\text{out}} = -7.2°$.

In order to better understand the result shown in Fig. 5.42, we next analyze the spatial power distributions of the surface wave ($k_{x,\text{sw}} = 9k_0/8$) and of the transmitted space wave ($k_{x,\text{out}} = -k_0/8$) along the metasurface system. From the data plotted in Figs. 5.41, it is possible to extract the power distribution of the different modes over the metasurface system. This is achieved by first isolating the modes of interest in the data of Fig. 5.41a by setting to zero everything except the relevant regions (appropriate peaks) – for example leaving only the peak centered at $k_{x,\text{t}} = 9k_0/8$ to isolate the surface wave – and then taking the inverse Fourier transform to generate the spatial distribution of the mode. The results are presented in Fig. 5.43, where the power distribution of the surface wave is represented by the solid black line and that of the space wave by the dashed red line.

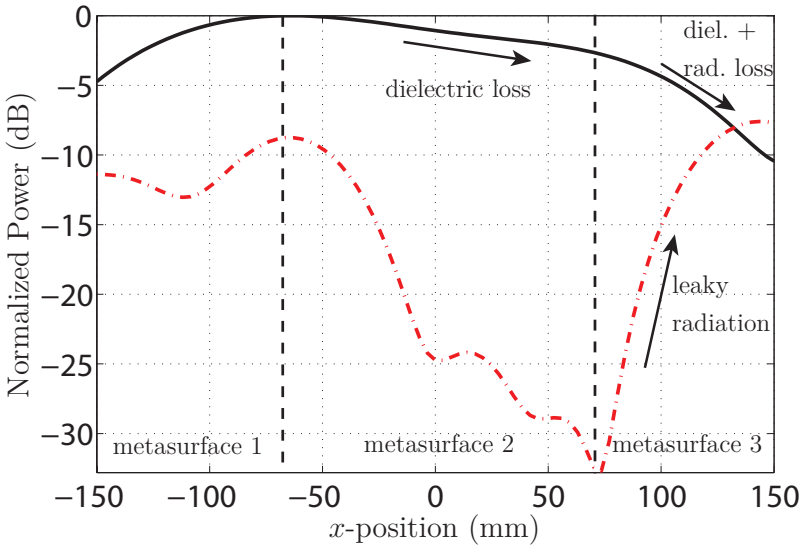

Figure 5.43 Normalized power distribution of the surface-wave mode (solid black line) and of the transmitted wave (dashed red line) over the metasurface system. The two vertical dashed black lines indicate the separation between the three metasurfaces.

As one moves along the x-axis, the power distribution of the surface wave (solid black curve) first increases, following the power distribution of the exciting horn antenna, which points at the junction between the first and second metasurfaces. At this point, it reaches a corresponding maximum. Then, it decreases as the wave propagates along the waveguiding metasurface while experiencing metallic and dielectric dissipation losses. Finally, it further

decreases on the third metasurface due to combined dissipation and radiation losses.

The power level of the transmitted space wave (dash red curve) is relatively high at the junction between the first and second metasurfaces, which is explained by spurious scattering of the incident wave at this discontinuity, similarly to the undesired scattering apparent in Figs. 5.34b and 5.34c. Then, this power rapidly decreases along the second metasurface, as expected from the fact that this surface does not radiate. Along the third metasurface, the power of the space wave progressively increases as it progressively leaks out due to the interaction between the surface wave and the phase-gradient of the metasurface.

The experimental results presented above are in good agreement with the expected response of the metasurface system, with the exception of a relatively low efficiency of about 10%. This low efficiency is due to a combination of effects that include surface-wave dissipation loss, scattering at each of the two metasurface discontinuities, the limited coupling of the incident wave which is effectively converted to a surface wave, and the imperfect conversion between space wave and surface wave (and vice-versa) due to the simplified synthesis technique used for the implementation of the phase-gradient metasurfaces. Several of these issues may be addressed by further optimization. In addition, in the current design, the guided wave exists on both sides of the middle metasurface. This means that, upon interaction with the phase-gradient metasurface on the right, the transmitted space wave is actually leaking out on both sides of the metasurface system, which further decreases the efficiency. This may be avoided by considering longitudinally asymmetric (bianisotropic) metasurfaces that would only radiate the transmitted wave on one side of the metasurface system.

5.6.4 Other Potential Applications

The concept of space-wave routing via surface waves may lead to a diversity of other potential applications. As an illustration, we will discuss two of them in this section.

Compact Beam Expander

An optical beam expander is a device that is used in telescopes or microscopes: it increases (or decreases) the lateral size of the incoming beam. The simplest way to realize such a device is to cascade two thin lenses of different focal lengths. We propose here an alternative beam expanding system, based on the concept of space-wave routing via surface waves. Compared to the lens system, this routing system presents two significant advantages. First, it uses a single (composite) metasurface instead of two lenses. Second, in contrast to the lens system, it does not require any separation distance, where such a distance at optical frequencies

represents several thousands of wavelengths, and hence leads to a very compact system.

We present here two different beam expander designs, both increasing the beamwidth of the incident beam by a factor 3. One performs a direct conversion (without any lateral shift) while the other one performs an offset (laterally shifted) beam expansion. The direct beam expander is made of three metasurfaces, the middle one transforming the incident beam into two contra-propagating surface waves that are then both transformed back into space waves by the two end metasurfaces. The simulation showing this direct expansion is presented in Fig. 5.44a. As may be seen in this plot, the presence of the two metasurface discontinuities induces non-negligible spurious scattering.

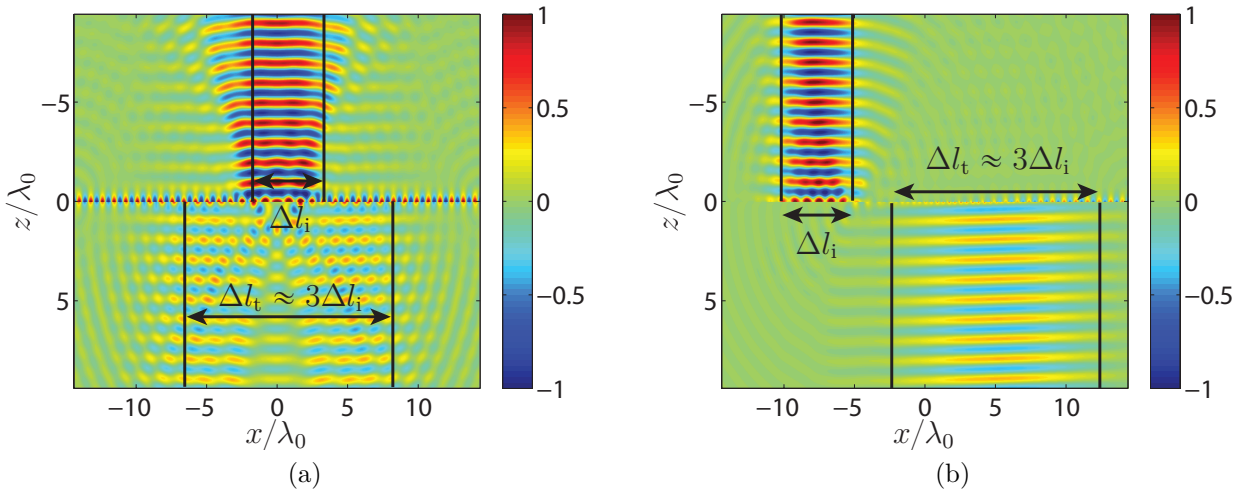

Figure 5.44 FDFD simulations of a beam expander with (a) direct transformation and (b) offset transformation. The metasurface system is designed to increase the beamwidth of the incident wave by a factor 3.

The simulation of the offset beam expander is shown in Fig. 5.44b. The system is identical to that of Fig. 5.34c except that both the incident and transmitted angles are now normal to the surface. For the two structures in Figs. 5.44, the beam expansion of the transmitted wave is about three times that of the incident wave. Consequently, the amplitude of the transmitted wave is also three times less.

Multi-Wave Refractor

The capability to route beams via surface waves may also be leveraged to implement a multi-wave refractor, i.e. system performing several refractive transformations with a single metasurface system, in contrast to a conventional metasurface that can only perform two independent refraction transformations, one for an x-polarized wave and one for a y-polarized

wave. The proposed system is realized by inserting a metasurface at the Fourier plane of an optical 4f-system. A 4f-system is generally used as a spatial filter where a mask is placed at the Fourier plane to filter out certain spatial components of the incident wave [159]. Here, the metasurface placed at the Fourier plane is not used to filter out spatial components but, instead, to shift the spatial components of the incident waves to other regions of the Fourier plane, which effectively changes the direction of propagation of the transmitted waves. The concept is depicted in Fig. 5.45a, where two input beams, Ψ_1 and Ψ_2, are transformed in terms of their spectral contents in the 4f-system.

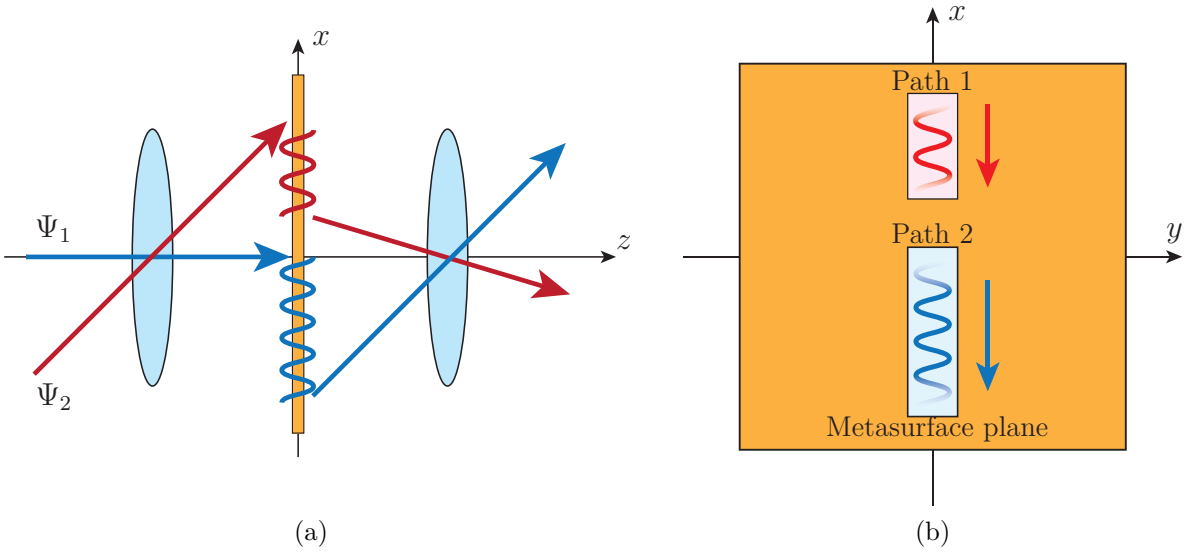

Figure 5.45 Multi-wave refractor concept. (a) A 4f-system, with 2 routing metasurface systems in its Fourier plane, refracts the input waves Ψ_1 and Ψ_2 into different directions. (b) Representation of the metasurface at the Fourier plane of (a) with the two optical routes shifting the waves Ψ_1 and Ψ_2 to different locations in the Fourier plane.

In the figure, the first lens focalizes the two beams at different locations in the Fourier plane, where a metasurface system is placed. This metasurface system consists of two "optical routes", as shown in Fig. 5.45b, each composed of three different metasurfaces successively transforming the incident space wave into a surface wave, guiding this surface wave along the Fourier plane to the appropriate (k_x, k_y) point, and transforming it back into a space wave in the desired direction. In this example, the two beams have been shifted along the negative x-direction in the Fourier plane. Their respective momentum along x has therefore been decreased. Consequently, the two beams exit the system, collimated by the second lens, with transmission angle depending on the points to which they have been shifted in the Fourier plane. Such a metasurface system might be populated with several additional "optical routes" so as to achieve even more refraction transformations.

5.7 Nonreciprocal Nongyrotropic Metasurface

All metasurfaces presented so far in this chapter are reciprocal structures, we are now interested in extending the range of applications of the synthesis technique to the topic of nonreciprocal metasurfaces[11]. Nonreciprocal devices are at the basis of many applications such as isolators and circulators. Here, we will discuss the synthesis of a nonreciprocal and nongyrotropic (no rotation of polarization) metasurface that acts as a one-way screen.

Nonreciprocity can be achieved by breaking the time reversal symmetry of the system that is considered. There are several methods available to do that, which are notably based on: the magneto-optical effect used in Faraday isolators, nonlinearity or even time modulation. Most of these methods however present certain drawbacks like, for instance, being bulky, requiring magnet or distorting the field by rotation of polarization. The metasurface that is discussed here has the advantage of not requiring any magnet, of being lighter and more compact than conventional magneto-optical systems and, additionally, does not induce any distortion of the field such as rotation of polarization. In this section, we will address the susceptibility synthesis of this metasurface and establish its equivalence with a moving medium. Note that the physical realization of the metasurface is not discussed here, since I was not the main investigator of this work, but it is presented in details in [220].

To synthesize a nonreciprocal nongyrotropic metasurface, one needs to control the transmission and reflection coefficients from both sides of the metasurface. This means that the synthesis must be performed for two sets of waves and such that no rotation of polarization takes place. In that case, the metasurface may be synthesize in the exact same fashion as done for the perfectly refracting metasurface discussed in Sec. 3.3. Consequently, to achieve a nonreciprocal nongyrotropic response the metasurface needs to be bianisotropic. The metasurface is synthesized assuming normally propagating waves with respect to the metasurface and for any polarization. However, to illustrate the synthesis procedure, we will, in a first place, consider only x-polarized waves and later include both x and y contributions. Since normal wave propagation is considered, it is convenient to express the susceptibilities not in terms of the fields but rather directly in terms of the scattering parameters, as done in Eqs. (3.17) where the scattering parameters are expressed in terms of bianisotropic susceptibility components. Reversing relations (3.17) to obtain the susceptibilities in terms of the

[11] This section is based on a slightly modified version of [220, 221].

scattering parameters leads to

$$\chi_{\mathrm{ee}}^{xx} = \frac{2j}{k_0}\left(\frac{S_{11}+S_{21}S_{12}+S_{22}-S_{11}S_{22}-1}{S_{21}+S_{12}+S_{21}S_{12}-S_{11}S_{22}+1}\right), \tag{5.12a}$$

$$\chi_{\mathrm{mm}}^{yy} = \frac{2j}{k_0}\left(\frac{S_{21}S_{12}-S_{22}-S_{11}-S_{11}S_{22}-1}{S_{21}+S_{12}+S_{21}S_{12}-S_{11}S_{22}+1}\right), \tag{5.12b}$$

$$\chi_{\mathrm{em}}^{xy} = \frac{2j}{k_0}\left(\frac{S_{11}-S_{22}+S_{21}-S_{12}}{S_{21}+S_{12}+S_{21}S_{12}-S_{11}S_{22}+1}\right), \tag{5.12c}$$

$$\chi_{\mathrm{me}}^{yx} = \frac{2j}{k_0}\left(\frac{S_{22}-S_{11}+S_{21}-S_{12}}{S_{21}+S_{12}+S_{21}S_{12}-S_{11}S_{22}+1}\right). \tag{5.12d}$$

The nonreciprocal nongyrotropic transformation that we are interested in is depicted in Fig. 5.46 where the incident wave $\Psi_{1,\mathrm{i}}$ is transmitted with a transmission coefficient S_{21} while the incident wave $\Psi_{2,\mathrm{i}}$ is fully absorbed ($S_{12}=0$) by the metasurface. Moreover, the

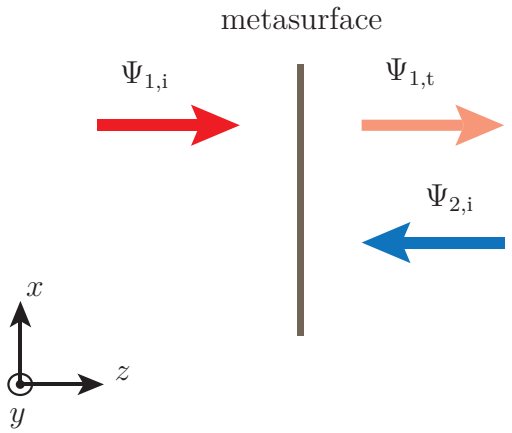

Figure 5.46 Operation of the nonreciprocal nongyrotropic metasurface. The forward propagating wave Ψ_1 is transmitted with transmission coefficient $S_{21}=\Psi_{1,\mathrm{t}}/\Psi_{1,\mathrm{i}}$. The backward propagating wave Ψ_2 is fully absorbed by the metasurface ($S_{12}=0$).

metasurface is reflectionless from both sides leading to $S_{11}=S_{22}=0$. Using these definitions of the scattering parameters, relations (5.12) reduce to

$$\chi_{\mathrm{ee}}^{xx} = -\frac{2j}{k_0}\left(\frac{1}{S_{21}+1}\right), \tag{5.13a}$$

$$\chi_{\mathrm{mm}}^{yy} = -\frac{2j}{k_0}\left(\frac{1}{S_{21}+1}\right), \tag{5.13b}$$

$$\chi_{\mathrm{em}}^{xy} = -\frac{2j}{k_0}\left(\frac{S_{21}}{S_{21}+1}\right), \tag{5.13c}$$

$$\chi_{\mathrm{me}}^{yx} = -\frac{2j}{k_0}\left(\frac{S_{21}}{S_{21}+1}\right). \tag{5.13d}$$

By the same token used to derive relations (5.12) and (5.13), one can obtain the equivalent relations corresponding to y-polarized waves and which define the susceptibilities χ_{ee}^{yy}, χ_{mm}^{xx}, χ_{em}^{yx} and χ_{me}^{xy}. The final susceptibility tensors for both x- and y-polarized waves are given by

$$\overline{\overline{\chi}}_{\mathrm{ee}} = -\frac{2j}{k_0(S_{21}+1)}\begin{pmatrix}1 & 0\\ 0 & 1\end{pmatrix}, \quad \overline{\overline{\chi}}_{\mathrm{mm}} = -\frac{2j}{k_0(S_{21}+1)}\begin{pmatrix}1 & 0\\ 0 & 1\end{pmatrix}, \tag{5.14a}$$

$$\overline{\overline{\chi}}_{\mathrm{em}} = \frac{2jS_{21}}{k_0(S_{21}+1)}\begin{pmatrix}0 & 1\\ -1 & 0\end{pmatrix}, \quad \overline{\overline{\chi}}_{\mathrm{me}} = \frac{2jS_{21}}{k_0(S_{21}+1)}\begin{pmatrix}0 & -1\\ 1 & 0\end{pmatrix}. \tag{5.14b}$$

Using relations (2.10), one can easily verify that the susceptibility tensors (5.14a) are reciprocal while the susceptibility tensors (5.14b) are nonreciprocal. In fact, the only way to achieve a nonreciprocal nongyrotropic response is through the magnetoelectric coupling coefficients. This is because nongyrotropy requires $\overline{\overline{\chi}}_{\mathrm{ee}}$ and $\overline{\overline{\chi}}_{\mathrm{mm}}$ to be diagonal tensors which necessarily satisfies the reciprocity conditions.

As can be seen, the susceptibilities in (5.14a) are complex values which, assuming that $|S_{21}| \leqslant 1$, correspond to loss according to (2.11) and more specifically relations (2.12b) and (2.12c). However, the susceptibilities in (5.14b) correspond to loss or to gain depending on the direction of wave propagation, as evidenced by the presence of $\boldsymbol{E}$ and $\boldsymbol{H}$ in the last term of (2.12d) and (2.12e). For instance, assuming x-polarized waves propagating in the z-direction, the components of (5.14a) correspond to loss while the corresponding components of (5.14b) correspond to gain, since both E_x and H_y have the same sign at $z = 0$, such that gain and loss combine together so as to produce the expected transmission coefficient S_{21}. In the case of x-polarized waves propagating in the negative z-direction, the components of (5.14a) still correspond to loss while those of (5.14b) now also correspond to loss, since E_x and H_y have opposite sign at $z = 0$, effectively cancelling the transmission ($S_{12} = 0$).

The realization of a nonreciprocal nongyrotropic metasurface would therefore require the implementation of a lossy/active structure with nonreciprocal magnetoelectric coupling. Such a structure would be particularly difficult to realize in practice. In [220], we have fabricated a structure that exhibits the expected nonreciprocal nongyrotropic response using a surface-circuit-surface architecture that consists of two patch-antenna arrays connected to each other with transistors which act as unilateral devices. This structure is based on the same principle as the interconnected array lens of Fig. 1.1c.

In the following subsection, we will see how the metasurface, given by the susceptibility tensors in (5.14), may be alternatively implemented via a moving medium.

5.7.1 Equivalence with a Moving Metasurface

From a general perspective, a nonreciprocal medium can be characterized by the properties of its medium parameter tensors. The nonreciprocal behavior of the metasurface discussed above stems from the susceptibility tensors (5.14b) which are antisymmetric. This classifies this kind of nonreciprocal structure as a moving medium [254]. We will see in the following lines how this equivalence comes about and compute what should be the required medium permittivity, permeability and velocity so as to achieve the specified scattering parameters given above.

For simplicity, it is convenient to express the metasurface medium parameters using the following constitutive relations

$$\boldsymbol{D} = \overline{\overline{\epsilon}} \cdot \boldsymbol{E} + \overline{\overline{\xi}} \cdot \boldsymbol{H}, \tag{5.15a}$$

$$\boldsymbol{B} = \overline{\overline{\zeta}} \cdot \boldsymbol{E} + \overline{\overline{\mu}} \cdot \boldsymbol{H}, \tag{5.15b}$$

instead of those given in (2.9). The equivalence between (2.9) and (5.15) is given by

$$\overline{\overline{\epsilon}} = \epsilon_0(\overline{\overline{I}} + \overline{\overline{\chi}}_{\mathrm{ee}}), \quad \overline{\overline{\mu}} = \mu_0(\overline{\overline{I}} + \overline{\overline{\chi}}_{\mathrm{mm}}), \tag{5.16a}$$

$$\overline{\overline{\xi}} = \overline{\overline{\chi}}_{\mathrm{em}}/c_0, \quad \overline{\overline{\zeta}} = \overline{\overline{\chi}}_{\mathrm{me}}/c_0. \tag{5.16b}$$

We will now proceed to show that the medium parameters in (5.14) correspond to those of a moving uniaxial medium as seen by an observer in a rest frame of reference [157]. A uniaxial medium has the following medium parameters

$$\begin{pmatrix} \overline{\overline{\epsilon}}' & \overline{\overline{\xi}}' \\ \overline{\overline{\zeta}}' & \overline{\overline{\mu}}' \end{pmatrix} = \begin{pmatrix} \epsilon' & 0 & 0 & 0 & 0 & 0 \\ 0 & \epsilon' & 0 & 0 & 0 & 0 \\ 0 & 0 & \epsilon_z & 0 & 0 & 0 \\ 0 & 0 & 0 & \mu' & 0 & 0 \\ 0 & 0 & 0 & 0 & \mu' & 0 \\ 0 & 0 & 0 & 0 & 0 & \mu_z \end{pmatrix}, \tag{5.17}$$

where the primes denote the moving frame of reference and where ϵ_z and μ_z can take arbitrary values. We assume that the motion is only in the positive z-direction. Because the medium is moving, a coupling occurs between the electric and magnetic components such that this uniaxial medium becomes bianisotropic for an observer at rest, which can be verified using the Lorentz transform operation [157]

$$\overline{\overline{C}} = \overline{\overline{L}}_6^{-1} \cdot \overline{\overline{C}}' \cdot \overline{\overline{L}}_6, \tag{5.18}$$

where the matrices $\overline{\overline{C}}$ and $\overline{\overline{C}}'$ respectively correspond to the medium parameters in the rest frame of reference and in the moving frame of reference and $\overline{\overline{L}}_6$ is the Lorentz matrix. The matrices $\overline{\overline{C}}$ and $\overline{\overline{C}}'$ can be expressed as follows[12]

$$\overline{\overline{C}} = \begin{pmatrix} c_0(\overline{\overline{\epsilon}} - \overline{\overline{\xi}} \cdot \overline{\overline{\mu}}^{-1} \cdot \overline{\overline{\zeta}}) & \overline{\overline{\xi}} \cdot \overline{\overline{\mu}}^{-1} \\ -\overline{\overline{\mu}}^{-1} \cdot \overline{\overline{\zeta}} & \overline{\overline{\mu}}^{-1}/c_0 \end{pmatrix}, \tag{5.19}$$

and the matrix $\overline{\overline{L}}_6$ as

$$\overline{\overline{L}}_6 = \gamma \begin{pmatrix} 1 & 0 & 0 & 0 & -\beta & 0 \\ 0 & 1 & 0 & \beta & 0 & 0 \\ 0 & 0 & 1/\gamma & 0 & 0 & 0 \\ 0 & \beta & 0 & 1 & 0 & 0 \\ -\beta & 0 & 0 & 0 & 1 & 0 \\ 0 & 0 & 0 & 0 & 0 & 1/\gamma \end{pmatrix}, \tag{5.20}$$

where $\gamma = 1/\sqrt{1-\beta^2}$, $\beta = v/c_0$, with v the velocity of the medium and c_0 the speed of light in vacuum. The medium parameters in the rest frame of reference can then be obtained by inserting (5.17) into (5.18) using (5.19) and (5.20), which leads to

$$\begin{pmatrix} \overline{\overline{\epsilon}} & \overline{\overline{\xi}} \\ \overline{\overline{\zeta}} & \overline{\overline{\mu}} \end{pmatrix} = \begin{pmatrix} \epsilon & 0 & 0 & 0 & \xi & 0 \\ 0 & \epsilon & 0 & -\xi & 0 & 0 \\ 0 & 0 & \epsilon_z & 0 & 0 & 0 \\ 0 & -\xi & 0 & \mu & 0 & 0 \\ \xi & 0 & 0 & 0 & \mu & 0 \\ 0 & 0 & 0 & 0 & 0 & \mu_z \end{pmatrix}. \tag{5.21}$$

We can now compare the parameters in (5.21) to those in (5.14). This comparison reveals that there is a perfect match between the parameters of a nonreciprocal nongyrotropic metasurface and a uniaxial moving metasurface as seen from a rest frame of reference. Note that since the metasurface in (5.14) is reflectionless, we have that $\epsilon = \mu$ and $\xi = \zeta$ in (5.21).

From this point, we are interested in finding the values of ϵ' and μ' in (5.17), as well as the velocity v, such that the parameters in (5.21) take the same values as those in (5.14). This is accomplished by solving (5.18) to obtain ϵ', μ' and v in terms of ϵ, μ and ξ. The

[12] $\overline{\overline{C}}'$ is found using the primed tensors given in (5.17).

corresponding solutions read

$$\epsilon' = \mu' = -\frac{c_0^2\left(\xi^2 - \epsilon\mu\right) - 1 + \sqrt{\left(c_0^2\left(\xi^2 - \epsilon\mu\right) + 1\right)^2 - 4c_0^2\xi^2}}{2c_0^2\mu}, \tag{5.22a}$$

$$v = \frac{c_0^2\left(\xi^2 - \epsilon\mu\right) + 1 - \sqrt{\left(c_0^2\left(\xi^2 - \epsilon\mu\right) + 1\right)^2 - 4c_0^2\xi^2}}{2\xi}. \tag{5.22b}$$

By making use of (5.14) and (5.16), the uniaxial moving metasurface parameters are thus readily obtained as functions of the bianisotropic metasurface susceptibilities in (5.14). We see from the expressions in (5.22) that ϵ' and v may in general both be complex values. The corresponding real and imaginary parts of $\chi' = \epsilon'/\epsilon_0 - 1$ are plotted in Figs 5.47a and 5.47b versus S_{21}, respectively. Similarly, the real and imaginary parts of v are plotted in Figs 5.47c and 5.47d versus S_{21}, respectively.

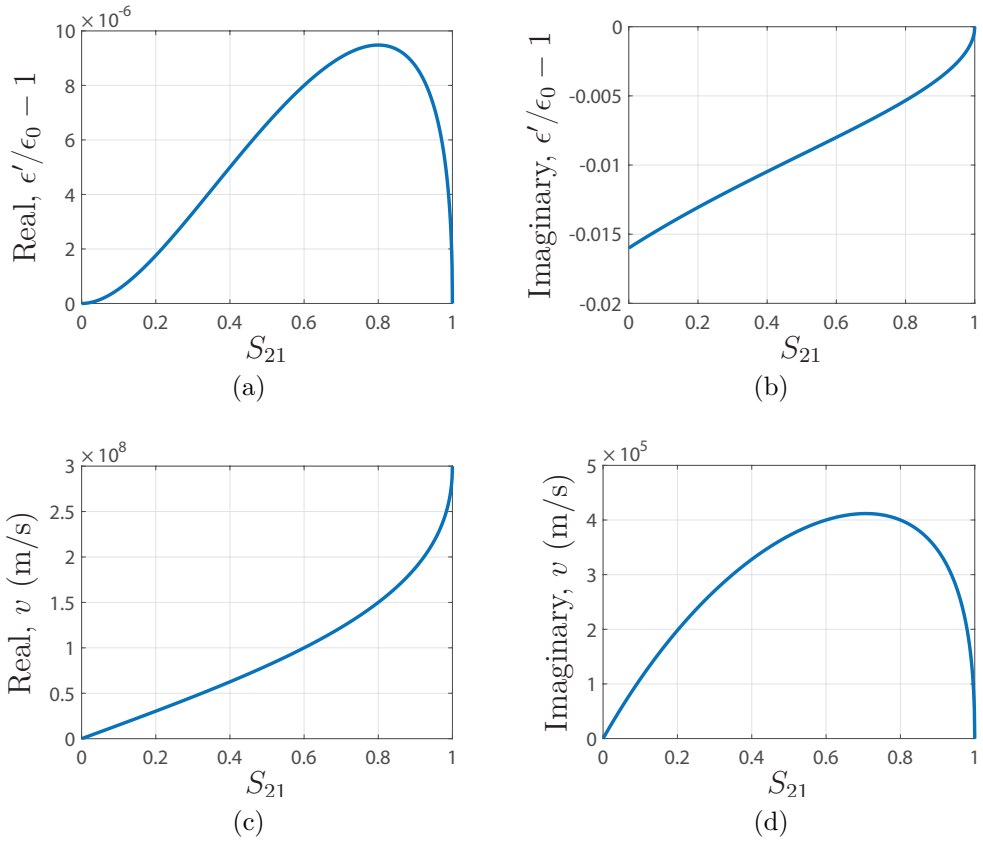

Figure 5.47 Moving uniaxial metasurface medium parameters and velocity versus S_{21} and for an arbitrary value of $k_0 = 125$ m^{-1}. (a) Real and (b) imaginary parts of $\chi' = \epsilon'/\epsilon_0 - 1$. (c) Real and (d) imaginary parts of v.

The results in Figs. 5.47 may be interpreted as follows: if $S_{21} = 0$, then the structure is

reciprocal and fully absorbs the incident waves from both sides, therefore $v = 0$ and χ' has purely negative imaginary value (loss). If $S_{21} = 1$, we see that $\chi' = 0$ and $v = c_0$. In that case, the forward propagating wave would simply fully transmit through a "moving vacuum", while the backward propagating wave would never be able to catch-up with it, since it moves at the speed of light, and thus never pass through. If $0 < S_{21} < 1$, both χ' and v are complex. The physical meaning of an imaginary velocity is not clear at this point but one may speculates that it plays a role in the partial absorption of the forward propagating wave. Note that the transmission through a moving metasurface (or similarly through a moving material slab) does not involve any Doppler effect, and thus does not change the frequency of the wave, if the medium on both sides of the metasurface is the same, which is the case here [255].

5.8 LEDs Emission Enhancement

This work aims at increasing the light emission of light-emitting diodes (LEDs) using one or several metasurfaces. LEDs are composed of a semiconductor P-N junction that emits light due to electron-hole recombinations when a suitable bias voltage is applied. As most LEDs have a Lambertian type radiation pattern, a metasurface could be used to obtain a more directive radiation pattern. Moreover, due to the higher refractive index of the P-N junction compared to the surrounding medium, LEDs suffer from total internal reflection (TIR) which traps part of the light emitted by the junction inside the active region, thus dramatically decreasing the light extraction efficiency. Metasurfaces could consequently be used to reduce the TIR and increase the light extraction efficiency of LEDs. This work is part of a collaboration in which several other people are involved, I will therefore only present a brief description of this project, while more information may be found in [2, 222, 256].

As an initial guess, that is used to simplify the metasurface synthesis, the LED junction is assumed to be a monochromatic single-photon source and is modelled as an embedded electric dipole in a reflector-backed material slab, as shown in Fig. 5.48a. The dipole is placed in the center of the slab of permittivity $\epsilon_r = 6.0$ (corresponding to GaN), thickness $t = 900$ nm and operating wavelength $\lambda_0 = 490$ nm (blue light). In Fig. 5.48a, the blue lines represent the light rays whose first interaction is with the top interface (GaN – air) while the red lines represent the light rays that are first reflected by the bottom interface (PEC). As can be seen, the difference of refractive indices between the GaN and the air is causing most of the light to be trapped inside the slab since the critical angle is only $\theta_c = 24.1°$.

There are three different metasurface configurations that have been considered to enhance the light emission efficiency of the structure in Fig. 5.48a. The first configuration is shown in

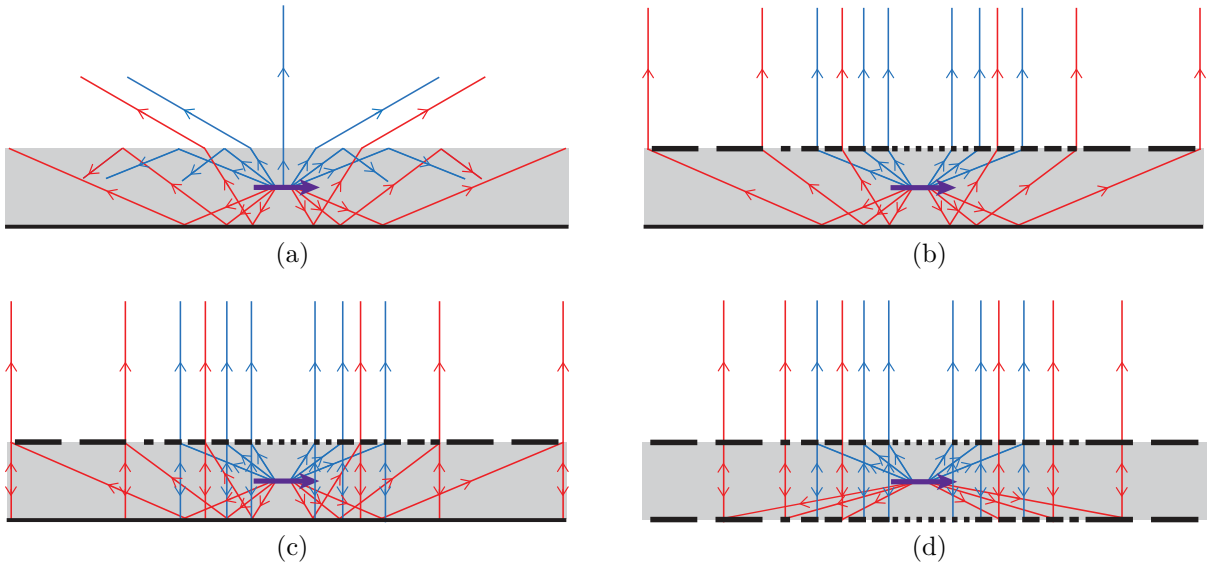

Figure 5.48 Different LED models. (a) Bare LED structure with a single dipole emitter embedded in GaN slab with a back-reflector. (b) Reflectionless metasurface, placed on top of the GaN slab, that collimates the dipole fields. (c) Same configuration but with a partially reflective metasurface that forms a Fabry-Pérot cavity. (d) Double metasurface cavity, the metasurface at the top interface is partially reflective while that at the bottom interface is fully reflective.

Fig. 5.48b and consists of a single reflectionless metasurface, placed at the interface between GaN and air, which collimates all incident fields coming either directly from the dipole source or from the reflection from the back reflector. The second configuration forms a partially reflective metasurface cavity (PRMC) and is shown in Fig. 5.48c where the metasurface is partially reflective and normally transmits and normally reflects the dipole fields with a given reflection coefficient. The normally reflected plane wave from the metasurface undergoes multiple reflections inside the cavity. For each reflection, part of the energy is normally transmitted into a plane wave. Consequently, the junction becomes a Fabry-Pérot cavity that, depending on its thickness, effectively increases the light extraction efficiency. Finally, the third configuration, which is also a PRMC, is shown in Fig. 5.48d where now two metasurfaces are used. The bottom one normally reflects the dipole fields, while the metasurface on the top is partially reflective as the one in Fig. 5.48c. The details of the metasurface synthesis for the three designs in Fig. 5.48 are not presented here but may be found in [2].

Full-wave simulations were performed using COMSOL to compare the difference in light emission between the bare structure of Fig. 5.48a and the double metasurface structure of Fig. 5.48d. The simulated energy flux density of the bare structure is shown in Fig. 5.49a, where most of the light is trapped inside the slab and very little escapes, as expected. The

simulation result for the double metasurface structure is shown in Fig. 5.49b, where now almost all the light is allowed to escape. The measured enhancement of the light extraction

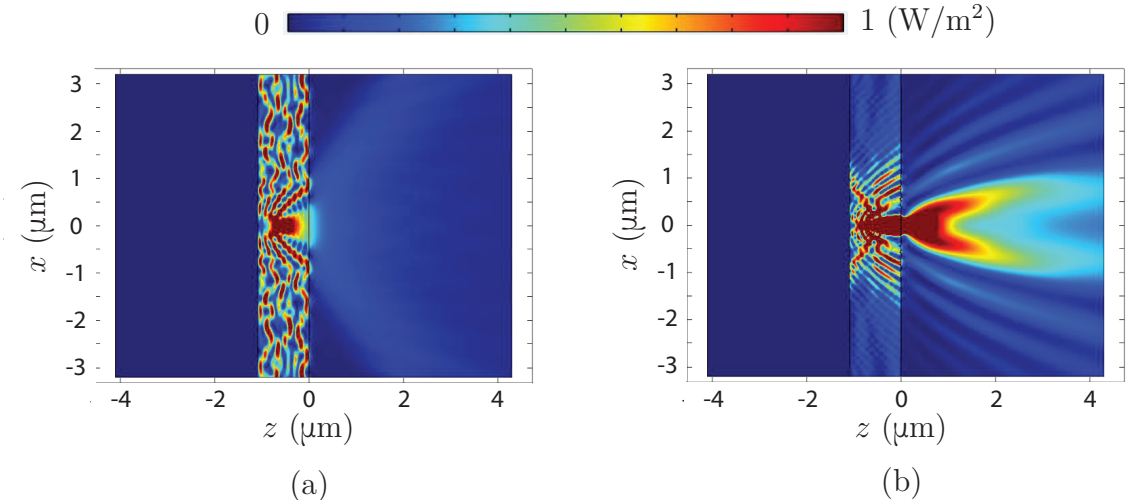

Figure 5.49 COMSOL simulated energy flux densities for a dipole emitter embedded in a slab of GaN. (a) Same configuration as in Fig. 5.48a. (b) Same configuration as in Fig. 5.48d. Original images from [2].

efficiency between Figs. 5.49a and 5.49b was found to be as much as a factor of 4 [2].

Note that the designs in Figs. 5.48c and 5.48d improve not only the light extraction efficiency but also the spontaneous emission rate (SER) of the source, which also plays a role in the overall efficiency of the LED. The improvement of the SER comes as a consequence of light confinement near the dipole emitter that is due to the reflection from the metasurface(s) and which increases the local density of states [2].

The three configurations in Figs. 5.48 behave differently and their performance, in terms of the improvement of the light emission efficiency, may vary significantly. Moreover, the design constraints and the feasibility of the metasurfaces also greatly differ. Therefore, these different metasurface systems must be optimized, via full-wave simulations, and compared to each other so as to find the most appropriate design to meet the project specifications. It must be noted that the designs described above are valid when the LED is modeled as a single dipole emitter, while a more realistic model for the LED would be to consider an emitting layer made of randomly placed and randomly polarized dipole sources each emitting with arbitrary phases. Consequently, further investigations will be required to find the best possible designs and the corresponding results and fabricated LED structures will be the topic of future works.

5.9 Metasurface "Solar Sail" for Radiation Pressure Control

Solar sail is a spacecraft propulsion method based on radiation pressure. Although the force exerted by light upon scattering by an object is very small, such a force is sufficient for propulsion if the scattering area is sufficiently large. This technology may, one day, allow humanity to travel among the stars [257]. However, solar sails are, as of now, restricted to the generation of *repulsive* forces, which limits the spacecraft range of motion.

In this work, we extend the range of operation of usual solar sails by introducing metasurface solar sails. We propose to leverage the electromagnetic transformation capabilities of metasurfaces to control radiation pressure. While most studies on optical forces have been so far restricted to the manipulation of forces acting on small particles [92, 258–261], our goal here is to design a metasurface system, which consists of a metasurface attached to an object to be moved (e.g. satellite), and whose motion can be controlled by the illumination emerging either from a star or from high-power lasers. Different forces may then be obtained by changing the polarization and/or wavelength of the illumination. It follows that the most optimal situation would be to control the motion of a spacecraft in the vicinity of the earth using high-power lasers emitted either from the earth or from other spacecrafts such as satellites. In what follows, we propose a prospective study on the capabilities of metasurfaces to control radiation pressure.

5.9.1 Electromagnetic Force on a Stationary Object

An electromagnetic wave carries both energy and momentum. When it is scattered or absorbed by an object, the latter is subjected to a force as a consequence of the conservation of momentum law, which reads [262]

$$\boldsymbol{f} + \epsilon\mu\frac{\partial \boldsymbol{S}}{\partial t} = \nabla \cdot \overline{\overline{T}}_{\text{em}}, \tag{5.23}$$

where $\boldsymbol{f}$ is the volume force density, $\boldsymbol{S}$ is the Poynting vector and $\overline{\overline{T}}_{\text{em}}$ is the Maxwell stress tensor, which is itself given by

$$\overline{\overline{T}}_{\text{em}} = \boldsymbol{DE} + \boldsymbol{BH} - \frac{1}{2}\overline{\overline{I}}(\boldsymbol{D}\cdot\boldsymbol{E} + \boldsymbol{B}\cdot\boldsymbol{H}), \tag{5.24}$$

where $\overline{\overline{I}}$ is the identity tensor and $\boldsymbol{E}, \boldsymbol{D}, \boldsymbol{B}$ and $\boldsymbol{H}$ correspond to the total electromagnetic fields. Let us assume, for simplicity, that the object is not moving and hence that the total field (incident and scattered fields) around the object is not changing with time. In that case, the time derivative of the Poynting vector in (5.23) vanishes. By making use of Gauss

integration law, the time-averaged force acting on the object is thus given by

$$\langle \boldsymbol{F} \rangle = \int_V \nabla \cdot \langle \overline{\overline{T}}_{\rm em} \rangle \, dV = \oint_S \langle \overline{\overline{T}}_{\rm em} \rangle \cdot \hat{\boldsymbol{n}} \, dS, \tag{5.25}$$

where $\hat{\boldsymbol{n}}$ is the unit vector normal to the surface surrounding the object and $\langle \cdot \rangle$ denotes the time-average operation. Assume now that the object to be moved is the metasurface system surrounded by vacuum that is depicted in Fig. 5.50. The forces acting on this metasurface, which is located at $z = 0$ in the xy-plane, are calculated using (5.25). The surface integration in (5.25) is performed on two planar surfaces, which are located at $z = 0^+$ and $z = 0^-$ and for which $\hat{\boldsymbol{n}} = +\hat{\boldsymbol{z}}$ and $\hat{\boldsymbol{n}} = -\hat{\boldsymbol{z}}$, respectively.

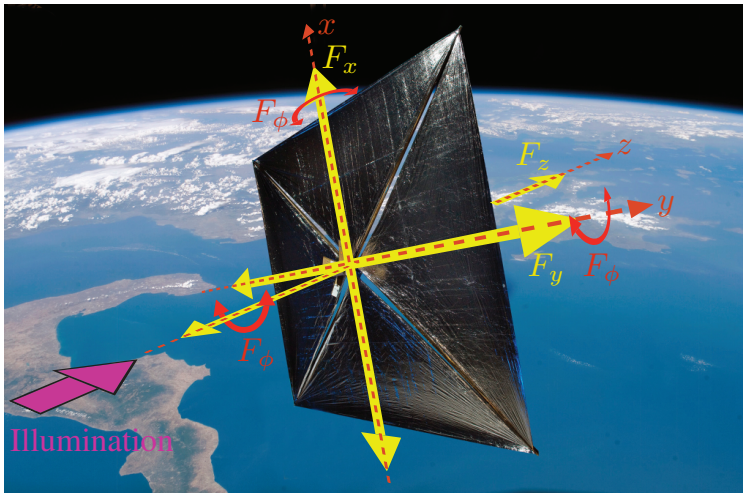

Figure 5.50 Proposed metasurface solar sail with two lateral forces ($\pm F_x$ and $\pm F_y$), a repulsive/attractive force ($\pm F_z$) and three rotational forces ($\pm F_\phi$). Credit: NASA.

Let us now assume that the interactions between the incident, reflected and transmitted waves and the metasurface take place only in the xz-plane. The forces that an incident plane wave, impinging at an angle $\theta_{\rm i}$ from broadside, exert on the metasurface are found from (5.25) to be

$$\langle F_x \rangle^{\rm i} = \frac{1}{2} \epsilon_0 E_0^2 L_x L_y \cos(\theta_{\rm i}) \sin(\theta_{\rm i}), \tag{5.26a}$$

$$\langle F_z \rangle^{\rm i} = \frac{1}{2} \epsilon_0 E_0^2 L_x L_y \cos(\theta_{\rm i})^2, \tag{5.26b}$$

where E_0 is the amplitude of the wave. Similarly, the forces due to the reflected and transmitted waves may be straightforwardly deduced from (5.26) to be $\langle F_x \rangle^{\rm r} = -\langle F_x \rangle^{\rm i}$ and $\langle F_z \rangle^{\rm r} = \langle F_z \rangle^{\rm i}$, and $\langle F_x \rangle^{\rm t} = -\langle F_x \rangle^{\rm i}$ and $\langle F_z \rangle^{\rm t} = -\langle F_z \rangle^{\rm i}$.

In order to evaluate the forces in a more realistic scenario, we also consider the case of Gaussian illumination. Let us consider a 2D Gaussian beam with a Gaussian profile $E \propto e^{-\boldsymbol{r}^2/w}$, where w is related to the half-maximum beamwidth, L, through $L = 2\sqrt{w\ln(2)}$. The forces that are exerted on the metasurface are again found from (5.25) and read

$$\langle F_x\rangle^{\mathrm{i}} = \frac{E_0^2\epsilon_0 L_y}{4k_0^2}\sqrt{w_{\mathrm{i}}}\sin(\theta_{\mathrm{i}})\bigg[2L_x\sqrt{w_{\mathrm{i}}}\cos(\theta_{\mathrm{i}})e^{-L_x^2\cos(\theta_{\mathrm{i}})^2/(2w_{\mathrm{i}})} + \sqrt{2\pi}(k_0^2 - w_{\mathrm{i}})\mathrm{Erf}\Big(\frac{L_x\cos(\theta_{\mathrm{i}})}{\sqrt{2w_{\mathrm{i}}}}\Big)\bigg], \tag{5.27a}$$

$$\begin{aligned}\langle F_z\rangle^{\mathrm{i}} = \frac{E_0^2\epsilon_0 L_y\sqrt{w_{\mathrm{i}}}}{8k_0^2}\bigg[&2L_x\sqrt{w_{\mathrm{i}}}\cos(2\theta_{\mathrm{i}})e^{-L_x^2\cos(\theta_{\mathrm{i}})^2/(2w_{\mathrm{i}})} \\ &+ \sqrt{2\pi}\big(k_0^2 + (k_0^2 - w_{\mathrm{i}})\cos(2\theta_{\mathrm{i}})\big)\sec(\theta_{\mathrm{i}})\mathrm{Erf}\Big(\frac{L_x\cos(\theta_{\mathrm{i}})}{\sqrt{2w_{\mathrm{i}}}}\Big)\bigg],\end{aligned} \tag{5.27b}$$

where $\mathrm{Erf}(x)$ is the error function. In the case of a 3D Gaussian illumination, the forces are directly found to be

$$\langle F_x\rangle^{\mathrm{i}}_{\mathrm{3D}} = \sqrt{\frac{\pi}{2}}\mathrm{Erf}\left(\frac{L_y}{\sqrt{2}}\right)\langle F_x\rangle^{\mathrm{i}}_{\mathrm{2D}}, \tag{5.28a}$$

$$\langle F_z\rangle^{\mathrm{i}}_{\mathrm{3D}} = \sqrt{\frac{\pi}{2}}\mathrm{Erf}\left(\frac{L_y}{\sqrt{2}}\right)\langle F_z\rangle^{\mathrm{i}}_{\mathrm{2D}}, \tag{5.28b}$$

where the terms with the subscripts "2D" refer to the forces in (5.27). With these expressions, we now have the tools required to numerically investigate the different field configurations to achieve the desired forces.

5.9.2 Radiation Pressure Control with Metasurfaces

We are now interested in finding what should be the incident, reflected and transmitted waves, acting on the metasurface system in Fig. 5.50, so as to generate repulsive, attractive, lateral and rotational forces. The four different field configurations to achieve these forces are presented in Figs. 5.51, where they respectively correspond to the operations of: specular reflection, wave combination, negative refraction and Bessel beam generation (for in-plane rotation). In what follows, we will investigate in more details the electromagnetic behavior of these different cases.

Repulsive Force

Achieving a repulsive force with a flat structure is rather easy. The maximal repulsive force is simply obtained with a perfectly reflective surface [202]. Consider the illustration in Fig. 5.51a

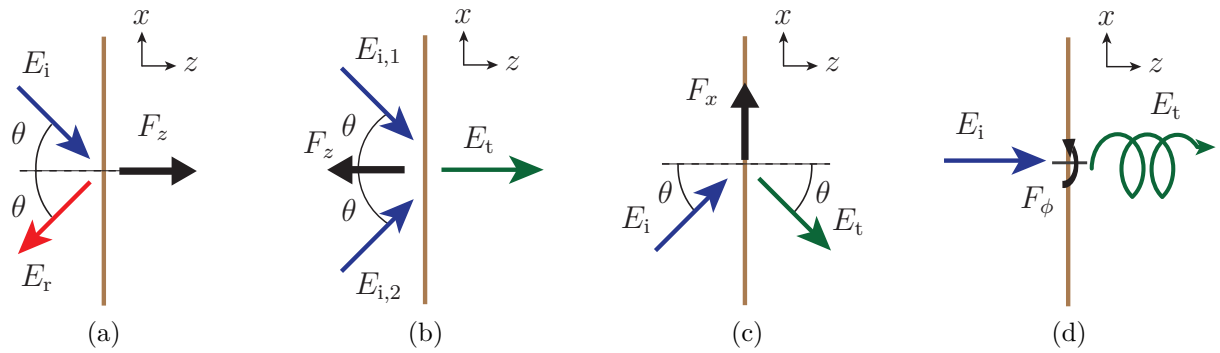

Figure 5.51 Four different field configurations corresponding to: (a) a repulsive force, (b) an attractive force, (c) a lateral force and (d) an in-plane rotational force.

where an obliquely incident wave is specularly reflected with reflection coefficient $|R| = 1$. In that case, the force acting on the object is only in the z-direction since the contributions along x of the incident and reflected waves cancel each other. When plane wave illumination is considered, the longitudinal force is, from (5.26b), given by

$$\langle F_z \rangle = \langle F_z \rangle^\mathrm{i} + \langle F_z \rangle^\mathrm{r} = 2\langle F_z \rangle^\mathrm{i} = \epsilon_0 E_0^2 L_x L_y \cos(\theta)^2. \tag{5.29}$$

The same procedure can be used to obtain the force due to a 2D Gaussian illumination using (5.27b). Note that in that specific case of specular reflection, the beamwidth of the incident and reflected Gaussian beams are equal since $\theta_\mathrm{i} = \theta_\mathrm{r}$ and thus $w_\mathrm{i} = w_\mathrm{r}$. To illustrate the differences between the repulsive forces obtained with a plane wave illumination and with a Gaussian illumination, we plot these forces as functions of the incidence angle in Fig. 5.52 with the following parameters: $E_0 = 120\pi$ V/m, $L_x = L_y = 9$ m, $\lambda_0 = 500$ nm and $w_\mathrm{i} = 8$. We see that both illuminations lead to the same force profile. As expected, the force due to the Gaussian illumination is smaller than the one due to the plane wave illumination since, in the former case, less energy is impinging on the metasurface. The maximum force is naturally obtained when the incident wave is normally impinging on the metasurface.

Attractive Force

A metasurface can be subjected to an attractive force if the incident waves are transformed into transmitted waves with momentum in the z-direction larger than that of the incident waves. This change of momentum results in a negative longitudinal force. Consider the reflectionless transformation depicted in Fig. 5.51b, where the metasurface combines two incident waves both impinging with opposite incidence angles. Here, we are using two incident

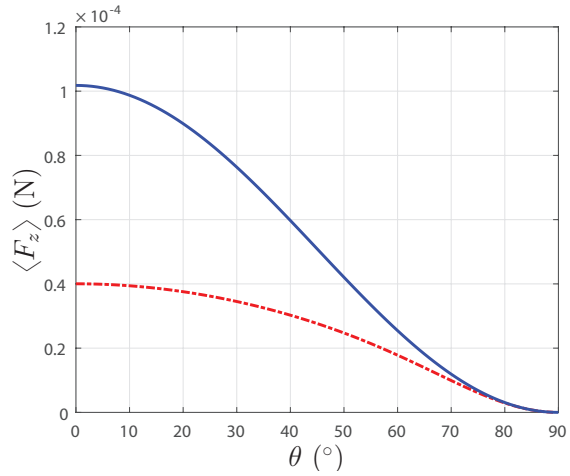

Figure 5.52 Repulsive forces exerted on a perfectly reflective surface assuming plane wave illumination (solid blue line) and Gaussian illumination (dashed red line) with $w_\mathrm{i} = 8$.

waves propagating with opposite k_x wavenumber so as to avoid any force in the x-direction. Moreover, we assume that the metasurface is fully efficient. To achieve this specification, the two incident waves *must* be orthogonally polarized and thus be treated independently from each other by the metasurface. Indeed, if the two incident waves had the same polarization, then the metasurface would act as a beam combiner or, if used in its reciprocal operation state, as a beam splitter. In that case, the efficiency would necessarily be limited to at best 50%, as was already discussed for the metasurface in Fig. 5.25. Therefore, the only way to efficiently realize the operation in Fig. 5.51b is to consider two orthogonally polarized incident waves being normally refracted by the metasurface, which should be bianisotropic as discussed in Sec. 3.3 for maximum efficiency.

Considering the discussion in Sec. 3.2, we know that the beamwidth of the incident waves is smaller than that of the transmitted waves when $\theta_\mathrm{i} > \theta_\mathrm{t}$. Note that the opposite situation, i.e. when $\theta_\mathrm{i} < \theta_\mathrm{t}$, is illustrated in Fig. 3.5. Accordingly, the relation between these beamwidths is $w_\mathrm{t} = w_\mathrm{i} \cos(\theta_\mathrm{t})^2 / \cos(\theta_\mathrm{i})^2$, while, to satisfy power conservation, the relation between the amplitude of the waves is $E_\mathrm{t} = E_0 \sqrt{\cos(\theta_\mathrm{i}) / \cos(\theta_\mathrm{t})}$, where E_t is the amplitude of the transmitted waves.

Taking into account these considerations, the attractive force exerted on the bianisotropic metasurface by the two incident plane waves and as function of the incidence angle, with $\theta_\mathrm{t} = 0°$ for maximum force, is given by

$$\langle F_z \rangle = -2 L_x L_y \epsilon_0 E_0^2 \cos(\theta_\mathrm{i}) \sin\left(\frac{\theta_\mathrm{i}}{2}\right)^2. \tag{5.30}$$

Interestingly, the maximum attractive force is achieved when $\theta_t = 0°$ and $\theta_i = 60°$. The corresponding attractive force for Gaussian illumination is found, using the same considerations as the ones made above, to be

$$\langle F_z \rangle = \frac{E_0^2 \epsilon_0 L_y \sqrt{w_i} \sec(\theta_i)^2}{2k_0^2} \Big[L_x \sqrt{w_i} \cos(\theta_i)(\cos(\theta_i)\cos(2\theta_i) - 1) e^{-L_x^2 \cos(\theta_i)^2/(2w_i)} + \sqrt{2\pi}\big(2w_i(1-\cos(\theta_i)) - k_0^2 + (k_0^2 - w_i)\cos(2\theta_i)\big) \sin\left(\frac{\theta_i}{2}\right)^2 \mathrm{Erf}\Big(\frac{L_x \cos(\theta_i)}{\sqrt{2w_i}}\Big) \Big]. \tag{5.31}$$

The relations (5.30) and (5.31) are now plotted for comparison in Fig. 5.53 and with the same parameters as those used before. As can be seen in the figure, the maximum attractive force,

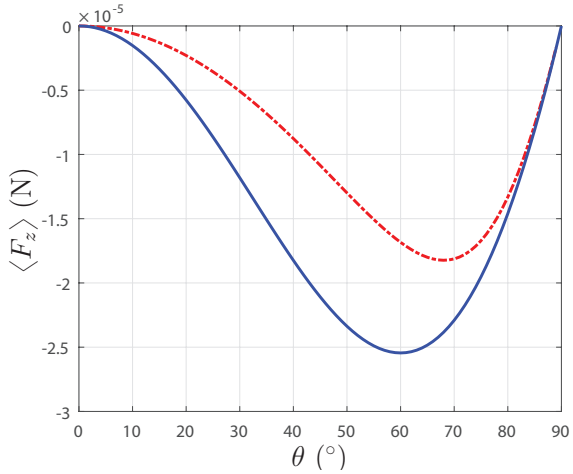

Figure 5.53 Attractive forces exerted on the metasurface assuming plane wave illumination (solid blue line) and Gaussian illumination (dashed red line) with $w_i = 8$.

in the case of Gaussian illumination, is shifted towards higher incidence angles compared to the case of plane wave illumination. This may be understood by first understanding why, in the plane wave illumination case, the maximum force is at $\theta_i = 60°$. The force exerted on the metasurface is, by conservation of momentum, due to a change in the direction of wave propagation. Intuitively, the maximum attractive force should thus be obtained when $\theta_i = 90°$ and $\theta_t = 0°$. However, as θ_i increases, less and less energy is passing through the metasurface until, eventually, no power passes through when $\theta_i = 90°$. The combination of these two effects is the reason why the maximum attractive force is at $\theta_i = 60°$. Now let us consider Gaussian illumination. In that case, even for relatively large incidence angles, most of the incident power still remains within the surface area of the metasurface due to the Gaussian profile and thus the confined nature of the field amplitude of this illumination. This effectively shifts the maximum force towards $\theta_i = 90°$. Obviously, the smaller the beamwidth

(w_i), the more confined is the incident power and thus the more important is the shift.

The plots in Fig. 5.53 represent the forces exerted on the metasurface for *specified* incidence angles. The question that arises now is: how would these forces be affected if the metasurface was illuminated by incident waves impinging at angles that are different from the specified incidence angle used to synthesize the metasurface? In order to evaluate this effect on the longitudinal force, we have performed 2D FDFD simulations with five different metasurfaces synthesized with the following specified incidence angles: $\theta_{\mathrm{i,spec}} = \{15°, 30°, 45°, 60°, 75°\}$. To maximize the refraction efficiency, the metasurfaces are bianisotropic, according to the discussion in Sec. 3.3, and the corresponding susceptibilities are obtained from relations (3.16). The simulation results are plotted in Fig. 5.54. Note that in the simulations, the metasurfaces are illuminated with Gaussian illumination with a beamwidth that is smaller ($w_\mathrm{i} = 1$) than the one used in Fig. 5.53 where $w_\mathrm{i} = 8$.

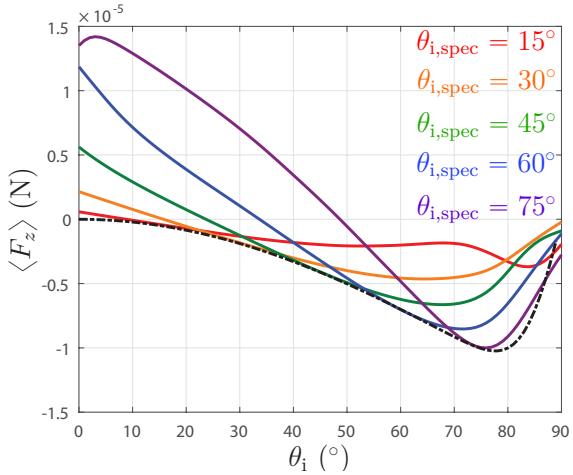

Figure 5.54 Attractive forces exerted on five different metasurfaces when the incidence angle deviates from the specified incidence angle used in the synthesis. The dashed black line corresponds to the longitudinal force for specified incidence angles, it is the same as the one plotted in Fig. 5.53 but with $w_\mathrm{i} = 1$.

As can be seen, the attractive force is more important when $\theta_{\mathrm{i,spec}}$ is large, as expected. We can also see that the simulation results are in good agreement with the expected values at the points where $\theta_\mathrm{i} = \theta_{\mathrm{i,spec}}$ (corresponding to the dashed black line). Moreover, the acceptance angle, defined as the total angle variation from the specified incidence angle under which the metasurface is still subjected to an attractive force, is particularly important. This means that the generation of an attractive force, with such metasurfaces, is robust to a deviation from the specified illumination. Note that, to obtain the results in Fig. 5.54, we have assumed that the incidence angles of the two incident waves are the same meaning that the force along the x-direction is zero for all angles.

Lateral Force

The realization of *only* a lateral force requires that the longitudinal momentum of the waves, on both sides of the metasurface, vanishes while the variation of momentum in the lateral direction (e.g. x-direction) is maximized. This may be achieved with the negative refractive transformation depicted in Fig. 5.51c where the incidence and transmission angles are equal to each other. Because these two angles are the same, the beamwidth as well as the amplitude of both incident and transmitted waves are the same. As before, the time-averaged forces acting on the metasurface are computed and the resulting longitudinal force is $\langle F_z \rangle = 0$ while the lateral force is, from (5.26a), readily found to be

$$\langle F_x \rangle = \frac{1}{2}\epsilon_0 E_0^2 L_x L_y \cos(\theta_\mathrm{i}) \sin(\theta_\mathrm{i}) - \frac{1}{2}\epsilon_0 E_0^2 L_x L_y \cos(\theta_\mathrm{t}) \sin(\theta_\mathrm{t}) = \frac{1}{2} L_x L_y \epsilon_0 E_0^2 \sin 2\theta, \quad (5.32)$$

where $\theta_\mathrm{t} = -\theta_\mathrm{i}$. It is interesting to note that this force reaches a maximum for $\theta = 45°$. The lateral force for Gaussian illumination can be obtained following the same procedure but with (5.27a) and by setting $w_\mathrm{t} = w_\mathrm{i}$. The lateral forces acting on the metasurface for plane wave and Gaussian illuminations are plotted in Fig. 5.55 versus specified incidence angles. As was the case for the attractive force discussed above, we see that the maximum of the

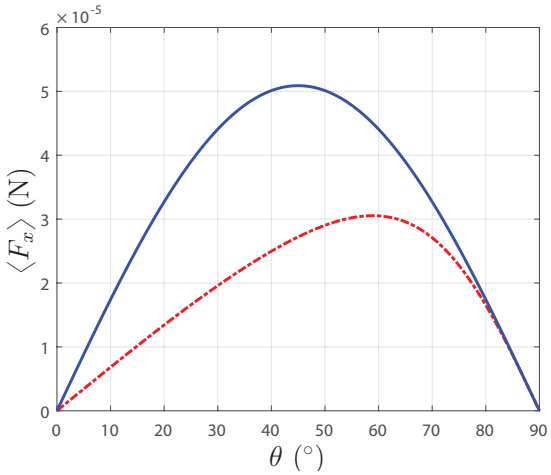

Figure 5.55 Lateral forces exerted on the metasurface assuming plane wave illumination (solid blue line) and Gaussian illumination (dashed red line) with $w_\mathrm{i} = 8$.

force, in the case of Gaussian illumination, is shifted towards larger incidence angles. The explanation for this effect is the same as the one given previously.

Let us now evaluate the behavior of this metasurface when the incidence angle deviates from the specified one. We consider five different metasurfaces synthesized for the following specified incidence angles: : $\theta_\mathrm{i,spec} = \{15°, 30°, 45°, 60°, 75°\}$. The susceptibilities are obtained,

assuming monoisotropic metasurfaces, with the exact relations in (2.18) and read

$$\chi_{\mathrm{ee}} = \frac{2}{k_z}\tan\left(k_x x\right), \tag{5.33a}$$

$$\chi_{\mathrm{mm}} = \frac{2k_z}{k_0^2}\tan\left(k_x x\right). \tag{5.33b}$$

This specific case of negative refraction is the only situation where the susceptibilities (2.18) lead to purely real and thus passive, lossless and fully efficient refractive metasurfaces. FDFD simulations are used to evaluate the forces acting on these five metasurfaces under Gaussian illumination for varying incidence angles and the results are plotted in Figs. 5.56. We see that

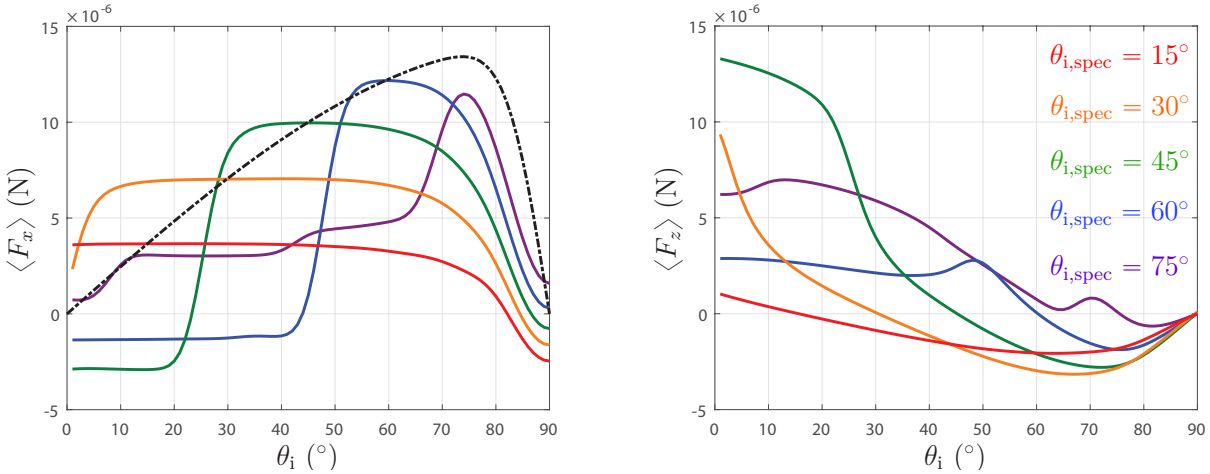

Figure 5.56 Forces exerted on five different metasurfaces when the incidence angle deviates from the specified incidence angle used in the synthesis. (a) Lateral forces and (b) longitudinal forces. The dashed black line corresponds to the lateral force for specified incidence angles, it is the same as the one plotted in Fig. 5.55 but with $w_{\mathrm{i}} = 1$.

the longitudinal forces are zero only when $\theta_{\mathrm{i}} = \theta_{\mathrm{i,spec}}$. When the incidence angle deviates from the specified one, then the longitudinal forces are either repulsive or attractive. Similarly, the curves corresponding to the lateral forces in Fig. 5.56a cross the dashed black line at the expected values precisely when $\theta_{\mathrm{i}} = \theta_{\mathrm{i,spec}}$, except for the metasurface synthesized for $\theta_{\mathrm{i,spec}} = 75°$. This may be explained by the fact that, for such large angles, undesired scattering occurs in our simulation scheme due to the way the incident wave is numerically generated.

In-Plane Rotational Force

Generating an in-plane rotational force, corresponding to a rotation of the metasurface in the xy-plane, may be realized with the transformation of an incident plane wave into a transmitted wave possessing angular momentum. The conservation of angular momentum will result in a rotation of the metasurface in the opposite direction than that of the beam. A common example of such beam, is the Bessel beam with topological charge $m \neq 0$. For simplicity, we consider the transformation of a normally incident plane wave into a normally transmitted TM-polarized ($H_z = 0$) Bessel beam of order m, as depicted in Fig. 5.51d. The longitudinal electric field of the Bessel beam is given, in cylindrical coordinates, by [235]

$$E_z(\rho, \phi) = Ae^{jm\phi}e^{-jk_z z}J_m(k_\rho \rho), \tag{5.34}$$

where A is a complex constant, m is the order of the Bessel beam, k_z and k_ρ are the longitudinal and transverse wavenumbers, respectively. From (5.34), all the field components can be computed and the corresponding rotational force due to the transmitted Bessel beam and which acts on the metasurface is found, by applying (5.25), to be

$$\langle F_\phi \rangle^{\mathrm{t}} = -\frac{A^2 k_z m \epsilon_0}{2k_\rho^2} \iint\limits_S \frac{J_m(k_\rho \rho)^2}{\rho}\, \rho d\rho d\phi. \tag{5.35}$$

It is possible to obtain a closed form expression of the force by performing the integration in (5.35) over a circular surface. Accordingly, we next assume that the metasurface has a circular shape of radius r. In that case, the rotational force due to the transmitted wave is

$$\langle F_\phi \rangle^{\mathrm{t}} = -\frac{A^2 k_z m \sqrt{\pi}(k_\rho r)^{2m} \epsilon_0 \Gamma\left(m+\frac{1}{2}\right)^2}{\Gamma(m+1)\Gamma(m+\frac{3}{2})\Gamma(2m+1)}\, {}_2F_3\left(m+\frac{1}{2}, m+\frac{1}{2}; m+1, m+\frac{3}{2}, 2m+1; -k_\rho^2 r^2\right), \tag{5.36}$$

where $\Gamma(x)$ is the gamma function and ${}_2F_3(a, b; x)$ is a generalized hypergeometric function. Note that because the incident wave is a plane wave, the only contribution to the rotational force is due to the transmitted wave. In (5.36), the parameter A must be determined so as to satisfy power conservation between the power of the incident plane wave and the power of the transmitted Bessel beam. This is achieved by integrating the z-component of the Poynting vector of the Bessel beam over the circular area of the metasurface to find the transmitted power. The parameter A is then found by equalizing the incident power to the transmitted power.

In order to evaluate the rotational force that would be exerted on the metasurface, we have

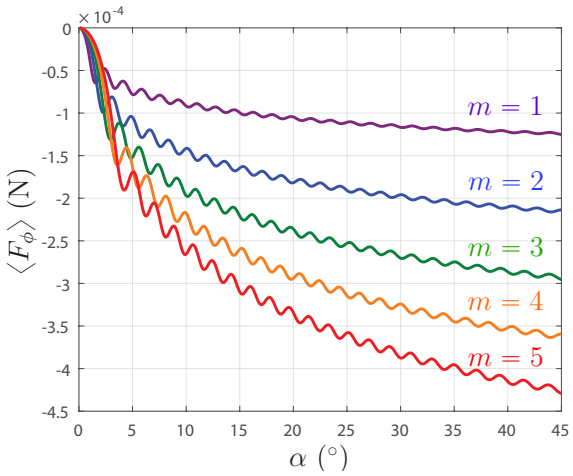

Figure 5.57 Rotational forces for Bessel beams of different topological charges and cone angles.

plotted relation (5.36) for $m = 1, 2, 3, 4, 5$ versus the Bessel beam cone angle[13], α. The radius of the metasurface is such that the total surface area is the same as that of the rectangular metasurfaces of dimensions $L_x \times L_y$ discussed previously, the radius is thus given by $r = \sqrt{L_x L_y / \pi}$. The corresponding results are plotted in Fig. 5.57.

As expected, the rotational force is proportional to the topological charge since the latter is directly related to the angular momentum. Due to the complex nature of this transformation, we have not investigated the variation of the rotational force under different incidence angles since it would involve 3D FDFD simulations. More thorough evaluation are thus left for potential future works.

5.10 Summary

In this chapter, we have presented and discussed nine metasurface concepts and applications.

We have proposed to use metasurfaces for real-time signal processing and, more specifically, use them to implement the spatial counterparts of phasers, which were so far limited to integrated guided-wave components. Accordingly, we have realized dielectric metasurfaces, which exhibit broadband and flat transmission response while still providing a frequency dependent group delay, which is necessary for the implementation of temporal dispersion engineering systems. These metasurfaces have been realized based on a new design architecture consisting of dielectric resonators held together by dielectric connections and meant to be used in the microwave regime. The fabricated structures were found to perform the expected operation.

[13]This angle is used to define the transverse and longitudinal wavenumbers of the Bessel beam, i.e. $k_\rho = k_0 \sin(\alpha)$ and $k_z = k_0 \cos(\alpha)$.

We have then been interested by the concept of birefringent metasurfaces. We have first realized electromagnetic half- and quarter-wave plates with both dielectric and metallic scattering particles. They respectively perform the operations of rotation of polarization and linear-to-circular polarization conversion. Since these metasurfaces are perfectly uniform, their resulting scattering performance were not affected by spurious coupling between adjacent unit cells and the realized wave plates thus exhibit very good transmission efficiencies. Two other types of birefringent metasurfaces were also designed. One to perform the operation of polarization beam splitting, the other one to generate orbital angular momentum (OAM) with topological charge depending on the polarization of the illumination. The polarization beam splitting metasurface was designed to spatially separate s- and p-polarized normally incident plane waves. The refraction angles for the two polarizations were chosen to be the same for simplicity. It follows that the metasurface had to be nonuniform but still perfectly periodic with same phase-gradient periods for the two polarizations. The OAM generating metasurface was designed to transform s- and p-polarized normally incident plane waves into hypergeometric Gaussian beams with topological charge $m = -1$ and $m = +1$, respectively. Due to the particular field distribution of the hypergeometric Gaussian beams, the birefringent metasurface had to be nonuniform and also aperiodic, which made its implementation more complicated. However, it was found that many unit cells were in fact exhibiting the same scattering responses of the previously realized wave plate structures thus reducing the number of unit cells to be designed. The measured responses of the fabricated metasurfaces, performing the beam splitting and OAM generation operations, were in good agreement with the expected responses but suffered from lower transmission efficiencies, compared to the wave plate structures, because of non-negligible spurious coupling between the unit cells due to their nonuniformity.

Next, we have introduced the concept of coherent spatial light processing based on bianisotropic metasurfaces. The general idea consists in a bianisotropic metasurface that combines two orthogonally polarized incident waves, an input wave and a control wave, into a single transmitted wave with a unique polarization state. By varying the amplitude and phase of the control wave, it is thus possible to affect the field distribution on the transmit side of the metasurface. This allows one to control the amplitude, phase, polarization and direction of propagation of the transmitted wave. We have used this concept to realize two slightly different coherent modulators, one where both the input and the control waves are normally impinging on the metasurface, and one where the control wave is obliquely incident thus spatially separating the position of the input and control wave sources. In both cases, the phase of the control wave was used to modulate the transmitted wave amplitude by constructive/destructive interference. The two fabricated metasurfaces were in very good

agreement with the expected results.

Then the concept of space-wave routing via surface waves was introduced as an extension of the synthesis method to the particular cases of: space-wave conversion into surface waves and surface-wave guidance. These two cases are not conventional since most metasurface structures are generally used in reflection or in transmission and thus do not to perform surface-wave transformations. Additionally, this concept also introduces the idea of metasurface systems where several metasurfaces are required to perform a specific electromagnetic transformation. To illustrate the concept, we have realized a three-metasurface system that acts as an "electromagnetic periscope" by first transforming an incident space wave into a surface wave that is guided along the structure over a given distance and is then re-transformed into a space wave. The resulting scattering performance of the fabricated system were in relatively good agreement with the expected behavior but the system suffered from a low efficiency, which is due to several effects such as: dissipation loss, undesired scattering, imperfect coupling and leakage from both sides of the structure due to its longitudinal symmetry. Nevertheless, this concept opens up an interesting avenue for future research, which may consists in developing efficient space-wave to surface-wave conversion, the potential capability of controlling several surface waves simultaneously with a bianisotropic metasurface and a susceptibility description of leaky-wave radiation.

Then, the topics of nonreciprocal nongyrotropic metasurfaces and LEDs emission enhancement were introduced. Since these projects involve many other people, they were only briefly discussed. Accordingly, we have first presented the concept of a nonreciprocal nongyrotropic metasurface, which consists in a one-way screen that does not alter the polarization state of the incident wave. We have seen that this operation may be achieved either with a bianisotropic nonreciprocal metasurface, or with a monoisotropic uniaxial moving metasurface. Then, we have succinctly introduced our proposed concept for the emission enhancement of LEDs using single or double metasurface cavities. This project may find applications in the lighting industry as well as in the research area of single-photon sources and quantum emitters.

Finally, we have proposed a prospective study on the capabilities of metasurfaces to control radiation pressure. Different field configurations were mathematically and numerically investigated so as to achieve repulsive, attractive, lateral and rotational forces.

CHAPTER 6 Fundamental Limitations

6.1 Limitations of Metasurfaces

Metasurfaces, and metamaterials in general, are composed of metallic or dielectric subwavelength resonant particles. This fact results in several drawbacks and limitations. Metallic structures usually present high losses especially at optical frequencies. Resonant particles have limited bandwidth, which prevents the implementation of broadband applications. Moreover, it is difficult to design resonant particles that are much smaller than the wavelength because the smaller the particles are, the less they interact with the incident field and, consequently, the less they can control it. For this reason, metasurfaces having susceptibilities with very rapid spatial variations over subwavelength distances (e.g. refractive metasurface with very large angle of refraction) may not be implementable since the required unit cell size would be so small, to satisfy Nyquist criterion, that the scattering particles would not resonate. For instance, the metallic scattering particles discussed in Sec. 4.1 have a transverse size of $\lambda_0/5$. Reaching smaller unit cell size, while maintaining a strong control in terms of transmission phase and amplitude of the incident field, is challenging.

Metasurfaces have been presented as 2D reductions of volume metamaterials and are consequently less bulky, less lossy and easier to fabricate. The synthesis technique presented in this document shows that a metasurface has the capability to mathematically transform an arbitrary incident fields into arbitrary reflected and transmitted fields. But, does the reduction from 3D metamaterials to 2D metasurfaces imply reduced processing power or functionalities? Is there anything that a metasurface cannot do, due to its reduced dimensionality, that a 3D metamaterial can achieve? One example could be the electromagnetic cloaks (used in transmission) that require the object to be hidden to be surrounded by a metamaterial structure to bend the light around it and thus, metasurfaces would not be appropriate in such a situation. Another example is that of beam expanders (or telescopes), usually used in optics [159] to increase the width of an incident Gaussian beam. Such systems would also be difficult to realize with a metasurface. Although a possible implementation has been presented in Sec. 5.6.4, it provides an optical transfer function that is much more limited in terms of acceptance angle than its 3D optical counterpart. In general, metasurfaces are limited to perform only the specified transformations. In other words, if the incident field deviates from the initial specifications, then the scattering behavior of the metasurface deteriorates rapidly. Therefore, metasurfaces exhibit accurate responses only for the specified incident field. Note that this is true for metamaterials (both 2D and 3D) in general since they

suffer from spatial dispersion due to the fact that the coupling between scattering particles depends on the direction of wave propagation. However, this issue of being dependent on the specified fields is more problematic to metasurfaces due to the way they are designed, i.e. the susceptibilities are, from the synthesis technique, directly dependent on the specified fields. Whereas 3D metamaterial are not necessarily synthesized in terms of specified fields but rather to provide specific values of permittivity and permeability and thus depend less on the initial specifications.

We now consider the following synthesis example: find the susceptibilities of a metasurface performing the operation of an optical analog processing system. This example is used to illustrate the disadvantage brought by the reduced dimensionality of metasurfaces as well as the scattering behavior dependence on the specified incident field. The optical analog processing operation is synthesized based on Fourier optics principles [142]. An optical analog processing system, often referred to as a 4f-system, is composed of two identical lenses placed one after the other. The distance between the two lenses corresponds to the sum of their focal length. Each lens successively performs the spatial Fourier transform of the light emerging from an object placed at the input plane of the system, one focal length away from the first lens. The overall system thus performs two successive Fourier transforms. At the center of the system lies the Fourier plane where the Fourier components of the object are accessible and can be controlled by using a mask. Since the mask can block or attenuate certain spatial components of the input field, such a system effectively acts as a spatial filter. The output field corresponds to the input field convolved with the Fourier transform of the mask function. It is easy to show that this system can be implemented with a zero-thickness metasurface but with important limitations. Assume that the metasurface is synthesized with the susceptibilities in (2.18). Here, for simplicity only the component χ_{ee}^{xx} is presented. The corresponding spatial filtering metasurface is given by

$$\chi_{\mathrm{ee}}^{xx} = \frac{-\Delta H_y}{j\omega\epsilon_0 E_{x,\mathrm{av}}} = \frac{2j}{\omega\epsilon_0}\frac{H_y^{\mathrm{t}} - H_y^{\mathrm{i}}}{E_x^{\mathrm{t}} + E_x^{\mathrm{i}}} = \frac{2j}{\omega\epsilon_0}\frac{\mathcal{F}\{M\} * H_y^{\mathrm{i}} - H_y^{\mathrm{i}}}{\mathcal{F}\{M\} * E_x^{\mathrm{i}} + E_x^{\mathrm{i}}}, \tag{6.1}$$

where M is a mask function and is a function of x and y. The presence of convolution products in (6.1) shows that the susceptibilities are inherently proportional to the specified incident field. As a consequence, the metasurface acts as a spatial filtering device but only for the specified incident field, so that different incident fields result in different transformations in contrast to what happens in an optical 4f-system that performs the same filtering operation independently of the incident beam.

These limitations might seem to be detrimental to the future of metasurfaces. However solutions exist to overcome some of these difficulties. For example, the problems arising

due to the reduced dimensionality of metasurfaces can be mitigated by cascading several metasurfaces instead of using just one. In that case, an optical system that has a length of several focal lengths, like the 4f-system for example, corresponding to several thousand of wavelengths could be implemented with a length of only a few tens of wavelengths using metamaterials [102]. The issues caused by the high losses of metallic scattering particles and limited bandwidth of resonant structures could be addressed by using dielectric resonators and highly coupled particles as done, for instance, in [112].

6.2 Limitations of the Synthesis Technique

6.2.1 Absorbing Metasurface

The mathematical synthesis technique presented in this document is certainly powerful but its main drawback is that it describes a zero-thickness metasurface, a fictitious interface that obviously cannot be exactly realized. In general, we have assumed that if the physical metasurface is very thin compared to the free-space wavelength, then it is accurately modeled by the GSTCs. In this section, we will see an example which illustrates the divergence between the ideal model and the reality.

When the synthesis technique is used to model a subwavelength-thick metasurface, the GSTCs provide relatively accurate results only to some extent. The GSTCs are, by definition, intended to deal with discontinuities. Consequently, a material slab (even deeply subwavelength) can not be accurately modeled by such continuity conditions and must rather be analyzed as a two-interface problem using the usual boundary conditions. Usually when ideal susceptibilities, obtained using the synthesis technique, are associated to a subwavelength metasurface, discrepancies appear between the simulated metasurface response and the expected response.

In order to evaluate the discrepancies introduced by the metasurface thickness, a simple numerical experiment is next conducted. A metasurface is synthesised to absorb a normally incident plane wave. The incident plane wave has an electric field defined by $\boldsymbol{E}_{\mathrm{i}} = \hat{\boldsymbol{x}} e^{-jk_0 z}$ and the transmitted plane wave has an electric field defined by $\boldsymbol{E}_{\mathrm{t}} = \hat{\boldsymbol{x}} T e^{-jk_0 z}$, where the transmission coefficient T can vary between 0 and 1. Inserting these fields into (2.18a) and (2.18d) yields

$$\chi = \chi_{\mathrm{ee}}^{xx} = \chi_{\mathrm{mm}}^{yy} = \frac{2j}{k_0}\frac{(T-1)}{(T+1)} \tag{6.2}$$

Since similar relations can be obtained for y-polarized waves, the susceptibilities in (6.2) can

be easily converted into the isotropic electric permittivity, $\epsilon_r = 1 + \chi_{\text{ee}}/t$, and the isotropic magnetic permeability, $\mu_r = 1 + \chi_{\text{mm}}/t$, where t is the thickness of the metasurface, as explained in Sec. 2.6.

Electromagnetic simulations are performed using COMSOL for different values of T and the results are reported in Fig. 6.1. As can be seen, for $T > 0.5$ the simulated transmission is in good agreement with the specification. But for $T < 0.5$ a discrepancy appears, increasing as T is reduced to 0.

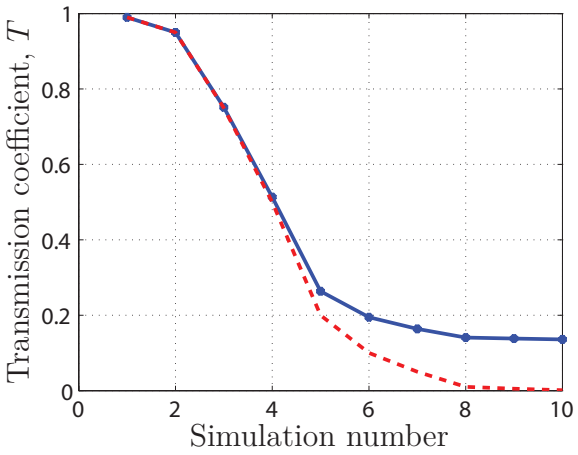

Figure 6.1 The dashed red line corresponds to the specified transmission coefficient. The solid blue line corresponds to the simulated transmission coefficients for a metasurface of thickness $t = \lambda_0/100$.

In order to understand the results presented in Fig. 6.1, the problem is analyzed as a two-interface problem where the surrounding medium 1 is vacuum with parameters

$$n_1 = 1, \qquad Z_1 = \sqrt{\frac{\mu_0}{\epsilon_0}}, \tag{6.3}$$

and where medium 2, corresponding to the metasurface, can be defined easily by noting that the electric and magnetic susceptibilities are equal to each other, as shown in (6.2). Consequently, we have that

$$n_2 = \sqrt{(1+\chi/t)^2} = 1 + \frac{\chi}{t}, \qquad Z_2 = \sqrt{\frac{\mu_0}{\epsilon_0}}\sqrt{\frac{1+\chi/t}{1+\chi/t}} = Z_1. \tag{6.4}$$

The transmission coefficient, T_{21}, from medium 1 to medium 2 and the reflection coefficient, R, inside the metasurface are given by

$$T_{21} = \frac{2Z_2}{Z_1 + Z_2} = 1, \qquad R = \frac{Z_1 - Z_2}{Z_1 + Z_2} = 0. \tag{6.5}$$

Here we see that the metasurface is reflectionless as initially specified. Since there is no reflection within the metasurface, the transmitted amplitude simply reads

$$|T_{\text{trs}}| = |e^{-jk_0 n_2 t}| = |e^{-jk_0 t}||e^{-jk_0 \chi}| = \exp\left[2\frac{(T-1)}{(T+1)}\right] \tag{6.6}$$

The expression (6.6) precisely agrees with the simulated results (solid blue line) of Fig. 6.1. It is clear that as T decreases to 0, the total transmission from the subwavelength-thick metasurface converges to $e^{-2} \approx 13.5\%$. This simple example illustrates how the GSTCs fail to accurately model the response of this metasurface. For this very specific case, where only normal incidence and transmission are considered, it is possible to modify the ideal susceptibilities of the zero-thickness metasurface such that the response of the subwavelength-thick metasurface exactly matches the response of the zero-thickness one. If the ideal susceptibility, χ, is defined from (6.2), then the "corrected" susceptibility is

$$\chi_{\text{corr}} = \chi\frac{f}{t}, \tag{6.7}$$

where f is a correcting factor. Following the same procedure as used from (6.3) to (6.6) with (6.7) instead of (6.2), the factor f can be found and equation (6.2) becomes

$$\chi_{\text{corr}} = \chi\frac{\ln T}{2t}\frac{T+1}{T-1} = \frac{j\ln T}{k_0 t}. \tag{6.8}$$

The corrected susceptibility (6.8) gives the expected transmission coefficient $|T_{\text{trs}}| = |T|$. From (6.8), we see that the corrected susceptibility of the subwavelength-thick metasurface is proportional to the natural logarithm of T meaning that, as T decreases to 0, the electric and magnetic susceptibilities both converge to $-j\infty$ whereas the ideal susceptibilities (6.2) converge to $-2j/k_0$. The important difference between (6.2) and (6.8) illustrates how implementing the ideal susceptibilities can become impracticable when the thickness of the metasurface is taken into account and how much the corrected susceptibilities diverge from the ideal ones.

The particular example presented here yields the simple corrected expression (6.8) but in general no analytical forms would exist for the corrected susceptibilities. One possibility that has been considered, to reduce the aforementioned discrepancies, is to derive boundary conditions of higher orders than the GSTCs. As they stand, the GSTCs only account for a zeroth order discontinuity meaning that only the discontinuities of the fields are taken into account but not the discontinuities of the derivatives of the fields. Higher order boundary conditions that take into considerations the first derivative of the fields may therefore yield

more accurate results. The derivation of higher-order GSTCs will be addressed in the next chapter.

6.2.2 Refractive Metasurface

We have seen how a thin metasurface slab fails to properly perform the expected transformation in the case of normally propagating waves. We will now briefly discuss the case of refractive metasurfaces with nonzero thicknesses and see how their performance compares with expected results.

For illustration, let us consider the case of a normally incident Gaussian beam being refracted at different angles θ_t by reflectionless metasurfaces. The metasurfaces are synthesized using the exact susceptibility method discussed in Sec. 3.1 and where the electromagnetic fields are expressed as in (3.3). The metasurfaces are then simulated in COMSOL as material slabs of thickness t. The metasurface slab parameters are defined as $\overline{\overline{\epsilon}}_r = \overline{\overline{I}} + \overline{\overline{\chi}}_{\rm ee}/t$ and $\overline{\overline{\mu}}_r = \overline{\overline{I}} + \overline{\overline{\chi}}_{\rm mm}/t$, as explained in Sec. 2.6.

We consider four different transformations where $\theta_{\rm t} = [20^\circ, 30^\circ, 45^\circ, 60^\circ]$ and for metasurface thicknesses ranging between $t = \lambda_0/100$ to $t = 4\lambda_0$. For each simulation, the amplitude of the refracted wave is computed by taking the Fourier transform of the magnetic field along a line on the transmit side of the metasurface and isolating the contribution that corresponds to the expected angle of transmission. The resulting scattered field amplitudes (normalized to the incident wave amplitude) are plotted in Fig. 6.2.

This figure first reveals that the metasurface thickness does not play a substantial role as long as $t < \lambda_0/5$. This is expected since, as long as the metasurface remains deeply subwavelength, the effect that the metasurface exerts on the electromagnetic field is the same, independently of the value of t. This is because the slab parameters have been obtained by "diluting" the surface susceptibilities over the metasurface thickness. Thus, increasing the thickness of the metasurface means decreasing its material parameters and vice-versa. The second information that may be obtained from the figure is that, for the four different specified refraction angles and for thin ($t < \lambda_0/5$) metasurfaces, the amplitude of the desired refracted waves remain the same with $H_{\rm t}/H_0 \approx 0.55$ whereas the expected ideal value should rather be $H_{\rm t}/H_0 = 1$. The reasons for this low efficiency will be detailed shortly. The fact that all transmitted angles have the same transmission amplitude is expected since, as discussed in Sec. 3.2, only the transmitted power is expected to change for different angles of transmission while the transmission amplitude remains the same.

Figure 6.2 also reveals that for a "thick" ($t \approx \lambda_0$) metasurface, the larger the refraction angle,

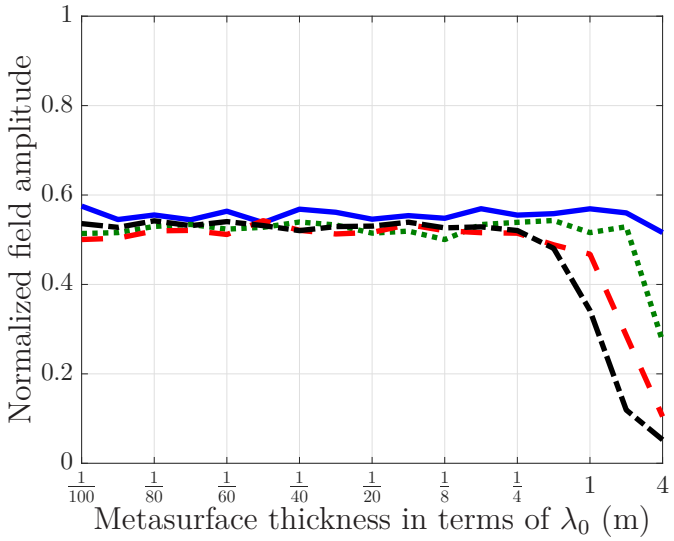

Figure 6.2 Normalized magnetic field amplitude of the refracted wave versus the metasurface thickness for refraction angles of 20° (solid blue line), 30° (dotted green line), 45° (dashed red line) and 60° (dashed-dot black line).

the less is the amount of energy going into the desired diffraction order. To understand why this happens, we show the simulations corresponding to $\theta_t = 45°$ and $t = [1/100, 1, 2, 4]\lambda_0$ in Figs. 6.3. The refraction transformation in Fig. 6.3a is relatively close to the expected result. We can see that the refracted wave has a smaller beamwidth compared to the incident one, as expected from the discussion in Sec. 3.2. However, the amplitude is less than expected and we also see the presence of undesired diffraction orders. When the metasurface thickness is increased to $t = \lambda_0$, as in Fig. 6.3b, more diffraction orders appear which further decreases the efficiency, as already pointed out in Fig. 6.2. The two extreme cases of Figs. 6.3c and 6.3d illustrate one of the issue that exists with thick metasurfaces. In these two figures, we see the presence of periodically repeating vertical lines inside the metasurfaces. These vertical lines correspond to wave scattering inside the metasurfaces due to susceptibilities with very large values. Indeed, a refractive metasurface exhibit periodically repeating susceptibilities with values approaching infinity as evidenced in Figs. 3.1. This is verified by noting that the period of the susceptibility functions, for the transformation of Figs. 6.3, is $P = \lambda_0/\sin\theta_t = \sqrt{2}\lambda_0$, which exactly corresponds to the period of the vertical lines that is visible in Figs. 6.3c and 6.3d. Therefore, the incident wave impinging on the metasurface starts to transform into the desired transmitted wave right at the top interface. The waves inside the metasurfaces that propagate obliquely scatter on the regions of high susceptibility values. This is notably visible in Fig. 6.3d where we can see the wave zigzagging inside the metasurface. Consequently, the major reasons for the generation of spurious diffraction or-

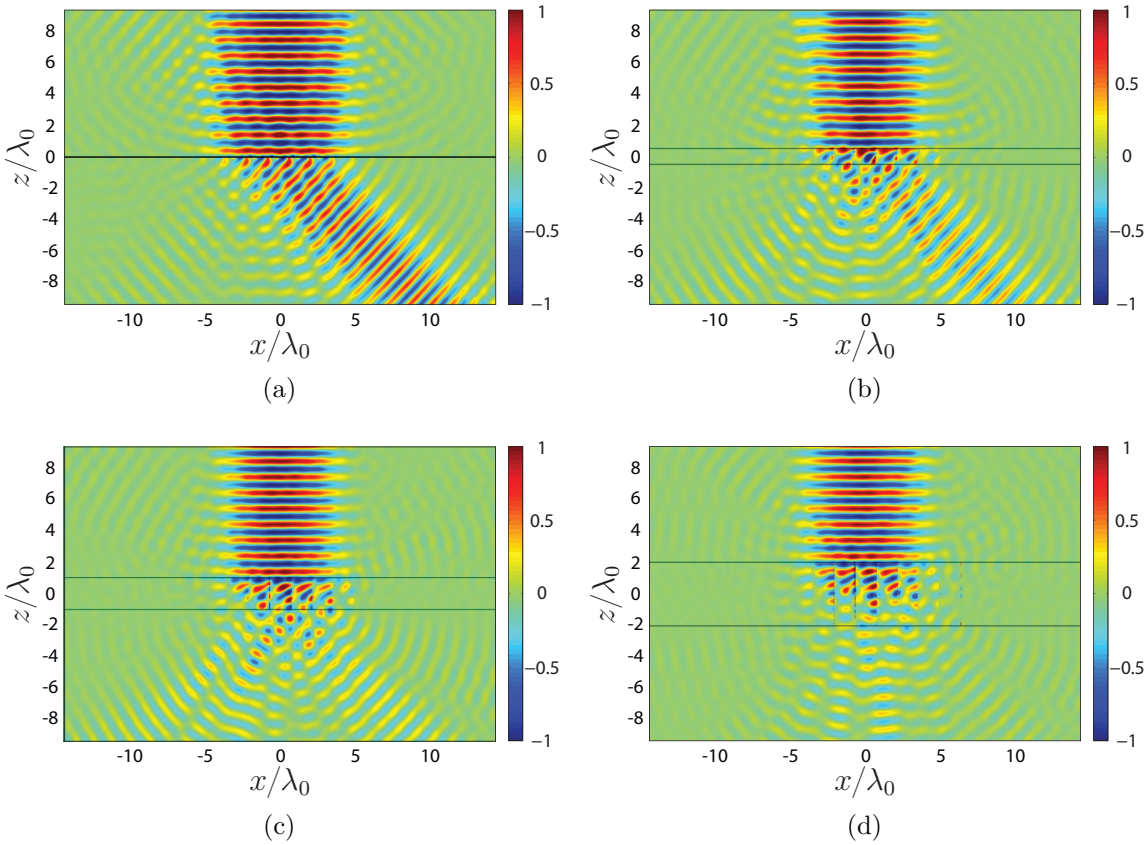

Figure 6.3 Normalized magnetic field simulated with COMSOL for refractive ($\theta_t = 45°$) metasurfaces of thickness: (a) $t = \lambda_0/100$, (b) $t = \lambda_0$, (c) $t = 2\lambda_0$ and (d) $t = 4\lambda_0$.

ders is the scattering occurring inside the metasurfaces themselves due to interactions with the periodic material which constitutes them.

To better understand what is going on inside the metasurface, we further analyze the case presented in Fig. 6.3b, where $\theta_t = 45°$ and $t = \lambda_0$. The magnetic field is measured along several line cuts for different position along z inside the metasurface. For each line cut, the Fourier transform of the field is used to obtain the spatial harmonics existing at that corresponding z-position. The corresponding result is shown in Fig. 6.4a, where the amplitude of the spatial harmonics, normalized to that of the incident wave, is plotted versus the normalized x-wavenumber as well as the position inside the slab ranging from $z = 0$ (metasurface top interface) to $z = \lambda_0$ (metasurface bottom interface).

The evolutions of the spatial harmonic corresponding to the incident wave ($k_x/k_0 = 0$) and the spatial harmonic corresponding to the desired refracted wave ($k_x/k_0 = \sqrt{2}/2$) are plotted in Fig. 6.4b in solid blue line and dashed red line, respectively.

We see from these two figures, that the amplitude of the incident wave decreases exponentially

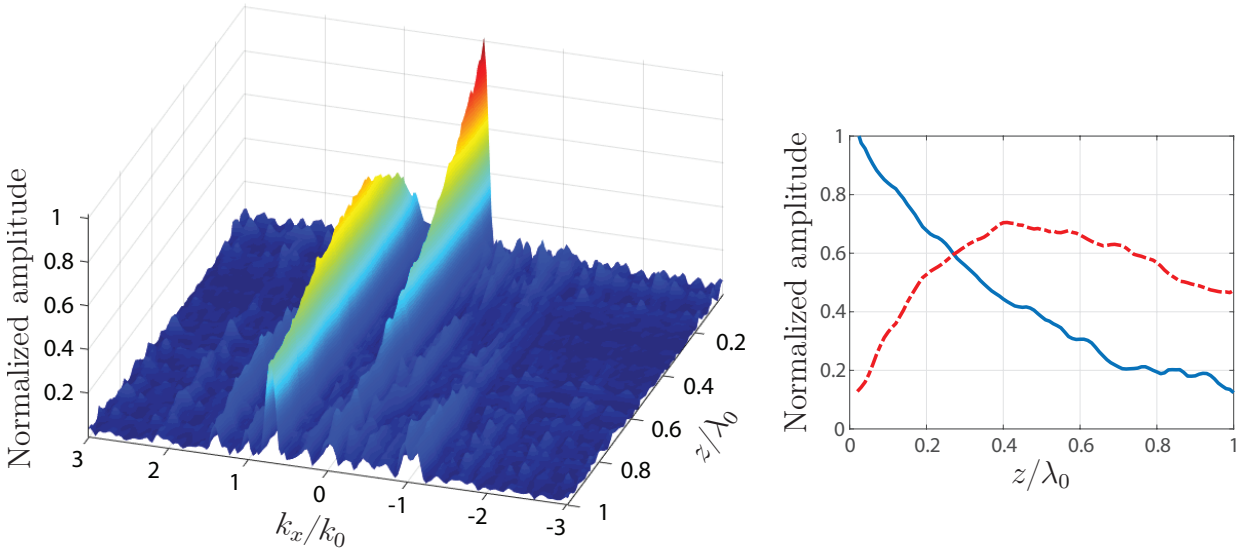

(a) (b)

Figure 6.4 Spatial harmonics amplitude inside the refractive metasurface of Fig. 6.3b as function of the position along the z-direction. (a) All the spatial harmonics with x-wavenumber in the range $-3 \leqslant k_x/k_0 \leqslant 3$. (b) Spatial harmonic corresponding to $k_x/k_0 = 0$ (incident wave) in solid blue line and spatial harmonic corresponding to $k_x/k_0 = \sqrt{2}/2$ (refracted wave) in dashed red line.

as it propagates inside the metasurface with parts of its energy being transferred to the desired refracted wave. However, due to the scattering inside the metasurface, these two waves also couple to undesired spatial harmonics notably those corresponding to $k_x/k_0 = \sqrt{2}$ and $k_x/k_0 = -\sqrt{2}/2$ and, to a lesser extent, to surface wave modes, i.e $|k_x/k_0| > 1$. Moreover, all the spatial harmonics propagating inside the metasurface experience attenuation due to the lossy nature of this structure, as discussed in Sec. 3.2. Therefore, the combined effects of coupling into undesired modes and attenuation due to loss explain the low efficiency that was achieved in Figs. 6.3. Unfortunately, It is difficult to evaluate the exact impact of the metasurface thickness on the efficiency of the transformation since the coupling mechanism between the different modes is particularly complex and depends on the value of t and θ_t.

6.3 Summary

In this chapter, we have first seen that the reduction from 3D metamaterials to 2D metasurfaces reduces loss, weight, bulkiness and fabrication complexity but comes at the cost of reduced electromagnetic transformation capabilities and higher dependance on the illumination specifications. Moreover, metamaterial structures, whether they are 3D or 2D, are inherently dependant on the electromagnetic responses of their constituting scattering par-

ticles, which are subwavelength resonators and are thus limited in terms of bandwidth and suffer from temporal and spatial dispersion.

Next, we have presented two examples to illustrate the discrepancies between the expected scattering responses and the simulated ones when the zero-thickness susceptibilities are applied to thin material slabs. There are two main sources of discrepancies: going from a single interface to two interfaces, and increasing the thickness. If the transformation does not change the direction of wave propagation, then the slab thickness has no additional effect beyond the initial change, as is the case of the absorber that was presented above. Note that transformations like rotation of polarization or wave retardation are not affected by the nonzero thickness due to the susceptibility "dilution" process. However, if the direction of wave propagation is affect by the metasurface, then important undesired scattering occurs, which increases with increasing thickness.

CHAPTER 7 Conclusions and Future Works

In this thesis, we have presented an extended discussion on the mathematical synthesis and practical realization of electromagnetic metasurfaces. The work developed throughout this document is based on a collection of several published papers that have been extended and modified to form a coherent text. The main goal of this work was to provide the reader with a metasurface synthesis framework which is as comprehensive as possible.

Metasurfaces were introduced in Chapters 1 and 2 as thin electromagnetic discontinuities being the two-dimensional reductions of 3D metamaterials. In order to simplify the mathematical synthesis problem and obtain the susceptibilities of the metasurface in terms of the specified fields, the metasurface was assumed to be of exactly zero-thickness. Upon this basis, Chapters 2 introduced a rigorous metasurface synthesis method based on susceptibility tensors. The method can be used to perform any electromagnetic transformation, without needing to resort to case-specific synthesis techniques. In most cases, the technique provides closed-form expressions for selected electric and magnetic susceptibility components to theoretically treat electromagnetic transformations where the incident, reflected and transmitted waves can be specified arbitrarily. We have notably seen that several different combinations of susceptibilities produce the exact same scattered fields. Another important consideration which was pointed out is the fact that a fully bianisotropic metasurface has enough degrees of freedom to simultaneously transform several independent sets of incident, reflected and transmitted waves. Chapter 2 also discussed the conversion from susceptibilities to scattering parameters, which is of fundamental importance for the practical realization of metasurfaces. Finally, we have proposed an extension of the synthesis technique to include second-order nonlinear susceptibility tensors and provided the reflectionless conditions of nonlinear metasurfaces with corresponding full-wave scattering analyses.

Chapter 3 put into practice and further detailed several of the concepts previously developed and discussed in Chapter 2. In this chapter, we have investigated the synthesis of monoanisotropic and bianisotropic refractive metasurfaces. We have seen that monoanisotropic metasurfaces lead to lossy and relatively inefficient transformations, while perfect refraction can be achieved with bianisotropic metasurfaces. We provided another method to perform the synthesis of metasurfaces, which consists in specifying the transformation in terms of scattering parameters instead of exact electromagnetic fields. This alternative synthesis method, while not being perfectly rigorous when a change in the direction of wave propagation is required, still provides a good efficiency that approaches that of bianisotropic refractive

metasurfaces.

Chapter 4 addressed the practical realization of metasurfaces. We have presented two different candidates for the implementation of the metasurface scattering particles: unit cells composed of cascaded metallic layers, and dielectric resonators. Both structures present their own advantages and disadvantages in terms of loss, fabrication complexity, unit cell size and number of available degrees of freedom to control the electromagnetic fields.

Chapter 5 presented a collection of several metasurface concepts and applications, among which many structures have been fabricated and measured. Dielectric resonator metasurfaces were implemented to engineer the temporal dispersion of spatial structures and electromagnetic wave plates. Metasurfaces with metallic scattering particles were then fabricated to perform various operations such as: wave plate transformations, polarization beam separation, orbital angular momentum generation, coherent spatial beam modulation and space wave to surface wave conversion. Additionally, we have also discussed other concepts such as: the synthesis of a nonreciprocal nongyrotropic metasurface and metasurfaces controlling radiation pressure. Finally, we have briefly presented the topic of metasurface cavities to enhance the light emission of single-photon sources or light-emitting diodes, which is still an on going research project involving several other people.

Finally, Chapter 6 developed on the inherent limitations of metasurfaces as well as the limitations of the synthesis technique. We have seen that the main drawbacks of metasurfaces are: their limited bandwidth due to the resonant nature of the scattering particles, the minimal size of the unit cells which prevents the realization of rapid spatial variations of the susceptibility functions and, to some extent, the fact that their ideal scattering behavior is mostly limited to the specified excitation.

Overall, metasurfaces are part of a very rich area of research that may lead to a wealth of possible new concepts and applications. While this work covers a large number of topics related to the synthesis and realization of metasurfaces, there remain several major research topics that need to be tackled and investigated. Here, we provide a non-exhaustive list of proposed future research directions:

- Increasing the bandwidth of metasurfaces and enabling the capabilities of multi-wavelength transformations. This is one of the most important improvements that is required for the realization of many practical metasurface applications.

- Developing better models to relate the shape of the scattering particles to their material parameters. The realization of the metasurface scattering particles is always a tedious

and time-consuming task. Any improvement, either in the mathematical modelling of scatterers or in the numerical simulation performance of commercial software, would be welcome for large scale developments of metasurface systems.

- Investigating in more depth the topic of nonlinear metasurfaces, which is still a relatively new and almost unexplored area of research and which definitively deserves further theoretical and experimental developments. For instance, one could perform an experimental verification of the nonreciprocal and reflectionless scattering behavior of the second-order electric and magnetic nonlinear metasurfaces discussed in Chapter 1.

- Deriving a complete synthesis procedure for the conversion of space waves to surface waves that would be more efficient than the one used in this work and that would also provide the exact susceptibilities of leaky-wave type metasurfaces. Indeed, the GSTCs based synthesis of the space wave to surface wave metasurface system concept discussed in Chapter 5 is limited and requires a complicated combination of gain and loss. Thus, it may be possible to find a more adequate way to perform the synthesis that would not lead to such intricate susceptibility functions.

- Improving the metasurface boundary conditions so as to take into account higher-order multipole moments and thus achieve a more accurate description of the metasurface response. Multipole moments may provide additional degrees of freedom and a better control of the electromagnetic fields in certain situations. This particular topic is further discussed in the next section.

7.1 Boundary Conditions of Higher-Order

The generalized sheet transition conditions (GSTCs) used to derive the synthesis method described in this document are developed assuming that the metasurface induces discontinuities of the fields but not discontinuities of the field derivatives. As such they correspond to zeroth-order boundary conditions and may only account for induced dipolar moments.

To illustrate a situation where these zeroth-order GSTCs lead to unpractical susceptibility results, we provide a simple example. Let us consider the synthesis of a reflectionless metasurface that exhibits a transmission phase shift, ϕ, when illuminated by a normally incident plane wave. For this specific case of normally propagating waves, we can rigorously use

relations (2.31) to obtain the susceptibilities, which read

$$\chi_{\mathrm{ee}} = \chi_{\mathrm{mm}} = -\frac{2}{k_0}\tan\left(\frac{\phi}{2}\right). \tag{7.1}$$

We directly see that when $\phi = \pi$, the susceptibilities become infinite. It is not really surprising that such an abrupt and complete phase reversal leads to infinite susceptibilities since we are considering zeroth-order discontinuities. In which case, the fields at the metasurface are proportional to a Dirac delta distribution, which is symmetric around the discontinuity. It would therefore seem more appropriate to consider first-order boundary conditions where the fields at the metasurface are proportional to the first derivative of a Dirac delta distribution, which is asymmetric around the discontinuity.

Accordingly, we will now derive the first-order boundary conditions which apply to zero-thickness interfaces. The following derivations are based on the same principles that were already used to derive the GSTCs in Appendix A and which are based on the work of Idemen [155].

Assume that each term in Maxwell equations can be written in the following form:

$$f(z) = \{f\} + f_0\delta(z) + f_1\delta(z)', \tag{7.2}$$

where at $z = 0$, the position of the metasurface, each term and its first derivative can be both discontinuous. This means that the terms f_k are all zero for $k \geqslant 2$ whereas, for the GSTCs, they were all zero for $k \geqslant 1$. The boundary conditions are ultimately given by (A.9) but one first needs to recursively solve the compatibility relations (A.10). Solutions must be found for $k = 1$ and inserted into the relations for $k = 0$ and finally substituted into the boundary conditions (A.9). Knowing that all terms are zero for $k = 2$, relations (A.10) expressed for $k = 1$ yields

$$\hat{\boldsymbol{z}} \times \boldsymbol{H_1} = 0, \quad \hat{\boldsymbol{z}} \times \boldsymbol{E_1} = 0, \quad \hat{\boldsymbol{z}} \cdot \boldsymbol{D_1} = 0, \quad \hat{\boldsymbol{z}} \cdot \boldsymbol{B_1} = 0. \tag{7.3}$$

Using $\boldsymbol{D} = \epsilon_0\boldsymbol{E} + \boldsymbol{P}$ and $\boldsymbol{B} = \mu_0(\boldsymbol{H} + \boldsymbol{M})$ along with (7.3), one can find the tangential components of $\boldsymbol{D}$ and $\boldsymbol{B}$ and the normal component of $\boldsymbol{E}$ and $\boldsymbol{H}$, which read

$$\boldsymbol{D_{1,\parallel}} = \epsilon_0\boldsymbol{E_{1,\parallel}} + \boldsymbol{P_{1,\parallel}} = \boldsymbol{P_{1,\parallel}}, \tag{7.4a}$$

$$\boldsymbol{B_{1,\parallel}} = \mu_0\boldsymbol{H_{1,\parallel}} + \mu_0\boldsymbol{M_{1,\parallel}} = \mu_0\boldsymbol{M_{1,\parallel}}, \tag{7.4b}$$

$$H_{1,z} = \frac{1}{\mu_0}B_{1,z} - M_{1,z} = -M_{1,z}, \tag{7.4c}$$

$$E_{1,z} = \frac{1}{\epsilon_0} D_{1,z} - \frac{1}{\epsilon_0} P_{1,z} = -\frac{1}{\epsilon_0} P_{1,z}. \tag{7.4d}$$

Inserting (7.4) into the compatibility relations (A.10) for $k = 0$ yields

$$\hat{\boldsymbol{z}} \times \boldsymbol{H}_0 = j\omega \boldsymbol{P}_{\mathbf{1},\parallel} + \nabla_\parallel \times M_{1,z}, \tag{7.5a}$$

$$\hat{\boldsymbol{z}} \times \boldsymbol{E}_0 = -j\omega\mu_0 \boldsymbol{M}_{\mathbf{1},\parallel} + \nabla_\parallel \times \frac{1}{\epsilon_0} P_{1,z}, \tag{7.5b}$$

$$\hat{\boldsymbol{z}} \cdot \boldsymbol{D}_0 = -\nabla_\parallel \cdot \boldsymbol{P}_{\mathbf{1},\parallel}, \tag{7.5c}$$

$$\hat{\boldsymbol{z}} \cdot \boldsymbol{B}_0 = -\nabla_\parallel \cdot \mu_0 \boldsymbol{M}_{\mathbf{1},\parallel}. \tag{7.5d}$$

The same method used to go from (7.3) to (7.4) is applied here with (7.5), which gives

$$\boldsymbol{D}_{\mathbf{0},\parallel} = \hat{\boldsymbol{z}} \times j\omega\epsilon_0\mu_0 \boldsymbol{M}_{\mathbf{1},\parallel} - \hat{\boldsymbol{z}} \times \nabla_\parallel \times P_{1,z} + \boldsymbol{P}_{\mathbf{0},\parallel}, \tag{7.6a}$$

$$\boldsymbol{B}_{\mathbf{0},\parallel} = -\hat{\boldsymbol{z}} \times j\omega\mu_0 \boldsymbol{P}_{\mathbf{1},\parallel} - \hat{\boldsymbol{z}} \times \nabla_\parallel \times \mu_0 M_{1,z} + \mu_0 \boldsymbol{M}_{\mathbf{0},\parallel}, \tag{7.6b}$$

$$H_{0,z} = -\nabla_\parallel \cdot \boldsymbol{M}_{\mathbf{1},\parallel} - M_{0,z}, \tag{7.6c}$$

$$E_{0,z} = -\nabla_\parallel \cdot \frac{1}{\epsilon_0} \boldsymbol{P}_{\mathbf{1},\parallel} - \frac{1}{\epsilon_0} P_{0,z}. \tag{7.6d}$$

Finally, all the required $k = 0$ components are defined with (7.5) and (7.6). The boundary conditions can be directly obtained by substituting them into (A.9), which leads to

$$\hat{\boldsymbol{z}} \times [[\boldsymbol{H}]] = j\omega \left(\hat{\boldsymbol{z}} \times j\omega\epsilon_0\mu_0 \boldsymbol{M}_{\mathbf{1},\parallel} - \hat{\boldsymbol{z}} \times \nabla_\parallel \times P_{1,z} + \boldsymbol{P}_{\mathbf{0},\parallel} \right) - \hat{\boldsymbol{z}} \times \nabla_\parallel \left(\nabla_\parallel \cdot \boldsymbol{M}_{\mathbf{1},\parallel} + M_{0,z} \right), \tag{7.7a}$$

$$\hat{\boldsymbol{z}} \times [[\boldsymbol{E}]] = j\omega \left(\hat{\boldsymbol{z}} \times j\omega\mu_0 \boldsymbol{P}_{\mathbf{1},\parallel} + \hat{\boldsymbol{z}} \times \nabla_\parallel \times \mu_0 M_{1,z} - \mu_0 \boldsymbol{M}_{\mathbf{0},\parallel} \right) - \hat{\boldsymbol{z}} \times \nabla_\parallel \frac{1}{\epsilon_0} \left(\nabla_\parallel \cdot \boldsymbol{P}_{\mathbf{1},\parallel} + P_{0,z} \right), \tag{7.7b}$$

$$\hat{\boldsymbol{z}} \cdot [[\boldsymbol{D}]] = -\nabla_\parallel \cdot \left(\hat{\boldsymbol{z}} \times j\omega\epsilon_0\mu_0 \boldsymbol{M}_{\mathbf{1},\parallel} - \hat{\boldsymbol{z}} \times \nabla_\parallel \times P_{1,z} + \boldsymbol{P}_{\mathbf{0},\parallel} \right), \tag{7.7c}$$

$$\hat{\boldsymbol{z}} \cdot [[\boldsymbol{B}]] = -\mu_0 \nabla_\parallel \cdot \left(\boldsymbol{M}_{\mathbf{0},\parallel} - \hat{\boldsymbol{z}} \times j\omega \boldsymbol{P}_{\mathbf{1},\parallel} - \hat{\boldsymbol{z}} \times \nabla_\parallel \times M_{1,z} \right). \tag{7.7d}$$

Relations (7.7) are the boundary conditions of first order. They can be compared to the GSTCs of zeroth-order given in (A.14). One can easily verify that if all terms with subscript 1 (corresponding to $k = 1$) are dropped, relations (7.7) will reduce to (A.14). Similarly to what has been done to obtain relations (2.14), the normal component of $\boldsymbol{P}$ and $\boldsymbol{M}$ can be dropped yielding boundary conditions expressed only in terms of tangential surface polarization densities

$$\hat{\boldsymbol{z}} \times [[\boldsymbol{H}]] = j\omega \left(\hat{\boldsymbol{z}} \times j\omega\epsilon_0\mu_0 \boldsymbol{M}_{\mathbf{1},\parallel} + \boldsymbol{P}_{\mathbf{0},\parallel} \right) - \hat{\boldsymbol{z}} \times \nabla_\parallel \left(\nabla_\parallel \cdot \boldsymbol{M}_{\mathbf{1},\parallel} \right), \tag{7.8a}$$

$$\hat{\boldsymbol{z}} \times [[\boldsymbol{E}]] = j\omega \left(\hat{\boldsymbol{z}} \times j\omega\mu_0 \boldsymbol{P}_{\mathbf{1},\parallel} - \mu_0 \boldsymbol{M}_{\mathbf{0},\parallel} \right) - \hat{\boldsymbol{z}} \times \nabla_\parallel \frac{1}{\epsilon_0} \left(\nabla_\parallel \cdot \boldsymbol{P}_{\mathbf{1},\parallel} \right), \tag{7.8b}$$

$$\hat{\boldsymbol{z}} \cdot [[\boldsymbol{D}]] = -\nabla_\parallel \cdot \left(\hat{\boldsymbol{z}} \times j\omega\epsilon_0\mu_0 \boldsymbol{M}_{\mathbf{1},\parallel} + \boldsymbol{P}_{\mathbf{0},\parallel} \right), \tag{7.8c}$$

$$\hat{\boldsymbol{z}} \cdot [[\boldsymbol{B}]] = -\mu_0 \nabla_\parallel \cdot \left(\boldsymbol{M}_{\mathbf{0},\parallel} - \hat{\boldsymbol{z}} \times j\omega \boldsymbol{P}_{\mathbf{1},\parallel} \right). \tag{7.8d}$$

Compared to (2.14), the last term of relations (7.8a) and (7.8b) contain spatial derivatives. Meaning that solving (7.8) may be more involved than the usual GSTCs.

At this stage, we know that $\boldsymbol{P}_0$ and $\boldsymbol{M}_0$ may take the general form of (2.7). However, the exact form that $\boldsymbol{P}_1$ and $\boldsymbol{M}_1$ should take remains unknown. As a consequence, this work deserves further investigation not only to properly define all the relevant quantities in (7.7) but also to evaluate the usefulness of the boundary conditions in (7.7) compared to those in (2.4).

REFERENCES

[1] M. G. Moharam and T. K. Gaylord, "Rigorous coupled-wave analysis of planar-grating diffraction," *J. Opt. Soc. Am.*, vol. 71, no. 7, pp. 811–818, Jul 1981.

[2] L. Chen, K. Achouri, E. Kallos, and C. Caloz, "Simultaneous enhancement of light extraction and spontaneous emission using a partially reflecting metasurface cavity," *Phys. Rev. A*, vol. 95, p. 053808, May 2017.

[3] Y. Vahabzadeh, N. Chamanara, and C. Caloz, "Generalized sheet transition condition FDTD simulation of metasurface," *arXiv preprint arXiv:1701.08760v2*, 2017.

[4] R. W. Ziolkowski, "Metamaterials: The early years in the usa," *EPJ Applied Metamaterials*, vol. 1, p. 5, 2014.

[5] C. Caloz and T. Itoh, *Electromagnetic metamaterials: transmission line theory and microwave applications*. John Wiley & Sons, 2005.

[6] N. Engheta and R. W. Ziolkowski, *Metamaterials: physics and engineering explorations*. John Wiley & Sons, 2006.

[7] F. Capolino, *Theory and phenomena of metamaterials*. CRC Press, 2009.

[8] S. A. Tretyakov, "A personal view on the origins and developments of the metamaterial concept," *J. Opt.*, vol. 19, no. 1, p. 013002, 2016.

[9] D. L. Schodek, P. Ferreira, and M. F. Ashby, *Nanomaterials, nanotechnologies and design: an introduction for engineers and architects*. Butterworth-Heinemann, 2009.

[10] J. C. Maxwell, *A treatise on electricity and magnetism*. Clarendon press, 1881, vol. 1.

[11] J. C. Bose, "On the rotation of plane of polarisation of electric waves by a twisted structure," *Proc. R. Soc. A*, vol. 63, no. 389-400, pp. 146–152, 1898.

[12] K. F. Lindman, "Über eine durch ein isotropes system von spiralförmigen resonatoren erzeugte rotationspolarisation der elektromagnetischen wellen," *Ann. Phys.*, vol. 368, no. 23, pp. 621–644, 1920.

[13] W. E. Kock, "Metallic delay lenses," *Bell Labs Technical Journal*, vol. 27, no. 1, pp. 58–82, 1948.

[14] S. A. Schelkunoff and H. T. Friis, *Antennas: theory and practice*. Wiley New York, 1952, vol. 639.

[15] J. Brown, "Artificial dielectrics having refractive indices less than unity," *Proceedings of the IEE-Part IV: Institution Monographs*, vol. 100, no. 5, pp. 51–62, 1953.

[16] W. Rotman, "Plasma simulation by artificial dielectrics and parallel-plate media," *IRE Trans. Antennas Propag.*, vol. 10, no. 1, pp. 82–95, January 1962.

[17] V. G. Veselago, "The electrodynamics of substances with simultaneously negative values of ϵ and μ," *Physics-Uspekhi*, vol. 10, no. 4, pp. 509–514, 1968.

[18] R. A. Shelby, D. R. Smith, and S. Schultz, "Experimental verification of a negative index of refraction," *Science*, vol. 292, no. 5514, pp. 77–79, 2001.

[19] J. B. Pendry, "Negative refraction makes a perfect lens," *Phys. Rev. Lett.*, vol. 85, pp. 3966–3969, Oct 2000.

[20] J. B. Pendry, D. Schurig, and D. R. Smith, "Controlling electromagnetic fields," *Science*, vol. 312, no. 5781, pp. 1780–1782, 2006.

[21] D. Schurig, J. J. Mock, B. J. Justice, S. A. Cummer, J. B. Pendry, A. F. Starr, and D. R. Smith, "Metamaterial electromagnetic cloak at microwave frequencies," *Science*, vol. 314, no. 5801, pp. 977–980, 2006.

[22] J. D. Joannopoulos, S. G. Johnson, J. N. Winn, and R. D. Meade, *Photonic crystals: molding the flow of light*. Princeton university press, 2011.

[23] F. Yang and Y. Rahmat-Samii, *Electromagnetic band gap structures in antenna engineering*. Cambridge university press Cambridge, UK, 2009.

[24] R. M. Walser, "Electromagnetic metamaterials," in *International Symposium on Optical Science and Technology*. International Society for Optics and Photonics, 2001, pp. 1–15.

[25] C. Holloway, A. Dienstfrey, E. F. Kuester, J. F. O'Hara, A. K. Azad, and A. J. Taylor, "A discussion on the interpretation and characterization of metafilms/metasurfaces: the two-dimensional equivalent of metamaterials," *Metamaterials*, vol. 3, no. 2, pp. 100–112, Oct. 2009.

[26] C. Holloway, E. F. Kuester, J. Gordon, J. O'Hara, J. Booth, and D. Smith, "An overview of the theory and applications of metasurfaces: the two-dimensional equivalents of metamaterials," *IEEE Antennas Propag. Mag.*, vol. 54, no. 2, pp. 10–35, April 2012.

[27] A. E. Minovich, A. E. Miroshnichenko, A. Y. Bykov, T. V. Murzina, D. N. Neshev, and Y. S. Kivshar, "Functional and nonlinear optical metasurfaces," *Laser & Photonics Reviews*, vol. 9, no. 2, pp. 195–213, Mar. 2015.

[28] S. B. Glybovski, S. A. Tretyakov, P. A. Belov, Y. S. Kivshar, and C. R. Simovski, "Metasurfaces: from microwaves to visible," *Phys. Rep.*, vol. 634, pp. 1 – 72, 2016.

[29] H. Lamb, "On the reflection and transmission of electric waves by a metallic grating," *Proceedings of the London Mathematical Society*, vol. 1, no. 1, pp. 523–546, 1897.

[30] G. Marconi and C. Franklin, "Reflector for use in wireless telegraphy and telephony." Apr. 22 1919, US Patent 1,301,473.

[31] L. V. Buskirk and C. Hendrix, "The zone plate as a radio-frequency focusing element," *IRE Trans. Antennas Propag.*, vol. 9, no. 3, pp. 319–320, May 1961.

[32] B. A. Munk, *Frequency Selective Surfaces: theory and design.* John Wiley & Sons, 2000.

[33] A. K. Rashid, B. Li, and Z. Shen, "An overview of three-dimensional frequency-selective structures," *IEEE Antennas Propag. Mag.*, vol. 56, no. 3, pp. 43–67, June 2014.

[34] J. Huang and J. A. Encinar, *Reflectarray antenna.* Wiley Online Library, 2007.

[35] D. Berry, R. Malech, and W. Kennedy, "The reflectarray antenna," *IEEE Trans. Antennas Propag.*, vol. 11, no. 6, pp. 645–651, Nov 1963.

[36] C. Malagisi, "Microstrip disc element reflect array," in *EASCON'78: Electronics and Aerospace Systems Convention*, vol. 1, 1978, pp. 186–192.

[37] J. Montgomery, "A microstrip reflectarray antenna element," in *Annales d'Astrophysique*, 1978.

[38] J. Stangel, "The thinned lens approach to phased array design," in *1965 Antennas and Propagation Society International Symposium*, vol. 3, Aug 1965, pp. 10–13.

[39] P. J. Kahrilas, "Hapdar 8212: An operational phased array radar," *Proceedings of the IEEE*, vol. 56, no. 11, pp. 1967–1975, Nov 1968.

[40] D. McGrath, "Planar three-dimensional constrained lenses," *IEEE Trans. Antennas Propag.*, vol. 34, no. 1, pp. 46–50, January 1986.

[41] D. M. Pozar, "Flat lens antenna concept using aperture coupled microstrip patches," *Electron. Lett.*, vol. 32, no. 23, pp. 2109–2111, Nov 1996.

[42] K.-W. Lam, S.-W. Kwok, Y. Hwang, and T. K. Lo, "Implementation of transmitarray antenna concept by using aperture-coupled microstrip patches," in *Proceedings of 1997 Asia-Pacific Microwave Conference*, vol. 1, Dec 1997, pp. 433–436 vol.1.

[43] S. Datthanasombat, A. Prata, L. R. Arnaro, J. A. Harrell, S. Spitz, and J. Perret, "Layered lens antennas," in *IEEE Antennas and Propagation Society International Symposium. 2001 Digest. Held in conjunction with: USNC/URSI National Radio Science Meeting (Cat. No.01CH37229)*, vol. 2, Jul. 2001, pp. 777–780 vol.2.

[44] N. Gagnon, A. Petosa, and D. McNamara, "Thin microwave quasi-transparent phase-shifting surface (PSS)," *IEEE Trans. Antennas Propag.*, vol. 58, no. 4, pp. 1193–1201, April 2010.

[45] M. F. Imani and A. Grbic, "An analytical investigation of near-field plates," *Metamaterials*, vol. 4, no. 2, pp. 104–111, 2010.

[46] A. Grbic, L. Jiang, and R. Merlin, "Near-field plates: subdiffraction focusing with patterned surfaces," *Science*, vol. 320, no. 5875, pp. 511–513, 2008.

[47] M. Imani and A. Grbic, "Planar near-field plates," *IEEE Trans. Antennas Propag.*, vol. 61, no. 11, pp. 5425–5434, Nov 2013.

[48] B. Fong, J. Colburn, J. Ottusch, J. Visher, and D. Sievenpiper, "Scalar and tensor holographic artificial impedance surfaces," *IEEE Trans. Antennas Propag.*, vol. 58, no. 10, pp. 3212–3221, Oct 2010.

[49] S. Maci, G. Minatti, M. Casaletti, and M. Bosiljevac, "Metasurfing: addressing waves on impenetrable metasurfaces," *IEEE Antennas Wireless Propag. Lett.*, vol. 10, pp. 1499–1502, 2011.

[50] K. Song, X. Zhao, Y. Liu, Q. Fu, and C. Luo, "A frequency-tunable 90°-polarization rotation device using composite chiral metamaterials," *Appl. Phys. Lett.*, vol. 103, no. 10, p. 101908, 2013.

[51] L. Martinez-Lopez, J. Rodriguez-Cuevas, J. Martinez-Lopez, and A. Martynyuk, "A multilayer circular polarizer based on bisected split-ring frequency selective surfaces," *IEEE Antennas Wireless Propag. Lett.*, vol. 13, pp. 153–156, 2014.

[52] J. Gao, K. Zhang, G. Yang, and Q. Wu, "A novel four-face polarization twister based on three-dimensional magnetic toroidal dipoles," *IEEE Trans. Magn.*, vol. 50, no. 1, pp. 1–4, Jan 2014.

[53] L. Wu, Z. Yang, Y. Cheng, R. Gong, M. Zhao, Y. Zheng, J. Duan, and X. Yuan, "Circular polarization converters based on bi-layered asymmetrical split ring metamaterials," *Appl. Phys. A*, vol. 116, no. 2, pp. 643–648, 2014.

[54] S.-C. Jiang, X. Xiong, Y.-S. Hu, Y.-H. Hu, G.-B. Ma, R.-W. Peng, C. Sun, and M. Wang, "Controlling the polarization state of light with a dispersion-free metastructure," *Phys. Rev. X*, vol. 4, p. 021026, May 2014.

[55] C. Huang, X. Ma, M. Pu, G. Yi, Y. Wang, and X. Luo, "Dual-band 90° polarization rotator using twisted split ring resonators array," *Opt. Commun.*, vol. 291, no. 0, pp. 345 – 348, 2013.

[56] J.-X. Zhao, B.-X. Xiao, X.-J. Huang, and H.-L. Yang, "Multiple-band reflective polarization converter based on complementary l-shaped metamaterial," *Microw. Opt. Technol. Lett.*, vol. 57, no. 4, pp. 978–983, 2015.

[57] Q. Levesque, M. Makhsiyan, P. Bouchon, F. Pardo, J. Jaeck, N. Bardou, C. Dupuis, R. Haïdar, and J.-L. Pelouard, "Plasmonic planar antenna for wideband and efficient linear polarization conversion," *Appl. Phys. Lett.*, vol. 104, no. 11, pp. –, 2014.

[58] G. Kenanakis, R. Zhao, A. Stavrinidis, G. Konstantinidis, N. Katsarakis, M. Kafesaki, C. M. Soukoulis, and E. N. Economou, "Flexible chiral metamaterials in the terahertz regime: a comparative study of various designs," *Opt. Mater. Express*, vol. 2, no. 12, pp. 1702–1712, Dec 2012.

[59] M. Li, L. Guo, J. Dong, and H. Yang, "An ultra-thin chiral metamaterial absorber with high selectivity for LCP and RCP waves," *J. Phys. D*, vol. 47, no. 18, p. 185102, 2014.

[60] B. Bian, S. Liu, S. Wang, X. Kong, H. Zhang, B. Ma, and H. Yang, "Novel triple-band polarization-insensitive wide-angle ultra-thin microwave metamaterial absorber," *J. Appl. Phys.*, vol. 114, no. 19, pp. –, 2013.

[61] C. A. Valagiannopoulos, A. Tukiainen, T. Aho, T. Niemi, M. Guina, S. A. Tretyakov, and C. R. Simovski, "Perfect magnetic mirror and simple perfect absorber in the visible spectrum," *Phys. Rev. B*, vol. 91, p. 115305, Mar. 2015.

[62] Y. Wen, W. Ma, J. Bailey, G. Matmon, X. Yu, and G. Aeppli, "Planar broadband and high absorption metamaterial using single nested resonator at terahertz frequencies," *Opt. Lett.*, vol. 39, no. 6, pp. 1589–1592, Mar. 2014.

[63] F. Dincer, O. Akgol, M. Karaaslan, E. Unal, and C. Sabah, "Polarization angle independent perfect metamaterial absorbers for solar cell applications in the microwave, infrared, and visible regime," *Prog. Electromagn. Res.*, vol. 144, pp. 93–101, 2014.

[64] M. Yoo and S. Lim, "Polarization-independent and ultrawideband metamaterial absorber using a hexagonal artificial impedance surface and a resistor-capacitor layer," *IEEE Trans. Antennas Propag.*, vol. 62, no. 5, pp. 2652–2658, May 2014.

[65] Y. Ra'di, V. Asadchy, and S. Tretyakov, "Total absorption of electromagnetic waves in ultimately thin layers," *IEEE Trans. Antennas Propag.*, vol. 61, no. 9, pp. 4606–4614, Sept 2013.

[66] N. Yu, P. Genevet, M. A. Kats, F. Aieta, J.-P. Tetienne, F. Capasso, and Z. Gaburro, "Light propagation with phase discontinuities: generalized laws of reflection and refraction," *Science*, vol. 334, no. 6054, pp. 333–337, 2011.

[67] N. Yu and F. Capasso, "Flat optics with designer metasurfaces," *Nature Mater.*, vol. 13, no. 2, pp. 139–150, 2014.

[68] P. Genevet and F. Capasso, "Breakthroughs in photonics 2013: flat optics: wavefronts control with Huygens' interfaces," *Photonics Journal, IEEE*, vol. 6, no. 2, pp. 1–4, April 2014.

[69] J. Shi, X. Fang, E. T. F. Rogers, E. Plum, K. F. MacDonald, and N. I. Zheludev, "Coherent control of snell's law at metasurfaces," *Opt. Express*, vol. 22, no. 17, pp. 21 051–21 060, Aug 2014.

[70] Q. Yang, J. Gu, D. Wang, X. Zhang, Z. Tian, C. Ouyang, R. Singh, J. Han, and W. Zhang, "Efficient flat metasurface lens for terahertz imaging," *Opt. Express*, vol. 22, no. 21, pp. 25 931–25 939, Oct 2014.

[71] S. Asadchy, V. Y. Ra'di, J. Vehmas, and A. Tretyakov, S. "Functional metamirrors using bianisotropic elements," *Phys. Rev. Lett.*, vol. 114, p. 095503, Mar. 2015.

[72] G. Lipworth, A. Mrozack, J. Hunt, D. L. Marks, T. Driscoll, D. Brady, and D. R. Smith, "Metamaterial apertures for coherent computational imaging on the physical layer," *J. Opt. Soc. Am. A*, vol. 30, no. 8, pp. 1603–1612, Aug 2013.

[73] J. Hunt, T. Driscoll, A. Mrozack, G. Lipworth, M. Reynolds, D. Brady, and D. R. Smith, "Metamaterial apertures for computational imaging," *Science*, vol. 339, no. 6117, pp. 310–313, 2013.

[74] F. Liu, S. Xiao, A. Sihvola, and J. Li, "Perfect co-circular polarization reflector: a class of reciprocal perfect conductors with total co-circular polarization reflection," *IEEE Trans. Antennas Propag.*, vol. 62, no. 12, pp. 6274–6281, Dec 2014.

[75] D. Germain, D. Seetharamdoo, S. Nawaz Burokur, and A. de Lustrac, "Phase-compensated metasurface for a conformal microwave antenna," *Appl. Phys. Lett.*, vol. 103, no. 12, p. 124102, 2013.

[76] C. Holloway, "Sub-wavelength resonators: on the use of metafilms to overcome the $\lambda/2$ size limit," *IET Microwaves, Antennas and Propagation*, vol. 2, pp. 120–129(9), Mar. 2008.

[77] Y. Ra'di, V. Asadchy, and S. Tretyakov, "Tailoring reflections from thin composite metamirrors," *IEEE Trans. Antennas Propag.*, vol. 62, no. 7, pp. 3749–3760, Jul. 2014.

[78] A. Abdelrahman, A. Elsherbeni, and F. Yang, "Transmitarray antenna design using cross-slot elements with no dielectric substrate," *IEEE Antennas Wireless Propag. Lett.*, vol. 13, pp. 177–180, 2014.

[79] H. Shi, J. Li, A. Zhang, Y. Jiang, J. Wang, Z. Xu, and S. Xia, "Gradient metasurface with both polarization-controlled directional surface wave coupling and anomalous reflection," *IEEE Antennas Wireless Propag. Lett.*, vol. 14, pp. 104–107, 2015.

[80] K. Miyamoto, "The phase fresnel lens," *J. Opt. Soc. Am.*, vol. 51, no. 1, pp. 17–20, Jan 1961.

[81] M. Neviere, "Electromagnetic study of transmission gratings," *Appl. Opt.*, vol. 30, no. 31, pp. 4540–4547, Nov 1991.

[82] N. Destouches, A. V. Tishchenko, J. C. Pommier, S. Reynaud, O. Parriaux, S. Tonchev, and M. A. Ahmed, "99% efficiency measured in the -1st order of a resonant grating," *Opt. Express*, vol. 13, no. 9, pp. 3230–3235, May 2005.

[83] J. Nye and M. Berry, "Dislocations in wave trains," in *Proc. R. Soc. A A: Mathematical, Physical and Engineering Sciences*, vol. 336, no. 1605, 1974, pp. 165–190.

[84] E. Karimi, S. A. Schulz, I. De Leon, H. Qassim, J. Upham, and R. W. Boyd, "Generating optical orbital angular momentum at visible wavelengths using a plasmonic metasurface," *Light: Science & Applications*, vol. 3, no. 5, p. e167, 2014.

[85] C. Pfeiffer and A. Grbic, "Controlling vector bessel beams with metasurfaces," *Phys. Rev. Applied*, vol. 2, p. 044012, Oct 2014.

[86] X. Yi, X. Ling, Z. Zhang, Y. Li, X. Zhou, Y. Liu, S. Chen, H. Luo, and S. Wen, "Generation of cylindrical vector vortex beams by two cascaded metasurfaces," *Opt. Express*, vol. 22, no. 14, pp. 17 207–17 215, Jul 2014.

[87] M. Veysi, C. Guclu, and F. Capolino, "Vortex beams with strong longitudinally polarized magnetic field and their generation by using metasurfaces," *J. Opt. Soc. Am. B*, vol. 32, no. 2, pp. 345–354, Feb 2015.

[88] J. Sun, X. Wang, T. Xu, Z. A. Kudyshev, A. N. Cartwright, and N. M. Litchinitser, "Spinning light on the nanoscale," *Nano Lett.*, vol. 14, no. 5, pp. 2726–2729, 2014.

[89] J. Lin, P. Genevet, M. A. Kats, N. Antoniou, and F. Capasso, "Nanostructured holograms for broadband manipulation of vector beams," *Nano Lett.*, vol. 13, no. 9, pp. 4269–4274, 2013.

[90] J. Hunt, J. Gollub, T. Driscoll, G. Lipworth, A. Mrozack, M. S. Reynolds, D. J. Brady, and D. R. Smith, "Metamaterial microwave holographic imaging system," *J. Opt. Soc. Am. A*, vol. 31, no. 10, pp. 2109–2119, Oct 2014.

[91] G. Zheng, H. Mühlenbernd, M. Kenney, G. Li, T. Zentgraf, and S. Zhang, "Metasurface holograms reaching 80% efficiency," *Nat. Nanotechnol.*, 2015.

[92] C. Pfeiffer and A. Grbic, "Generating stable tractor beams with dielectric metasurfaces," *Phys. Rev. B*, vol. 91, p. 115408, Mar. 2015.

[93] H. Da, Q. Bao, R. Sanaei, J. Teng, K. P. Loh, F. J. Garcia-Vidal, and C.-W. Qiu, "Monolayer graphene photonic metastructures: giant Faraday rotation and nearly perfect transmission," *Phys. Rev. B*, vol. 88, p. 205405, Nov 2013.

[94] A. Degiron and D. R. Smith, "One-way glass for microwaves using nonreciprocal metamaterials," *Phys. Rev. E*, vol. 89, p. 053203, May 2014.

[95] Y. Ra'di, V. S. Asadchy, and S. A. Tretyakov, "One-way transparent sheets," *Phys. Rev. B*, vol. 89, p. 075109, Feb 2014.

[96] T. Kodera, D. L. Sounas, and C. Caloz, "Artificial Faraday rotation using a ring metamaterial structure without static magnetic field," *Appl. Phys. Lett.*, vol. 99, no. 3, p. 031114, 2011.

[97] D. Sounas, T. Kodera, and C. Caloz, "Electromagnetic modeling of a magnetless non-reciprocal gyrotropic metasurface," *IEEE Trans. Antennas Propag.*, vol. 61, no. 1, pp. 221–231, Jan 2013.

[98] Y. Zhu, X. Hu, Z. Chai, H. Yang, and Q. Gong, "Active control of chirality in nonlinear metamaterials," *Appl. Phys. Lett.*, vol. 106, no. 9, p. 091109, 2015.

[99] V. K. Valev, J. Baumberg, B. De Clercq, N. Braz, X. Zheng, E. Osley, S. Vandendriessche, M. Hojeij, C. Blejean, J. Mertens *et al.*, "Nonlinear superchiral metasurfaces: tuning chirality and disentangling non-reciprocity at the nanoscale," *Adv. Mater.*, vol. 26, no. 24, pp. 4074–4081, 2014.

[100] J. Lee, M. Tymchenko, C. Argyropoulos, P.-Y. Chen, F. Lu, F. Demmerle, G. Boehm, M.-C. Amann, A. Alù, and M. A. Belkin, "Giant nonlinear response from plasmonic metasurfaces coupled to intersubband transitions," *Nature*, vol. 511, no. 7507, pp. 65–69, 2014.

[101] A. Pors, M. G. Nielsen, and S. I. Bozhevolnyi, "Analog computing using reflective plasmonic metasurfaces," *Nano Lett.*, vol. 15, no. 1, pp. 791–797, 2015.

[102] A. Silva, F. Monticone, G. Castaldi, V. Galdi, A. Alù, and N. Engheta, "Performing mathematical operations with metamaterials," *Science*, vol. 343, no. 6167, pp. 160–163, 2014.

[103] J. Ortiz, J. Baena, V. Losada, F. Medina, and J. Araque, "Spatial angular filtering by fsss made of chains of interconnected SRRs and CSRRs," *IEEE Microw. Compon. Lett.*, vol. 23, no. 9, pp. 477–479, 2013.

[104] Y. Shen, D. Ye, L. Wang, I. Celanovic, L. Ran, J. D. Joannopoulos, and M. Soljačić, "Metamaterial broadband angular selectivity," *Phys. Rev. B*, vol. 90, p. 125422, Sep 2014.

[105] Y. Shen, D. Ye, I. Celanovic, S. G. Johnson, J. D. Joannopoulos, and M. Soljačić, "Optical broadband angular selectivity," *Science*, vol. 343, no. 6178, pp. 1499–1501, 2014.

[106] L. Liu, X. Zhang, M. Kenney, X. Su, N. Xu, C. Ouyang, Y. Shi, J. Han, W. Zhang, and S. Zhang, "Broadband metasurfaces with simultaneous control of phase and amplitude," *Adv. Mater.*, vol. 26, no. 29, pp. 5031–5036, 2014.

[107] K. Konstantinidis, A. Feresidis, and P. Hall, "Broadband sub-wavelength profile high-gain antennas based on multi-layer metasurfaces," *IEEE Trans. Antennas Propag.*, vol. 63, no. 1, pp. 423–427, Jan 2015.

[108] L. Luo, I. Chatzakis, J. Wang, F. B. Niesler, M. Wegener, T. Koschny, and C. M. Soukoulis, "Broadband terahertz generation from metamaterials," *Nat. Commun.*, vol. 5, 2014.

[109] Y.-P. Jia, Y.-L. Zhang, X.-Z. Dong, M.-L. Zheng, J. Li, J. Liu, Z.-S. Zhao, and X.-M. Duan, "Complementary chiral metasurface with strong broadband optical activity and enhanced transmission," *Appl. Phys. Lett.*, vol. 104, no. 1, p. 011108, 2014.

[110] Q. Wu, C. Scarborough, D. Werner, E. Lier, and X. Wang, "Design synthesis of metasurfaces for broadband hybrid-mode horn antennas with enhanced radiation pattern and polarization characteristics," *IEEE Trans. Antennas Propag.*, vol. 60, no. 8, pp. 3594–3604, Aug 2012.

[111] B. Li, L. He, Y.-Z. Yin, W. Guo, and X.-W. Sun, "A symmetrical dual-band terahertz metamaterial with cruciform and square loops," *Prog. Electromagn. Res. C*, vol. 33, pp. 259–267, 2012.

[112] F. Aieta, M. A. Kats, P. Genevet, and F. Capasso, "Multiwavelength achromatic metasurfaces by dispersive phase compensation," *Science*, vol. 347, no. 6228, pp. 1342–1345, 2015.

[113] S. A. Maier, *Plasmonics: fundamentals and applications: fundamentals and applications*. Springer Science & Business Media, 2007.

[114] A. K. Sarychev and V. M. Shalaev, *Electrodynamics of metamaterials*. World Scientific, 2007.

[115] D. Lin, P. Fan, E. Hasman, and M. L. Brongersma, "Dielectric gradient metasurface optical elements," *Science*, vol. 345, no. 6194, pp. 298–302, 2014.

[116] A. Arbabi, Y. Horie, M. Bagheri, and A. Faraon, "Dielectric metasurfaces for complete control of phase and polarization with subwavelength spatial resolution and high transmission," *Nat. Nanotechnol.*, 2015.

[117] B. Slovick, Z. G. Yu, M. Berding, and S. Krishnamurthy, "Perfect dielectric-metamaterial reflector," *Phys. Rev. B*, vol. 88, p. 165116, Oct 2013.

[118] M. Decker, I. Staude, M. Falkner, J. Dominguez, D. N. Neshev, I. Brener, T. Pertsch, and Y. S. Kivshar, "High-efficiency dielectric Huygens surfaces," *Advanced Optical Materials*, vol. 3, no. 6, pp. 813–820, 2015.

[119] R. E. Collin, *Field theory of guided waves.* Wiley-IEEE Press, 1991.

[120] D. R. Smith, S. Schultz, P. Markoš, and C. M. Soukoulis, "Determination of effective permittivity and permeability of metamaterials from reflection and transmission coefficients," *Phys. Rev. B*, vol. 65, p. 195104, Apr 2002.

[121] A. D. Scher and E. F. Kuester, "Extracting the bulk effective parameters of a metamaterial via the scattering from a single planar array of particles," *Metamaterials*, vol. 3, no. 1, pp. 44 – 55, 2009.

[122] Y. Zhao, N. Engheta, and A. Alù, "Homogenization of plasmonic metasurfaces modeled as transmission-line loads," *Metamaterials*, vol. 5, no. 2–3, pp. 90 – 96, 2011.

[123] E. Martini, G. M. Sardi, and S. Maci, "Homogenization processes and retrieval of equivalent constitutive parameters for multisurface-metamaterials," *IEEE Trans. Antennas Propag.*, vol. 62, pp. 2081–2092, 2014.

[124] C. R. Simovski and S. A. Tretyakov, "Local constitutive parameters of metamaterials from an effective-medium perspective," *Phys. Rev. B*, vol. 75, p. 195111, May 2007.

[125] M. Albooyeh, Y. Ra'di, M. Q. Adil, and C. R. Simovski, "Revised transmission line model for electromagnetic characterization of metasurfaces," *Phys. Rev. B*, vol. 88, p. 085435, Aug 2013.

[126] X. Chen, T. M. Grzegorczyk, B.-I. Wu, J. Pacheco, and J. A. Kong, "Robust method to retrieve the constitutive effective parameters of metamaterials," *Phys. Rev. E*, vol. 70, p. 016608, Jul 2004.

[127] E. F. Kuester, M. Mohamed, M. Piket-May, and C. Holloway, "Averaged transition conditions for electromagnetic fields at a metafilm," *IEEE Trans. Antennas Propag.*, vol. 51, no. 10, pp. 2641–2651, Oct 2003.

[128] K. Achouri, M. A. Salem, and C. Caloz, "General metasurface synthesis based on susceptibility tensors," *IEEE Trans. Antennas Propag.*, vol. 63, no. 7, pp. 2977–2991, Jul. 2015.

[129] M. A. Salem, K. Achouri, and C. Caloz, "Metasurface synthesis for time-harmonic waves: Exact spectral and spatial methods," *Prog. Electromagn. Res.*, vol. 149, pp. 205–216, 2014.

[130] M. A. Salem and C. Caloz, "Manipulating light at distance by a metasurface using momentum transformation," *Opt. Express*, vol. 22, no. 12, pp. 14 530–14 543, Jun 2014.

[131] C. Pfeiffer, N. K. Emani, A. M. Shaltout, A. Boltasseva, V. M. Shalaev, and A. Grbic, "Efficient light bending with isotropic metamaterial Huygens' surfaces," *Nano Lett.*, vol. 14, no. 5, pp. 2491–2497, 2014.

[132] C. Pfeiffer and A. Grbic, "Metamaterial Huygens' surfaces: tailoring wave fronts with reflectionless sheets," *Phys. Rev. Lett.*, vol. 110, p. 197401, May 2013.

[133] C. Pfeiffer and A. Grbic, "Millimeter-wave transmitarrays for wavefront and polarization control," *IEEE Trans. Microwave Theory Tech.*, vol. 61, no. 12, pp. 4407–4417, Dec 2013.

[134] C. Pfeiffer and A. Grbic, "Bianisotropic metasurfaces for optimal polarization control: Analysis and synthesis," *Phys. Rev. Applied*, vol. 2, p. 044011, Oct 2014.

[135] J. P. Wong, M. Selvanayagam, and G. V. Eleftheriades, "Design of unit cells and demonstration of methods for synthesizing Huygens metasurfaces," *Photonics and Nanostructures - Fundamentals and Applications*, vol. 12, no. 4, pp. 360 – 375, 2014, metamaterials-2013 Congress.

[136] M. Selvanayagam and G. Eleftheriades, "Polarization control using tensor Huygens surfaces," *IEEE Trans. Antennas Propag.*, vol. 62, no. 12, pp. 6155–6168, Dec 2014.

[137] A. Epstein and G. Eleftheriades, "Passive lossless Huygens metasurfaces for conversion of arbitrary source field to directive radiation," *IEEE Trans. Antennas Propag.*, vol. 62, no. 11, pp. 5680–5695, Nov 2014.

[138] T. Niemi, A. Karilainen, and S. Tretyakov, "Synthesis of polarization transformers," *IEEE Trans. Antennas Propag.*, vol. 61, no. 6, pp. 3102–3111, June 2013.

[139] Y. Ra'di, V. Asadchy, and S. Tretyakov, "Total absorption of electromagnetic waves in ultimately thin layers," *IEEE Trans. Antennas Propag.*, vol. 61, no. 9, pp. 4606–4614, Sept 2013.

[140] F. Falcone, T. Lopetegi, M. A. G. Laso, J. D. Baena, J. Bonache, M. Beruete, R. Marqués, F. Martín, and M. Sorolla, "Babinet principle applied to the design of metasurfaces and metamaterials," *Phys. Rev. Lett.*, vol. 93, p. 197401, Nov 2004.

[141] A. V. Kildishev, A. Boltasseva, and V. M. Shalaev, "Planar photonics with metasurfaces," *Science*, vol. 339, no. 6125, p. 1232009, 2013.

[142] J. W. Goodman *et al.*, *Introduction to Fourier optics*. McGraw-hill New York, 1968, vol. 2.

[143] C. Sabah and F. Urbani, "Experimental analysis of λ-shaped magnetic resonator for mu-negative metamaterials," *Opt. Commun.*, vol. 294, no. 0, pp. 409 – 413, 2013.

[144] Y. Yang, R. Huang, L. Cong, Z. Zhu, J. Gu, Z. Tian, R. Singh, S. Zhang, J. Han, and W. Zhang, "Modulating the fundamental inductive-capacitive resonance in asymmetric double-split ring terahertz metamaterials," *Appl. Phys. Lett.*, vol. 98, no. 12, p. 121114, 2011.

[145] J. Vehmas, Y. Ra'di, A. Karilainen, and S. Tretyakov, "Eliminating electromagnetic scattering from small particles," *IEEE Trans. Antennas Propag.*, vol. 61, no. 7, pp. 3747–3756, Jul. 2013.

[146] F. Monticone, N. M. Estakhri, and A. Alù, "Full control of nanoscale optical transmission with a composite metascreen," *Phys. Rev. Lett.*, vol. 110, p. 203903, May 2013.

[147] M. Durán-Sindreu, J. Naqui, J. Bonache, and F. Martín, "Split rings for metamaterial and microwave circuit design: A review of recent developments," *International Journal of RF and Microwave Computer-Aided Engineering*, vol. 22, no. 4, pp. 439–458, 2012.

[148] A. Arbabi and A. Faraon, "Fundamental limits of ultrathin metasurfaces," *arXiv preprint arXiv:1411.2537*, 2014.

[149] M. Albooyeh, S. Kruk, C. Menzel, C. Helgert, M. Kroll, A. Krysinski, M. Decker, D. Neshev, T. Pertsch, C. Etrich *et al.*, "Resonant metasurfaces at oblique incidence: interplay of order and disorder," *Sci. Rep.*, vol. 4, 2014.

[150] V. S. Asadchy, I. A. Faniayeu, Y. Ra'di, and S. A. Tretyakov, "Determining polarizability tensors for an arbitrary small electromagnetic scatterer," *Photonics and Nanostructures-Fundamentals and Applications*, vol. 12, no. 4, pp. 298–304, 2014.

[151] K. Achouri, B. A. Khan, S. Gupta, G. Lavigne, M. A. Salem, and C. Caloz, "Synthesis of electromagnetic metasurfaces: principles and illustrations," *EPJ Applied Metamaterials*, vol. 2, p. 12, 2015.

[152] K. Achouri, M. A. Salem, and C. Caloz, "Electromagnetic metasurface performing up to four independent wave transformations," in *2015 IEEE Conference on Antenna Measurements Applications (CAMA)*, Nov 2015, pp. 1–3.

[153] K. Achouri, Y. Vahabzadeh, and C. Caloz, "Mathematical synthesis and analysis of nonlinear metasurfaces," *arXiv preprint arXiv:1703.09082*, 2017.

[154] S. Schelkunoff, "On teaching the undergraduate electromagnetic theory," *IEEE Trans. Educ.*, vol. 15, no. 1, pp. 15–25, Feb 1972.

[155] M. M. Idemen, *Discontinuities in the Electromagnetic Field*. John Wiley & Sons, 2011.

[156] M. Albooyeh, S. Tretyakov, and C. Simovski, "Electromagnetic characterization of bianisotropic metasurfaces on refractive substrates: General theoretical framework," *Ann. Phys.*, vol. 528, no. 9-10, pp. 721–737, 2016.

[157] J. Kong, *Electromagnetic wave theory*, ser. A Wiley-Interscience publication. John Wiley & Sons, 1986.

[158] A. H. Sihvola, A. J. Viitanen, I. V. Lindell, and S. A. Tretyakov, *Electromagnetic waves in chiral and bi-isotropic media*, ser. The Artech House Antenna Library. Artech House, 1994.

[159] B. Saleh and M. Teich, *Fundamentals of Photonics*, ser. Wiley Series in Pure and Applied Optics. Wiley, 2007.

[160] C. Pfeiffer, N. K. Emani, A. M. Shaltout, A. Boltasseva, V. M. Shalaev, and A. Grbic, "Efficient light bending with isotropic metamaterial Huygens' surfaces," *Nano Lett.*, vol. 14, no. 5, pp. 2491–2497, 2014.

[161] V. S. Asadchy and I. A. Fanyaev, "Simulation of the electromagnetic properties of helices with optimal shape, which provides radiation of a circularly polarized wave," *Journal of Advanced Research in Physics*, vol. 2, no. 1, 2011.

[162] C. Holloway, M. Mohamed, E. F. Kuester, and A. Dienstfrey, "Reflection and transmission properties of a metafilm: with an application to a controllable surface composed of resonant particles," *IEEE Trans. Electromagn. Compat.*, vol. 47, no. 4, pp. 853–865, Nov 2005.

[163] Y. Vahabzadeh, K. Achouri, and C. Caloz, "Simulation of metasurfaces in finite difference techniques," *IEEE Trans. Antennas Propag.*, vol. 64, no. 11, pp. 4753–4759, 2016.

[164] N. Chamanara, K. Achouri, and C. Caloz, "Efficient analysis of metasurfaces in terms of spectral-domain GSTC integral equations," *arXiv preprint arXiv:1704.06801*, 2017.

[165] T. Kodera, D. L. Sounas, and C. Caloz, "Artificial Faraday rotation using a ring metamaterial structure without static magnetic field," *Appl. Phys. Lett.*, vol. 99, no. 3, pp. 031 114:1–3, Jul. 2011.

[166] D. L. Sounas and C. Caloz, "Electromagnetic non-reciprocity and gyrotropy of graphene," *Appl. Phys. Lett.*, vol. 98, no. 2, pp. 021 911:1–3, Jan. 2011.

[167] J. A. Gordon, C. L. Holloway, and A. Dienstfrey, "A physical explanation of angle-independent reflection and transmission properties of metafilms/metasurfaces," *IEEE Antennas Wireless Propag. Lett.*, vol. 8, pp. 1127–1130, 2009.

[168] A. Di Falco, Y. Zhao, and A. Alú, "Optical metasurfaces with robust angular response on flexible substrates," *Appl. Phys. Lett.*, vol. 99, no. 16, p. 163110, 2011.

[169] Y. Ra'di and S. Tretyakov, "Angularly-independent Huygens' metasurfaces," in *2015 IEEE International Symposium on Antennas and Propagation & USNC/URSI National Radio Science Meeting*. IEEE, 2015, pp. 874–875.

[170] H. Wakatsuchi, S. Kim, J. J. Rushton, and D. F. Sievenpiper, "Waveform-dependent absorbing metasurfaces," *Phys. Rev. Lett.*, vol. 111, no. 24, p. 245501, 2013.

[171] P.-Y. Chen and A. Alù, "Optical nanoantenna arrays loaded with nonlinear materials," *Phys. Rev. B*, vol. 82, no. 23, p. 235405, 2010.

[172] Y. Yang, W. Wang, A. Boulesbaa, I. I. Kravchenko, D. P. Briggs, A. Puretzky, D. Geohegan, and J. Valentine, "Nonlinear fano-resonant dielectric metasurfaces," *Nano Lett.*, vol. 15, no. 11, pp. 7388–7393, 2015.

[173] R. W. Boyd, "Nonlinear optics," in *Handbook of Laser Technology and Applications (Three-Volume Set)*. Taylor & Francis, 2003, pp. 161–183.

[174] G. Wang and J. Huang, "Nonlinear magnetic susceptibility of ferrofluids," *Chem. Phys. Lett.*, vol. 421, no. 4, pp. 544–548, 2006.

[175] T. Kato, *Perturbation theory for linear operators*. Springer Science & Business Media, 2013, vol. 132.

[176] M. Selvanayagam and G. V. Eleftheriades, "Circuit modeling of Huygens surfaces," *IEEE Antennas Wireless Propag. Lett.*, vol. 12, pp. 1642–1645, 2013.

[177] S. Tretyakov, *Analytical modeling in applied electromagnetics*. Artech House, 2003.

[178] B. O. Zhu and Y. Feng, "Passive metasurface for reflectionless and arbitary control of electromagnetic wave transmission," *IEEE Trans. Antennas Propag.*, vol. 63, no. 12, pp. 5500–5511, Dec 2015.

[179] V. S. Asadchy, M. Albooyeh, S. N. Tcvetkova, A. Díaz-Rubio, Y. Ra'di, and S. A. Tretyakov, "Perfect control of reflection and refraction using spatially dispersive metasurfaces," *Phys. Rev. B*, vol. 94, p. 075142, Aug 2016.

[180] V. S. Asadchy, M. Albooyeh, S. N. Tcvetkova, A. Díaz-Rubio, Y. Ra'di, and S. A. Tretyakov, "Perfect control of reflection and refraction using spatially dispersive metasurfaces," *Phys. Rev. B*, vol. 94, p. 075142, Aug 2016.

[181] A. Epstein and G. V. Eleftheriades, "Synthesis of passive lossless metasurfaces using auxiliary fields for reflectionless beam splitting and perfect reflection," *Phys. Rev. Lett.*, vol. 117, no. 25, p. 256103, 2016.

[182] A. Epstein and G. V. Eleftheriades, "Reflectionless wide-angle beam splitter based on omega-type bianisotropic metasurface," in *2016 IEEE International Symposium on Antennas and Propagation (APSURSI)*, June 2016, pp. 97–98.

[183] J. P. S. Wong, A. Epstein, and G. V. Eleftheriades, "Reflectionless wide-angle refracting metasurfaces," *IEEE Antennas Wireless Propag. Lett.*, vol. 15, pp. 1293–1296, 2016.

[184] A. Epstein and G. V. Eleftheriades, "Arbitrary power-conserving field transformations with passive lossless omega-type bianisotropic metasurfaces," *IEEE Trans. Antennas Propag.*, vol. 64, no. 9, pp. 3880–3895, Sept 2016.

[185] M. Chen, E. Abdo-Sánchez, A. Epstein, and G. V. Eleftheriades, "Experimental verification of reflectionless wide-angle refraction via a bianisotropic Huygens' metasurface," *arXiv preprint arXiv:1703.06669*, 2017.

[186] G. Lavigne, K. Achouri, V. Asadchy, S. Tretyakov, and C. Caloz, "Refracting metasurfaces without spurious diffraction," *arXiv preprint arXiv:1705.09286v2*, 2017.

[187] K. Achouri, G. Lavigne, and C. Caloz, "Comparison of two synthesis methods for birefringent metasurfaces," *J. Appl. Phys.*, vol. 120, no. 23, p. 235305, 2016.

[188] M. A. Joyal and J. J. Laurin, "Analysis and design of thin circular polarizers based on meander lines," *IEEE Trans. Antennas Propag.*, vol. 60, no. 6, pp. 3007–3011, June 2012.

[189] H. Nematollahi, J. J. Laurin, J. E. Page, and J. A. Encinar, "Design of broadband transmitarray unit cells with comparative study of different numbers of layers," *IEEE Trans. Antennas Propag.*, vol. 63, no. 4, pp. 1473–1481, April 2015.

[190] C. Pfeiffer and A. Grbic, "Cascaded metasurfaces for complete phase and polarization control," *Appl. Phys. Lett.*, vol. 102, no. 23, 2013.

[191] D. M. Pozar, *Microwave Engineering*, 4th ed. Wiley, 2011.

[192] J.-S. G. Hong and M. J. Lancaster, *Microstrip filters for RF/microwave applications*. John Wiley & Sons, 2004, vol. 167.

[193] G. Mie, "Beiträge zur optik trüber medien, speziell kolloidaler metallösungen," *Ann. Phys.*, vol. 330, no. 3, pp. 377–445, 1908.

[194] M. Kerker, *The scattering of light and other electromagnetic radiation: physical chemistry: a series of monographs*. Academic press, 2013, vol. 16.

[195] A. Krasnok, S. Makarov, M. Petrov, R. Savelev, P. Belov, and Y. Kivshar, "Towards all-dielectric metamaterials and nanophotonics," *Proc. SPIE*, vol. 9502, pp. 950 203–950 203–17, 2015.

[196] A. Arbabi, Y. Horie, M. Bagheri, and A. Faraon, "Dielectric metasurfaces for complete control of phase and polarization with subwavelength spatial resolution and high transmission," *Nat. Nanotechnol.*, 2015.

[197] Y. Yang, I. I. Kravchenko, D. P. Briggs, and J. Valentine, "All-dielectric metasurface analogue of electromagnetically induced transparency," *Nat. Commun.*, vol. 5, no. 5753, pp. 366–368, Nov 2014.

[198] J. Sautter, I. Staude, M. Decker, E. Rusak, D. N. Neshev, I. Brener, and Y. S. Kivshar, "Active tuning of all-dielectric metasurfaces," *ACS Nano*, vol. 9, no. 4, pp. 4308–4315, 2015.

[199] M. I. Shalaev, J. Sun, A. Tsukernik, A. Pandey, K. Nikolskiy, and N. M. Litchinitser, "High-efficiency all-dielectric metasurfaces for ultracompact beam manipulation in transmission mode," *Nano Lett.*, vol. 15, no. 9, pp. 6261–6266, 2015.

[200] S. Gupta, K. Achouri, and C. Caloz, "All-pass metasurfaces based on interconnected dielectric resonators as a spatial phaser for real-time analog signal processing," in *2015 IEEE Conference on Antenna Measurements Applications (CAMA)*, Nov 2015, pp. 1–3.

[201] K. Achouri, A. Yahyaoui, S. Gupta, H. Rmili, and C. Caloz, "Dielectric resonator metasurface for dispersion engineering," *IEEE Trans. Antennas Propag.*, vol. 65, no. 2, pp. 673–680, Feb 2017.

[202] L. Novotny and B. Hecht, *Principles of nano-optics*. Cambridge university press, 2012.

[203] C. A. Balanis, *Antenna theory: analysis and design*. John Wiley & Sons, 2016.

[204] C. Pfeiffer, C. Zhang, V. Ray, L. J. Guo, and A. Grbic, "High performance bianisotropic metasurfaces: asymmetric transmission of light," *Phys. Rev. Lett.*, vol. 113, p. 023902, Jul 2014.

[205] M. Kim, A. M. Wong, and G. V. Eleftheriades, "Optical Huygens' metasurfaces with independent control of the magnitude and phase of the local reflection coefficients," *Phys. Rev. X*, vol. 4, no. 4, p. 041042, 2014.

[206] K. Achouri, M. A. Salem, and C. Caloz, "Birefringent generalized refractive metasurface," in *2015 IEEE International Symposium on Antennas and Propagation USNC/URSI National Radio Science Meeting*, Jul. 2015, pp. 878–879.

[207] F. Ding, Z. Wang, S. He, V. M. Shalaev, and A. V. Kildishev, "Broadband high-efficiency half-wave plate: a supercell-based plasmonic metasurface approach," *ACS nano*, vol. 9, no. 4, pp. 4111–4119, 2015.

[208] A. Pors, M. G. Nielsen, and S. I. Bozhevolnyi, "Broadband plasmonic half-wave plates in reflection," *Opt. Lett.*, vol. 38, no. 4, pp. 513–515, 2013.

[209] N. Yu, F. Aieta, P. Genevet, M. A. Kats, Z. Gaburro, and F. Capasso, "A broadband, background-free quarter-wave plate based on plasmonic metasurfaces," *Nano Lett.*, vol. 12, no. 12, pp. 6328–6333, 2012.

[210] Y. Zhao and A. Alù, "Manipulating light polarization with ultrathin plasmonic metasurfaces," *Phys. Rev. B*, vol. 84, no. 20, p. 205428, 2011.

[211] A. Pors, O. Albrektsen, I. P. Radko, and S. I. Bozhevolnyi, "Gap plasmon-based metasurfaces for total control of reflected light," *Sci. Rep.*, vol. 3, 2013.

[212] M. Farmahini-Farahani and H. Mosallaei, "Birefringent reflectarray metasurface for beam engineering in infrared," *Opt. Lett.*, vol. 38, no. 4, pp. 462–464, Feb 2013.

[213] J. H. Lee, J. W. Yoon, M. J. Jung, J. K. Hong, S. H. Song, and R. Magnusson, "A semiconductor metasurface with multiple functionalities: A polarizing beam splitter with simultaneous focusing ability," *Appl. Phys. Lett.*, vol. 104, no. 23, p. 233505, 2014.

[214] C.-F. Chen, C.-T. Ku, Y.-H. Tai, P.-K. Wei, H.-N. Lin, and C.-B. Huang, "Creating optical near-field orbital angular momentum in a gold metasurface," *Nano Lett.*, vol. 15, no. 4, pp. 2746–2750, 2015.

[215] W. Wang, Y. Li, Z. Guo, R. Li, J. Zhang, A. Zhang, and S. Qu, "Ultra-thin optical vortex phase plate based on the metasurface and the angular momentum transformation," *J. Opt.*, vol. 17, no. 4, p. 045102, 2015.

[216] K. Achouri, G. Lavigne, M. A. Salem, and C. Caloz, "Metasurface spatial processor for electromagnetic remote control," *IEEE Trans. Antennas Propag.*, vol. 64, no. 5, pp. 1759–1767, 2016.

[217] K. Achouri, M. A. Salem, and C. Caloz, "Transistor metasurface," in *2015 9th International Congress on Advanced Electromagnetic Materials in Microwaves and Optics (METAMATERIALS)*, Sept 2015, pp. 1–3.

[218] K. Achouri and C. Caloz, "Space-wave routing via surface waves using a metasurface system," *arXiv preprint arXiv:1612.05576*, 2016.

[219] K. Achouri and C. Caloz, "Surfacewave routing of beams by a transparent birefringent metasurface," in *2016 10th International Congress on Advanced Electromagnetic Materials in Microwaves and Optics (METAMATERIALS)*, Sept 2016, pp. 13–15.

[220] S. Taravati, B. A. Khan, S. Gupta, K. Achouri, and C. Caloz, "Nonreciprocal nongyrotropic magnetless metasurface," *IEEE Trans. Antennas Propag.*, vol. PP, no. 99, pp. 1–1, 2017.

[221] K. Achouri, B. A. Khan, C. Caloz, V. Asadchy, and S. Tretyakov, "Synthesis of a nongyrotropic nonreciprocal metasurface as an equivalent to a moving medium," in *2016 IEEE International Symposium on Antennas and Propagation (APSURSI)*, June 2016, pp. 371–372.

[222] M. A. Salem, K. Achouri, C. Caloz, E. Kallos, and G. Palikaras, "Cavity-backed non-uniform partially reflective metasurface (PRM) for enhanced directivity and power extraction," in *2015 9th International Congress on Advanced Electromagnetic Materials in Microwaves and Optics (METAMATERIALS)*, Sept 2015, pp. 271–273.

[223] D. Dragoman and M. Dragoman, "Time-frequency signal processing of terahertz pulses," *Appl. Opt.*, vol. 43, no. 19, pp. 3848–3853, Jul 2004.

[224] C. Caloz, S. Gupta, Q. Zhang, and B. Nikfal, "Analog signal processing," *Microw. Mag.*, vol. 14, no. 6, pp. 87–103, Sept. 2013.

[225] S. Gupta, Q. Zhang, L. Zou, L. J. Jiang, and C. Caloz, "Generalized coupled-line all-pass phasers," vol. 63, no. 3, pp. 1007–1018, Mar. 2015.

[226] M. Khorasaninejad, F. Aieta, P. Kanhaiya, M. A. Kats, P. Genevet, D. Rousso, and F. Capasso, "Achromatic metasurface lens at telecommunication wavelengths," *Nano Lett.*, vol. 15, no. 8, pp. 5358–5362, 2015.

[227] V. S. Asadchy, I. A. Faniayeu, Y. Ra'di, S. A. Khakhomov, I. V. Semchenko, and S. A. Tretyakov, "Broadband reflectionless metasheets: frequency-selective transmission and perfect absorption," *Phys. Rev. X*, vol. 5, p. 031005, Jul 2015.

[228] S. Kruk, B. Hopkins, I. I. Kravchenko, A. Miroshnichenko, D. N. Neshev, and Y. S. Kivshar, "Broadband highly efficient dielectric metadevices for polarization control," *APL Photonics*, vol. 1, no. 3, 2016.

[229] Y. Yang, W. Wang, P. Moitra, I. I. Kravchenko, D. P. Briggs, and J. Valentine, "Dielectric meta-reflectarray for broadband linear polarization conversion and optical vortex generation," *Nano Lett.*, vol. 14, no. 3, pp. 1394–1399, 2014.

[230] Y. F. Yu, A. Y. Zhu, R. Paniagua-Domínguez, Y. H. Fu, B. Luk'yanchuk, and A. I. Kuznetsov, "High-transmission dielectric metasurface with 2π phase control at visible wavelengths," *Laser & Photonics Reviews*, vol. 9, no. 4, pp. 412–418, 2015.

[231] J. Cheng, D. Ansari-Oghol-Beig, and H. Mosallaei, "Wave manipulation with designer dielectric metasurfaces," *Opt. Lett.*, vol. 39, no. 21, pp. 6285–6288, Nov 2014.

[232] J. Cheng and H. Mosallaei, "Truly achromatic optical metasurfaces: a filter circuit theory-based design," *J. Opt. Soc. Am. B*, vol. 32, no. 10, pp. 2115–2121, Oct 2015.

[233] A. Ahmadi and H. Mosallaei, "Physical configuration and performance modeling of all-dielectric metamaterials," *Phys. Rev. B*, vol. 77, no. 4, p. 045104, 2008.

[234] R. C. Rumpf, "Simple implementation of arbitrarily shaped total-field/scattered-field regions in finite-difference frequency-domain," *Prog. Electromagn. Res. B*, vol. 36, pp. 221–248, 2012.

[235] H. E. Hernández-Figueroa, M. Zamboni-Rached, and E. Recami, *Localized waves*. John Wiley & Sons, 2007, vol. 194.

[236] E. Recami and M. Zamboni-Rached, "Localized waves: a review," *Advances in Imaging and Electron Physics*, vol. 156, pp. 235–353, 2009.

[237] K. Volke-Sepulveda, V. Garcés-Chávez, S. Chávez-Cerda, J. Arlt, and K. Dholakia, "Orbital angular momentum of a high-order bessel light beam," *J. Opt. B: Quantum and Semiclassical Optics*, vol. 4, no. 2, p. S82, 2002.

[238] J. Wang, J.-Y. Yang, I. M. Fazal, N. Ahmed, Y. Yan, H. Huang, Y. Ren, Y. Yue, S. Dolinar, M. Tur *et al.*, "Terabit free-space data transmission employing orbital angular momentum multiplexing," *Nat. Photon.*, vol. 6, no. 7, pp. 488–496, 2012.

[239] E. Karimi, G. Zito, B. Piccirillo, L. Marrucci, and E. Santamato, "Hypergeometric-gaussian beams," *Opt. Lett.*, vol. 32, no. 21, pp. 3053–3055, 2007.

[240] S. M. Sze and K. K. Ng, *Physics of semiconductor devices*. John Wiley & Sons, 2006.

[241] S. N. Burokur, J.-P. Daniel, P. Ratajczak, and A. de Lustrac, "Tunable bilayered metasurface for frequency reconfigurable directive emissions," *Appl. Phys. Lett.*, vol. 97, no. 6, p. 064101, 2010.

[242] A. Fallahi and J. Perruisseau-Carrier, "Design of tunable biperiodic graphene metasurfaces," *Phys. Rev. B*, vol. 86, p. 195408, Nov 2012.

[243] S. Saadat and H. Mosallaei, "Tunable and active metasurface-based on-chip antennas," in *Antennas and Propagation Society International Symposium (APSURSI), 2012 IEEE*, Jul. 2012, pp. 1–2.

[244] B. O. Zhu, J. Zhao, and Y. Feng, "Active impedance metasurface with full 360 [deg] reflection phase tuning," *Sci. Rep.*, vol. 3, 2013.

[245] Z. Xie, X. Wang, J. Ye, S. Feng, W. Sun, T. Akalin, and Y. Zhang, "Spatial terahertz modulator," *Sci. rep.*, vol. 3, 2013.

[246] S. E. Harris, "Electromagnetically induced transparency," *Phys. Today*, vol. 50, no. 7, pp. 36–42, 2008.

[247] J. Zhang, K. F. MacDonald, and N. I. Zheludev, "Controlling light-with-light without nonlinearity," *Light: Science & Applications*, vol. 1, no. 7, p. e18, 2012.

[248] X. Fang, K. F. MacDonald, and N. I. Zheludev, "Controlling light with light using coherent metadevices: all-optical transistor, summator and invertor," *Light: Science & Applications*, vol. 4, no. 5, p. e292, 2015.

[249] M. J. Lockyear, A. P. Hibbins, and J. R. Sambles, "Microwave surface-plasmon-like modes on thin metamaterials," *Phys. Rev. Lett.*, vol. 102, no. 7, p. 073901, 2009.

[250] D. Sievenpiper, L. Zhang, R. F. Broas, N. G. Alexopolous, and E. Yablonovitch, "High-impedance electromagnetic surfaces with a forbidden frequency band," *IEEE Trans. Microw. Theory Techn.*, vol. 47, no. 11, pp. 2059–2074, 1999.

[251] S. Sun, Q. He, S. Xiao, Q. Xu, X. Li, and L. Zhou, "Gradient-index meta-surfaces as a bridge linking propagating waves and surface waves," *Nat. Mat.*, vol. 11, no. 5, pp. 426–431, 2012.

[252] Y. Xu, Y. Fu, and H. Chen, "Steering light by a sub-wavelength metallic grating from transformation optics," *Sci. Rep.*, vol. 5, 2015.

[253] Y. Fan, J. Wang, H. Ma, J. Zhang, D. Feng, M. Feng, and S. Qu, "In-plane feed antennas based on phase gradient metasurface," *IEEE Trans. Antennas Propag.*, vol. 64, no. 9, pp. 3760–3765, Sept 2016.

[254] A. Serdi͡ukov, I. Semchenko, S. Tretyakov, and A. Sihvola, *Electromagnetics of bi-anisotropic materials-Theory and Application*. Gordon and Breach science publishers, 2001, vol. 11.

[255] C. Yeh and K. F. Casey, "Reflection and transmission of electromagnetic waves by a moving dielectric slab," *Phys. Rev.*, vol. 144, pp. 665–669, Apr 1966.

[256] K. Achouri, M. A. Salem, and C. Caloz, "Metasurface susceptibility range dependence on longitudinal phase and polarization angle," in *2015 9th European Conference on Antennas and Propagation (EuCAP)*, May 2015, pp. 1–3.

[257] L. Johnson, M. Whorton, A. Heaton, R. Pinson, G. Laue, and C. Adams, "Nanosail-d: A solar sail demonstration mission," *Acta Astronaut.*, vol. 68, no. 5, pp. 571–575, 2011.

[258] V. Shvedov, A. R. Davoyan, C. Hnatovsky, N. Engheta, and W. Krolikowski, "A long-range polarization-controlled optical tractor beam," *Nat. Photon.*, vol. 8, no. 11, pp. 846–850, 2014.

[259] J. Chen, J. Ng, Z. Lin, and C. Chan, "Optical pulling force," *Nat. Photon.*, vol. 5, no. 9, pp. 531–534, 2011.

[260] S. Wang and C. Chan, "Lateral optical force on chiral particles near a surface," *Nat. Commun.*, vol. 5, p. 3307, 2014.

[261] M. M. Salary and H. Mosallaei, "Tailoring optical forces for nanoparticle manipulation on layered substrates," *Phys. Rev. B*, vol. 94, no. 3, p. 035410, 2016.

[262] E. J. Rothwell and M. J. Cloud, *Electromagnetics*. CRC press, 2008.

[263] A. Barybin, "Modal expansions and orthogonal complements in the theory of complex media waveguide excitation by external sources for isotropic, anisotropic, and bianisotropic media," *Prog. Electromagn. Res.*, vol. 19, pp. 241–300, 1998.

[264] T. P. Niemi, "Polarization transformations in bianisotropic arrays," Master's thesis, Aalto University, Finland, 2012.

APPENDIX A Distribution Based Generalized Sheet Transition Conditions

In this appendix, we provide a comprehensive derivation of the generalized sheet transition conditions. The following work is based on [127,128,155]. Note that an alternative derivation of the GSTCs is also proposed in [156]. A function $f(z)$ that is discontinuous up to the N^{th} order at $z = 0$ may be expressed in the sense of distributions as

$$f(z) = \{f(z)\} + \sum_{k=0}^{N} f_k \delta^{(k)}(z). \tag{A.1}$$

In this relation, $\{f(z)\}$ and $\sum_{k=0}^{N} f_k \delta^{(k)}(z)$ are the regular and singular parts of $f(z)$, respectively. The regular part is defined for $z \neq 0$ in the sense of usual functions as

$$\{f(z)\} = f_+(z)U(z) + f_-(z)U(-z), \tag{A.2}$$

where $U(x)$ is the unit step function and $f_\pm(z)$ denote the parts of $f(z)$ in the regions $z \gtrless 0$. The singular part, defined at $z = 0$, is a Taylor-type series, where $\delta^{(k)}(z)$ is the k^{th} derivative of the Dirac delta function, and f_k is the corresponding weighting coefficient, which is z-independent.

The function $f(z)$ in (A.1) represents here any of the quantities in Maxwell equations. Since these equations involve spatial derivatives, the question arises as how to compute the z-derivative of $f(z)$. Since f_k does not depend on z, taking the z-derivatives of the singular part of (A.1) only increases the derivative order of the Dirac delta function, from k to $k + 1$. On the other hand, the derivative of the regular part, given by (A.2), involves the derivative of $U(\cdot)$, which may be expressed in the sense of distributions, in connection with a test function ϕ, as

$$\langle U', \phi \rangle = -\langle U, \phi' \rangle = \langle \delta, \phi \rangle, \tag{A.3}$$

where $\langle \cdot, \cdot \rangle$ represents the functional inner product. In (A.3), the first equality was obtained by integrating by part and taking into account the fact that ϕ has a finite support, while the second equality follows from setting the lower bound of the integral to zero for eliminating U, using the fact that the primitive of ϕ' is ϕ, by definition, and again that ϕ has a finite support, and finally applying the sifting property of the Dirac delta function according to which $\phi(0) = \langle \delta, \phi \rangle$. In other words, the derivative of the unit step function is the Dirac

delta function. Therefore, using (A.3), the z-derivative of (A.2) is obtained as

$$\frac{d}{dz}\{f(z)\} = \left\{f'_+(z)U(z) + f'_-(z)U(-z)\right\} + [f_+(0) - f_-(0)]\delta(z) = \{f'\} + [[f]]\,\delta(z), \quad \text{(A.4)}$$

where $\{f'\}$ (curl bracket term in the second equality) represents the regular part of the derivative of $f(z)$, defined at $z \neq 0$, and the term $[[f]]$ (square bracket term in the second equality) represents the singularity, at $z = 0$. Remember that the unit of $\delta(z)$ is $(z)^{-1}$ since $\int_{-\infty}^{+\infty}\delta(z)dz = 1$ is dimensionless.

Rigorous GSTCs can now be derived using (A.1) and (A.4). The derivation is performed here only for Maxwell-Ampère equation, as the derivations for the other Maxwell equations are essentially similar. Maxwell-Ampère equation in the monochromatic regime reads

$$\nabla \times \boldsymbol{H} = \boldsymbol{J} + j\omega\boldsymbol{D}. \quad \text{(A.5)}$$

Expressing $\boldsymbol{H}$ in the form (A.1) and using the transverse-longitudinal decomposition $\nabla = \nabla_\parallel + \hat{\boldsymbol{z}}\frac{\partial}{\partial z}$ transforms the left-hand side of (A.5) into

$$\nabla \times \boldsymbol{H} = \nabla_\parallel \times \{\boldsymbol{H}\} + \hat{\boldsymbol{z}} \times \frac{\partial}{\partial z}\{\boldsymbol{H}\} + \sum_{k=0}^{N} \nabla_\parallel \times \boldsymbol{H}_k\delta^{(k)}(z) + \sum_{k=0}^{N} \hat{\boldsymbol{z}} \times \frac{\partial}{\partial z}\boldsymbol{H}_k\delta^{(k)}(z). \quad \text{(A.6)}$$

In the right-hand side of (A.6), the second term can be evaluated using (A.4) while the derivative in the last term only affects the Dirac delta function since $\boldsymbol{H}_k$ does not depend on z. Therefore, Eq. (A.6) becomes

$$\nabla \times \boldsymbol{H} = \nabla_\parallel \times \{\boldsymbol{H}\} + \hat{\boldsymbol{z}} \times \left\{\frac{\partial}{\partial z}\boldsymbol{H}\right\} + \hat{\boldsymbol{z}} \times [[\boldsymbol{H}]]\,\delta(z) + \sum_{k=0}^{N} \nabla_\parallel \times \boldsymbol{H}_k\delta^{(k)}(z) + \sum_{k=0}^{N} \hat{\boldsymbol{z}} \times \boldsymbol{H}_k\delta^{(k+1)}(z), \quad \text{(A.7)}$$

where the first two terms and the last two terms are the regular and singular parts, respectively.

Substituting (A.7) along with the (A.1) expressions of $\boldsymbol{D}$ and $\boldsymbol{J}$ into (A.5) finally transforms Maxwell-Ampère equation into

$$\begin{aligned}&\nabla_\parallel \times \{\boldsymbol{H}\} + \hat{\boldsymbol{z}} \times \left\{\frac{\partial}{\partial z}\boldsymbol{H}\right\} + \hat{\boldsymbol{z}} \times [[\boldsymbol{H}]]\,\delta(z) + \sum_{k=0}^{N} \nabla_\parallel \times \boldsymbol{H}_k\delta^{(k)}(z) + \sum_{k=0}^{N} \hat{\boldsymbol{z}} \times \boldsymbol{H}_k\delta^{(k+1)}(z) \\ &= \{\mathbf{J}(z)\} + \sum_{k=0}^{N} \mathbf{J}_k\delta^{(k)}(z) + j\omega\{\mathbf{D}(z)\} + j\omega\sum_{k=0}^{N} \mathbf{D}_k\delta^{(k)}(z),\end{aligned} \quad \text{(A.8)}$$

where $\{\boldsymbol{J}(z)\}$ is a volume current, measured in $(\mathrm{A/m^2})$, while $\mathbf{J}_k$ represents surface currents, measured in $(\mathrm{A{\cdot}m^{k-1}})$ since the unit of $\delta^{(k)}(z)$ is $(1/\mathrm{m}^{k+1})$. One may now equate the terms of the same discontinuity orders, i.e. of same Dirac derivative orders, in this equation and in the other three corresponding Maxwell equations[1]. The result is, for the terms of order $\delta^{(0)}(z) = \delta(z)$,

$$\hat{\boldsymbol{z}} \times [[\boldsymbol{H}]] + \nabla_{\parallel} \times \boldsymbol{H}_0 = \boldsymbol{J}_0 + j\omega \boldsymbol{D}_0, \tag{A.9a}$$

$$\hat{\boldsymbol{z}} \times [[\boldsymbol{E}]] + \nabla_{\parallel} \times \boldsymbol{E}_0 = -\boldsymbol{K}_0 - j\omega \boldsymbol{B}_0, \tag{A.9b}$$

$$\hat{\boldsymbol{z}} \cdot [[\boldsymbol{D}]] + \nabla_{\parallel} \cdot \boldsymbol{D}_0 = \rho_0, \tag{A.9c}$$

$$\hat{\boldsymbol{z}} \cdot [[\boldsymbol{B}]] + \nabla_{\parallel} \cdot \boldsymbol{B}_0 = m_0, \tag{A.9d}$$

and, for the terms of order $\delta^{(k)}(z)$ with $k \geqslant 1$,

$$\hat{\boldsymbol{z}} \times \boldsymbol{H}_{k-1} + \nabla_{\parallel} \times \boldsymbol{H}_k = \boldsymbol{J}_k + j\omega \boldsymbol{D}_k, \tag{A.10a}$$

$$\hat{\boldsymbol{z}} \times \boldsymbol{E}_{k-1} + \nabla_{\parallel} \times \boldsymbol{E}_k = -\boldsymbol{K}_k - j\omega \boldsymbol{B}_k, \tag{A.10b}$$

$$\hat{\boldsymbol{z}} \cdot \boldsymbol{D}_{k-1} + \nabla_{\parallel} \cdot \boldsymbol{D}_k = \rho_k, \tag{A.10c}$$

$$\hat{\boldsymbol{z}} \cdot \boldsymbol{B}_{k-1} + \nabla_{\parallel} \cdot \boldsymbol{B}_k = m_k. \tag{A.10d}$$

Equations (A.9) are the *universal boundary conditions for monochromatic waves at a planar surface at rest*, while Eqs. (A.10) are *compatibility relations* that must to be recursively applied to determine the unknown terms in (A.9) [155]. Note, letting $z \to 0$ in the regular parts of (A.9), the presence of additional terms compared to the case of conventional boundary conditions (e.g. Eq. (A.9a), where $[[\boldsymbol{H}]] = [H(z = 0_+) - H(z = 0_-)]$ and $\mathbf{J}_0$ is the sheet surface current, includes the additional terms $\nabla_{\parallel} \times \mathbf{H}_0$ and $j\omega\mathbf{D}_0$).

Let us now specialize to the case of interest: an *infinitesimal sheet discontinuity in free space*. This means that the quantities $\boldsymbol{J}_k$, $\boldsymbol{K}_k$, ρ_k and m_k exclusively reside at $z = 0$, so that $\boldsymbol{J}_k \equiv \boldsymbol{K}_k \equiv \rho_k \equiv m_k \equiv 0$ for $k \geqslant 1$, meaning that only the term $k = 0$ survives in the series (A.1) for these quantities. However, the situation is different for the fields $\boldsymbol{E}_k$, $\boldsymbol{E}_k$, $\boldsymbol{D}_k$ and $\boldsymbol{B}_k$, since these fields exist also at $z \neq 0$. Strictly, $N \to \infty$ for these fields. However, since the discontinuity is purely concentrated at $z = 0$, the Taylor-type series in (A.1) includes only a small number of significant terms, and the series can be safely truncated at some value of N. Choosing some value for N (e.g. $N = 2$), Eqs. (A.10) may be solved recursively for $k = N$ to $k = 1$, with $\boldsymbol{D}_k = \epsilon \boldsymbol{E}_k$ and $\boldsymbol{B}_k = \mu \boldsymbol{H}_k$. This procedure reduces the compatibility

[1]Rigorously, the Dirac delta function disappears upon integrating over z terms of equal discontinuity order.

relations to

$$\hat{\boldsymbol{z}} \times \boldsymbol{H}_0 = 0, \tag{A.11a}$$

$$\hat{\boldsymbol{z}} \times \boldsymbol{E}_0 = 0, \tag{A.11b}$$

$$\hat{\boldsymbol{z}} \cdot \boldsymbol{D}_0 = 0, \tag{A.11c}$$

$$\hat{\boldsymbol{z}} \cdot \boldsymbol{B}_0 = 0. \tag{A.11d}$$

One may now introduce the electric and magnetic polarization densities, $\mathbf{P}$ and $\mathbf{M}$, respectively, to account for the action of the scattering particles forming the metasurface. For this purpose, the standard constitutive relations $\boldsymbol{D} = \epsilon_0 \boldsymbol{E} + \boldsymbol{P}$ and $\boldsymbol{B} = \mu_0(\boldsymbol{H} + \boldsymbol{M})$ are in a form that properly models the first order surface discontinuity in (A.9), namely

$$\boldsymbol{D}_0 = \epsilon_0 \boldsymbol{E}_0 + \boldsymbol{P}_0, \tag{A.12a}$$

$$\boldsymbol{H}_0 = \frac{1}{\mu_0} \boldsymbol{B}_0 - \boldsymbol{M}_0, \tag{A.12b}$$

where $\boldsymbol{P}_0$ and $\boldsymbol{M}_0$ represent the (first-order) electric and magnetic *surface* polarization densities, respectively. In the absence of sources ($\boldsymbol{J}_0 = \boldsymbol{K}_0 = \rho_0 = m_0 = 0$), substitution of (A.12) and application of (A.11) transforms (A.9) into

$$\hat{\boldsymbol{z}} \times [[\boldsymbol{H}]] = j\omega \boldsymbol{D}_0 - \nabla_\parallel \times \boldsymbol{H}_0 = j\omega \boldsymbol{P}_{0,\parallel} + \nabla_\parallel \times \boldsymbol{M}_{0,\mathrm{n}}, \tag{A.13a}$$

$$\hat{\boldsymbol{z}} \times [[\boldsymbol{E}]] = -j\omega \boldsymbol{B}_0 - \nabla_\parallel \times \boldsymbol{E}_0 = -j\omega\mu_0 \boldsymbol{M}_{0,\parallel} + \frac{1}{\epsilon_0} \nabla_\parallel \times \boldsymbol{P}_{0,\mathrm{n}}, \tag{A.13b}$$

$$\hat{\boldsymbol{z}} \cdot [[\boldsymbol{D}]] = -\nabla_\parallel \cdot \boldsymbol{D}_0 = -\nabla_\parallel \cdot \boldsymbol{P}_{0,\parallel}, \tag{A.13c}$$

$$\hat{\boldsymbol{z}} \cdot [[\boldsymbol{B}]] = -\nabla_\parallel \cdot \boldsymbol{B}_0 = -\mu_0 \nabla_\parallel \cdot \boldsymbol{M}_{0,\parallel}, \tag{A.13d}$$

where the subscripts $\parallel$ and n denote transverse and normal components, respectively.

Using the relation $\nabla_\parallel \times (\hat{\boldsymbol{z}}\psi) = -\hat{\boldsymbol{z}} \times \nabla_\parallel \psi$ and the difference notation (2.5), Eqs. (A.13) finally take the form

$$\hat{\boldsymbol{z}} \times \Delta \boldsymbol{H} = j\omega \boldsymbol{P}_\parallel - \hat{\boldsymbol{z}} \times \nabla_\parallel M_z, \tag{A.14a}$$

$$\Delta \boldsymbol{E} \times \hat{\boldsymbol{z}} = j\omega\mu_0 \boldsymbol{M}_\parallel - \nabla_\parallel \left(\frac{P_z}{\epsilon_0} \right) \times \hat{\boldsymbol{z}}, \tag{A.14b}$$

$$\hat{\boldsymbol{z}} \cdot \Delta \boldsymbol{D} = -\nabla \cdot \boldsymbol{P}_\parallel, \tag{A.14c}$$

$$\hat{\boldsymbol{z}} \cdot \Delta \boldsymbol{B} = -\mu_0 \nabla \cdot \boldsymbol{M}_\parallel. \tag{A.14d}$$

APPENDIX B Bianisotropic Poynting Theorem

In the following lines, we present a step-by-step derivation of the time-average bianisotropic Poynting theorem in terms of susceptibility tensors. Even though the Poynting theorem is well documented in the literature [157, 262, 263], it is important to present a detailed derivation of this theorem, using the same conventions and material parameters (susceptibilities) used throughout this document, for the completeness and self-consistency of this work.

The Maxwell-Faraday and the Maxwell-Ampère equations, assuming the presence of electric current sources $\boldsymbol{J}_{\mathrm{e}}$ and magnetic current sources $\boldsymbol{J}_{\mathrm{m}}$, are respectively given by

$$\nabla \times \boldsymbol{E} = -\boldsymbol{J}_{\mathrm{m}} - \frac{\partial \boldsymbol{B}}{\partial t}, \tag{B.1a}$$

$$\nabla \times \boldsymbol{H} = \boldsymbol{J}_{\mathrm{e}} + \frac{\partial \boldsymbol{D}}{\partial t}, \tag{B.1b}$$

with the bianisotropic constitutive relations defined by

$$\boldsymbol{B} = \mu_0(\boldsymbol{H} + \boldsymbol{M}), \qquad \boldsymbol{M} = \overline{\overline{\chi}}_{\mathrm{mm}} \cdot \boldsymbol{H} + \frac{1}{\eta_0}\overline{\overline{\chi}}_{\mathrm{me}} \cdot \boldsymbol{E}, \tag{B.2a}$$

$$\boldsymbol{D} = \epsilon_0 \boldsymbol{E} + \boldsymbol{P}, \qquad \boldsymbol{P} = \epsilon_0 \overline{\overline{\chi}}_{\mathrm{ee}} \cdot \boldsymbol{E} + \frac{1}{c_0}\overline{\overline{\chi}}_{\mathrm{em}} \cdot \boldsymbol{H}. \tag{B.2b}$$

Pre-Multiplying (B.1a) by $\boldsymbol{H}$ and (B.1b) by $\boldsymbol{E}$ and subtracting both equations yields

$$\boldsymbol{H} \cdot (\nabla \times \boldsymbol{E}) - \boldsymbol{E} \cdot (\nabla \times \boldsymbol{H}) = -\boldsymbol{E} \cdot \boldsymbol{J}_{\mathrm{e}} - \boldsymbol{H} \cdot \boldsymbol{J}_{\mathrm{m}} - \boldsymbol{E} \cdot \frac{\partial \boldsymbol{D}}{\partial t} - \boldsymbol{H} \cdot \frac{\partial \boldsymbol{B}}{\partial t}. \tag{B.3}$$

The left-hand side of (B.3) may be simplified using the following vectorial identity:

$$\boldsymbol{H} \cdot (\nabla \times \boldsymbol{E}) - \boldsymbol{E} \cdot (\nabla \times \boldsymbol{H}) = \nabla \cdot (\boldsymbol{E} \times \boldsymbol{H}), \tag{B.4}$$

where the cross product $\boldsymbol{E} \times \boldsymbol{H}$ corresponds to the Poynting vector $\boldsymbol{S}$. This transforms (B.3) into

$$\nabla \cdot \boldsymbol{S} = -\boldsymbol{E} \cdot \boldsymbol{J}_{\mathrm{e}} - \boldsymbol{H} \cdot \boldsymbol{J}_{\mathrm{m}} - \boldsymbol{E} \cdot \frac{\partial \boldsymbol{D}}{\partial t} - \boldsymbol{H} \cdot \frac{\partial \boldsymbol{B}}{\partial t}. \tag{B.5}$$

The two last terms of (B.5) may be further simplified so as to obtain the final form of the bianisotropic Poynting theorem. Here, we show only the derivations for $-\boldsymbol{E} \cdot \frac{\partial \boldsymbol{D}}{\partial t}$ but very similar considerations can be made about $-\boldsymbol{H} \cdot \frac{\partial \boldsymbol{B}}{\partial t}$. Using the fact that $\boldsymbol{D} = \epsilon_0 \boldsymbol{E} + \boldsymbol{P}$, we

have that

$$-\boldsymbol{E}\cdot\frac{\partial \boldsymbol{D}}{\partial t} = -\boldsymbol{E}\cdot\frac{\partial}{\partial t}(\epsilon_0\boldsymbol{E}+\boldsymbol{P}) = -\epsilon_0\boldsymbol{E}\cdot\frac{\partial}{\partial t}\boldsymbol{E} - \boldsymbol{E}\cdot\frac{\partial}{\partial t}\boldsymbol{P}. \tag{B.6}$$

Splitting each term into two equal parts and rearranging them leads to

$$-\boldsymbol{E}\cdot\frac{\partial \boldsymbol{D}}{\partial t} = -\frac{1}{2}\epsilon_0\boldsymbol{E}\cdot\frac{\partial}{\partial t}\boldsymbol{E} - \frac{1}{2}\boldsymbol{E}\cdot\frac{\partial}{\partial t}\boldsymbol{P} - \frac{1}{2}\epsilon_0\boldsymbol{E}\cdot\frac{\partial}{\partial t}\boldsymbol{E} - \frac{1}{2}\boldsymbol{E}\cdot\frac{\partial}{\partial t}\boldsymbol{P}. \tag{B.7}$$

Further slight manipulations of the terms on the right-hand side of (B.7) as well as the addition of the two following extra terms: $\frac{1}{2}\boldsymbol{P}\cdot\frac{\partial}{\partial t}\boldsymbol{E} - \frac{1}{2}\boldsymbol{P}\cdot\frac{\partial}{\partial t}\boldsymbol{E}$, which is a neutral addition since these two terms cancel each other, leads to

$$-\boldsymbol{E}\cdot\frac{\partial \boldsymbol{D}}{\partial t} = -\frac{1}{2}\boldsymbol{E}\cdot\frac{\partial}{\partial t}\epsilon_0\boldsymbol{E} - \frac{1}{2}\boldsymbol{E}\cdot\frac{\partial}{\partial t}\boldsymbol{P} - \frac{1}{2}\frac{\partial}{\partial t}\boldsymbol{E}\cdot\epsilon_0\boldsymbol{E} - \frac{1}{2}\frac{\partial}{\partial t}\boldsymbol{E}\cdot\boldsymbol{P} - \frac{1}{2}\boldsymbol{E}\cdot\frac{\partial}{\partial t}\boldsymbol{P} + \frac{1}{2}\boldsymbol{P}\cdot\frac{\partial}{\partial t}\boldsymbol{E}, \tag{B.8}$$

which, by grouping together the two first, middle and last terms, reduces to

$$-\boldsymbol{E}\cdot\frac{\partial \boldsymbol{D}}{\partial t} = -\frac{1}{2}\boldsymbol{E}\cdot\frac{\partial}{\partial t}(\epsilon_0\boldsymbol{E}+\boldsymbol{P}) - \frac{1}{2}\frac{\partial}{\partial t}\boldsymbol{E}\cdot(\epsilon_0\boldsymbol{E}+\boldsymbol{P}) - \frac{1}{2}\left(\boldsymbol{E}\cdot\frac{\partial}{\partial t}\boldsymbol{P} - \boldsymbol{P}\cdot\frac{\partial}{\partial t}\boldsymbol{E}\right). \tag{B.9}$$

Again making use of $\boldsymbol{D} = \epsilon_0\boldsymbol{E} + \boldsymbol{P}$, we have that

$$-\boldsymbol{E}\cdot\frac{\partial \boldsymbol{D}}{\partial t} = -\frac{1}{2}\boldsymbol{E}\cdot\frac{\partial}{\partial t}\boldsymbol{D} - \frac{1}{2}\frac{\partial}{\partial t}\boldsymbol{E}\cdot\boldsymbol{D} - \frac{1}{2}\left(\boldsymbol{E}\cdot\frac{\partial}{\partial t}\boldsymbol{P} - \boldsymbol{P}\cdot\frac{\partial}{\partial t}\boldsymbol{E}\right). \tag{B.10}$$

Finally, grouping together the two first terms yields

$$-\boldsymbol{E}\cdot\frac{\partial \boldsymbol{D}}{\partial t} = -\frac{1}{2}\frac{\partial}{\partial t}(\boldsymbol{E}\cdot\boldsymbol{D}) - \frac{1}{2}\left(\boldsymbol{E}\cdot\frac{\partial}{\partial t}\boldsymbol{P} - \boldsymbol{P}\cdot\frac{\partial}{\partial t}\boldsymbol{E}\right). \tag{B.11}$$

As said above, very similar considerations can be made for the term $-\boldsymbol{H}\cdot\frac{\partial \boldsymbol{B}}{\partial t}$ in (B.5) which becomes

$$-\boldsymbol{H}\cdot\frac{\partial \boldsymbol{B}}{\partial t} = -\frac{1}{2}\frac{\partial}{\partial t}(\boldsymbol{H}\cdot\boldsymbol{B}) - \frac{\mu_0}{2}\left(\boldsymbol{H}\cdot\frac{\partial}{\partial t}\boldsymbol{M} - \boldsymbol{M}\cdot\frac{\partial}{\partial t}\boldsymbol{H}\right). \tag{B.12}$$

Now substituting (B.11) and (B.12) into (B.5) allows one to express the bianisotropic Poynting theorem as

$$\frac{\partial w}{\partial t} + \nabla\cdot\boldsymbol{S} = -I_{\mathrm{Je}} - I_{\mathrm{Jm}} - I_{\mathrm{P}} - I_{\mathrm{M}}, \tag{B.13}$$

where w is the energy density, $\boldsymbol{S}$ is the Poynting vector and I_{Je}, I_{Jm}, I_{P} and I_{M} correspond

to work done on "charges". These quantities are respectively defined by

$$w = \frac{1}{2}\left(\boldsymbol{E}\cdot\boldsymbol{D} + \boldsymbol{H}\cdot\boldsymbol{B}\right) \tag{B.14a}$$

$$I_{\mathrm{Je}} = \boldsymbol{E}\cdot\boldsymbol{J}_{\mathrm{e}} \tag{B.14b}$$

$$I_{\mathrm{Jm}} = \boldsymbol{H}\cdot\boldsymbol{J}_{\mathrm{m}} \tag{B.14c}$$

$$I_{\mathrm{P}} = \frac{1}{2}\left(\boldsymbol{E}\cdot\frac{\partial}{\partial t}\boldsymbol{P} - \boldsymbol{P}\cdot\frac{\partial}{\partial t}\boldsymbol{E}\right) \tag{B.14d}$$

$$I_{\mathrm{M}} = \frac{\mu_0}{2}\left(\boldsymbol{H}\cdot\frac{\partial}{\partial t}\boldsymbol{M} - \boldsymbol{M}\cdot\frac{\partial}{\partial t}\boldsymbol{H}\right) \tag{B.14e}$$

For the purpose of this work, it is more useful to look at the time-average version of (B.13) which is given by

$$\left\langle\frac{\partial w}{\partial t}\right\rangle + \nabla\cdot\left\langle\boldsymbol{S}\right\rangle = -\left\langle I_{\mathrm{Je}}\right\rangle - \left\langle I_{\mathrm{Jm}}\right\rangle - \left\langle I_{\mathrm{P}}\right\rangle - \left\langle I_{\mathrm{M}}\right\rangle, \tag{B.15}$$

where $\langle\cdot\rangle$ corresponds to the time-average operation. For time-harmonic fields, it is straightforward to show that $\left\langle\frac{\partial w}{\partial t}\right\rangle = 0$ and that $\left\langle\boldsymbol{S}\right\rangle = \frac{1}{2}\,\mathrm{Re}(\boldsymbol{E}\times\boldsymbol{H}^*)$. The terms $\left\langle I_{\mathrm{Je}}\right\rangle$ and $\left\langle I_{\mathrm{Jm}}\right\rangle$ may be expressed as functions of the electric and magnetic susceptibility tensors by first considering that $\boldsymbol{J}_{\mathrm{e}} = \overline{\overline{\sigma}}_{\mathrm{e}}\cdot\boldsymbol{E}$ and $\boldsymbol{J}_{\mathrm{m}} = \overline{\overline{\sigma}}_{\mathrm{m}}\cdot\boldsymbol{H}$. And, secondly, by considering that the electric and magnetic conductivity tensors read

$$\overline{\overline{\sigma}}_{\mathrm{e}} = -\omega\epsilon_0\,\mathrm{Im}(\overline{\overline{\chi}}_{\mathrm{ee}}) = \frac{j\omega\epsilon_0}{2}(\overline{\overline{\chi}}_{\mathrm{ee}} - \overline{\overline{\chi}}^*_{\mathrm{ee}}), \tag{B.16a}$$

$$\overline{\overline{\sigma}}_{\mathrm{m}} = -\omega\mu_0\,\mathrm{Im}(\overline{\overline{\chi}}_{\mathrm{mm}}) = \frac{j\omega\mu_0}{2}(\overline{\overline{\chi}}_{\mathrm{mm}} - \overline{\overline{\chi}}^*_{\mathrm{mm}}), \tag{B.16b}$$

leading to

$$\left\langle I_{\mathrm{Je}}\right\rangle = \frac{1}{2}\,\mathrm{Re}(\boldsymbol{E}^*\cdot\boldsymbol{J}_{\mathrm{e}}) = \frac{1}{2}\,\mathrm{Re}(\boldsymbol{E}^*\cdot\overline{\overline{\sigma}}_{\mathrm{e}}\cdot\boldsymbol{E}) = \frac{1}{4}\,\mathrm{Re}\left[j\omega\epsilon_0\boldsymbol{E}^*\cdot(\overline{\overline{\chi}}_{\mathrm{ee}} - \overline{\overline{\chi}}^*_{\mathrm{ee}})\cdot\boldsymbol{E}\right], \tag{B.17a}$$

$$\left\langle I_{\mathrm{Jm}}\right\rangle = \frac{1}{2}\,\mathrm{Re}(\boldsymbol{H}^*\cdot\boldsymbol{J}_{\mathrm{m}}) = \frac{1}{2}\,\mathrm{Re}(\boldsymbol{H}^*\cdot\overline{\overline{\sigma}}_{\mathrm{m}}\cdot\boldsymbol{H}) = \frac{1}{4}\,\mathrm{Re}\left[j\omega\mu_0\boldsymbol{H}^*\cdot(\overline{\overline{\chi}}_{\mathrm{mm}} - \overline{\overline{\chi}}^*_{\mathrm{mm}})\cdot\boldsymbol{H}\right]. \tag{B.17b}$$

Now, the terms $\left\langle\boldsymbol{I}_{\mathrm{P}}\right\rangle$ and $\left\langle\boldsymbol{I}_{\mathrm{M}}\right\rangle$ in (B.15) are expressed in the frequency domain, which transforms the time-derivatives in (B.14d) and (B.14e) into $\frac{\partial}{\partial t}\rightarrow j\omega$. Consequently, these

terms become

$$\left\langle I_{\mathrm{P}}\right\rangle = \frac{1}{4}\,\mathrm{Re}\left[\boldsymbol{E}^{*}\cdot(j\omega\boldsymbol{P}) - \boldsymbol{P}^{*}\cdot(j\omega\boldsymbol{E})\right] = \frac{1}{4}\,\mathrm{Re}\left[j\omega(\boldsymbol{E}^{*}\cdot\boldsymbol{P} - \boldsymbol{P}^{*}\cdot\boldsymbol{E})\right], \tag{B.18a}$$

$$\left\langle I_{\mathrm{M}}\right\rangle = \frac{\mu_0}{4}\,\mathrm{Re}\left[\boldsymbol{H}^{*}\cdot(j\omega\boldsymbol{M}) - \boldsymbol{M}^{*}\cdot(j\omega\boldsymbol{H})\right] = \frac{1}{4}\,\mathrm{Re}\left[j\omega\mu_0(\boldsymbol{H}^{*}\cdot\boldsymbol{M} - \boldsymbol{M}^{*}\cdot\boldsymbol{H})\right]. \tag{B.18b}$$

Substituting $\boldsymbol{P}$ and $\boldsymbol{M}$ in (B.18) by their definition given in (B.2) transforms (B.18) into

$$\left\langle I_{\mathrm{P}}\right\rangle = \frac{1}{4}\,\mathrm{Re}\left[j\omega\epsilon_0(\boldsymbol{E}^{*}\cdot(\overline{\overline{\chi}}_{\mathrm{ee}}\cdot\boldsymbol{E} + \eta_0\overline{\overline{\chi}}_{\mathrm{em}}\cdot\boldsymbol{H}) - \boldsymbol{E}\cdot(\overline{\overline{\chi}}_{\mathrm{ee}}\cdot\boldsymbol{E} + \eta_0\overline{\overline{\chi}}_{\mathrm{em}}\cdot\boldsymbol{H})^{*})\right], \tag{B.19a}$$

$$\left\langle I_{\mathrm{M}}\right\rangle = \frac{1}{4}\,\mathrm{Re}\left[j\omega\mu_0(\boldsymbol{H}^{*}\cdot(\overline{\overline{\chi}}_{\mathrm{mm}}\cdot\boldsymbol{H} + \overline{\overline{\chi}}_{\mathrm{me}}\cdot\boldsymbol{E}/\eta_0) - \boldsymbol{H}\cdot(\overline{\overline{\chi}}_{\mathrm{mm}}\cdot\boldsymbol{H} + \overline{\overline{\chi}}_{\mathrm{me}}\cdot\boldsymbol{E}/\eta_0)^{*})\right]. \tag{B.19b}$$

Finally, rearranging and simplifying the terms in (B.19) leads to

$$\left\langle I_{\mathrm{P}}\right\rangle = \frac{1}{4}\,\mathrm{Re}\left[j\omega\epsilon_0(\boldsymbol{E}^{*}\cdot(\overline{\overline{\chi}}_{\mathrm{ee}} - \overline{\overline{\chi}}_{\mathrm{ee}}^{\dagger})\cdot\boldsymbol{E} + 2\eta_0\boldsymbol{E}^{*}\cdot\overline{\overline{\chi}}_{\mathrm{em}}\cdot\boldsymbol{H})\right], \tag{B.20a}$$

$$\left\langle I_{\mathrm{M}}\right\rangle = \frac{1}{4}\,\mathrm{Re}\left[j\omega\mu_0(\boldsymbol{H}^{*}\cdot(\overline{\overline{\chi}}_{\mathrm{mm}} - \overline{\overline{\chi}}_{\mathrm{mm}}^{\dagger})\cdot\boldsymbol{H} - 2\boldsymbol{E}^{*}\cdot\overline{\overline{\chi}}_{\mathrm{me}}^{\dagger}\cdot\boldsymbol{H}/\eta_0)\right], \tag{B.20b}$$

where the operator † corresponds to the transpose conjugate operation. The final expression of the time-average bianisotropic Poynting theorem for time-harmonic fields is given by

$$\nabla\cdot\left\langle\boldsymbol{S}\right\rangle = -\left\langle I_{\mathrm{Je}}\right\rangle - \left\langle I_{\mathrm{Jm}}\right\rangle - \left\langle I_{\mathrm{P}}\right\rangle - \left\langle I_{\mathrm{M}}\right\rangle, \tag{B.21}$$

where $\left\langle I_{\mathrm{Je}}\right\rangle$, $\left\langle I_{\mathrm{Jm}}\right\rangle$, $\left\langle I_{\mathrm{P}}\right\rangle$ and $\left\langle I_{\mathrm{M}}\right\rangle$ are respectively provided in (B.17) and (B.20).

The physical interpretation of (B.21) is that the amount of loss or gain that an electromagnetic field experiences when propagating through a volume of a given medium is related to the difference of electromagnetic energy entering and existing that volume. If the medium is perfectly lossless and passive, the divergence of the average Poynting vector is zero, i.e. $\nabla\cdot\left\langle\boldsymbol{S}\right\rangle = 0$, meaning that the amount of electromagnetic energy entering and exiting the medium is equal. In the case of a lossy medium, there is more energy entering than leaving the volume leading to $\nabla\cdot\left\langle\boldsymbol{S}\right\rangle < 0$ and vice-versa for a gain medium where $\nabla\cdot\left\langle\boldsymbol{S}\right\rangle > 0$. Note that the fact that $\nabla\cdot\left\langle\boldsymbol{S}\right\rangle = 0$ is a necessary but not sufficient condition to assert that the medium is passive and lossless since compensation between the terms on the right-hand side of (B.21) may occur.

By substituting (B.17) and (B.20) into (B.21), we obtain an alternative form of the Poynting

theorem which reads

$$\nabla \cdot \langle \boldsymbol{S} \rangle = -\frac{1}{4} \operatorname{Re} \Big[j\omega(\epsilon_0 \boldsymbol{E}^* \cdot (2\overline{\overline{\chi}}_{\mathrm{ee}} - \overline{\overline{\chi}}_{\mathrm{ee}}^* - \overline{\overline{\chi}}_{\mathrm{ee}}^\dagger) \cdot \boldsymbol{E} + \mu_0 \boldsymbol{H}^* \cdot (2\overline{\overline{\chi}}_{\mathrm{mm}} - \overline{\overline{\chi}}_{\mathrm{mm}}^* - \overline{\overline{\chi}}_{\mathrm{mm}}^\dagger) \cdot \boldsymbol{H} + 2k_0 \boldsymbol{E}^* \cdot (\overline{\overline{\chi}}_{\mathrm{me}} - \overline{\overline{\chi}}_{\mathrm{em}}^\dagger) \cdot \boldsymbol{H}) \Big]. \tag{B.22}$$

The general conditions for passivity and losslessness can be easily obtained from (B.22). Assuming that the medium is also reciprocal[1], these relations read

$$\overline{\overline{\chi}}_{\mathrm{ee}}^{\mathrm{T}} = \overline{\overline{\chi}}_{\mathrm{ee}}^*, \quad \overline{\overline{\chi}}_{\mathrm{mm}}^{\mathrm{T}} = \overline{\overline{\chi}}_{\mathrm{mm}}^*, \quad \overline{\overline{\chi}}_{\mathrm{me}}^{\mathrm{T}} = \overline{\overline{\chi}}_{\mathrm{em}}^*. \tag{B.23}$$

[1]The reciprocity conditions are given by $\overline{\overline{\chi}}_{\mathrm{ee}}^{\mathrm{T}} = \overline{\overline{\chi}}_{\mathrm{ee}}, \quad \overline{\overline{\chi}}_{\mathrm{mm}}^{\mathrm{T}} = \overline{\overline{\chi}}_{\mathrm{mm}}, \quad \overline{\overline{\chi}}_{\mathrm{me}}^{\mathrm{T}} = -\overline{\overline{\chi}}_{\mathrm{em}}$.

APPENDIX C Relations Between Susceptibilities and Polarizabilities

Here, we provide the expressions that relate the susceptibilities, used throughout this work, and the polarizabilities, which are at the basis of the synthesis technique developed by the group of Prof. Sergei Tretyakov[1]. The susceptibilities and the polarizabilities are related to each other through the expressions of the microscopic electric and magnetic dipole moments, $\boldsymbol{p}$ and $\boldsymbol{m}$, and the surface polarization densities, $\boldsymbol{P}$ and $\boldsymbol{M}$, as $\boldsymbol{P} = \boldsymbol{p}/S$ and $\boldsymbol{M} = \boldsymbol{m}/S$, where S is the unit cell area. The first step is to express the difference and the average of the fields on both sides of the metasurface using the formalism in [264]. We have that the backward radiated fields from the metasurface induced dipole moments are

$$\boldsymbol{E}_{\text{back,p}} = -\frac{j\omega}{2S}\eta_0\boldsymbol{p}, \qquad \boldsymbol{E}_{\text{back,m}} = \frac{j\omega}{2S}\boldsymbol{n}\times\boldsymbol{m}, \tag{C.1}$$

where the normal vector $\boldsymbol{n} = -\hat{\boldsymbol{z}}$. Similarly, the forward radiated fields are

$$\boldsymbol{E}_{\text{forw,p}} = -\frac{j\omega}{2S}\eta_0\boldsymbol{p}, \qquad \boldsymbol{E}_{\text{forw,m}} = -\frac{j\omega}{2S}\boldsymbol{n}\times\boldsymbol{m}. \tag{C.2}$$

The electric fields on both sides of the metasurface are respectively given by

$$\boldsymbol{E}\big|_{z=0^-} = \boldsymbol{E}_{\text{inc}} + \boldsymbol{E}_{\text{back,p}} + \boldsymbol{E}_{\text{back,m}}, \tag{C.3a}$$

$$\boldsymbol{E}\big|_{z=0^+} = \boldsymbol{E}_{\text{inc}} + \boldsymbol{E}_{\text{forw,p}} + \boldsymbol{E}_{\text{forw,m}}. \tag{C.3b}$$

Noting that, for plane waves propagating along z, the magnetic field may be expressed as $\boldsymbol{H} = -\boldsymbol{n}\times\boldsymbol{E}/\eta_0$, which leads to

$$\boldsymbol{H}\big|_{z=0^-} = -\boldsymbol{n}\times\frac{\boldsymbol{E}_{\text{inc}}}{\eta_0} + \boldsymbol{n}\times\frac{\boldsymbol{E}_{\text{back,p}}}{\eta_0} + \boldsymbol{n}\times\frac{\boldsymbol{E}_{\text{back,m}}}{\eta_0}, \tag{C.4a}$$

$$\boldsymbol{H}\big|_{z=0^+} = -\boldsymbol{n}\times\frac{\boldsymbol{E}_{\text{inc}}}{\eta_0} - \boldsymbol{n}\times\frac{\boldsymbol{E}_{\text{forw,p}}}{\eta_0} - \boldsymbol{n}\times\frac{\boldsymbol{E}_{\text{forw,m}}}{\eta_0}. \tag{C.4b}$$

[1]The following relations have never been published and were originally derived by Viktar Asadchy who, at the time of writing, was pursing a PhD in electromagnetics under the supervision of Prof. Sergei Tretyakov in Aalto University.

Finally, upon insertion of (C.1) and (C.2) into (C.3) and (C.4), the average fields are

$$\boldsymbol{E}_{\mathrm{av}} = \frac{1}{2}\left(\boldsymbol{E}|_{z=0^-} + \boldsymbol{E}|_{z=0^+}\right) = \boldsymbol{E}_{\mathrm{inc}} - \frac{j\omega\eta_0}{2S}\boldsymbol{p}, \tag{C.5a}$$

$$\boldsymbol{H}_{\mathrm{av}} = \frac{1}{2}\left(\boldsymbol{H}|_{z=0^-} + \boldsymbol{H}|_{z=0^+}\right) = \boldsymbol{H}_{\mathrm{inc}} - \frac{j\omega}{2S\eta_0}\boldsymbol{m}. \tag{C.5b}$$

Now that the average fields have been obtained as functions of the induced dipole moments, we may use the microscopic constitutive relations to relate the polarization densities to the polarizabilities. The microscopic constitutive relations, expressed in terms of the incident electromagnetic field and the effective polarizabilities, read [264]

$$\boldsymbol{p} = \overline{\overline{\hat{\alpha}}}_{\mathrm{ee}} \cdot \boldsymbol{E}_{\mathrm{inc}} + \overline{\overline{\hat{\alpha}}}_{\mathrm{em}} \cdot \boldsymbol{H}_{\mathrm{inc}}, \tag{C.6a}$$

$$\boldsymbol{m} = \overline{\overline{\hat{\alpha}}}_{\mathrm{me}} \cdot \boldsymbol{E}_{\mathrm{inc}} + \overline{\overline{\hat{\alpha}}}_{\mathrm{mm}} \cdot \boldsymbol{H}_{\mathrm{inc}}. \tag{C.6b}$$

Substituting (C.5) into (C.6) and making use of the fact that $\boldsymbol{P} = \boldsymbol{p}/S$ and $\boldsymbol{M} = \boldsymbol{m}/S$, leads to

$$\boldsymbol{P} \cdot S = \overline{\overline{\hat{\alpha}}}_{\mathrm{ee}} \cdot \left(\boldsymbol{E}_{\mathrm{av}} + \frac{j\omega\eta_0}{2}\boldsymbol{P}\right) + \overline{\overline{\hat{\alpha}}}_{\mathrm{em}} \cdot \left(\boldsymbol{H}_{\mathrm{av}} + \frac{j\omega}{2\eta_0}\boldsymbol{M}\right), \tag{C.7a}$$

$$\boldsymbol{M} \cdot S = \overline{\overline{\hat{\alpha}}}_{\mathrm{me}} \cdot \left(\boldsymbol{E}_{\mathrm{av}} + \frac{j\omega\eta_0}{2}\boldsymbol{P}\right) + \overline{\overline{\hat{\alpha}}}_{\mathrm{mm}} \cdot \left(\boldsymbol{H}_{\mathrm{av}} + \frac{j\omega}{2\eta_0}\boldsymbol{M}\right). \tag{C.7b}$$

This linear system of equations may be solved so as to express $\boldsymbol{P}$ and $\boldsymbol{M}$ as functions of the effective polarizabilities as

$$\boldsymbol{P} = \overline{\overline{C}}_{\mathrm{p}}^{-1} \cdot \left[\overline{\overline{\hat{\alpha}}}_{\mathrm{ee}} \cdot \boldsymbol{E}_{\mathrm{av}} + \overline{\overline{\hat{\alpha}}}_{\mathrm{em}} \cdot \boldsymbol{H}_{\mathrm{av}} + \overline{\overline{\hat{\alpha}}}_{\mathrm{em}} \frac{j\omega}{2\eta_0} \cdot \left(S\overline{\overline{I}}_{\mathrm{t}} - \overline{\overline{\hat{\alpha}}}_{\mathrm{mm}} \frac{j\omega}{2\eta_0}\right)^{-1} \cdot \left(\overline{\overline{\hat{\alpha}}}_{\mathrm{me}} \cdot \boldsymbol{E}_{\mathrm{av}} + \overline{\overline{\hat{\alpha}}}_{\mathrm{mm}} \cdot \boldsymbol{H}_{\mathrm{av}}\right)\right], \tag{C.8a}$$

$$\boldsymbol{M} = \overline{\overline{C}}_{\mathrm{m}}^{-1} \cdot \left[\overline{\overline{\hat{\alpha}}}_{\mathrm{me}} \cdot \boldsymbol{E}_{\mathrm{av}} + \overline{\overline{\hat{\alpha}}}_{\mathrm{mm}} \cdot \boldsymbol{H}_{\mathrm{av}} + \overline{\overline{\hat{\alpha}}}_{\mathrm{me}} \frac{j\omega\eta_0}{2} \cdot \left(S\overline{\overline{I}}_{\mathrm{t}} - \overline{\overline{\hat{\alpha}}}_{\mathrm{ee}} \frac{j\omega\eta_0}{2}\right)^{-1} \cdot \left(\overline{\overline{\hat{\alpha}}}_{\mathrm{ee}} \cdot \boldsymbol{E}_{\mathrm{av}} + \overline{\overline{\hat{\alpha}}}_{\mathrm{em}} \cdot \boldsymbol{H}_{\mathrm{av}}\right)\right], \tag{C.8b}$$

where $\overline{\overline{I}}_{\mathrm{t}}$ is the tangential unit dyadic and the tensors $\overline{\overline{C}}_{\mathrm{p}}$ and $\overline{\overline{C}}_{\mathrm{m}}$ read

$$\overline{\overline{C}}_{\mathrm{p}} = S\overline{\overline{I}}_{\mathrm{t}} - \overline{\overline{\hat{\alpha}}}_{\mathrm{ee}} \frac{j\omega\eta_0}{2} + \frac{\omega^2}{4}\overline{\overline{\hat{\alpha}}}_{\mathrm{em}} \cdot \left(S\overline{\overline{I}}_{\mathrm{t}} - \overline{\overline{\hat{\alpha}}}_{\mathrm{mm}} \frac{j\omega}{2\eta_0}\right)^{-1} \cdot \overline{\overline{\hat{\alpha}}}_{\mathrm{me}}, \tag{C.9a}$$

$$\overline{\overline{C}}_{\mathrm{m}} = S\overline{\overline{I}}_{\mathrm{t}} - \overline{\overline{\hat{\alpha}}}_{\mathrm{mm}} \frac{j\omega}{2\eta_0} + \frac{\omega^2}{4}\overline{\overline{\hat{\alpha}}}_{\mathrm{me}} \cdot \left(S\overline{\overline{I}}_{\mathrm{t}} - \overline{\overline{\hat{\alpha}}}_{\mathrm{ee}} \frac{j\omega\eta_0}{2}\right)^{-1} \cdot \overline{\overline{\hat{\alpha}}}_{\mathrm{em}}. \tag{C.9b}$$

In (C.8), the polarization densities, $\boldsymbol{P}$ and $\boldsymbol{M}$, have been expressed in terms of the microscopic effective polarizabilities. They can now be related to the macroscopic susceptibilities via the constitutive relations used throughout this work and which are given by

$$\boldsymbol{P} = \epsilon_0 \overline{\overline{\chi}}_{\mathrm{ee}} \cdot \boldsymbol{E}_{\mathrm{av}} + \overline{\overline{\chi}}_{\mathrm{em}} \frac{1}{c_0} \cdot \boldsymbol{H}_{\mathrm{av}}, \tag{C.10a}$$

$$\boldsymbol{M} = \overline{\overline{\chi}}_{\mathrm{mm}} \cdot \boldsymbol{H}_{\mathrm{av}} + \overline{\overline{\chi}}_{\mathrm{me}} \frac{1}{\eta_0} \cdot \boldsymbol{E}_{\mathrm{av}}. \tag{C.10b}$$

Finally, the susceptibilities can be expressed as functions of the polarizabilities by inserting (C.8) into (C.10) and associating the terms that multiply the average electric and magnetic fields in both equations. This leads to the following relations

$$\overline{\overline{\chi}}_{\mathrm{ee}} = \frac{1}{\epsilon_0} \overline{\overline{C}}_{\mathrm{p}}^{-1} \cdot \left[\overline{\overline{\hat{\alpha}}}_{\mathrm{ee}} + \frac{j\omega}{2\eta_0} \overline{\overline{\hat{\alpha}}}_{\mathrm{em}} \cdot \left(S \overline{\overline{I}}_{\mathrm{t}} - \overline{\overline{\hat{\alpha}}}_{\mathrm{mm}} \frac{j\omega}{2\eta_0} \right)^{-1} \cdot \overline{\overline{\hat{\alpha}}}_{\mathrm{me}} \right], \tag{C.11a}$$

$$\overline{\overline{\chi}}_{\mathrm{em}} = c_0 \overline{\overline{C}}_{\mathrm{p}}^{-1} \cdot \left[\overline{\overline{\hat{\alpha}}}_{\mathrm{em}} + \frac{j\omega}{2\eta_0} \overline{\overline{\hat{\alpha}}}_{\mathrm{em}} \cdot \left(S \overline{\overline{I}}_{\mathrm{t}} - \overline{\overline{\hat{\alpha}}}_{\mathrm{mm}} \frac{j\omega}{2\eta_0} \right)^{-1} \cdot \overline{\overline{\hat{\alpha}}}_{\mathrm{mm}} \right], \tag{C.11b}$$

$$\overline{\overline{\chi}}_{\mathrm{me}} = \eta_0 \overline{\overline{C}}_{\mathrm{m}}^{-1} \cdot \left[\overline{\overline{\hat{\alpha}}}_{\mathrm{me}} + \frac{j\omega\eta_0}{2} \overline{\overline{\hat{\alpha}}}_{\mathrm{me}} \cdot \left(S \overline{\overline{I}}_{\mathrm{t}} - \overline{\overline{\hat{\alpha}}}_{\mathrm{ee}} \frac{j\omega\eta_0}{2} \right)^{-1} \cdot \overline{\overline{\hat{\alpha}}}_{\mathrm{ee}} \right], \tag{C.11c}$$

$$\overline{\overline{\chi}}_{\mathrm{mm}} = \overline{\overline{C}}_{\mathrm{m}}^{-1} \cdot \left[\overline{\overline{\hat{\alpha}}}_{\mathrm{mm}} + \frac{j\omega\eta_0}{2} \overline{\overline{\hat{\alpha}}}_{\mathrm{me}} \cdot \left(S \overline{\overline{I}}_{\mathrm{t}} - \overline{\overline{\hat{\alpha}}}_{\mathrm{ee}} \frac{j\omega\eta_0}{2} \right)^{-1} \cdot \overline{\overline{\hat{\alpha}}}_{\mathrm{em}} \right]. \tag{C.11d}$$

We see that the polarizabilities are related to the susceptibilities in a non-straightforward fashion. As can be seen, for instance, the purely electric susceptibility, $\overline{\overline{\chi}}_{\mathrm{ee}}$, is related to all bianisotropic polarizabilities except in the case where the magnetoelectric coupling tensors, $\overline{\overline{\hat{\alpha}}}_{\mathrm{em}}$ and $\overline{\overline{\hat{\alpha}}}_{\mathrm{me}}$, are zero.

APPENDIX D Nonlinear Metasurface Simulation in Finite-Difference Time-Domain

Here, we present how the metasurface 1D finite-difference time-domain (FDTD) simulation scheme developed in [3] may be modified to account for nonlinear susceptibility components. We use the exact same conventions as in [3] to avoid any possible confusion.

This FDTD scheme consists in using traditional FDTD update equations everywhere on the simulation grid at the exception of the nodes that are before and after the metasurface. For these specific nodes, the update equations are modified, using the GSTCs relations, to take into account the effect of the metasurface. The conventional FDTD 1D equations, for a Yee grid, are given by

$$H_x^{n+\frac{1}{2}}(i) = H_x^{n-\frac{1}{2}}(i) + \frac{\Delta t}{\mu_0 \Delta z}\left(E_y^n(i+1) - E_y^n(i)\right), \tag{D.1a}$$

$$E_y^n(i) = E_y^{n-1}(i) + \frac{\Delta t}{\epsilon_0 \Delta z}\left(H_x^{n-\frac{1}{2}}(i) - H_x^{n-\frac{1}{2}}(i-1)\right), \tag{D.1b}$$

where i and n correspond to the cell number and time coordinates and Δz and Δt are their respective position and time step. In the FDTD scheme, the metasurface is inserted at a virtual node in between the positions $i = n_d$ and $i = n_d + 1$, corresponding to a position between an electric and a magnetic node, as depicted in Fig. D.1. To take into account the effect of the metasurface, a virtual electric node is created right before the metasurface (at $i = 0^-$) and a virtual magnetic node is created right after the metasurface (at $i = 0^+$). From (D.1), the update equations for $H_x^{n+\frac{1}{2}}(n_d)$ and $E_y^n(n_d+1)$ are connected to these virtual nodes via the following relations

$$H_x^{n+\frac{1}{2}}(n_d) = H_x^{n-\frac{1}{2}}(n_d) + \frac{\Delta t}{\mu_0 \Delta z}\left(E_y^n(0^-) - E_y^n(n_d)\right), \tag{D.2a}$$

$$E_y^n(n_d+1) = E_y^{n-1}(n_d+1) + \frac{\Delta t}{\epsilon_0 \Delta z}\left(H_x^{n-\frac{1}{2}}(n_d+1) - H_x^{n-\frac{1}{2}}(0^+)\right), \tag{D.2b}$$

where the value of the electric and magnetic fields at the virtual nodes are obtained from the GSTCs relations given by

$$\Delta H_x = \epsilon_0 \chi_{\text{ee}}^{(1)} \frac{\partial}{\partial t} E_{y,\text{av}} + \epsilon_0 \chi_{\text{ee}}^{(2)} \frac{\partial}{\partial t} E_{y,\text{av}}^2, \tag{D.3a}$$

$$\Delta E_y = \mu_0 \chi_{\text{mm}}^{(1)} \frac{\partial}{\partial t} H_{x,\text{av}} + \mu_0 \chi_{\text{mm}}^{(2)} \frac{\partial}{\partial t} H_{x,\text{av}}^2. \tag{D.3b}$$

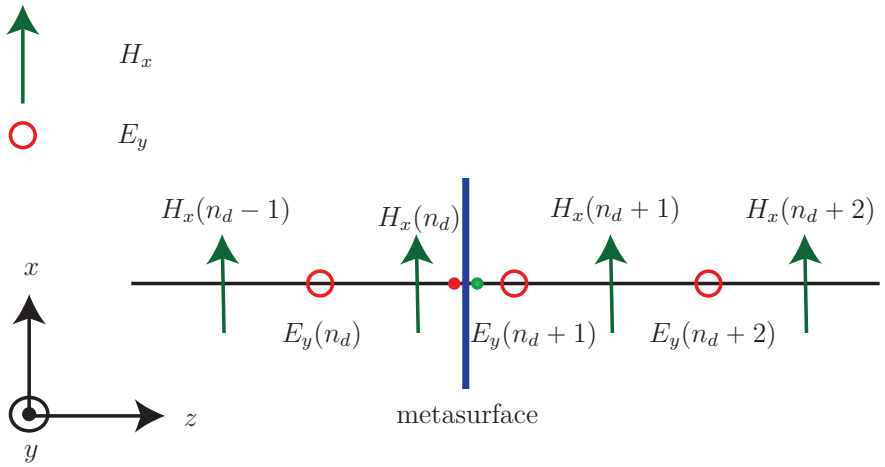

Figure D.1 1D FDTD Yee grid with a metasurface placed in between the nodes. The two small circles, before and after the metasurface, represent the electric and magnetic virtual nodes, respectively. Original image from [3].

Note that, to remain consistent with the developments in [3], the GSTCs are here given for y-polarized waves instead of x-polarized waves as in (2.60). Using (D.3), the expression of the electric and magnetic fields at the virtual nodes in (D.2) read

$$H_x^{n-\frac{1}{2}}(0^+) = H_x^{n-\frac{1}{2}}(n_d) + \frac{\epsilon_0\chi_{\mathrm{ee}}^{(1)}}{\Delta t}\left(E_{y,\mathrm{av}}^{n} - E_{y,\mathrm{av}}^{n-1}\right) + \frac{\epsilon_0\chi_{\mathrm{ee}}^{(2)}}{\Delta t}\left((E_{y,\mathrm{av}}^{n})^2 - (E_{y,\mathrm{av}}^{n-1})^2\right), \tag{D.4a}$$

$$E_y^{n}(0^-) = E_y^{n}(n_d+1) - \frac{\mu_0\chi_{\mathrm{mm}}^{(1)}}{\Delta t}\left(H_{x,\mathrm{av}}^{n+\frac{1}{2}} - H_{x,\mathrm{av}}^{n-\frac{1}{2}}\right) - \frac{\mu_0\chi_{\mathrm{mm}}^{(2)}}{\Delta t}\left((H_{x,\mathrm{av}}^{n+\frac{1}{2}})^2 - (H_{x,\mathrm{av}}^{n-\frac{1}{2}})^2\right), \tag{D.4b}$$

where the average electric field is defined by

$$E_{y,\mathrm{av}}^{n} = \frac{E_y^{n}(n_d) + E_y^{n}(n_d+1)}{2}, \tag{D.5}$$

and similarly for the average magnetic field. Substituting (D.4) along with (D.5) into (D.2) leads to two quadratic equations that may be independently solved to obtain the final update equations. These two quadratic equations yield, each one of them, two possible solutions but only one of the two corresponds to a physical behavior. The two solutions that produce physical results are

$$H_x^{n+\frac{1}{2}}(n_d) = \frac{-(2dz + \chi_{\mathrm{ee}}^{(1)} + H_x^{n+\frac{1}{2}}(n_d+1)\chi_{\mathrm{ee}}^{(2)})\mu_0 + \sqrt{\Delta_{\mathrm{h}}}}{\mu_0\chi_{\mathrm{ee}}^{(1)}}, \tag{D.6a}$$

$$E_y^{n}(n_d+1) = \frac{-(2dz + \chi_{\mathrm{mm}}^{(1)} + E_y^{n}(n_d)\chi_{\mathrm{mm}}^{(2)})\epsilon_0 + \sqrt{\Delta_{\mathrm{e}}}}{\epsilon_0\chi_{\mathrm{mm}}^{(1)}}, \tag{D.6b}$$

where the discriminant Δ_{h} is given by

$$\begin{aligned}\Delta_{\mathrm{h}} =&\mu_0\Big\{4\Delta t(E_y^n(n_d+1)-E_y^n(n_d))\chi_{\mathrm{ee}}^{(2)}+\mu_0\Big[4\Delta z^2+(\chi_{\mathrm{ee}}^{(1)}+\\ &(H_x^{n-\frac{1}{2}}(n_d)+H_x^{n+\frac{1}{2}}(n_d+1))\chi_{\mathrm{ee}}^{(2)})^2+4\Delta z(\chi_{\mathrm{ee}}^{(1)}+\\ &(H_x^{n-\frac{1}{2}}(n_d)+H_x^{n+\frac{1}{2}}(n_d+1))\chi_{\mathrm{ee}}^{(2)})\Big]\Big\},\end{aligned} \tag{D.7}$$

and the discriminant Δ_{e} is given by

$$\begin{aligned}\Delta_{\mathrm{e}} =&\epsilon_0\Big\{4\Delta t(H_x^{n-\frac{1}{2}}(n_d+1)-H_x^{n-\frac{1}{2}}(n_d))\chi_{\mathrm{mm}}^{(2)}+\epsilon_0\Big[4\Delta z^2+(\chi_{\mathrm{mm}}^{(1)}+\\ &(E_y^{n-1}(n_d)+E_y^{n-1}(n_d+1))\chi_{\mathrm{mm}}^{(2)})^2+4\Delta z(\chi_{\mathrm{mm}}^{(1)}+\\ &(E_y^{n}(n_d)+E_y^{n-1}(n_d+1))\chi_{\mathrm{mm}}^{(2)})\Big]\Big\}.\end{aligned} \tag{D.8}$$

Because of the square roots in (D.6), the update equations may lead to nonphysical behaviors depending on the values of the two discriminants. This limits the range of allowable values that the susceptibilities and the amplitude of the incident field may take.

APPENDIX E List of Publications and Awards

Peer-Reviewed Journal Publications

1. G. Lavigne, K. Achouri, V. Asadchy, S. Tretyakov, and C. Caloz, "Refracting metasurfaces without spurious diffraction," *arXiv preprint arXiv:1705.09286v2*, 2017.

2. N. Chamanara, K. Achouri, and C. Caloz, "Efficient analysis of metasurfaces in terms of spectral-domain GSTC integral equations," *arXiv preprint arXiv:1704.06801*, 2017

3. K. Achouri, Y. Vahabzadeh, and C. Caloz, "Mathematical synthesis and analysis of nonlinear metasurfaces," *arXiv preprint arXiv:1703.09082*, 2017.

4. K. Achouri and C. Caloz, "Space-wave routing via surface waves using a metasurface system," *arXiv preprint arXiv:1612.05576*, 2016

5. L. Chen, K. Achouri, E. Kallos, and C. Caloz, "Simultaneous enhancement of light extraction and spontaneous emission using a partially reflecting metasurface cavity," *Phys. Rev. A*, vol. 95, p. 053808, May 2017

6. S. Taravati, B. A. Khan, S. Gupta, K. Achouri, and C. Caloz, "Nonreciprocal nongyrotropic magnetless metasurface," *IEEE Trans. Antennas Propag.*, vol. PP, no. 99, pp. 1–1, 2017.

7. K. Achouri, A. Yahyaoui, S. Gupta, H. Rmili, and C. Caloz, "Dielectric resonator metasurface for dispersion engineering," *IEEE Trans. Antennas Propag.*, vol. 65, no. 2, pp. 673–680, Feb 2017

8. K. Achouri, G. Lavigne, and C. Caloz, "Comparison of two synthesis methods for birefringent metasurfaces," *J. Appl. Phys.*, vol. 120, no. 23, p. 235305, 2016

9. Y. Vahabzadeh, K. Achouri, and C. Caloz, "Simulation of metasurfaces in finite difference techniques," *IEEE Trans. Antennas Propag.*, vol. 64, no. 11, pp. 4753–4759, 2016

10. K. Achouri, G. Lavigne, M. A. Salem, and C. Caloz, "Metasurface spatial processor for electromagnetic remote control," *IEEE Trans. Antennas Propag.*, vol. 64, no. 5, pp. 1759–1767, 2016

11. K. Achouri, B. A. Khan, S. Gupta, G. Lavigne, M. A. Salem, and C. Caloz, "Synthesis of electromagnetic metasurfaces: principles and illustrations," *EPJ Applied Metamaterials*, vol. 2, p. 12, 2015

12. K. Achouri, M. A. Salem, and C. Caloz, "General metasurface synthesis based on susceptibility tensors," *IEEE Trans. Antennas Propag.*, vol. 63, no. 7, pp. 2977–2991, July 2015

13. M. A. Salem, K. Achouri, and C. Caloz, "Metasurface synthesis for time-harmonic waves: Exact spectral and spatial methods," *Prog. Electromagn. Res.*, (invited), vol. 149, pp. 205–216, 2014

Conference Publications

1. K. Achouri and C. Caloz, "Scattering from a nonlinear metasurface," *in 11th International Congress on Advanced Electromagnetic Materials in Microwaves and Optics (METAMATERIALS)*, 2017, (to be published)

2. G. Lavigne, K. Achouri, C. Caloz, V. Asadchy, and S. Tretyakov, "Perfectly refractive metasurface using bianisotropy," *in IEEE International Symposium on Antennas and Propagation (APSURSI)*, 2017, (to be published)

3. K. Achouri and C. Caloz, "Metasurface solar sail," *in IEEE International Symposium on Antennas and Propagation (APSURSI)*, 2017, (to be published)

4. K. Achouri and C. Caloz, "Controllable angular scattering with a bianisotropic metasurface," *in IEEE International Symposium on Antennas and Propagation (APSURSI)*, 2017, (to be published)

5. L. Chen, K. Achouri, E. Kallos, and C. Caloz, "Manipulating light in nanophotonics devices using double-metasurface cavity," *in IEEE International Symposium on Antennas and Propagation (APSURSI)*, 2017, (to be published)

6. C. Caloz, K. Achouri, G. Lavigne, Y. Vahabzadeh, L. Chen, and N. Chamanara, "A guided tour in metasurface land: discontinuity conditions, design and applications," *in IEEE International Conference on Computational Electromagnetics (ICCEM)*, 2017, (to be published)

7. N. Chamanara, Y. Vahabzadeh, K. Achouri, and C. Caloz, "Exact polychromatic metasurface design: The GSTC approach," *in 10th International Congress on Advanced*

Electromagnetic Materials in Microwaves and Optics (METAMATERIALS), Sept 2016, pp. 91–93

8. K. Achouri and C. Caloz, "Surfacewave routing of beams by a transparent birefringent metasurface," *in 10th International Congress on Advanced Electromagnetic Materials in Microwaves and Optics (METAMATERIALS)*, Sept 2016, pp. 13–15

9. K. Achouri and C. Caloz, "Metasurface diffraction orders analysis," *in IEEE International Symposium on Antennas and Propagation (APSURSI)*, June 2016, pp. 1081–1082

10. K. Achouri, B. A. Khan, C. Caloz, V. Asadchy, and S. Tretyakov, "Synthesis of a nongyrotropic nonreciprocal metasurface as an equivalent to a moving medium," *in IEEE International Symposium on Antennas and Propagation (APSURSI)*, June 2016, pp. 371–372

11. N. Chamanara, Y. Vahabzadeh, K. Achouri, and C. Caloz, "Spacetime processing metasurfaces: GSTC synthesis and prospective applications," *in IEEE International Symposium on Antennas and Propagation (APSURSI)*, June 2016, pp. 365–366

12. C. Caloz, K. Achouri, Y. Vahabzadeh, and N. Chamanara, "Spacetime metasurfaces," *in Photonics North (PN)*, May 2016, pp. 1–2

13. S. Gupta, K. Achouri, and C. Caloz, "All-pass metasurfaces based on interconnected dielectric resonators as a spatial phaser for real-time analog signal processing," *in IEEE Conference on Antenna Measurements Applications (CAMA)*, Nov 2015, pp. 1–3

14. K. Achouri, M. A. Salem, and C. Caloz, "Electromagnetic metasurface performing up to four independent wave transformations," *in IEEE Conference on Antenna Measurements Applications (CAMA)*, Nov 2015, pp. 1–3

15. K. Achouri, M. A. Salem, and C. Caloz, "Improvement of metasurface continuity conditions," *in International Symposium on Antennas and Propagation (ISAP)*, Nov 2015, pp. 1–3

16. K. Achouri, M. A. Salem, and C. Caloz, "Transistor metasurface," *in 9th International Congress on Advanced Electromagnetic Materials in Microwaves and Optics (METAMATERIALS)*, Sept 2015, pp. 1–3

17. M. A. Salem, K. Achouri, C. Caloz, E. Kallos, and G. Palikaras, "Cavity-backed non-uniform partially reflective metasurface (PRM) for enhanced directivity and power

extraction," *in 9th International Congress on Advanced Electromagnetic Materials in Microwaves and Optics (METAMATERIALS)*, Sept 2015, pp. 271–273

18. K. Achouri, M. A. Salem, and C. Caloz, "Birefringent generalized refractive metasurface," *in IEEE International Symposium on Antennas and Propagation USNC/URSI National Radio Science Meeting*, July 2015, pp. 878–879

19. K. Achouri, M. A. Salem, and C. Caloz, "Metasurface susceptibility range dependence on longitudinal phase and polarization angle," *in 9th European Conference on Antennas and Propagation (EuCAP)*, May 2015, pp. 1–3

20. C. Caloz, M. Salem, and K. Achouri, "Metasurfaces for moulding waves: Synthesis and implementation roads," *in 8th International Congress on Advanced Electromagnetic Materials in Microwaves and Optics (METAMATERIALS)*, 2014, pp. 73–75

21. K. Achouri, M. Salem, and C. Caloz, "Metasurface synthesis using reduced susceptibility tensors," *in 8th International Congress on Advanced Electromagnetic Materials in Microwaves and Optics (METAMATERIALS)*, 2014, pp. 4–6

Awards

1. *1st Prize*, Student Paper Competition in Electromagnetic Materials in Microwaves and Optics (METAMATERIALS), Marseille, France, August-September 2017.

2. *Finalist*, Student Paper Competition in Electromagnetic Materials in Microwaves and Optics (METAMATERIALS), Chania, Greece, September 2016.

3. *Honorable Mention*, Student Paper Competition in IEEE Antenna and Propagation Symposium (AP-S), Vancouver, Canada, June 2015.